Preparation, Functionalization, and Characterization of Electro-spun and Phase-inverted Cellulose acetate Membranes for Advanced Wastewater Treatment Applications

Thesis

Submitted in Partial Fulfilment of the Requirements
For the degree of

DOCTOR OF PHILOSOPHY

by

Kibrom Alebel Gebru

Department of Chemical Engineering
Indian Institute of Technology Guwahati
Guwahati-781039, Assam, India
February, 2017

Preparation, Functionalization, and Characterization of Electro-spun and Phase-inverted Cellulose acetate Membranes for Advanced Wastewater Treatment Applications

Kibrom Alebel Gebru

Preparation, Functionalization, and Characterization of Electro-spun and Phase-inverted Cellulose acetate Membranes for Advanced Wastewater Treatment Applications

Thesis
Submitted in Partial Fulfilment of the Requirements
For the degree of

DOCTOR OF PHILOSOPHY

by

Kibrom Alebel Gebru

Roll No.: 136107031

Supervisor:

Chandan Das

Department of Chemical Engineering
Indian Institute of Technology Guwahati
Guwahati-781039, Assam, India
February, 2017

DEDICATION

To my Family

and

My Lovely wife, Luwam Luel (Leena)

DECLARATION

I hereby declare that the work embodied in this thesis entitled **'Preparation, Functionalization, and Characterization of Electro-spun and Phase-inverted Cellulose acetate Membranes for Advanced Wastewater Treatment Applications'** is the outcome of my investigations carried out under the supervision of **Dr. Chandan Das**, Department of Chemical Engineering, Indian Institute of Technology Guwahati, Assam, India, for the award of the degree of Doctor of Philosophy. This work has not been submitted elsewhere for any degree to the best of my knowledge and belief.

Date:

Place: Guwahati

Kibrom Alebel Gebru
(Roll No. 136107031)
Department of Chemical Engineering
IIT Guwahati
Guwahati-781 039, Assam, India

भारतीय प्रौद्योगिकी संस्थान गुवाहाटी
गुवाहाटी ७८१ ०३९, असम, भारत
Indian Institute of Technology Guwahati
Guwahati 781 039, Assam, India

CERTIFICATE

It is certified that the work contained in the thesis entitled "**Preparation, Functionalization, and Characterization of Electro-spun and Phase-inverted Cellulose acetate Membranes for Advanced Wastewater Treatment Applications**", has been carried out under my guidance and supervision. The work documented in this thesis has not been submitted to any other University or Institute for the award of any other degree or diploma.

Date:

[Dr. Chandan Das]
Associate Professor
Department of Chemical Engineering
Indian Institute of Technology Guwahati
Guwahati-781039, India

ACKNOWLEDGEMENTS

Firstly, I would like to express my deepest appreciation and sincere gratitude to my supervisor, ***Dr. Chandan Das****, for the continuous support, instructions, encouragement, patience, motivation, and immense knowledge he provides to me throughout my PhD study at Indian Institute of Technology Guwahati. Undertaking this PhD work has been a really transformative experience for me, and it would not have been achievable without the support and guidance of him.*

Besides my supervisor, I would also like to thank the members of my doctoral committee: ***Prof. Mihir K. Purkait, Dr. Vaibhav V. Goud****,* ***Dr. Animes Kumar Golder,*** *Department of Chemical Engineering,* ***Prof. Pranab K. Ghosh****, Department of Civil Engineering, for their insightful comments, valuable suggestions, and contribution to my research work.*

I am also sincerely thankful to ***Dr. Mahuya De****,* ***Prof. Kaustubha Mohanty****,* ***Prof. Ramgopal Uppaluri****, Department of Chemical Engineering, and* ***Prof. Pranab K. Ghosh,*** *Department of Civil Engineering, for providing me an immense knowledge and understanding of courses like, Characterization of Materials (CL 514), Membranes (CL 629), Optimization Techniques (CL 615), and Industrial Wastewater Pollution Control (CE 664), respectively, which I found all the courses were supportive enough during my PhD work.*

I gratefully acknowledge the ***Ministry of Education (MOE), Government of Ethiopia****, for funding my research work. I am also grateful to* ***Adigrat University*** *for giving me this opportunity to study abroad.*

I am thankful to all the faculty members and students of the Department of Chemical Engineering for their generous cooperation during my PhD tenure in the department. I am also grateful to all staff members, Laboratory superintendents, especially

*to **Mr. Harsaraj Biswanath, Dr. Lukumoni Borah**, and **Mr. Jayanta Kumar Mout** for their sincere cooperation during my entire research work.*

*I am thankful to **Prof. A. Srinivasan** and his former PhD scholar **Dr. Nisha Shankhwar**, Department of Physics, for allowing me to use electro-spinning set-up in their laboratory. I am also grateful to **Prof. Bishnupada Mandal** and **Dr. Vimal Katiyar**, Department of chemical engineering, for allowing me their research facilities.*

*I am sincerely thankful to the **Central Instruments Facility** of IIT Guwahati for allowing me to carry out characterization of my samples using instruments such as, **Field Emission Scanning Electron Microscope (FESEM), Transmission Electron Microscope (TEM), Atomic Force Microscope (AFM), Surface Area and pore size analyser,** and **600 MHz Nuclear Magnetic Resonance (NMR) Spectrometer etc.,** which has been essential in this research work. I am also grateful to acknowledge the cooperative behaviour of **Mr. Kh. Kesho Singh**, Technical Superintendent, Central Instruments Facility, IIT Guwahati and all the operators assigned to these instruments.*

*I am grateful to all the Ethiopian students residing at Indian Institute of Technology Guwahati. Special thanks to **Mr. Abdisa Jabasa, Mr. Ali Shemsedin, Mr. Melakuu Tesfaye, Mr. Habtom Teklu,** and **Mr. Endalu Lema** for their friendly support and assistance.*

*I am thankful to my lab mates: My seniors **Dr. Manish Kumar Sinha, Dr. Vijay Singh, Dr. Arijit Das, Dr. Sujoy Bose, Mr. Suman Saha**, and my batch and juniors **Mr. Abhishek Shukla, Mr. Amit Baran Das, Mr. Kulbhushan Samal, Mr. Abhradip Pal, Ms. Sushma Chakraborty, and Ms. Aritra Das** for the enjoyable and memorable working experience with them.*

Special thanks to my family who raised me with love and supported me in all my pursuits. Words cannot express how grateful I am to my mother, my mother-in-law, father, father-in-law, brothers, and sisters for all of the sacrifices that you've made on my

behalf. Your prayer for me was what sustained me thus far. My family's support is very important during every stage of my PhD work even they are far away from me. Thanks for their continuous encouragement and motivation. And now, the most important person in my life: my wife, ***Luwam Luel****. I am very lucky to have you in my life. How can I ever thank you for all you have done for me. Most of all for your love, support, encouragement, and patience during the stages of this PhD work is so appreciated. Thank you, and I Love you.*

Finally, I thank my Almighty God, for letting me through all the difficulties, who is obviously the one has always guided me to work on the right path of life.

Kibrom Alebel Gebru

Abstract

Firstly, the background knowledge of this work for better understanding of the types of membranes, membrane preparation techniques, functionalization, characterization, and applications are investigated. Membrane technology presents an attractive character comprising of easy manufacturing, modification, operation, and compactness. Several membrane preparation techniques are assessed and compared in detail. Moreover, the functionalization using physical blending and grafting methods for the modification of polymer and/or membrane are discussed. Finally, the possible applications of the membrane processes have been extensively discussed for water and wastewater treatments.

Secondly, a detailed literature review about the preparation, modification and application of the polymeric membranes were discussed. A particular emphasises given to the phase inversion and electro-spinning techniques of membrane preparations. On the other hand, the functionalization and/or grafting effects on the resultant membrane structures were assessed regarding their specific applications. Moreover, the possible scopes for further enhancement on the preparation and modifications of the membranes are also identified. Furthermore, the specific objectives on the preparation, characterization, modification, and application of the polymeric membranes have been discussed extensively. Furthermore, valuable information on the chemicals used, methods of membrane preparation, and characterization techniques were provided. Detailed information on the preparation procedures, physicochemical and instrumental characterization techniques are also presented.

An empirical investigation into the impacts of time duration, voltage supply, concentration, and flow rate on the membrane average fiber diameter and surface pore size distribution was done using response surface methodology (RSM) based on central compact design (CCD) are presented. Additionally, the effect of glutaraldehyde on membrane crosslinking was also assessed for further studies. Secondly, hybrid membranes from cellulose acetate (CA) and titanium oxide (TiO_2) nanoparticles (NPs) were fabricated using a novel electro-spinning technique and evaluated as an adsorbent for the elimination of lead and copper metal ions. The impact of TiO_2 NPs contents on the electro-spun membranes matrix was studied in detailed. The impacts of various adsorption parameters, namely, pH, the amount of TiO_2 nanoparticles, contact time, temperature, and kinetics of metal uptake

were investigated using batch adsorption experiments. The model isotherms, such as Dubinin–Radushkevich (D-R), Freundlich, and Langmuir were used to analyse the adsorption equilibrium data. Both pseudo first-order and pseudo second order were preferred for kinetic model study.

An investigation on the effects of additives and solvents in the characteristics and performances of cellulose acetate (CA) ultrafiltration membranes was done. The effects of two different hydrophilic additives and two solvents on the membrane morphological structure, permeability property, and anti-fouling performances of cellulose acetate (CA) ultrafiltration membranes were also investigated. During the phase-inversion process cellulose acetate was selected as membrane forming polymer; polyethylene glycol (PEG) and polyvinyl pyrrolidone (PVP) were used as additives; acetone (Ac): N, N-Dimethylacetamide (DMAc) and N, N-Dimethylformamide (DMF) were used as solvents; and deionized (DI) water was used in the coagulation bath. All the prepared membranes were characterised in terms of hydraulic permeability (P_m), membrane resistance, average pore radius, and hydrophilicity. The top surface and cross-sectional view of the prepared membranes were also observed by using field emission scanning electron microscopy. Membrane fouling and rejection experimentations were done using a stirred batch-cell filtration set-up. The experimental studies of fouling/rinsing cycles, rejection, and permeate fluxes were used to investigate the effect of PEG and PVP additives and effect of the two solvents on the fabricated membranes using bovine serum albumin (BSA) as a model protein. Secondly, Modified cellulose acetate (CA) membranes were prepared by dissolving the polymers in a mixture of acetone (AC) and N, N- dimethylacetamide (DMAc) (70:30) solvent and deionized (DI) water were used in the coagulation bath. Effects of PEG additive and TiO_2 NPs on the preparation of phase-inverted CA ultrafiltration membrane were investigated in terms of morphology, equilibrium water content (EWC), pure water flux (PWF), hydraulic resistance, thermal stability, water contact angle (WCA) and anti-fouling performance. The anti-fouling performance and the flux recovery potential of the membranes were investigated using bovine serum albumin (BSA) protein. Thirdly, fouling resistant ultrafiltration membranes based on the blends of PVP, TiO_2 nanoparticles and cellulose acetate, CA-PVP-TiO_2 (CATP), for removal of bovine serum albumin (BSA) were prepared by using phase inversion process. The influences of PVP and TiO_2 on the preparation of phase inverted cellulose acetate (CA) ultrafiltration membrane were explored in terms of morphology study, equilibrium water content (EWC), hydraulic resistance, permeability performance,

hydrophilicity, and thermal stability. BSA protein removal efficiency, anti-fouling performance, and recycling potential of the UF membranes were investigated.

Moreover, TiO_2 nanoparticles (NPs) were modified using different amine groups, namely, ethylenediamine (EDA), hexamethylenetetramine (HMTA) and tetra ethylene pentamine (TEPA), using impregnation process. The prepared amine modified TiO_2 composite NPs were explored as an additive to fabricate ultrafiltration membranes with enhanced capacity towards the removal of chromium ions from aqueous solution. Membranes were prepared from cellulose acetate (CA) polymer blended with polyethylene glycol (PEG), and amine modified TiO_2 by using phase inversion technique. Fourier transform infrared spectroscopy (FTIR), zeta potential (ζ), thermo gravimetric analysis (TGA), field emission scanning electron microscopy (FESEM), water contact angle (WCA), and atomic absorption spectrophotometer (AAS) analysis were done to characterize the membranes in terms of chemical structure, electric charge, thermal stability, morphology, and hydrophilicity properties.

Secondly, graft copolymerization of cellulose acetate (CA) and poly (methyl methacrylate) (PMMA) was synthesised through free radical polymerization with the presence of cerium sulfate (CS) as an initiator under the nitrogen atmosphere in an aqueous solution. During the grafting reactions, the effects of polymerization time and temperature on the grafting were investigated. Furthermore, functionalization of the synthesized product was done using amine group. The results from Nuclear Magnetic Resonance (^{1}H NMR) spectra and Attenuated total reflectance-Fourier-transform infrared spectroscopy (ATR-FTIR) confirmed the successful grafting of PMMA on the CA membrane surfaces. Zeta potential (ζ), field emission scanning electron microscopy (FESEM), and atomic absorption spectrophotometer (AAS) studies were done to characterise the membranes in terms of surface charge, morphology, and HA removal percentage, respectively. Finally, the overall conclusions and scope of the future work are presented precisely.

Keywords: *Electro-spinning; RSM; Crosslinking; PVA; Cellulose acetate; Adsorbent; Removal capacity; Kinetics; Modification; phase inversion; solubility parameter; ultrafiltration; additives; solvents**;** thermal stability; TiO_2 NPs; Polyethylene glycol; anti-fouling; Impregnation; amines; chromium ion; Graft copolymerization; amination; HA removal.*

Research publications

Lists of publications

[1] **Kibrom Alebel Gebru**, Chandan Das "Removal of Pb (II) and Cu (II) ions from wastewater using electrospun cellulose acetate/ titanium oxide (TiO_2) membrane as adsorbent", ***Journal of Water Process Engineering 16 (2017) 1–13***

[2] **Kibrom Alebel Gebru**, Chandan Das "Effects of solubility parameter differences among PEG, PVP and CA on the preparation of ultrafiltration membranes: Impacts of solvents and additives on morphology, permeability and fouling performances", ***Chinese Journal of Chemical Engineering, DOI: 10.1016/j.cjche.2016.11.017***

[3] **Kibrom Alebel Gebru**, Chandan Das,"Removal of bovine serum albumin from wastewater using fouling resistant ultrafiltration membranes based on the blends of cellulose acetate, and PVP−TiO_2 nanoparticles", ***Journal of Environmental Management, 200 (2017) 283-294***

[4] **Kibrom Alebel Gebru**, Chandan Das "Response surface optimization of electro-spun polyvinyl alcohol nano-fiber membrane process parameters and its characterization", ***Journal of Membrane and Separation Technology, 5 (2017), 140-156***

[5] **Kibrom Alebel Gebru**, Chandan Das "Preparation and characterization of phase inversion CA–PEG−TiO_2 membranes: Effect of PEG and TiO_2 nanoparticles on the permeability properties and anti-fouling performance", ***Journal of Membrane Science and Research, 3 (2017) 90-101***

[6] **Kibrom Alebel Gebru**, Chandan Das "Cellulose acetate−modified−Titanium dioxide (TiO_2) nanoparticles electro-spun composite membranes: Fabrication and characterization", ***Journal of The Institution of Engineers, Article in press, (2017)***

[7] **Kibrom Alebel Gebru**, Chandan Das, "Removal of chromium (VI) ions from aqueous solutions by using environmentally friendlier amine-impregnated TiO_2 nanoparticles modified cellulose acetate membranes" ***Chemosphere (Revision Submitted)***

[8] **Kibrom Alebel Gebru**, Chandan Das, "Removal of humic acids using cellulose acetate-g-poly methyl methacrylate (PMMA)-a-tetraethylenepentamine (TEPA) adsorptive membranes" ***Separation and Purification Technology (Under Review)***

[9] **Kibrom Alebel Gebru**, Chandan Das, "Grafting polymerization of polymethyl methacrylate (PMMA) onto cellulose acetate modified with amine functional groups" ***European Polymer Journal (Submitted)***

International conferences

[1] Kibrom Alebel Gebru, Chandan Das, "Preparation and characterization of cellulose acetate/ TiO_2 composite electro-spun membranes using electro-spinning technique" Advances in Sustainable Polymers *(ASP-16), 4th-6th August 2016, Kyoto Institute of Technology,* ***Japan***

National conferences

[1] Kibrom Alebel Gebru, Chandan Das, "Fabrication and characterization of electro-spun cellulose acetate/ titanium oxide (TiO_2) composite membranes for adsorption of heavy metals" *Indian Chemical Engineering Congress (CHEMCON-2015), 27-30 December 2016, Guwahati,* ***India***

Table of Contents

DEDICATION i

DECLARATION ii

CERTIFICATE iii

ACKNOWLEDGEMENTS iv

Abstract vii

Research publications x

Table of Contents xii

List of abbreviation and symbols xix

List of Tables xxiv

List of Figures xxvii

Chapter 1: Introduction, literature survey, and objective of the work 1

1.1. Introduction 2

1.2. General Background 5

1.2.1. Preparation of synthetic membranes 5

1.2.2. Definition of Membrane 5

1.2.3. Types of membranes 6

1.2.4. Preparation Techniques 8

1.2.4.1 Sintering 8

1.2.4.2. Stretching 9

1.2.4.3. Track etching 9

1.2.4.4. Template leaching 10

1.2.4.5. Phase inversion 11

1.2.4.6. Electro-spinning 12

1.2.5. Functionalization of membranes 15

1.2.5.1. Functionalization techniques 17

Physical coating or blending 17

Graft copolymerization.....18

Plasma treatment.....19

Chemical treatment.....20

1.3. Literature survey and objective of the work.....20

1.3.1. Preparation and applications of electro-spun membranes.....20

1.3.2. Electro-spun membranes for water and wastewater treatment applications.....23

1.3.3. Preparation and application of phase-inverted membranes.....27

1.3.4. Modification of membranes for specific application.....29

1.4. Knowledge gap.....33

1.5. Objectives of the Work.....34

1.5.1. Preparation and modification electro-spun membranes.....34

Optimization of electro-spinning parameters.....34

Fabrication of CA/TiO_2 composite electro-spun adsorbent.....34

Adsorption study for removal of heavy metals from wastewater.....34

1.5.2. Preparation and modification of CA phase inverted membranes.....34

Comparative study on additives and solvents.....34

Modification of CA membrane using TiO_2 NPs.....34

Conducting permeability, fouling, and BSA removal performances studies.....34

1.5.3. Functionalization of membranes: physical blending and graft copolymerization.....34

CA membranes modified with amine-impregnated TiO_2 NPs.....34

Cerium (IV) initiated graft polymerization of PMMA on CA.....34

Removal of Cr (VI) and humic acids from contaminated water using modified membranes.....34

Chapter 2: Materials, preparation, and characterization methods.....35

2.1. Materials.....36

2.1.1. Chemicals.....36

2.2. Preparation Methods.....37

2.2.1. Electro-spinning technique 37

2.2.1.1. Preparation of electro-spun PVA and cellulose acetate 37

2.2.1.2. Response Surface Methodology using Design of Expert 39

2.2.1.3. Cross-linking of Electro-spun PVA 40

2.2.1.4. Batch adsorption experiments 42

2.2.2. Phase Inversion Method 43

2.2.2.1. Preparation of CA, CA-PEG, and CA-PVP membranes 43

2.2.2.2. Preparation of CA−PEG –TiO_2 membrane 45

2.2.2.3. Preparation of CA-PVP–TiO_2 membrane 46

2.2.3. Physical blending process 49

2.2.3.1. Preparation of amine-modified TiO_2 49

2.2.3.2. Preparation of CA/U-Ti, CA/Ti-EDA, CA/Ti-HMTA, and CA/Ti-TEPA membranes. 49

2.2.4. Grafting and amination process 50

2.2.4.1. Synthesis of CA-g-PMMA and CA-g-PMMA_TEPA 50

2.2.4.2. Preparation of Un-g-CA, CA-g-PMMA, and CA-g-PMMA_TEPA membranes. 53

2.3. Characterization Methods 54

2.3.1. Physicochemical Characterization 54

2.3.1.1. Pure water flux and hydraulic permeability 54

2.3.1.2. Membrane porosity measurements 55

2.3.1.3. Membrane fouling and rejection experiments 56

2.3.1.4. Average pore radius determination 57

2.3.1.5. Chromium removal performances 58

2.3.1.6. HA Ultrafiltration and regeneration performance 59

2.3.2. Instrumental Characterization 60

2.3.2.1. Field emission scanning electron microscopy (FESEM) 60

2.3.2.2. Thermo gravimetric analysis (TGA) 60

2.3.2.3. Nuclear Magnetic Resonance (NMR) analysis 60

2.3.2.4. ATR-FTIR Spectroscopy analysis 60

2.3.2.5. Zeta potential (ζ) analysis 61

2.3.2.6. Water contact angle (WCA) measurements 61

2.3.2.7. X-ray diffractometer (XRD) 61
2.3.2.8. Leica microscope 61
2.3.2.9. Atomic force microscopy (AFM) 61
2.3.2.10. Transmission electron microscopy (TEM) 61
2.3.2.11. Brunauer-Emmet-Teller (BET) isotherm 62
2.3.2.12. Atomic Absorption Spectrophotometer (AAS) 62
2.3.2.13. UV–vis Spectrophotometer (UV-2600) 62
Chapter 3: Preparation, characterization, and application of electro spun composite membranes 63
3.1. Preliminary investigation of electro-spinning process parameters 65
3.1.1. Results and discussion 65
3.1.1.1. Statistical analysis (ANOVA) and Response Surface of electro-spinning parameters 65
3.1.1.2. Membrane fiber diameter 66
3.1.1.3. Membrane surface pore diameter 70
3.1.1.4. Model Verification on the Basis of Statistical Analysis 71
3.1.1.5. Optimization Study 75
3.1.1.6. Morphological study (FESEM) 78
3.1.2. Summary 83
3.2. Preparation and characterization of CA_TiO_2 electro-spun composite membranes. 84
3.2.1. Results and discussion 84
3.2.1.1. Solution composition 84
3.2.1.2. CA, CA_TiO_2 membrane fabrication 85
3.2.1.3. Study of TiO_2 Nanoparticles 86
3.2.1.4. Surface charge study 87
3.2.1.5. Membrane morphological study 88
3.2.1.5. Membrane crystallinity analysis 94
3.2.1.6. Surface roughness study 95
3.2.1.7. Thermal stability analysis 96
3.2.2. Summary 97

3.3. Removal of Pb (II) and Cu (II) ions from wastewater using composite electrospun cellulose acetate/ titanium oxide (TiO_2) adsorbent 99

3.3.1. Results and Discussion 99

3.3.1.1. Morphology and diameter distributions 99

3.3.1.2. Textural properties of the adsorbent 101

3.3.1.3. Infrared spectroscopy analysis 102

3.3.1.4. Specific surface area analysis 103

3.3.1.5. Energy dispersive X-ray analysis 105

3.3.1.6. Adsorption Study 107

Effect of contact time and temperature 107

Effect of pH 109

Effect of TiO_2 amount 111

3.3.1.7. Adsorption isotherms 112

3.3.1.8. Adsorption kinetics 116

3.3.2. Summery 118

Chapter 4: Preparation, characterization, and application of phase inverted membranes 119

4.1. Effects of solubility parameter differences among PEG, PVP and CA on the preparation of ultrafiltration membranes: Impacts of solvents and additives on morphology, permeability and fouling performances 121

4.1.1. Results and discussion 121

4.1.1.1. Morphological study 121

Effect of additives 123

Effect of solvents 124

4.1.1.2. Pure water flux and hydraulic permeability 125

Effect of additives 125

Effect of solvents 128

4.1.1.3. Membrane fouling and rejection experiments 134

Effect of additives and solvents 135

4.1.1.4. Rejection performance 139

4.1.2. Summary 140

4.2. Preparation and characterization of CA−PEG−TiO_2 membranes: Effect of PEG and TiO_2 on morphology, flux and fouling performance 142

4.2.1. Results and discussion 142

4.2.1.1. Morphological study 142

Effect of PEG additive and TiO_2 NPs 143

4.2.1.2. Thermal stability studies 146

4.2.1.3. Pure water flux performance 150

Effect of PEG and TiO_2 NPs 150

4.2.1.4. Membrane hydrophilicity and TiO_2 NPs stability 154

4.2.1.5. Fouling and rejection performance study 155

Effect of PEG additive and TiO_2 NPs on fouling 157

4.2.1.6. Rejection performance 160

4.2.2. Summary 163

4.3. Preparation and characterization of fouling resistant ultrafiltration membranes based on the blends of cellulose acetate and PVP−TiO_2 nanoparticles for removal of bovine serum albumin 164

4.3.1. Results and discussion 164

4.3.1.1. Study of TiO_2 nanoparticles 164

4.3.1.2. Morphological study 165

Effects of PVP and TiO_2 NPs 165

4.3.1.3. Thermal stability analysis 168

4.3.1.4. Pure water flux study 172

Effect of PVP and TiO_2 NPs 172

4.3.1.5. Membrane hydrophilicity and TiO_2 NPs stability 176

4.3.1.6. Membrane fouling experiments 178

4.3.1.7. Membrane anti-fouling performance 178

4.3.1.8. BSA removal performance 180

4.3.2. Summery 182

Chapter 5: Modification, characterization and application of cellulose acetate membranes 185

5.1. Functionalization and characterization of cellulose acetate membranes for chromium (VI) removal 187

5.1.1. Results and Discussions 187

5.1.1.1. TEM analysis of U-TiO_2 and M-TiO_2 NPs.....187
5.1.1.2. ATR-FTIR and zeta potential (ζ) and thermal analysis.....188
5.1.1.3. Morphology and hydrophilicity study.....192
5.1.1.4. PWF performance of membranes.....195
5.1.1.5. Cr (VI) removal efficiency of membranes.....197
5.1.1.6. Effect of Cr (VI) concentration.....202
5.1.1.7. Washing/regeneration performance study.....203
5.1.2. Summary.....205
5.2. Grafting copolymerization of poly methyl methacrylate (PMMA) onto cellulose acetate modified with amine group for removal of humic acids.....207
5.2.1. Results and discussion.....207
5.2.1.1. Graft polymerization.....207
5.2.1.2. Effect of polymerization time and temperature.....212
5.2.1.3. ATR-FTIR Spectroscopy and zeta potential analysis.....215
5.2.1.4. Membrane morphological and physicochemical studies.....216
5.2.1.5. Ultrafiltration of PW and HA solutions.....221
5.2.1.6. Membrane regeneration performance study.....224
5.2.2. Summary.....225
Chapter 6: Overall Conclusions and Scope of the Future Work.....227
6.1. Overall Conclusions.....227
6.2. Future recommendations.....229
Appendix.....231
References.....241

List of abbreviation and symbols

Nomenclature

A_m	Effective area of the membrane (m^2)
b	Langmuir constant (L mg^{-1})
C_o	initial concentrations of heavy metal ions (mg/L)
C_e	equilibrium concentration of metal ions (mg/L)
C_f	Concentration in the feed (mg/L)
C_p	Concentration in permeate (mg/L)
F_{ir}	Irreversible fouling
F_r	Reversible fouling
F_t	Total fouling
J_{B0}	BSA flux in the first run (L/m^2 h)
J_{B1}	BSA flux in the second run (L/m^2 h)
J_{B2}	BSA flux in the third run (L/m^2 h)
J_{BS}	Steady state BSa flux (L/m^2 h)
J_{w0}	Pure water flux (L/m^2 h)
J_{w1}	Initial water flux (L/m^2 h)
J_{w2}	Water flux in second run (L/m^2 h)
J_{w3}	Water flux in third run (L/m^2 h)
k_1	Pseudo first-order model rate constant (min^{-1})
k_2	Pseudo second-order model rate constant (g/ mg min^{-1})
K_{DR}	activity coefficient (mol^2 J^{-2})
k_f	Freundlich capacity factor (mg/g) $(mg/L)^n$
M_W	Molecular weight (Da)
M	mass of adsorbent membrane (g)
n	Intensity parameter
NFR	Normalized flux ratio (%)
P_m	Hydraulic permeability (L/m^2 h kPa)
Q_W	Water flow (m^3 s^{-1})

q_e adsorption capacities at equilibrium time (mg/g)

q_{DR} highest adsorption capability (mmol g^{-1})

q_{max} highest quantity of the metal ions per unit mass of adsorbents (mg/g)

q_t adsorption capacities at time t (mg/g)

R regression value

r_m Average pore radius (nm)

R_f Resistance due to fouled membrane

R_m Resistance due to membrane

R_P Resistance due to concentration polarization

R Solute rejection (%)

R_m Membrane resistance (m^{-1})

t Adsorption time (h)

t Experimental time interval (h)

V volume of the liquid in the solution (mL)

V Total volume permeated during an experimental time interval (L)

W_D Weight of dry membranes (g)

W_W Weight of wet membranes (g)

ΔP Operating pressure (kPa)

Greek letters

ε Membrane porosity (%)

ε Polanyi potential

ζ Membrane thickness (μm)

μ Dynamic water viscosity (Pa. s)

ρ_p Density of the polymer (g cm^{-3})

ρ_W Density of pure water at operating conditions (g cm^{-3})

Abbreviations

AAS Atomic Absorption Spectrophotometer

AC Acetone

AFM Atomic force microscopy

BET Brunauer-Emmet-Teller

BIS Bureau of Indian Standards

BPO Benzoyl peroxide

BSA Bovine serum albumin

BTEAC Benzyl triethylammonium chloride

CA Cellulose acetate

CAN Ceric ammonium nitrate

CB Cibacron Blue

CBT Coagulation bath temperature

CCD Central composite design

CE Cellulose esters

CF Compaction factor

CN Nitrocellulose

Cu Copper

CS Ceric sulphate

D-R Dubinin–Radushkevich

DI Deionized

DMAc N, N-Dimethylacetamide

DMF Dimethyl formamide

DOE Design of experiment

ECM Extracellular matrix

EDA Ethylenediamine

EDS Energy dispersive x-ray spectroscopy

EWC Equilibrium water content

FAO Food and Agriculture Organization

FESEM Field emission scanning electron microscopy

FD Fiber diameter

FTIR Fourier transform infrared

GA Glutaraldehyde

GMA Glycidyl methacrylate

HMTA Hexamethylenetetramine

ICMR Indian Council of Medical Research

MA Maleic anhydride

MAA Methacrylic acid

MMA Methyl methacrylate

MCL Maximum contaminant level

MWCO Molecular weight cut off

NF Nanofiltration

NMP N-methyl-2-pyrrolidone

NMR Nuclear Magnetic Resonance

PAN Polyacrilonitrile

Pb Lead

PC polycarbonate

PE Polyethylene

PEG Polyethylene glycol

PEGDMA Polyethylene glycol dimethacrylate

PEO Poly (ethylene oxide)

PES Polyethersulfone

PET Polyethylene terephthalate

PP Polypropylene

PS Polysulfone

PTFE Polytetrafluoroethylene

PWF Pure water flux

PVA Polyvinyl alcohol

PVC Polyvinylchloride

PVDF Polyvinylidene fluoride

PVP polyvinylpyrrolidone

RSM Response surface methodology

SPD Surface pore diameter

TEM Transmission electron microscopy

TEPA Tetraethylenepentamine

TFNC Thin film nanofibrous composite

TGA Thermogravimetric analysis

TiO_2 Titanium dioxide

THF Tetrahydrofuran

TMP Trans membrane pressure

TPEE Thermal plastic elastomer ester

UF Ultrafiltration

USEPA United states environmental protection agency

WC Water content

WHO World Health Organization

XRD X-ray powder diffractometer

List of Tables

Table No.	Title	Page No.
Table 1.1	List of inorganic chemicals and their maximum contaminant level (MCL) in drinking water [1, 2, and 3]	4
Table 1.2	Different membrane fabrication techniques and their properties	16
Table 2.1	Design summary: Input variables and their coded and actual values used in the response surface study	40
Table 2.2	Design of experiments summery and experimental responses for central composite design (CCD)	41
Table 2.3	Batch adsorption parameters	42
Table 2.4	Compositions and viscosity of the casting solution of polymeric additives with CA	44
Table 2.5	Solution compositions and viscosity of the casting solution: CA, PEG and TiO_2 nanoparticles	46
Table 2.6	Solution compositions and viscosity of the casting solution: CA, PVP additive, and TiO_2 nanoparticles	48
Table 2.7	Composition of amine modified TiO_2 nanoparticles	49
Table 2.8	Solution compositions of the casting solution: CA, PEG, U-TiO_2 and M-TiO_2 nanoparticles	50
Table 2.9	The variation of time and temperature on the polymerization reaction	52
Table 2.10	Solution casting compositions of all the prepared membranes	53

Table 3.1	Analysis of variance (ANOVA) for respective response surface quadratic models	68
Table 3.2	Optimized input variables calculated from CCD	77
Table 3.3	Solution compositions of CA_TiO_2 membranes	85
Table 3.4	Zeta potential values: Solution of CA and CA_TiO_2, and TiO_2	88
Table 3.5	Effect of TiO_2 content on adsorbent porosity and specific surface area	101
Table 3.6	Adsorption capacities of Pb (II) and Cu (II) for some adsorbents reported in the literature	112
Table 3.7	The three isotherms model parameters for metal adsorption onto CA/TiO_2 adsorbent	115
Table 3.8	Kinetic parameters of metal adsorption onto the CA/TiO_2 adsorbent	118
Table 4.1	Hansen solubility parameters for selected solvents, non-solvent, additives and cellulose acetate	130
Table 4.2	Compaction factor, hydraulic characteristics, EWC and porosity of all prepared membranes at 300 kPa	132
Table 4.3	Fouling study data of the prepared membranes	138
Table 4.4	Compaction and hydraulic characteristics of those prepared membranes at 250 kPa	152
Table 4.5	Results for flux losses caused by total fouling *(F_t)*, reversible fouling *(F_r)* and irreversible fouling *(F_{ir})*, of the three cycles	160

Table 4.6	Results for resistances due to the membrane (R_m), fouled layer (R_f) and polarization (R_P) of the three cycles	161
Table 4.7	Compaction and hydraulic characteristics of those prepared membranes	175
Table 4.8	Results for flux losses caused by total fouling (F_t), reversible fouling (F_r) and irreversible fouling (F_{ir}), of the three cycles.	181
Table 5.1	Zeta potential (ζ) results of unmodified and modified TiO_2 NPs	192
Table 5.2	Compaction and hydraulic characteristics of amine modified membranes at 250 kPa.	196
Table 5.3	^{1}H NMR results of prepared samples	211
Table 5.4	Compaction and hydraulic characteristics of the prepared membranes at 250 kPa	220

List of Figures

Figure No.	Title	Page No.
Figure 1.1	Schematic diagram of the basic membrane separation process	6
Figure 1.2	Schematic diagram for types of membranes	7
Figure 1.3	Sintering process	8
Figure 1.4	Preparation of porous membrane by track etching	10
Figure 1.5	Template leaching process	11
Figure 1.6	Membrane preparation by phase inversion methods	12
Figure 1.7	Basic schematic drawing of electro-spinning process	13
Figure 1.8	Schematic representation of (a) self-migration, (b) self-assembly, and (c) layer-by-layer adsorption techniques	18
Figure 1.9	The general scheme of how the surface of polymer can be grafted	19
Figure 1.10	Various applications of electro-spun membranes	21
Figure 2.1	Schematic of the electro-spinning equipment, syringe pump, needle, rotating collector, and voltage supply	38
Figure 2.2	Membrane preparation process	44

Figure 2.3	Schematic representation of casting film and coagulation bath interface: solvent *(J_2)* and non-solvent *(J_1)*	45
Figure 2.4	Flow diagram of the preparation method of flat sheet membranes	47
Figure 2.5	A flow diagram for the preparation process of flat sheet membranes	48
Figure 2.6	Schematic of the graft copolymerization process	51
Figure 2.7	Schematic diagram of the batch cell ultrafiltration set-up	55
Figure 3.1	Three dimensional Response surface plot of (a) voltage supply and time duration, (b) concentration and time duration, (c) flow rate and time duration, (d) flow rate and voltage supply, and (e) flow rate and concentration for membrane fiber diameter	69
Figure 3.2	Three dimensional Response surface plot of (a) flow rate and time duration, (b) concentration and voltage supply, (c) flow rate and voltage supply, and (d) flow rate and concentration for membrane surface pore diameter	72
Figure 3.3	The interaction plots of (a) time duration and voltage supply; (b) time duration and concentration; (c) time duration and flow rate;(d) flow rate and voltage supply; and (e) flow rate and concentration for membrane fiber diameter	73
Figure 3.4	The interaction plots of (a) time duration and flow rate; (b)	74

	voltage supply and concentration; (c) voltage supply and flow rate; and (d) flow rate and concentration for membrane surface pore diameter	
Figure 3.5	Plots of predicted versus actual values of membrane (a) fiber diameter (R^2 = 0.96) and (d) surface pore diameter (R^2 = 0.96); Normal probability plot of residual (b) membrane fiber diameter and (e) membrane surface pore diameter; Plot of residual vs. predicted of (c) membrane fiber diameter and (f) membrane surface pore diameter	76
Figure 3.6	Response surface plot of desirability operating region: voltage supply and concentration of 10.67 kV and 10.89 wt. %, respectively	78
Figure 3.7	FESEM images of the ePVA fibers and their corresponding fiber diameter distribution at different process time, (a_1, a_2) 25 min, (b_1, b_2) 35 min, (c_1, c_2) 45 min and (d_1, d_2) 60 min	80
Figure 3.8	% Surface pore size diameter distribution of e-PVA membranes obtained at different electro-spinning duration, 25 min, 35 min, 45 min and 60 min	82
Figure 3.9	Images of (a) fabricated CA membrane and (b) CA_TiO_2 hybrid membrane	86
Figure 3.10	TEM image of commercial TiO_2 nanoparticles	87

Figure 3.11	FESEM and EDS images of CA, CA_TiO_2 electro-spun fibers M_1 (a_1, a_2), M_2 (b_1, b_2), M_3 (c_1, c_2), M_4 (d_1, d_2) and M_5 (e_1, e_2)	90
Figure 3.12	Fiber diameter distribution of CA (M_1) and CA_TiO_2 electro-spun fibers (M_2, M_3, M_4 and M_5)	91
Figure 3.13	% Surface pore size diameter distribution of CA_TiO_2 membranes (M_1, M_2, M_3, M_4 and M_5)	93
Figure 3.14	X-ray diffraction patterns of TiO_2 nanoparticle, CA and CA_TiO_2 electro-spun membranes (M_1, M_2, M_3, M_4 and M_5)	94
Figure 3.15	Three-dimensional AFM images of CA (M_1) and CA_TiO_2 (M_2, M_3, M_4 and M_5) electro-spun membranes	95
Figure 3.16	TGA Analysis of (a) cellulose acetate and (b, c, d and e) cellulose acetate_TiO_2 hybrid membranes	97
Figure 3.17	FESEM images of electrospun adsorbents (AM0, AM1, AM2, AM3, and AM4)	100
Figure 3.18	X-ray diffraction patterns of TiO_2 nanoparticle, electrospun adsorbents (AM0, AM1, AM2, AM3, and AM4)	102
Figure 3.19	FTIR spectra of CA, TiO_2, and CA/TiO_2 adsorbents	103
Figure 3.20	Adsorption-desorption isotherm graph of adsorbents (TiO_2 nanoparticles and AM0, AM1, AM2, AM3, AM4)	105
Figure 3.21	FESEM and EDS images of (a_1, a_2) AM2 adsorbent, (b_1, b_2) after adsorption of Pb (II), (c_1, c_2) after adsorption of Cu (II), (d_1, d_2) after desorption of Pb (II), (e_1, e_2) after desorption of Cu	107

	(II)	
Figure 3.22	Effect of contact time on the Pb (II) and Cu (II) ions adsorption onto CA/TiO_2 adsorbent	108
Figure 3.23	Effect of temperature on the Pb (II) and Cu (II) ions adsorption onto CA/TiO_2 adsorbent	109
Figure 3.24	Effect of pH (a) on the Pb (II) and Cu (II) ions adsorption onto CA/TiO_2 adsorbent and (b) on zeta potential values of the adsorbent	110
Figure 3.25	Effect of TiO_2 nanoparticles amount on removal efficiency of Pb (II) and Cu (II) ions	112
Figure 3.26	Adsorption model: (a) Freundlich (b) Langmuir (c) D-R plots for copper and lead adsorption onto the adsorbent	114
Figure 3.27	(a) Adsorption-desorption cycles, (b) UV–vis absorption spectra of before and after adsorption and after desorption of AM2 adsorbent	116
Figure 3.28	Adsorption kinetics: (a) Pseudo- first-order and (b) Pseudo-second-order plots for copper and lead adsorption onto the adsorbent	117
Figure 4.1	(a) Top surface and (b) cross sectional FESEM images of CA membranes with different additives and solvents	127
Figure 4.2	(a, c) PWF profile during compaction study and (b, d) effect of operating pressure on PWF	132

Figure 4.3	(a) Water contact angle values and (b) images of water droplets of the prepared membranes. (Water droplet volume is about 2 µL at 0.16 mL/min)	135
Figure 4.4	Permeate flux versus filtration time for (a) CA/Ac: DMAc and (b) CA/DMF membranes: effect of solvents and additives on fouling performance (25 ºC, 150 kPa)	136
Figure 4.5	Rejection performance of different CA membranes: effect of solvents and additives (25 ºC, 150 kPa)	140
Figure 4.6	(a) Top surface and (b) cross-sectional FESEM images (c) EDS results of M_1 (CA), M_2 (CA-TiO_2), M_3 (CA-PEG-TiO_2) and M_4 (CA-PEG) membranes; (d) EDS mapping images of CA membranes with PEG and TiO_2 NPs	147
Figure 4.7	(a) TGA and (b) DTG analysis results of M_1, M_2, M_3, M_4 membranes and TiO_2 NPs	149
Figure 4.8	(a) PWF profile during compaction study (at 300 kPa), (b) Effect of transmembrane pressure on PWF	153
Figure 4.9	(a) Water contact angle values with different drop ages; (b) images of water droplets of the prepared membranes; and (c) TiO_2 NPs stability study (Water droplet volume is about 2 µL at 0.16 mL/min)	156
Figure 4.10	(a) Permeate flux versus filtration time for M_1 (CA), M_2 (CA-TiO_2), M_3 (CA-PEG-TiO_2) and M_4 (CA-PEG) membranes:	159

	effect of PEG and TiO_2 NPs on the anti-fouling performance of the membranes (25±2 ºC, 150 kPa), (b) NFR percentage results	
Figure 4.11	BSA rejection performances of M_1 (CA), M_2 (CA-TiO_2), M_3 (CA-PEG-TiO_2) and M_4 (CA-PEG) membranes: effect of PEG and TiO_2 NPs (25±2 ºC, 150 kPa)	162
Figure 4.12	(a) Top surface, (b) cross sectional, (c) EDS and (d) mapping images of CA, CA with PVP and TiO_2 NPs membranes	171
Figure 4.13	(a) TGA and (b) DTG analysis of all the prepared membranes and TiO_2 nanoparticles	172
Figure 4.14	(a) PWF profile during compaction study, (b) effect of trans membrane pressure on PWF	174
Figure 4.15	(a) Water contact angle values with different drop ages; (b) images of water droplets of the prepared membranes; and (c) TiO_2 NPs stability study	177
Figure 4.16	Permeate flux versus filtration time for CA, CAT, CATP and CAP membranes: effect of PVP and TiO_2 NPs on BSA removal and fouling performance (25 ºC, 150 kPa)	179
Figure 4.17	(a) BSA removal performances and (b) NFR percentage results of the prepared membranes: effect of PVP additive and TiO_2 NPs (25 ºC, 150 kPa)	182
Figure 5.1	TEM images of U-TiO_2 and M- TiO_2 nanoparticles	189

Figure 5.2	(a) ATR–FTIR results of unmodified TiO_2 and modified TiO_2 NPs; (b) TGA analysis CA/U-Ti, CA/Ti-HMTA, CA/Ti-EDA and CA/Ti-TEPA membranes	190
Figure 5.3	(a) FESEM images of U-TiO_2 and M- TiO_2 powder;(b) Top surface and (c) cross sectional FESEM images of CA/U-Ti, CA/Ti-HMTA, CA/Ti-EDA and CA/Ti-TEPA membranes	194
Figure 5.4	(a) Water contact angle values with different drop ages and (b) images of water droplets of the prepared membranes	195
Figure 5.5	(a) PWF profile during compaction study (at 250 kPa), (b) Effect of pressure on PWF	197
Figure 5.6	Permeate flux of Cr (VI) results of all the prepared membranes at (a) pH=3.5, (b) pH=7 and Cr (VI) removal % at (c) pH=3.5, (d) pH=7 (Cr (VI) concentration= 10 ppm, ΔP=150 kPa, @ 200 rpm)	201
Figure 5.7	Schematic diagram for the impregnated amine groups and deposition of Cr (VI) ions in ultrafiltration process	202
Figure 5.8	Effect of concentration on Cr (VI) ion permeate flux results of the CA/Ti-TEPA membrane at (a) pH=3.5, (b) pH=7 and Cr (VI) ion removal % at (c) pH=3.5, (d) pH=7 (ΔP=150 kPa, @ 200 rpm)	203
Figure 5.9	(a) Cr (VI) flux and (b) removal efficiency of CA/Ti-TEPA membrane during the filtration cycle (Cr (VI) concentration: 10	205

	ppm, pressure: 150 kPa, washing operation: 2.5 g/L KCl @ 200 rpm)	
Figure 5.10	Scheme for preparation of PMMA, CA-g-PMMA and, CA-g-PMMA_TEPA	210
Figure 5.11	^{1}H NMR spectra of CA, MMA, and CA -g- PMMA dissolved in DMSO-d6 at different polymerization time and temperature	215
Figure 5.12	(a) FTIR spectra and (b) zeta potential (ζ) results of the unmodified and modified CA	216
Figure 5.13	(a) Top surface and (b) cross sectional FESEM images of un-g-CA, CA-g-PMMA and CA-g-PMMA-TEPA membranes	219
Figure 5.14	Pore size distribution of CA, CA-g-PMMA and CA-g-PMMA-TEPA membranes	220
Figure 5.15	(a, b) pure water flux, (c) HA flux, and (d) removal % results of un-g-CA, CA-g-PMMA and CA-g-PMMA-TEPA membranes at pH=7, HA concentration= 10 ppm, ΔP=150 kPa, @ 200 rpm)	222
Figure 5.16	Schematic diagram for the membrane grafting and amination process and adsorption of HA in UF process	223
Figure 5.17	Washing/regeneration study of un-g-CA, CA-g-PMMA, and CA-g-PMMA-TEPA membranes at pH=7, HA concentration= 10 ppm, ΔP=150 kPa, @ 200 rpm)	225

Chapter 1

Introduction, literature survey, and objective of the work

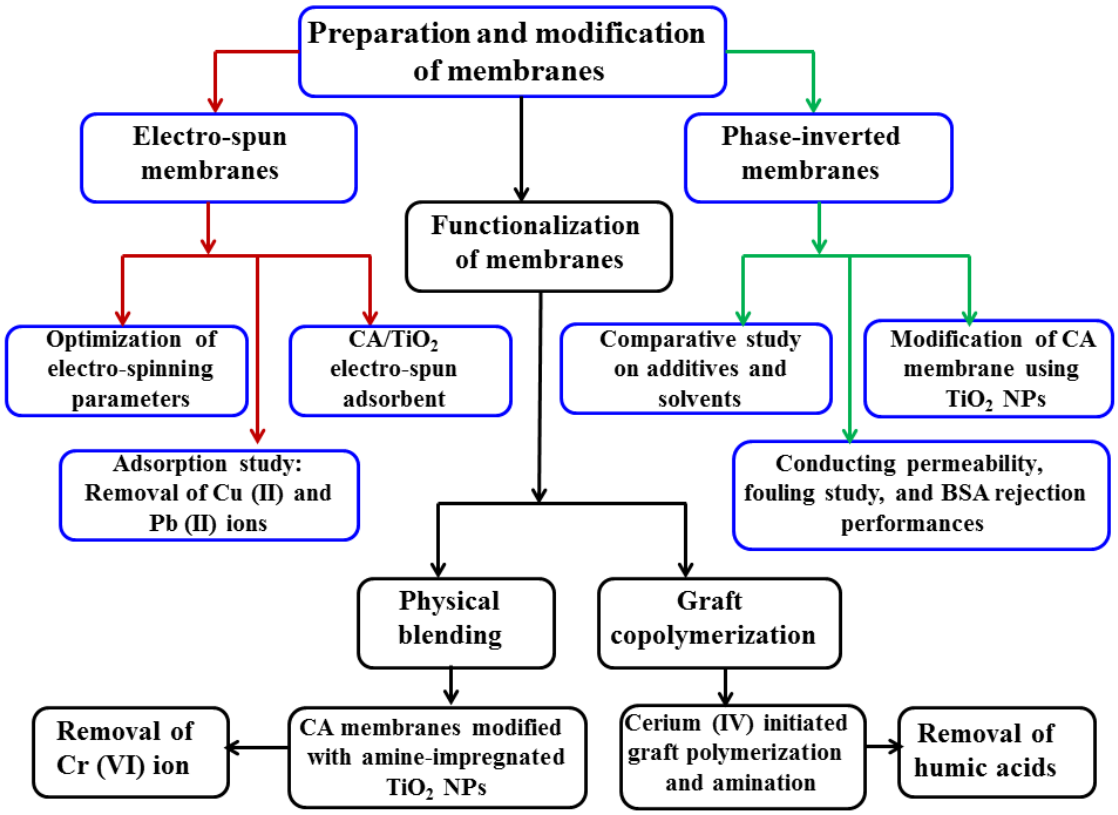

Chapter 1: Introduction, literature survey, and objective of the work

This chapter presents a platform to provide valuable information on the background knowledge of this work for better understanding of the types of membranes, membrane preparation techniques, functionalization, characterization and applications.Membrane technology presents an attractive character comprising of easy manufacturing, modification, operation, and compactness. Several membrane preparation techniques are assessed and compared in this chapter in detail. Moreover, the functionalization using physical blending and grafting methods for the modification of polymer and/or membrane are discussed. Finally, the possible applications of the membrane processes have been extensively discussed for water and wastewater treatments.

Secondly, the detail literature review about the preparation, modification, and application of the polymeric membranes were discussed. A particular emphasis was given to the phase inversion and electro-spinning techniques of membrane preparations. On the other hand, the functionalization and/or grafting effects on the resultant membrane structures were assessed in terms of their specific applications. Moreover, the possible scopes for further enhancement on the preparation and modifications of the membranes are also identified. Furthermore, the specific objectives on the preparation, characterization, modification and application of the polymeric membranes have been discussed extensively.

1.1. Introduction

Water is one of the most vital resources on the planet. Nowadays, fresh and clean water supplies have been falling at an alarming rate. Greater than one billion people do not have access to fresh water, and over two billion individuals are living in water shortage areas**[1].** Since the world population is rising and the environmental pollution is increasing rapidly, water purification has to be made more efficient and cost-effective.Access to clean water has been recognised as one and a serious challenge for world's social and economic growth.The advancement of alternative water supplies is crucial and essential. One of the current challenges

is to develop effective and less energy consuming process through treating and recovering of pure water from ground water, industrial, and brackish water **[2].** Removal of heavy metals and other contaminants from water and wastewater is a very important factor with respect to environmental pollution control and human health. Several methods have been used for the removal of heavy metal ions and other contaminants from aqueous solutions including ion exchange, chemical precipitation, electro-dialysis, and solvent extraction. However, these techniques are associated with problems such as excessive time requirements, high costs, and high energy consumption. Moreover, adsorption method can be considered as an effective and widely used process for removal of heavy metals and other contaminants from wastewater due to its simplicity, moderate operational conditions, and economic feasibility. The most important properties of any adsorbent are its surface area and structure. **[3].** However, particulate or powder adsorbents might re-pollute treated water because of the tremendous problems in recovery.

Among the different water purification technologies, the pressure-driven membrane filtration processes; microfiltration (MF), ultrafiltration (UF), nanofiltration (NF), and reverse osmosis (RO) are the most energy efficient processes. On the other hand, distillation process consumes more energy as compared to the membrane filtration processes which are relatively fast, efficient, and practical **[4].** Depending on the impact of various constituents of water on human health crops, and industrial processes, certain water and stream water standardshave been laid down by different standard institutions like, Bureau of Indian Standards (BIS), Indian Council of Medical Research (ICMR), World Health Organisation (WHO), and Food and Agriculture Organization (FAO) of United Nations for deciding the suitability of water for drinking and irrigation use. **Table1.1**summarizes the drinking water standards.

Table1.1. List of inorganic chemicals and their maximum contaminant level (MCL) in drinking water

Contaminant	MCL (mg/L)	Potential health effects : above the limit	Public health goal(mg/L)
Arsenic	0.01	Skin damage or problems with circulatory systems may have increased risk of getting cancer	Zero
Cadmium	0.005	Kidney damage	0.005
Chromium (total)	0.1	Allergic dermatitis	0.1
Copper	1.3	Liver or kidney damage	1.3
Fluoride	1.5	Pain and tenderness of the bones, Children may get mottled teeth	1.0
Iron	0.3	Water with brown-red colour, aesthetic problems	<0.3
Lead	0.015	Infants and children: Delays in physical or mental development; Adults: Kidney problems; high blood pressure	Zero
Mercury	0.002	Kidney damage	0.002

1. *US EPA's Safe Drinking Water Web site: http://www.epa.gov/safewater , USEPA's Safe Drinking Water Hotline: (800) 426-4791, USEPA 816-F-09-004 May 2009*
2. *MCL: Maximum contaminant level*

1.2. General Background

1.2.1. Preparation of synthetic membranes

Nowadays, membranes and membrane separation techniques have grown from a simple laboratory tool to an industrial process with considerable technical and commercial impact. Today, membranes are used on a large scale to produce potable water from the sea by reverse osmosis; to clean industrial effluents and recover valuable constituents by electro dialysis; to fractionate macromolecular solutions in the food and drug industry by ultrafiltration; to remove urea and other toxins from the blood stream by dialysis in an artificial kidney; and to release drugs at a predetermined rate in medical treatment. Although membrane processes may be very different in their mode of operation, in the structures used as separating barriers, and in the driving forces used for the transport of the different chemical components, they have several features in common which make them attractive as a separation tool. In several cases, membrane processes are faster, more efficient, and more economical than conventional separation techniques **[5]**. During membrane process, the separation is usually performed at ambient temperature, thus allowing temperature-sensitive solutions to be treated without the constituents being damaged or chemically altered.

1.2.2. Definition of Membrane

A synthetic membrane can be defined as a barrier which separates two phases and restricts the passage of numerous chemical species in a rather specific way.A membrane can be homogeneous or heterogeneous, symmetric or asymmetric in structure, solid or liquid, may carry positive or negative charges, or may be bipolar. Its thickness may vary between less than 100 nm to more than a centimeter. The mass transport through a membrane may be caused by convection or by diffusion of individual molecules, induced by an electric field, concentration, pressure or temperature gradient. The term membrane, therefore, includes a great variety of materials and structures, and a membrane can often be better described in terms of what it does rather than what it is.

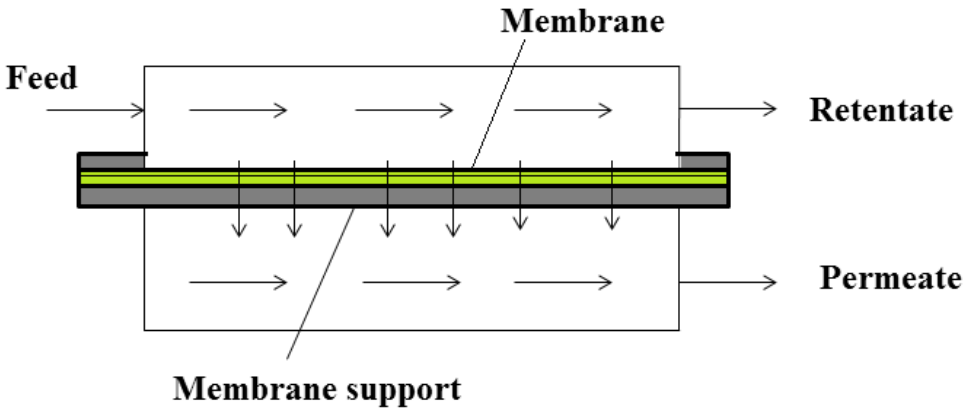

Fig 1.1 Schematic diagram of the basic membrane separation process

1.2.3. Types of membranes

A synthetic membrane is a synthetically created membrane which is usually intended for separation purposes in a laboratory or industry. Synthetic membranes have been successfully used for small and large-scale industrial processes since the middle of the twentieth century. A wide variety of synthetic membranes is known. They can be produced from organic materials such as polymers and liquids, as well as inorganic materials. Most commercially utilized synthetic membranes in separation industry are made of polymeric structures. Schematic diagram of the membrane types is presented in **Fig 1.2.**

(a) Polymeric membranes: Polymeric membranes lead the membrane separation industry market because they are very competitive in performance and economics. A polymer has to have appropriate characteristics for the intended application. The polymer sometimes has to offer a low binding affinity for separated molecules (as in the case of biotechnology applications) and has to withstand the harsh cleaning conditions. It has to be compatible with chosen membrane fabrication technology. The polymer has to be a suitable membrane former in terms of its chains rigidity, chain interactions and polarity of its functional groups. The polymers can form amorphous and semi-crystalline structures, affecting the membrane performance characteristics. The polymer has to be obtainable

and reasonably priced to comply with the low-cost criteria of membrane separation process. Many membrane polymers are grafted, custom-modified, or produced as copolymers to improve their properties. The most common polymers in membrane synthesis are cellulose acetate, nitrocellulose, cellulose esters (CA, CN, and CE), polysulfone (PS), polyethersulfone (PES), polyacrylonitrile (PAN), polyimide (PI), polyethylene(PE),polypropylene (PP), polytetrafluoroethylene (PTFE), polyvinylidene fluoride (PVDF), and polyvinylchloride (PVC).

(b) Ceramic membranes: Ceramic membranes are made from inorganic materials (such as alumina, titania, zirconia oxides, recrystallized silicon carbide or some glassy materials). By contrast with polymeric membranes, they can use in separations where aggressive media (acids, strong solvents) are present. They also have an excellent thermal stability which makes them usable in high temperature membrane operations. Even though ceramic membranes have a high weight and substantial production costs, they are ecologically friendly and have long working life.

(c) Liquid membranes: Liquid membranes refer to synthetic membranes made of non-rigid materials. Several types of liquid membranes can be encountered in industry: emulsion liquid membranes, immobilized (supported) liquid membranes, molten salts, and hollow fiber contained liquid membranes.Liquid membranes have been extensively studied but thus far have limited commercial applications. Maintaining adequate long-term stability is the problem, due to the tendency of membrane liquids to evaporate or dissolve in the phases in contact with them.

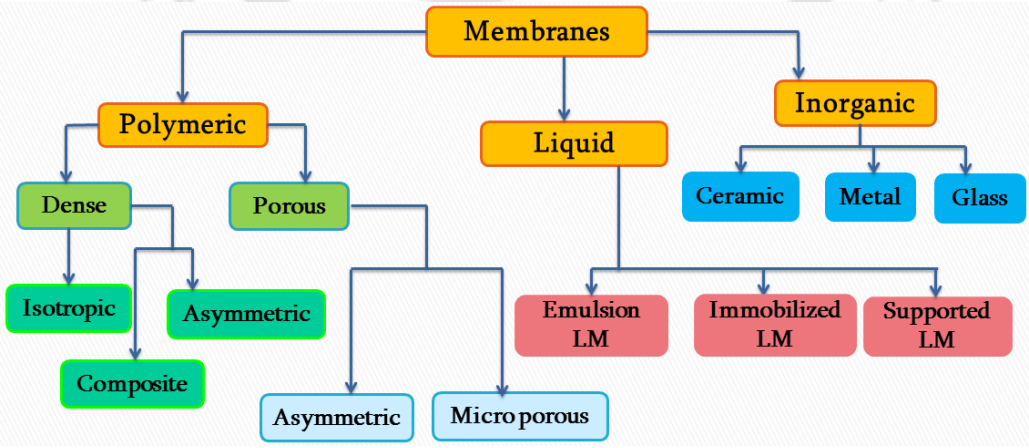

Fig 1.2 Schematic diagram for types of membranes

1.2.4. Preparation Techniques

The choice of a technique for polymeric membrane preparation depends on a selection of polymer and the required structure of the membrane **[6].**There are many processing techniques to fabricate membranes, which include sintering, stretching, track etching, template leaching, interfacial polymerization, phase inversion (different ways include immersion precipitation, thermally induced phase separation, evaporation induced phase separation, vapor induced phase separation andprecipitation by controlled evaporation), and electro-spinning.

1.2.4.1 Sintering

Sintering process (**Fig. 1.3**) is a unique and simple technique allowing porous material to be obtained from organic as well as from inorganic materials. The method involves compression of a powder consisting of particles of given size and sintering at elevated temperatures. The required temperature depends on the material used during sintering and the interfaces between the contacting particles. A wide range of different material can be used as powder of polymers (polyethylene, polytetrafluoroethylene, and polypropylene), metals (stainless steel and tungsten), ceramics (aluminium oxide and zirconium oxide), graphite (carbon), and glass (silicates). The pore size of the resulting membrane is determined by the particle size and particle size destruction of the powder. Narrow particle size distribution gives a narrow pore size distribution in the resulting membrane. This technique allows pore sizes of about 0.1 to 10 μm to be obtained, the lower limit being determined by the minimum particle size.

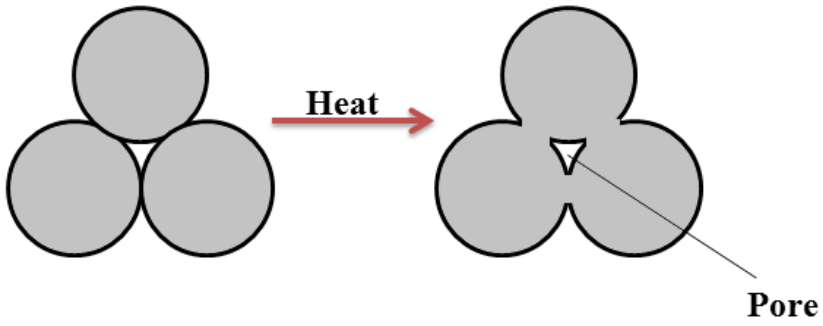

Fig. 1.3 Sintering process

Sintering is a very suitable technique for preparing of membranes from polytetrafluoroethylene because; this chemically and thermally very resistant polymer is not soluble. Only microfiltration membranes can be prepared via sintering. However, the porosity of porous polymeric membrane is low, normally in the range of 10 to 20% or sometimes a little higher.

1.2.4.2. Stretching

Another relatively simple procedure for preparing micro-porous membranes is the stretching of a homogeneous polymer film of partial crystallinity. This technique is mainly employed with films of polyethylene or polytetrafluoroethylene which have been extruded from a polymer powder and then stretched perpendicular to the direction of extrusion. This leads to a partial fracture of the film and relatively uniform pores with diameters of 1 to 20 μm. These membranes, which have a very high porosity, up to 90%, and a fairly regular pore size are now widely used for microfiltration of acid and caustic solutions, organic solvents, and, hot gases. They have to a large extent replaced the sintered materials used earlier in this application. Stretched membranes can be produced as flat sheets as well as tubes and capillaries. The stretched membrane made out of polytetrafluoroethylene is frequently used as a water repellent textile for clothing, such as parkas, tents, and sleeping bags, etc. This membrane has very high porosity, high permeability for gases and vapors, but, because of the hydrophobic nature of the basic polymer, is up to a certain hydrostatic pressure completely impermeable to aqueous solutions. Thus, the membrane is repellent to rain water but permits the water vapor from the body to permeate. More recently, this membrane has also been used for a novel process, generally referred to as membrane distillation, i.e., to remove ethanol from fermentation broths or wine and beer to produce low-alcohol products and for desalination of seawater. These membranes are also used for desalination of saline solutions and in medical applications, such as, burn dressings and artificial blood vessels.

1.2.4.3. Track etching

The simplest pore geometry in a membrane is an assembly of parallel cylindrical shaped pores of uniform dimension. Such structures can be obtained by track-etching, and the preparation method is presented in **Fig. 1.4**. In this method, a film or foil (often a polycarbonate)

is subjected to high energy particle radiation applied perpendicular to the film. The particles damage the polymer matrix and create tracks. The film is then immersed in an acid or alkaline bath, and the polymeric material is etched away along these tracks to form uniform cylindrical pores with a narrow pore size distribution. Pore sizes can range from 0.02 to 10 μm, but the surface porosity is low (about 10% at a maximum). The choice of the material depends mainly on the thickness of the film and the energy of the particles being applied (usually about 1 MeV). The maximum penetration thickness of particles with this energy is about 20 μm. When the energy of the particles is increased, the film thickness can also be increased, and even inorganic material (e.g., mica) can be used. The porosity is mainly determined by the radiation time whereas the pore diameter is determined by the etching time.

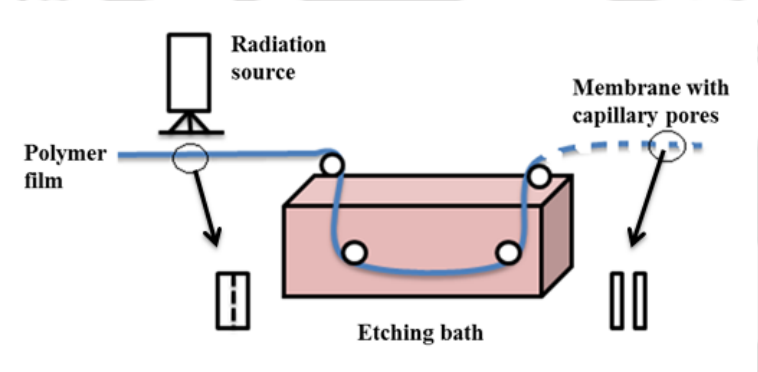

Fig. 1.4 Preparation of porous membrane by track etching

1.2.4.4. Template leaching

Template leaching is another method of producing isotropic micro porous membranes from insoluble polymers such as polyethylene, polypropylene, and poly (tetrafluoroethylene). In this process, a homogeneous melt is prepared from a mixture of the polymeric membrane matrix material and a leachable component. To finely disperse the leachable component in the polymer matrix, the mixture is often homogenized, extruded, and pelletized several times before final extrusion as a thin film. After formation of the film, the leachable component is removed with a suitable solvent, and a micro porous membrane is formed. The leachable component can be a soluble, low-molecular-weight solid, a liquid such as liquid paraffin, or even a polymeric material such as polystyrene. A drawing of a template leaching membrane production machine is shown in **Fig. 1.5.**

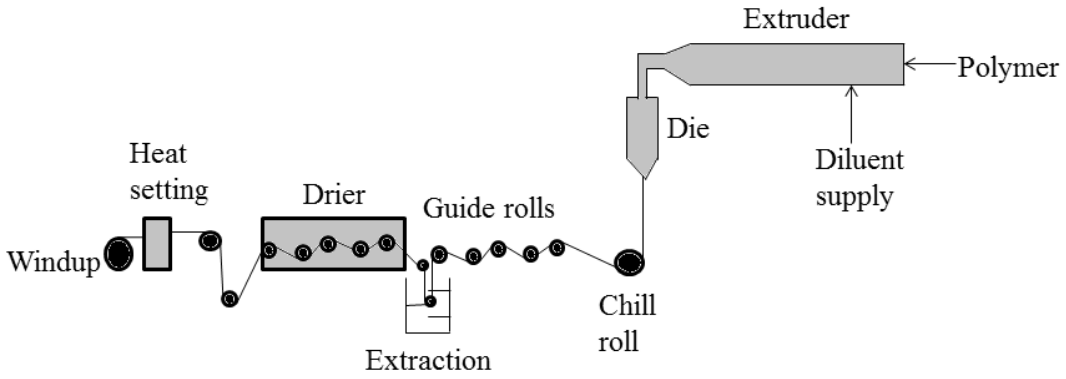

Fig. 1.5 Template leaching process

1.2.4.5. Phase inversion

Phase inversion is a process whereby a polymer is transformed in a controlled manner from a liquid phase to a solid phase. The process of solidification is very often initiated the transition from one liquid phase into two liquid phase (liquid-liquid demixing). At a certain stage during demixing one of the liquid phases (the high polymer concentration phase) will solidify so that a solid matrix is formed. By controlling the initial stage of phase inversion, the membrane morphology can be controlled i.e. porous as well nonporous membrane can be prepared. The concept of phase inversion covers a range of different technique, such as solvent evaporation, thermal precipitation, precipitation by controlled evaporation, perception from the vapor phase,and immersion precipitation. The majority of phase inverted membranes are prepared by immersion precipitation. In this process, a polymer solution is cast on a suitable support and then immersed in a coagulation bath containing a non-solvent, where an exchange of solvent and non-solvent takes place, and the membrane is formed. Schematic representation of phase inversion processes after polymer solution immersion in a non-solvent bath is shown in **Fig.1.6.** This type of membrane can be made from almost any polymer which is soluble in an appropriate solvent and can be precipitated in a non-solvent. By changing the type of polymer, the polymer concentration, the precipitation medium, and the precipitation temperature, micro porous phase inverted membranes can be made with a very large variety of pore sizes (from less than 0.1 to more than 20μm) with varying chemical, thermal, and mechanical properties.

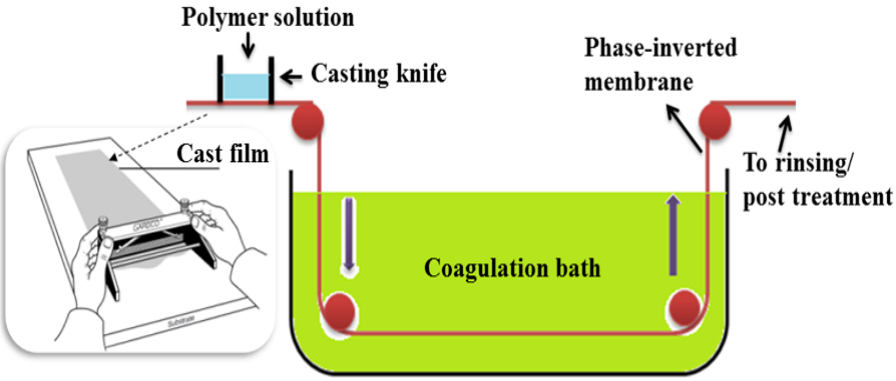

Fig. 1.6 Membrane preparation byphase inversion methods

1.2.4.6. Electro-spinning

Electro-spinning is a process that fabricates fibers through an electrically charged jet of polymer solution or polymer melt. To understand electro-spinning, one can look at the mechanism behind the production of polymer fibers. Conventional fibers of large diameter involve the drawing of molten polymer out through a die. The resultant stretched polymer melt will dry to form individual element of fiber. Similarly, electro-spinning also involves the drawing of fluid, either in the form of molten polymer or polymer solution. However, unlike conventional drawing method where there is an external mechanical force that pushes the molten polymer through a die, electro-spinning makes use of charges that are applied to the fluid to provide a stretching force to a collector where there is a potential gradient. When a sufficiently high voltage is applied, a jet of polymer solution will erupt from a polymer solution droplet. The polymer chain entanglements within the solution will prevent the electro-spinning jet from breaking up. While molten polymer used in both conventional fiber production method and electro-spinning method,it cools and solidifies to yield fiber in the atmosphere.On the other hand, the electro-spinning of polymer solution relies on the evaporation of the solvent for the polymer to solidify to form polymer fiber. **Fig. 1.7** shows the schematic diagram electro-spinning process and fiber formation.

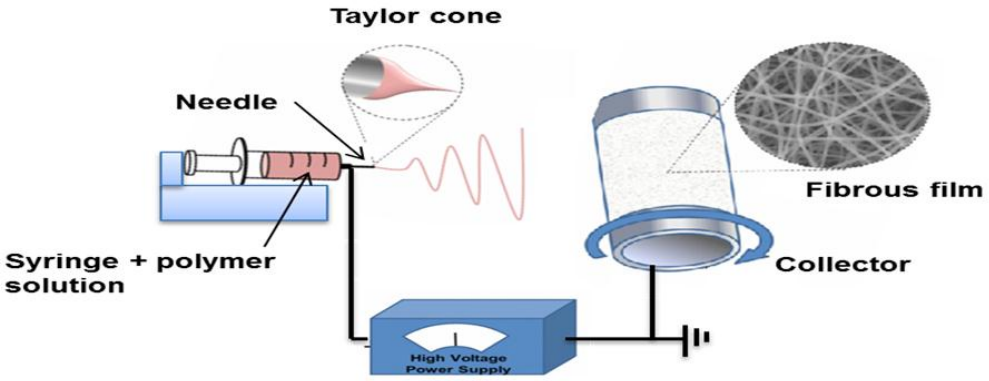

Fig. 1.7 Basic schematic drawing of electro-spinning process

Since electro-spinning is the drawing of a polymer fluid, there are many different types of polymers and precursors that can be electro-spun to form fibers. The materials to be electro-spun will depend on the applications. Materials such as polymers and polymer nanofibercomposites can be directly produced by electro-spinning technique. While other materials such as ceramics and carbon nanotubes require post processing of the electro-spun fibers.

Polymer solution parameters

The properties of the polymer solution have the most significant influence in the electro-spinning process and the resultant membrane morphology. The surface tension has a part to play in the formation of beads along the fiber length. The viscosity of the solution and its electrical properties will determine the extent of elongation of the solution**[7]**. One of the factors that affect the viscosity of the solution is the molecular weight of the polymer. When a polymer of higher molecular weight is dissolved in a solvent, its viscosity will be higher than solution of the same polymer but of a lower molecular weight. One of the conditions necessary for electro-spinning to occur where fibers are formed is that the solution must consist of polymer of sufficient molecular weight and the solution must be of sufficient viscosity. This will, in turn, have an effect on the diameter of the resultant electro-spun fibers.Koskiet. al. **[8]** have studied the effects of polymer average molecular weight on the fiber structure of electro-spun polyvinyl alcohol (PVA).They have reported an average fiber diameter between 250 nm and 2 μm and the fiber diameter increases with M_W and concentration. At lower M_W and/or concentrations, the fibers exhibit a circular cross-section. They have also observed flat fibers at high M_W and concentrations. The effect of viscosity on the membrane morphology has also studied by Mohammad et al.

[9]. According to this study, viscosity of the spinning solutions has played an important role on the morphology of the mullitenanofibers. Continuous electro-spun nanofibers with common cylindrical morphology were obtained when PVA content was 6wt. %. Further increasing the amount of PVA in the pre-spinning solution led to excessively high viscosity level, making the shape of the resulting mullitenanofibers wide and flat ribbon.

Processing conditions

Another important parameter that affects the electro-spinning process is the various external factors exerting on the electro-spinning jet. This includes supplied voltage, feed rate, temperature of the solution, type of collector, diameter of needle, and distance between the needle tip and collector. These parameters have a certain influence in the fiber morphology although they are less significant than the solution parameters.During the electro-spinning process, the droplet of polymer solution at the needle tip slowly elongates from a semi-circular shape to a conical shape or Taylor cone, as the applied voltage is increased**[10].** As the applied voltage increases further, it results in the eruption of a jet from the tip of the Taylor cone and the diameter of fibers collected decreases. Barhateet. al. **[11]** studied the effect of electro-spinning process parameters on structural and transport properties of the electro-spun membranes in detail.In the absence of an aerodynamically driven bending instability, electrical bending instability is the only mechanism that influences the way in which the jet is oriented before its deposition over the collector. The fiber crossing and pore size can be optimized to attain improved structural (pore size distribution, pore interconnectivity, and porosity) and transport (permeability) properties of the electro-spun filtering media.Finally, they have suggested that optimization can be attained by coordination of the applied voltage and collection rates. Since the jet follows a bending, winding, spiraling, and looping path in three-dimensions due to electrical bending instability before its deposition over the collector, the tip-to-collector distance is another parameter that may alter the morphology of the membrane. The area of the Taylor cone (resulting from the electrically driven bending instability) is an important parameter to consider when targeting uniform deposition of nanofibers. A summary of the various membrane fabrication techniques, range of pore size/ porosity, and their resultant properties are presented in **Table 1.2.**

1.2.5. Functionalization of membranes

To maintain membrane separations as economical alternatives to conventional water and wastewater treatment technologies, we must produce a high quality permeate at a fast rate, and be able to maintain that production for an extended period. However, the relationship between flux and selectivity along with fouling introduce a challenge that must be addressed for all membrane applications. There are three main areas of interest when it comes to improving membrane performance:

(i) ***Synthesis process:***Synthesis process improvement involves using the techniques, methods, and materials of the manufacturing processes to produce a high-performance membrane.

(ii) ***Applicationprocess****:* The application process involves the specific operating parameters for a membrane system. These include selecting the raw water characteristics, operating pressure, and cleaning intervals to allow the system to operate at maximum efficiency.

(iii) ***Modification (functionalization):*** Post or pre-synthesis modification involves functionalization of the polymer before synthesis and the modification of membrane after the initial preparation process is completed.

Functionalization or modification of membranes are mostly related to the introduction of functional groups into membranes such as, carboxylic (–COOH), amine ($-NH_2$), hydroxyl (–OH), thiol (−SH), epoxide, aldehyde, etc. **[12].** The functionalized membranes with proper activating groups can cover a great variety of applications such as an anti-fouling membrane (tunable permeation and separation), affinity membrane (toxic metal capture, nanoparticles immobilization for toxic organics degradation), membrane based biosensor, biomedical compatible biomaterials, and super hydrophobic or hydrophilic surfaces, etc.Many membranes are naturally hydrophobic due to the polymers that are used in the manufacturing process. A drawback of a membrane exhibiting a hydrophobic nature is that it increases the required transmembrane pressure (TMP) that must be utilized for operation since the solvent (i.e. water) is repelled by the surface of the membrane.

Table 1.2 Different membrane fabrication techniques and their properties *(Sources: Mulder, 1996; Ramakrishna, 2005)*

Fabrication technique	Pore diameter (μm)	Porosity (%)	Properties
Sintering	0.1–10	10–20	Outstanding chemical, thermal and mechanical stability, both organic and inorganic material can be used.
Stretching	01–20	90	High permeability for gases and vapors, can be produced as flat sheets, tubes or capillaries
Track etching	0.02–10	Max 10	Low tendency to plug, good long term flux stability
Template leaching	Min 0.05	Porous	High surface area
Phase inversion	< 0.21–>20	Porous and non-porous	Properties varied according to polymer used.
Electro-spinning	porous	Highly porous (>80)	Relatively high flux and less tendency to fouling, high surface area

However,if a membrane can be rendered hydrophilic, the solvent is attracted to and transported through the membrane at a much faster rate, which reduces the required TMP for operation. In addition, many solutes found in feed waters are hydrophobic, so utilizing a hydrophilic membrane could increase the membrane's selectivity and fouling resistance **[13].**Moreover, membranes with higher surface roughness have different peaks and valleys and

are more susceptible to fouling, and with a reduction of roughness, foulants are less likely to adhere to the membrane. Post-synthesis modifications may ultimately lead to a higher flux and selectivity and improved fouling resistance.

1.2.5.1. Functionalization techniques

Membrane modification or functionalization can be achieved through either covalent or non-covalent attachment. The membrane modification can be done using different techniques such as physical coating or blending, graft polymerization, plasma treatment, and chemical treatment, etc.

Physical coating or blending

This technique is the easiest and the most straight forward way to modify polymer surface by blending functional groups into the bulk polymer or just coating it on the polymer surface. The biggest drawback of this technique is the instability of the bulk polymer surface composition caused by the loss of the functional materials from the polymer. But it is still a good choice if this loss is too slow to be considered, or not fast enough to affect the application of the materials. Physical coating or blending of functional molecules into/onto the polymers was significantly developed by some new methods, such as self-migration **(a)**, self-assembly **(b),** and layer by layer **(c)** (**Fig. 1.8).** In a self-migration method, the functional group with special interest is mixed into the bulk polymer. By making it reach the lowest free energy state, the functional materials or molecules can automatically migrate towards the polymer surface and finally accumulated onto the polymer surface so that it can change the properties of the bulk polymer surface considerably **[14]**. On the other hand, in self-assembly method, the surfactant molecules coated onto substrate surface self-assembled into a thin film, driven by hydrophobic interaction, hydrogen bond, electrostatic interaction or chemical reaction **[15].** Furthermore, the layer-by-layer method is a special case of the self-assembly method and negatively and positively charged macromolecules are alternatively introduced onto the polymer surface through the strong electrostatic interaction **[16]**.

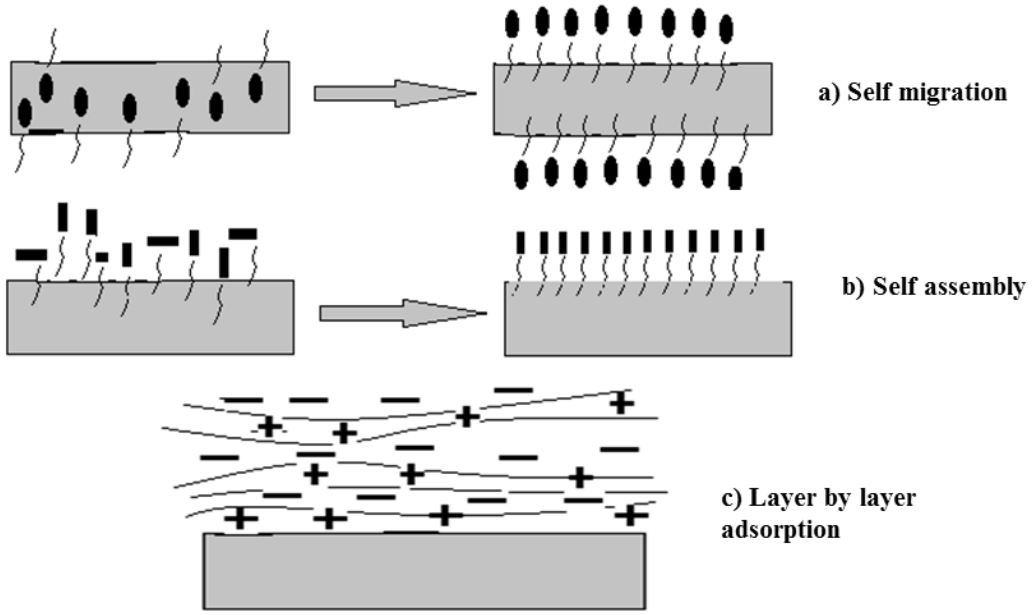

Fig. 1.8 Schematic representation of (a) self-migration, (b) self-assembly, and (c) layer-by-layer adsorption techniques

Graft copolymerization

Grafting is one of the chemical modification methods developed to date and has emerged as a simple, useful, and versatile approach to improving surface properties of polymers for a wide variety of applications. Grafting has numerous advantages:

- The ability to modify the polymer surface to have very distinct properties through the choice of different monomers.
- The ease and a controllable introduction of graft chains with a high density and exact localization of graft chains to the surface with the bulk properties unchanged.
- Covalent attachments of graft chains onto a polymer surface assuring the long-term chemical stability of introduced chains, in contrast to physically coated polymer chains.

For the graft copolymerization to be occurring, groups which can produce radicals must be introduced onto the polymer surface first to activate the polymer surface. Most of the chemically inert polymers can be activated via irradiation (UV, ɤ-ray, electron beams, etc.), plasma treatment, ozone or H_2O_2 oxidization, or Ce^{4+} oxidization (**Fig. 1.9**).

Plasma treatment

For plasma induced graft polymerization, an inert gas is often used to produce radicals on the polymer surface. While reactive gas such as O_2, SO_2, NH_3, and $CO_2$are used, chemical functional groups like hydroxyl, carboxyl, carbonyl, and sulfonate, etc. can be yielded on the polymer surface directly. However, the functional groups introduced on the polymer surface are not distinct. As mentioned above, plasma consists of a unique mixture of different positively charged or negatively charged ions, electrons, free radicals, atoms and molecules. The variety of the particles in a plasma chamber also causes a variety of the functional groups yielded on the polymer surface. Plasma treatment is usually not expected to introduce a specific functional group, but just to increase the polarity, hydrophilicity, and charge of the polymer surface to benefit applications like adhesion, dye removal ability, and blood compatibility, etc.

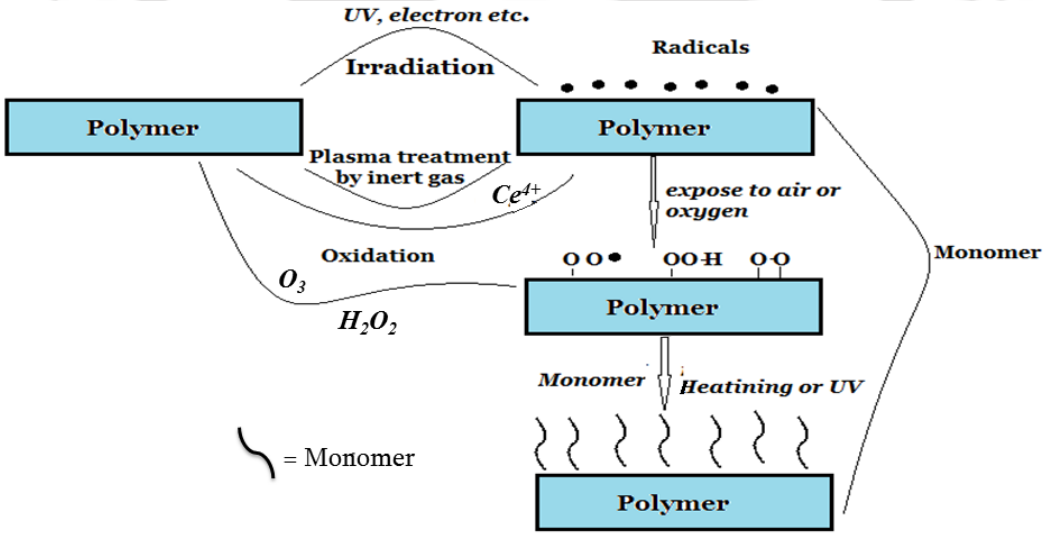

Fig. 1.9 The general scheme of how the surface of polymer can be grafted

Chemical treatment

Polymer molecules which possess functional groups like hydroxyl, carboxyl, amino and ester, etc., can be directly modified by chemical treatment. The chemical modification involves the introduction of one or more chemical species to a given surface so as to produce a surface

which has enhanced chemical and physical properties. Chemical reactions can be carried out at sites that are vulnerable to electrophilic or nucleophilic attack. Structures like benzene rings, hydroxyl groups, double bonds, halogen, ester groups, etc. qualify for such attacks. Wet chemical oxidation treatments are also commonly employed to introduce oxygen-containing functional groups (such as carbonyl, hydroxyl, and carboxylic groups) at the surface of the polymer. This can be conducted using gaseous reagents or with solutions of vigorous oxidants. The oxygen-containing functional groups increase the polarity and the ability to hydrogen bond, thus in turn results in the enhancement of wettability and adhesion.

1.3. Literature survey and objective of the work

1.3.1. Preparation and applications of electro-spun membranes

In the electro-spinning process, a number of parameters can affect the morphology of the attained fibers. The main parameters are polymer solution (concentration, viscosity, surface tension, and conductivity of the polymer solution), process conditions (applied voltage, tip-to-collector distance, and feed rate), and ambient parameters (temperature, relative humidity, and velocity of the surrounding air in the spinning chamber)**[17]**. Electro-spun membranes or fibers are normally collected in the form of non-woven mats, which are of interesting for a variety of applications such as, semi-permeable membranes, filters, composite reinforcement, and scaffolding used in tissue engineering, etc.**[18]**.

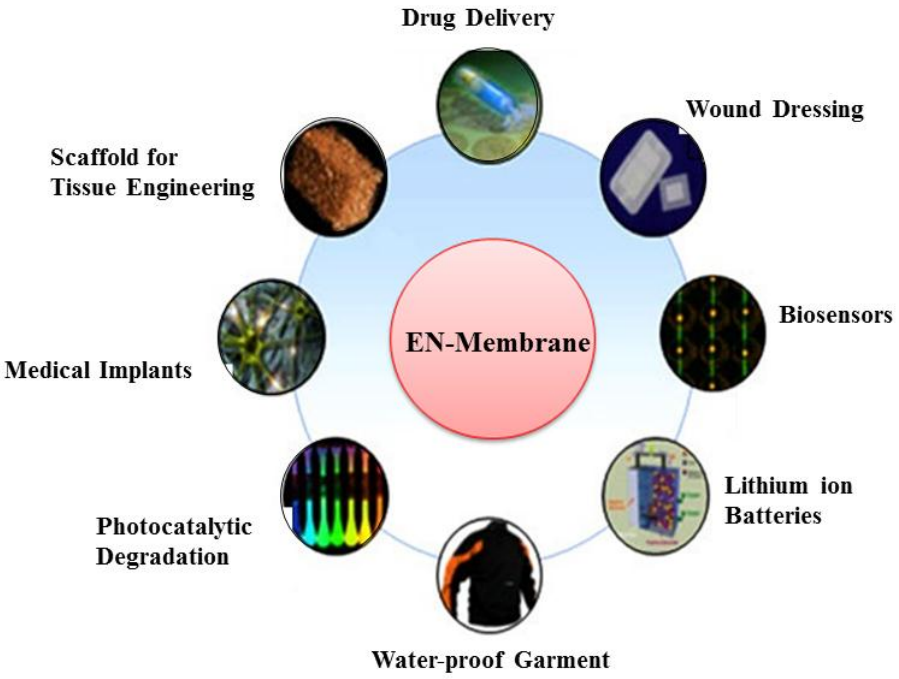

Fig. 1.10 Variousapplications of electro-spun membranes

Deitzel et al.**[18]**havereported the controlled deposition of electro-spun poly (ethylene oxide) fibers and the feasibility of dampening the instability of sub-micron polymer fibers less than 300 nm in diameter. Accordingly,poly(ethylene oxide) (PEO) with 10 wt.% in water was electro-spun at high voltage supply from 5 to15 kV to the vertically oriented syringe tip and collected to the plate situated at the bottom of the apparatus 17 cm apart. In their conclusion, they have shownthat the possibility to control the deposition of electro-spun fibers through the use of an electrostatic lens element and biased collection target. Moreover, the possible control or elimination of the bending instability occurred in electro-spinning experiments by applying a secondary external field of the same polarity as the surface charge on the jet was suggested. Krishnappa et al. **[19]**have electro-spun bisphenol-A polycarbonate using two solvents: chloroform and a 1:1 mixture of tetrahydrofuran (THF) and dimethylformamide (DMF). The polycarbonate concentrations in the solutions were 14% and 15% by weight; the tip to target distances was maintained between 80–120 mm; voltage was varied from 6 kV to 30 kV. The morphological features of the electro-spun polycarbonate fibers have been studied as a function of the solvent and processing voltage and the diameters of the fibers range from 100 nm to 500 nm. Finally, they have concluded that the surface tension, electrostatics, and viscosity, which are

a function of the concentration of the polymer in the solution, play a major role in determining the morphology of the spun material. Choi et al. **[20]**alsostudied the application of electro-spun PVDF nanofiber webs as an electrolyte binder or a separator for a battery where PVDF of 25 wt. % was dissolved in dimethylacetamide (DMAc); the distance between the needle tip and the rotating collector was 15 cm, and the applied voltage was kept at 10 kV. The diameters of the electro-spun PVDF nanofiberswere found to be 100–800 nm. Following thermal treatment at 150–160 $^{\circ}$C, the membrane's physical property, dimensional stability, tensile strength, and elongations at break as well as the tensile modulus were notably improved. Yang et al. **[21]**have spun polyvinyl alcohol (PVA) cross-linked with maleic anhydride (MA)at a positive voltage of 20 kV and a tip to collector distance of 20 cm. From water durability test they have found that the average mass loss and standard deviation of electro-spun 8% PVA/MA (20/1, mole/mole) membrane was the least after boiling in water for 1 h, and they have also observed that the average diameter of fibers in PVA/MA membrane was larger than that in PVA membrane. Moreover, their experimental results indicated that rapid evaporation of water and high electric field during electro-spinning process could promote esterification reaction. Tsioptsias et al. **[22]**have prepared cellulose acetate–Fe_2O_3 composite nanofibrous materials by electro-spinning process where 20% (w/v) CA solutions with dispersed Fe_2O_3 nanoparticles varying between 1.4% and 4.5% (w/v), and N,N−dimethylacetamide/acetone was used as solvent. During the electro-spinning process, they have kept the solution flow rate as 0.38 mL/h; needle to target distancewas 5 cm; high voltages (13, 16.5, and 20 kV);and the collecting target was a rotating drum covered with aluminium foil. Finally, they have recommended that these composite materials with enhanced thermal stability compared to pure cellulose acetate and fairly uniform composite fibrous structures for potential use in separation processes or biomedical applications. Tsai et al. **[23]**have prepared electro-spun chitosan–gelatine–polyvinyl alcohol hybrid nanofibrous mats using only a mild concentration (20 wt. %) of acetic acid (solvent) by electro-spinning. During the preparation, different concentrations were used, and the solution was loaded into a 3 mL syringe with a flow rate of (0.15–0.3 mL/h) which was controlled by a syringe pump. High electric voltages (15–30 kV) were applied, and the fiber mats were collected on a vertical collector where the distance was kept to be 15 cm. The optimum weight ratio of chitosan: gelatine:PVA to be 2:2:4, with resultant fiber diameters of around 150 nm and uniform nanofibers were obtained at an applied voltage of 20 kV. The stability and tensile strength of the

nanofibrous mats were both improved by glutaraldehyde vapour-crosslinking for 12 h. From cytocompatibility and 3-dimethylthiazol-2,5-diphenyltetrazolium bromide (MTT) assay (which measured cell activity) tests, they have found good results as compared to sponges and chitosan–gelatine–PVA nanofibrous mats were suggested as suitable for attachment and proliferation of KP-hMSCs, probably because the morphology and structure of nonwoven electro-spun nanofibers are similar to the extracellular matrix (ECM). Kimura et al.**[24]**have prepared poly (vinylidene fluoride-co-hexafluoropropylene) (PVDF-HFP-6/1/3) nanofiber membranes with different amounts of polyethylene glycol (PEG) and polyethylene glycol dimethacrylate (PEGDMA) oligomer via electro-spinning.The experiments were performed at room temperature, and the collecting roller distance was 12 cm from the tip, and a voltage of 11 kV was applied.The prepared nanofiber membrane had a higher porosity, electrolyte uptake, and bulk resistance value than existing separator and this membrane was suggested to be a promising candidate as a separator for lithium-ion batteries.

1.3.2. Electro-spun membranes for water and wastewater treatment applications

Permselectivity and flux are important specificity in membrane separation. Till now it is an ultimate dream for membranologists to simultaneously improve both perm-selectivity and flux, which generally show a trade-off relationship.An advancement in membrane separation would be realized by adopting membranes with higher surface area and higher porosity **[25]**.Polymer nanofibers are main class of nano-materials, which can be easily tuned to exhibit novel and significantly improved physical and chemical properties. In the last 10 years, they have got increasing attention because of their high surface-to-mass ratio and special characteristics which are attractive for advanced applications. Specifically, electro-spun nanofiber membranes have high porosity, inter-connected open pore structure, and tailorable membrane thickness **[26]**.Though nanofiber membranes have been commercially used for air filtration applications, their potential in water treatment is still largely unemployed **[27]**. Gopal et al. **[28]**have prepared electro-spunmembranes of polyvinylidene fluoride nanofibers by using electro-spinning process and characterized to relate its structural properties to membrane separation properties and performance.They have confirmed that the membranes have similar properties to that of conventional microfiltration membranes with fiber diameter 106-308 nm; thickness 300 μm;trans membrane pressure 0.5 bar; pore size 10.6-4.0 μm; and flux of 200

kg/m^2h. The electro-spun membranes were used to separate 1, 5, and 10 μm polystyrene particles and they were successful in rejecting more than 90% of the micro-particles from the solution. The authors suggested that these membranes could be employed in the separation technology as a potential membrane for pre-treatment of water prior to reverse osmosis or as pre-filters to minimize fouling and contamination prior to ultra- or nano-filtration. Wang et al. **[29]**,on the other hand, have developed high flux ultrafiltration (UF) membrane based on poly (vinyl alcohol) (PVA) electro-spun nanofibrous scaffold support and PVA hydrogel coating. They have found that the electro-spun scaffold fabricated by 96% hydrolysed PVA with relatively high molecular weight showed very good overall mechanical performance before and after crosslinking. The PVA hydrogel coating was also fabricated with different crosslinking conditions and used as the anti-fouling layer for high-throughput water ultrafiltration. Their ultrafiltration test specified that the hydrophilic nanofibrous composite membranes showed a flux rate (>130 L/m^2 h) which is significantly greater than commercial UF membranes but with similar filtration efficiency (rejection rate >99.5%). Yoon et al. **[30]**have reported about conventional ultrafiltration (UF)/nanofiltration (NF) filters for water treatments based onporous membranes, typically manufactured by the phase immersion method, where their torturous porosity usually results in a comparatively low flux rate. They have fabricated a new type of high flux UF/NF medium based on an electro-spun nanofibrous scaffold (polyacrylonitrile, PAN) attached with a thin top layer of hydrophilic, water-resistant, and water-permeable coating (chitosan).The average diameter was ranging from 124 to 720 nm and porosity of about 70 % together with a chitosan top layer having a thickness of about 1 μm. The flux and rejection studies also evaluated in this report in which the flux rate was an order of magnitude higher than commercial NF membranes in 24 h of operation, while maintaining the same rejection efficiency (>99.9%) for oily waste-water filtration. Kim et al. **[31]**have investigated electro-spun polycarbonate (PC) with quaternary ammonium salt (benzyl triethylammonium chloride, BTEAC) as an additive to develop antimicrobial nanofibrous membranes for ultrafiltration. They have found that the conductivity of the PC solution was a key parameter affecting the morphology and diameter of the electro-spun PC fibers. Finally their report showed that the PC nanofibrous membrane with BTEAC had an excellent antimicrobial activity and filtration performance. Zhang et al. **[32]**also have assessed an adsorptive membrane made from electro-spun cellulose acetate nanofibers as an ion-exchange medium for protein separations. They have

found that the electro-spun cellulose acetate nanofibers had diameters ranging from tens of nanometers to microns, and the pore sizes within the nanofiber felts were ranging from sub-microns to microns.The results have indicated that the diethylaminoethyl (DEAE) surface functionalized nanofiber felt showed the highest static binding capacity of 40.0 mg/g for BSA, compared to 33.5 mg/g, 14.5 mg/g, and 15.5 mg/g for the functionalized commercial membrane, cellulose microfiber medium, and cotton balls, respectively. The porous nature of the nanofiber felts caused in a higher permeability compared to the commercial membranes. Aussawasathien et al. **[33]**have preparedelectro-spun nylon-6 nanofibrous webs with fiber diameters in the range of 30–110 nm and was employed as a membrane material for water filtration due to its excellent chemical and thermal resistance as well as high wettability. They have reported that this membrane was able to separate all particles with sizes from 10 μm down to 1μm whereas roughly 90% separation was obtained for 0.5 μm particles, where low content of particles in the filtrate, indicated by the high separation factor. Finally, they have recommended that the prepared membrane could be used as pre-filters prior to ultrafiltration or nanofiltration to increase the filtration efficiency and prolong the life of downstream membranes. Yoon et al. **[34]**have demonstrated a high flux thin-film nanofibrous composite (TFNC) membrane system based on polyacrylonitrile (PAN) electro-spun scaffold (porosity of about 85%) attached with a thin barrier layer of cross-linked polyvinyl alcohol (PVA) on which its thickness was about 0.5μm. According to the authors report the TFNC membrane system shall be very useful for ultrafiltration (UF) applications, exhibiting a very high flux (12 times higher than that of conventional PAN UF membranes) and excellent rejection ratio, >99.5% for separation of oil/water mixture (1500ppm in water). The membranes were tested up to 190 h in a practical pressure range of up to 130 psig.In addition, the MWCO characteristics of PVA–PAN TFNC membrane (between 9–11 k and 35–45 k) was studied anda slightly lower than that of PAN10 UF membrane was attained. Xu et al. **[35]**have developed hierarchically nanofibrous membrane of thermal plastic elastomer ester (TPEE) and iron alkoxide with high crystallinity as well as hierarchical structure. The synthesized membranes have indicated high efficiency for the removal of Cr (VI)from water and were mainly attributed to the adsorption and reduction of Cr (VI) to Cr (III), because of the hierarchical structure and the exposed iron oxide active sites. Firstly, the adsorption of Cr (VI) on the surface of iron oxides by the electrostatic adsorption wasachieved and secondly, the reduction of Cr (VI) to Cr (III), which is much less toxic, and

almost all of Cr (VI) removal has been reported. Wang et al. **[4]**have preparedelectro-spun nanofibrous membranes for high flux microfiltration of polyacrylonitrile (PAN) on non-woven polyethylene terephthalate (PET) support, with a total thickness of 200±10 μm; average fiber diameter of 100±20 nm; high effective porosity (up to 80%); interconnected pores; and the optimized small pore size (maximum pore size of 0.62±0.03 μm and mean flow pore size of 0.22±0.01 μm). They have evaluated the membrane performance for microfiltration and showed significantly better in flux (1.5L/m^2h) (i.e. 2–3 times) over the Millipore GSWP 0.22 μm membranes, while maintaining a high rejection level in the micro-particle retention test, and achieved complete bacteria removal. Mahapatra et al. **[36]**have prepared iron oxide–alumina mixed nanocomposite fiber by electro-spinning with fibers diameters range of 200–500 nm for heavy metal ion adsorbent.The electro-spun nanofiber membranes were sintered at 1000 ˚C to convert them to pure oxide. The best isotherm fit for copper and lead was obtained with Langmuir adsorption isotherm while Freundlich was the best option for nickel and mercury and complete removal of mixed oxide nanocomposite fibers was reported as copper (21%), lead (52%), nickel (67%), and Hg (89%). Li et al. **[37]**have fabricated novel high performance hydrophilic poly (vinyl alcohol-co-ethylene) (PVA-co-PE) nanofiber membrane for filtration media. The investigation of the rejection rate of PVA-co-PE nanofibrous membrane to TiO_2 suspension was above 99%, and such unique hydrophilic nanofibrous membrane showed a higher flux rate than the commercial microfiltration membrane. According to their conclusion, the fabricated membrane indicated that good performances of flux and low fouling, and was suggested to be used for potential applications in the microfiltration fields. You et al. **[38]**have developed a new class of high-performance thin-film nanocomposite (TFNC) ultrafiltration membrane using electro-spinning technique combined with solution treatment method to separate an oil/water emulsion based on a polyacrylonitrile (PAN) nanofibrous substrate coupled with a thin hydrophilic nanocomposite barrier layer. The PVA–MWNT/PAN TFNC (10 wt. % MWNT) membrane showed a very high water flux (270.1 L/m^2h), and high rejection rate (99.5%) at a very low feeding pressure (0.1 MPa). Aliabadi et al. **[3]**have preparedpoly ethylene oxide (PEO)/chitosan nanofiber membrane by electro-spinning technique with the average diameter and surface area of 98 nm and 312.2 m^2 g^{-1}, respectively. The prepared membrane was evaluated for potential adsorption of nickel (Ni), cadmium (Cd), lead (Pb), and copper (Cu) from aqueous solution.It was found that the adsorption of metal ions onto the PEO/Chitosan nanofiber

membrane was feasible, spontaneous, and endothermic within the deceasing order of Pb (II), Cd (II), Cu (II), and Ni (II) and the adsorption percentages of these metal ions were obtained as 68 %, 72 %, 82 %, and 89 %, respectively. Liu et al. **[39]**have presented a novel class of high-flux microfiltration filters consisting of an electro-spun nanofibrous membrane and a conventional non-woven microfibrous support with an average fiber diameter of 100±19 nm; mean pore size 0.30 μm to 0.21 μm; and thickness varying from10 μm to 100 μm. The water permeability were found to be 3 to 7 times than the Millipore GSWP 0.22 μm membrane due to the high porosity of the microfiltration filters based on these electro-spun membranes. The nanofibrous PVA membranes with an average thickness of 20 μm could successfully reject more than 98% of the polycarboxylate microsphere particles with a diameter of 0.209 ± 0.011 μm, and still maintain 1.5 to 6 times higher permeate flux than that of the Millipore GSWP 0.22 μm membrane.

1.3.3. Preparation and application of phase-inverted membranes

Most commonly available commercial membranes are prepared by phase-inversion technique **[40]**. This technique is suitable for preparing membranes with all types of morphological structures. In this method, a casting solution comprising of polymer and solvent is immersed into a non-solvent coagulation bath, and a polymer is transformed from liquid phase to a solid phase in a controlled condition. The solidification process is very frequently started by the change from one liquid phase to two liquids (liquid-liquid de-mixing). At certain period during de-mixing, the polymer rich phase solidifies so that a solid membrane matrix is formed **[40, 41]**. Many researchers have tried to describe the membrane's fabrication mechanisms in the phase-inversion technique since several years. Membrane morphologies, particularly the pore sizedistributions can be controlled by selecting the different solvent, non-solvent, polymer, pore former, and fabrication parameters depending on the particular application **[42-45]**. Many researchers have prepared different membranes for various applications. Cellulose acetate is broadly applicable for the synthesis of membranes because of having tough, biocompatible, hydrophilic characteristics, good desalting nature, high flux, and moderately less expensive to be employed for reverse osmosis, ultrafiltration, microfiltration, and gas separation applications**[46-49]**. For this reason, cellulose acetate polymer based studies have been conducting for different applications. Cellulose acetate blended with polyvinylpyrrolidone (PVP) asymmetric membranes were prepared and evaluated for their performance. Membranes with different

polyvinylpyrrolidone concentration and coagulation-bath-temperature were prepared by a group of researchers **[50]**. They have found that the addition of 0 to 3 wt. % of PVP to the polymer solution increased the macro-voids development and consequently the pure water flux was high. Nevertheless, due to further addition of PVP to 6 wt. % the macro-voidformation was suppressed, and pure water flux (PWF) was reduced. On the other hand, increasing in coagulation-bath-temperature up to 25 °C resulted in increasing macro-voids formation. Another study was conducted to evaluate the effect of molecular weight of polyethylene glycol on membrane morphology and transport properties. In this study, the authors **[51]**prepared flat sheet polysulfone membranesfrom casting solutions by using NMP and DMAc solvents. Polyethylene glycol (PEG) of average molecular weights of 400 Da, 6000 Da, and 20000 Da were used as an additive. They have confirmed that PEG 6000 can be an appropriate additive for preparing asymmetric membranes with dense skin layer and a relatively macro-void free sponge-type support layer. The PWF and hydraulic permeability (P_m) were enhanced significantly as the PEG molecular weight was increased. A substantial increase in rejection of bovine serum albumin (BSA) solution was also reported due to increasing the molecular weight of PEG from 400 Da to 6000 Da in the membrane casting solutions. Kim et al. **[52]** haveinvestigated the effect of PEG additive as a pore-former on polysulfone/N-methyl-2-pyrrolidone (NMP) membrane formation using phase inversion process. Characterizations like light transmittance, coagulation value, and viscosity were used to study the kinetic and thermodynamic characteristics of membrane preparation method. The coagulation value was decreased as the PEG additive molecular weight (M_w) was increased. This result was explained due to theoccurrence of the thermodynamically less stable casting solution. Furthermore, the relationship between the observed precipitation rate and thermodynamic data was analyzed using the viscosity of the casting solution. It was also observed that the membrane surface pore size becomes larger and the top-layer appears more porous, and the distance from the top surface to the starting point of macro-void development becomes greater. In the case of using 15 wt. % of the polysufone casting solution, a symmetric cross-sections and macrovoid free structures were found. On the other hand, it wasreported that with increasing the PEG additive M_w, water flux increased and solute rejections were observed to decrease.It is well known that additives are important to improve the membrane properties like pore structure, mechanical stability, thermal stability, hydrophilicity, flux, and rejection capabilities. According to the literature,the most common additives are polyethylene glycol

(PEG) **[51-54]**and polyvinylpyrrolidone (PVP) **[50, 55-57]**. On the other hand, using organic-inorganic membranes, the separation properties of polymeric membranes can be enhanced and may possess properties such as selectivity, good permeability, thermal, and chemical stability and mechanical strength**[58].** Another challenge in the field of membrane process is fouling. Since membrane fouling is causing a severe decline of the solvent flux, it becomes essential to fabricate membranes with less susceptible to fouling by making some modification during preparation. In ultrafiltration processes, several attempts have been accomplished to decrease fouling, which in general include feed solution pre-treatment, membrane surface enhancements, and process modifications**[59, 60]**. In recent researches, it is confirmed that the introduction of nanoparticles in a membrane matrix develops the membrane hydrophilicity, anti-fouling property, and permeability. Accordingly, several inorganic oxide nanoparticles such as Al_2O_3, ZnO, TiO_2, and SiO_2 have been added with in polymer casting solution**[61-63]**. Current researchers have paid attention to TiO_2 due to its stable nature, easily available and the potential for different applications. Moreover, TiO_2 can enhance the hydrophilicity of different polymers to improve flux and decrease the fouling problem which is important parameters in water and wastewater treatment **[60, 64]**.In membrane filtration process factors like thermal, fouling and flux are very important properties, and our current study is focused on improving these properties simultaneously.

1.3.4. Modification of membranes for specific application

Ma et al. **[65]**have fabricatednon-woven polyethylene terephthalate nanofiber mats (PET NFM) by electro-spinning technique and weresurface modified to mimic the fibrous proteins in native extracellular matrix towards constructing a biocompatible surface forendothelial cells (ECs). Therefore, first,the electro-spun PET/NFM was treated in formaldehyde solution to yield hydroxyl groups on its surface,followed by grafting polymerization of methacrylic acid (MAA) initiated by Ce(IV). Finally, the PMAA-grafted PET/NFM wasagain grafted with gelatin using water-soluble carbodiimide as coupling agent and ECs were cultured on the original and gelatin-modified PET/NFM and the cell morphology, proliferation, and viability were studied. It was concluded that the gelatin grafting method can obviously improve the spreading and proliferation of the ECs on the PET/NFM, and moreover, can preserve the EC's phenotype. Zhang et al. **[32]**havedescribed a facile approach for the surface modification of polypropylene non-woven

fabric (NWF) by polyvinyl alcohol (PVA) to determine its filterability where the NWF surface modification involved the physical adsorption of PVA to immobilize PVA on the NWF surface. The protein fouling property of the modified NWF with PVA was studied and results showed that after PVA modification, the polar groups such as, C–O and C–O–C were introduced to the NWF surface; hydrophilicity was improved; and water static contact angles were decreased from 86±1° to 43±3°; the amount of bovine serum albumin (BSA) static adsorption on modified NWF was decreased by 83.4 %. The filterability nature of modified NWF was also tested by using membrane bioreactor for the treatment of a pharmaceutical wastewater and results revealed that flux declination of modified NWF was only 12% in comparison with the original NWF of 40%. Finally, the authors concluded that the anti-fouling property for the modified NWF was enhanced greatly. Saeed et al. **[66]**have prepared electro-spun polyacrylonitrile (PAN) nanofibers for metal adsorption on which the nitrile group in the PAN had chemically modified with amidoxime groups (hydroxylamine hydrochloride). It was confirmed that adsorption of the amidoxime-modified PAN (PAN-oxime) (25% conversion) nanofibers followed Langmuir isotherm and adsorption capacities for Cu(II) and Pb(II) was found to be 52.70 and 263.45 mg/g, respectively, indicating that the monolayer adsorption occurred on the nanofiber mats. Moreover, over 90% of metals were recovered from the metal-loaded PAN-oximenanofibers in a 1 mol/L HNO_3 solution after 1 h showing that the potential use of the PAN-oximenanofibers as a filter for recycling metals from waste water. Zhang et al. **[67]**have prepared electro-spun polyacrylonitrile (PAN) nanofiber membranes and surface modified. This membrane was studied as a novel affinity membrane, using bromelain as a research model. A series of modification have done where initially, chitosan(CS) was tethered onto the electro-spun membrane surface to form a dual-layer biomimetic membrane through the use of glutaraldehyde (GA). Secondly, the dye cibacronblue F3GA (CB) as a ligand was then covalently immobilized on the CS-coated membranes where, the content of CB attached onto the membrane was 370 μmol/g. The adsorption isotherm fitted to the Freundlich model well and the CB-attached PAN nanofibers membrane showed a capturing capacity of 161.6 mg/g towards bromelain. Finally, it was demonstrated that the modified electro-spun PAN nanofiber membrane has potential for affinity membrane applications in wastewater treatment system. Shi et al. **[68]**have developed a facile graft polymerization of methacrylic acid (MAA) onto polyethersulfone (PES) flakes using benzoyl peroxide (BPO) as chemical initiator. The polymerization was carried out in a heterogeneous polymer–monomer

reaction system using water as reaction medium where the crucial parameters affecting the graft yield, such as monomer concentration, reaction time, and temperature were studied. It was confirmed that the amount of grafted PMAA on PES was increased with increasing monomer concentration and reaction time. The optimum temperature for the grafting was around 75 ◦C. The synthesized PMAA-g-PES was cast into ultrafiltration membranes via phase inversion process. Finally, the results showed that the grafting of PMAA onto PES could not only increase the hydrophilicity where it was occurred during the coagulation step of PES membranes but also give the membranes with distinct pH sensitivity. Due to the pH-induced conformational change of the PMAA chains, the permeability of the membranes displayed pronounced pH dependence, which was large under low pH values and small under high pH values. Teng et al. **[69]** have reported the preparation of mesoporous polyvinyl alcohol (PVA)/SiO_2 composite nanofiber membrane functionalized with cyclodextrin groups by sol–gel/electro-spinning process. The mesoporous PVA/SiO_2 composite nanofiber membranes showed good performance in adsorption of indigo carmine dye in which the maximum adsorption capacity reached 495 mgg^{-1} where, the adsorption equilibrium was obtained in less than 40 min. Furthermore, it was confirmed that the membranes exhibited good recycling properties for practical usage. Taha et al. **[70]**have successfully prepared a novel NH_2-functionalized cellulose acetate (CA)/silica composite nanofibrous membranes by sole-gel combined with electro-spinning technology. They have employed tetraethoxysilane (TEOS) as a silica source, CA as precursor, and 3-ureidopropyltriethoxysilane as a coupling agent in membrane preparation.The results have confirmed that the composite nanofibrous membranes showed high specific surface area and porosity which were used for Cr (VI) ion removal from aqueous solution through static and dynamic adsorption experiments. The adsorption behavior of Cr (VI) was well described by the Langmuir adsorption model and the maximum adsorption capacity for Cr (VI) was estimated to be 19.46 mg/g where, for CA and CA/SiO_2 was found to be 1 mg/g and 3 mg/g, respectively, under a pH of 1.0 and membranecan be conveniently regenerated by alkalization. Abbasizadeh et al. **[71]** have synthesizeda novel polyvinyl alcohol (PVA)/titanium oxide (TiO_2) nanofiber adsorbent modified with mercapto groups by electro-spinning. They have studied the influence of several variables such as, TiO_2 and mercapto contents, adsorbent dose, pH, contact time, initial concentration of U (VI) and Th (IV) ions, and temperature in batch experiments. From the adsorption experiments they have presented that the sorption capacities of both metal ions for the

modified PVA/TiO_2nanofibers were remarkably greater than those of the unmodified nanofibers and a maximum sorption capacities of U (VI) and Th(IV) by Langmuir isotherm were estimated to be 196.1 and 238.1 (mg/g) at 45 ^oC with pH of 4.5 and 5.0, respectively. Yu et al. **[72]** have reported a multi-amino cellulose acetate adsorbent for arsenic adsorption. First cotton cellulose was treated with 100 mL of aqueous NaOH solution (20%, w/v) at 25 $^{\circ}C$ for 6 h in order to obtain alkali cellulose and glycidyl methacrylate (GMA) was grafted onto the surface of cotton cellulose using ceric ammonium nitrate (CAN) as the chemical initiator. Then, the introduced epoxy groups reacted with tetraethylenepentamine (TEPA) to obtain a multi-amino adsorbent. Then, the adsorbent was investigated for adsorption of arsenic and the results showed that Langmuir model could fit the experimental data perfectly and the adsorption capacities were 5.71 mg/g for As (III) and 75.13 mg/g for As (V), respectively. The adsorbent could be effectively regenerated for four cycles with 0.1 mol/L NaOH solution. Cellulose acetate is mostly abundant organic material and broadly applicable for the synthesis of different products because of having tough, biocompatible, hydrophilicity characteristics, and moderately less expensive **[46-48]**. The drawback of cellulose acetate membranes is that it is susceptible to thermal and mechanical stabilities depending on the environments and conditions of application **[73]**.Therefore, modification of cellulose acetate using graft copolymerization process gives a substantial way to modify the chemical andphysical properties**[74]**. Recently, the modifying of polymers has received great attention and grafting is one of the promising approaches. Grafting co-polymerization is an attractive technique to introduce different functional groups to the backbone of a polymer **[75]**.Moreover, grafting is one of thechemical modification methods advanced to date and has appeared as a simple and versatile method to develop surface properties of polymers for a various applications. Grafting method has numerous benefits, such as, the capacity of modifying the polymer surfaces to have a distinctive properties by choosing of various monomers; the ease and well-regulated introduction of grafting chains with a high density and an exact localization on the substrate surface without changing the bulk properties; and graft chains onto a substrate surface with covalent attachments promising a long-term chemical stability of introduced chains, in contrast to physically coated polymer chains. For the graft copolymerization to be occurring, groups which can generate radicals should be introduced onto the backbone of the polymer first in order to activate the polymer surface. Most of the polymers having chemically inert properties can be activated via UV irradiation **[76]**, plasma treatment

[77], ion and electron beam **[78-81]**, benzoic per oxide oxidization **[82-87]**, and Ce^{4+} oxidization **[88-91]**. In most of the grafting processes, the free radicals are initiated on the backbone of a polymer by numerous irradiations and free radical polymerizations of vinyl monomers or chemical initiators.

1.4. Knowledge gap

- Developments on the fabrication of electro-spun nanofiber membranes for wastewater treatment applications are yet fully unexplored.
- Advancement and modification of phase inverted membranes to meet the specific separation purpose are still required.
- Membranes with the capacity to perform heavy metal removal and less susceptible to membrane fouling are required.
- The restrictions can be filled using electro-spun, modification and functionalization of phase-inversion membranes.

1.5. Objectives of the Work

The main and sub-objectives of the thesis work are:

1.5.1. Preparation and modification electro-spun membranes

- Fabrication of CA/TiO_2 composite electro-spun adsorbent
- Optimization of electro-spinning parameters
- Adsorption study for removal of heavy metals from wastewater

1.5.2. Preparation and modification of CA phase inverted membranes

- Comparative study on additives and solvents
- Modification of CA membrane using TiO_2 NPs
- Conducting permeability, fouling, and BSA removal performances studies

1.5.3. Functionalization of membranes: physical blending and graft copolymerization

- CA membranes modified with amine-impregnated TiO_2 NPs
- Cerium (IV) initiated graft polymerization of PMMA on CA
- Removal of Cr (VI) and humic acids from contaminated water using modified membranes

Chapter 2

Materials, preparation and characterization methods

Cellulose acetate

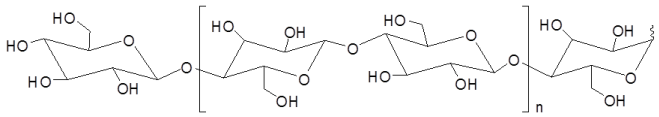

Methyl methacrylate (MMA)

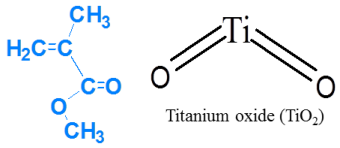

Titanium oxide (TiO_2)

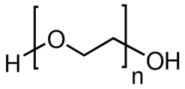

Polyethylene glycol (PEG)

Tetraethylenepentamine (TEPA)

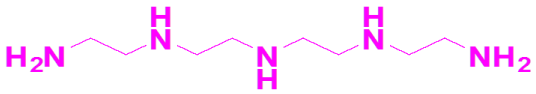

Field emission scanning electron microscopy (FESEM)

600 MHz Nuclear Magnetic Resonance (NMR)

Thermal gravimetric analysis (TGA)

UV–vis Spectrophotometer (UV-2600)

Delsa Nano

ATR-FTIR Spectroscopy

Atomic Absorption Spectrophotometer (AAS)

Water contact angle

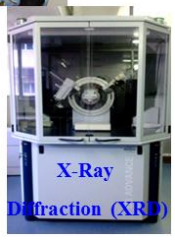

X-Ray Diffraction (XRD)

Brunauer-Emmet Teller (BET)

Chapter 2: Materials, preparation, and characterization methods

This chapter provides valuable information on the chemicals used, methods of membrane preparation, and characterization techniques. Detailed information on the preparation procedures, physicochemical and instrumental characterization techniques are presented.

2.1. Materials

2.1.1. Chemicals

Polyvinyl alcohol, MW 80,000, 98-99 mole % hydrolyzed, was purchased from Loba Chemie Pvt. Ltd, India, acetone (99.9 % purity), Glutaraldehyde (GA) (25 % aqueous solution) and hydrochloric acid (35 % aqueous solution) were purchased from Merck, India. First, the PVA solutions were prepared by dissolving the polymer in distilled water at 70 ^{o}C with continuous stirring overnight and subsequently cooled to room temperature (28±2 ^{o}C) earlier to electro-spinning process. Cellulose acetate polymer (acetyl: 29 to 45 % content, MW = 50,000 g/mol) was purchased from Loba Chemie, India. The degree of substitution for acetyl groups, DS (Ac), is usually defined as the number of acetyl groups per glycosidic ring and according to the ^{1}H NMR analysis, it is found to be 2.47. The two solvents, namely, N, N-dimethyl acetamide (DMAc) and acetone (both with an analytical purity of 99 %); deuterated dimethyl sulfoxide (DMSO-d6, deuteration degree min. 99.8 % for NMR spectroscopy) were obtained from Sigma-Aldrich Co., USA. Deionized water (DI) was used throughout this experiment. Titanium oxide (TiO_2) nanoparticles with 99.5 % purity were obtained from Sigma-Aldrich Co., USA. Copper chloride ($CuCl_2.2H_2O$) and lead nitrate ($Pb(NO_3)_2$) were used as the source for copper (II) and lead (II) stock solution, respectively. All the required solutions were prepared with analytical reagents and deionized water. 2.7 g of 99 % $CuCl_2.2H_2O$ and 1.6 g of 99 % $Pb(NO_3)_2$ (Merck Specialities Private Limited, Mumbai, India) was dissolved in deionized water of 1.0 L volumetric flask up to the mark to obtain 1000 mg/L of Cu (II) and Pb (II) stock solution. Synthetic samples of 50 mg/L of Cu (II) and Pb (II) were prepared from this stock solution by appropriate dilutions. The pH values of the prepared solutions were adjusted using 1 (N) of HCl

and NaOH. Deionized water (DI) was used throughout this experimentation to avoid side reactions and contamination of the solution. Polyethylene glycol 4000 and ethylenediamine (EDA) (Mw. 60 g/mol and with purity of 99 %) were obtained from Merck Specialities Private Limited, Mumbai, India; tetraethylenepentamine (TEPA) (Mw. 189.3 g/mol and with purity of 99 %) and hexamethylenetetramine (HMTA) (Mw. 140.2 g/mol and with purity of 99 %) were obtained from Sigma-Aldrich Co., USA. Polyvinylpyrrolidone (PVP, M_w of 40,000 Da) polymers were purchased from Loba Chemie, India. Deionized water (DI) was used as the non-solvent in the coagulation bath throughout this experiment which was purified using Millipore system. Bovine serum albumin (BSA) protein having a molecular weight of 66 kDa was purchased from SRL, India. Potassium chromate (K_2CrO_4) is used as the source for Cr (VI) (Merck Specialities Private Limited, Mumbai, India). Methyl methacrylate (MMA, 99 % purity and MW = 86.09) was purchased from Chemika Biochemika Reagents, Mumbai, India. Ceric (IV) sulfate (CS), hydroquinone (MW = 110.11 g/mol with 99.5 % purity) and sulfuric acid (98 % purity) were obtained from Merck (Germany). Methanol (with 99.8 % purity HPLC grade) was purchased from SRL, India. Ceric (IV) sulfate and sulfuric acid were analytical reagent grade and used without further purification. Humic acid (60-70%, dry basis) was purchased from Loba Chemie, India.

2.2. Preparation Methods

2.2.1. Electro-spinning technique

2.2.1.1. Preparation of electro-spun PVA and cellulose acetate

Electro-spun PVA membranes were prepared by using the electro-spinning technique. During electro-spinning process, a high voltage is supplied to a polymeric solution in the syringe pump such that charges are induced within the polymer solution **(Fig. 2.1)**. When charges inside the solution become sufficiently high amount and able to overcome the surface tension of the solution droplet, a solution jet erupts from the needle-tip drop resulting in the development of the so-called Taylor cone. Finally, the jet travels to the rotating collector with a state of lower potential. Electro-spinning was performed using NABOND NEU (China) electro-spinning unit at

room temperature (28±2 ºC). The polymer solution was loaded into a 50 mL syringe with a needle (inner diameter of 0.4 mm). According to the design of experiments summary (**Table 2.1**), a polymer solution varied from 6 to 19.5 wt. %, an electric field of 5 to 25 kV was applied throughout the process, and the fluid feed rate was 1 to 3 mL/h and the time duration between 25 to 77.5 min. All the prepared fibers were deposited on a rotating collector, where the gap between the needle-tip and the collecting plate was fixed at 100 mm. Using the optimized electro-spinning parameters (concentration, voltage supply, and feed rate), the PVA membranes were prepared for the selected time durations (i.e. 25, 35, 45, and 60 min) to further investigate the impact of deposition time on the surface pore diameters, fiber diameter, surface areas, porosity, and morphological structures of the electro-spun membranes. Surface tension, viscosity, and conductivities of the solutions were determined using a tensiometer (Kruss tensiometer K_9), Viscometer (Anton Paar, Physica MCR 30, Austria) and a conductivity meter (ELICO, India), respectively.

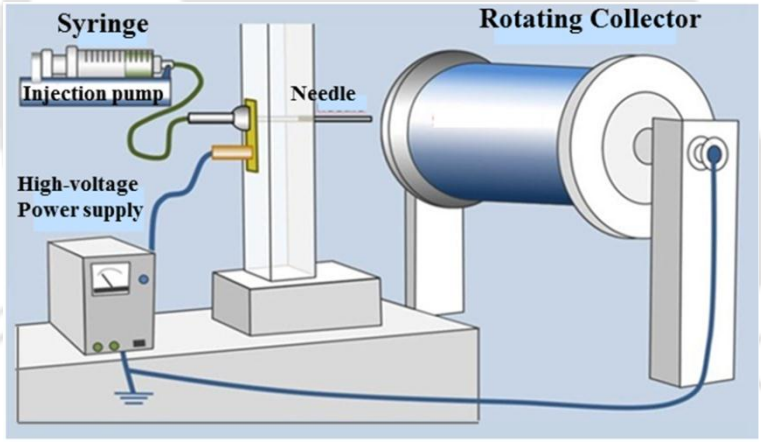

Fig. 2.1. Schematic of the electro-spinning equipment, syringe pump, needle, rotating collector, and voltage supply

On the other hand, during the preparation of the CA/TiO_2 composite membrane, the electric-field was 14 KV throughout the process, and the fluid flow rate was 2 mL/h. The fibers of cellulose acetate and CA_TiO_2 hybrid membranes were deposited on a rotating collector plate, where the distance from the collector plate to needle tip was kept at 100 mm. The fabrication and characterization of CA and CA/TiO_2 membrane are clearly mentioned below. Based on this study, the membrane was tested for adsorption of heavy metals (Pb (II) and Cu (II)) from

synthetic wastewater. The evaluation of CA/TiO_2 composite membrane as adsorbent is explained in the following sections. In this study, a mixture of acetone and dimethylacetamide (DMAc) was chosen as cellulose acetate solvent during electro-spinning. To get the optimum electro-spun membrane with smooth morphological structures, four different concentrations (25, 20, 15, and 13.5 Wt. %) of cellulose acetate were prepared and 13.5 wt. % was selected for the next experiment. Cellulose acetate solutions were prepared by uniformly dissolving in 2:1 ratio of acetone/DMAc **[92]**. Subsequently, different amounts of TiO_2 nanoparticles were added to the cellulose acetate to enhance the thermal, specific surface area, and mechanical property of cellulose acetate. Therefore, different amount (0, 1.0, 2.5, 4.5, and 6.5 wt. %) of TiO_2 nanoparticles were dispersed in 13.5 wt. % solution of CA. The mixed solution was stirred for 4 h at 200 rpm speed and sonicated for 3 h to ensure the optimum distributions of the TiO_2 nanoparticles in the CA solution.

2.2.1.2. Response Surface Methodology using Design of Expert

The design of experiment (DOE) has been known as an appropriate optimization tool to investigate and optimize the impact of electro-spinning parameters **[93, 94]**. The DOE technique is employed to reduce the number of experiments to be performed. Moreover, one of the effective optimization techniques to obtain the optimal conditions in a multi-variable scheme, is response surface methodology (RSM) **[95, 96]**. Recently, the RSM optimization technique has been effectively employed in numerous processes to attain the optimal conditions. Furthermore, the central composite design (CCD) is a suitable experimental design technique among various approaches, which provides high-quality estimates in studying interaction, quadratic, and linear effects of parameters **[97]**. Therefore, the optimization of the above parameters for polyvinyl alcohol based solutions was the preliminary point of this work. The theory and definition of some terms regarding RSM optimization process have been explained in detailed by Bezerra et al.**[95]**, Yordem et al.**[94]**, and Ahmadipourroudposht et al. **[98]**. The design plan in this study includes four input factors (i.e., time duration (min), voltage supply (kV), polymer concentration (wt. %), and feed rate (mL/h) and responses (R_1 and R_2 i.e. membrane fiber diameter and membrane surface pore diameter, respectively). Those four input factors have been selected for designing purpose, and their results are chosen based on preliminary investigation. The input

factors are varied over five levels: high value (+1), the center point (0), low level (−1) and two outer points (-α and +α value), details are outlined in **Table 2.1**.

Table 2.1 Design summary: Input variables and their coded and actual values used in the response surface study

Factors	Name	(-)alpha	(-)1 level	(0)center	(+1) level	(+)alpha
A	Time duration (min)	7.5	25	42.5	60	77.5
B	Voltage supply (kV)	5	10	15	20	25
C	Concentration (wt. %)	1.5	6	10.5	15	19.5
D	Flow rate (mL/h)	0	1	2	3	4

CCD comprises of design points and axial points, consisting of a total of 30 experimental runs which are used to examine the experimental data. These data are finally used to optimize the electro-spinning process parameters. The output variables (i.e. membrane fiber diameter and membrane surface pore diameter) are measured from the selected mathematical model with significant terms, and the model was not aliased. **Table 2.2** presents the summary of the design of experiments and experimental responses for central composite design (CCD).

2.2.1.3. Cross-linking of Electro-spun PVA

The effect of crosslinking of electro-spun PVA nanofibers membranes was studied. The cross-linking procedure and optimization have been done following the procedure suggested by Wang et al., 2006. Accordingly, electro-spun PVA samples were dipped in a solution containing 0.01N hydrochloric acid and 30 mM of glutaraldehyde/acetone for about 1 day. The cross-linked PVA membranes were withdrawn and rinsed using distilled water for several times and then dried out.

Table 2.2 Design of experiments summary and experimental responses for central composite design (CCD)

Run	Factor1, A: Time duration (min)	Factor 2,B: Voltage supply (kV)	Factor 3, C: Concentration (Wt. %)	Factor 4, D:Flow rate (mL/h)	Response 1, Fiber diameter (nm)	Response 2, Surface pore diameter (nm)
1	42.5	15.0	10.5	4.0	179	155
2	25.0	20.0	6.0	3.0	95	90
3	42.5	15.0	10.5	2.0	105	109
4	25.0	10.0	15.0	1.0	117	180
5	25.0	10.0	6.0	1.0	106	144
6	7.5	15.0	10.5	2.0	129	267
7	60.0	10.0	15.0	1.0	125	207
8	60.0	20.0	6.0	1.0	76	132
9	42.5	15.0	10.5	2.0	100	107
10	42.5	15.0	10.5	2.0	103	111
11	60.0	10.0	15.0	3.0	78	192
12	25.0	20.0	15.0	1.0	50	193
13	42.5	15.0	1.5	2.0	46	90
14	60.0	10.0	6.0	1.0	47	149
15	60.0	20.0	15.0	3.0	39	270
16	42.0	15.0	10.5	2.0	107	108
17	42.5	15.0	10.5	0.0	135	200
18	25.0	20.0	15.0	3.0	25	290
19	60.0	20.0	6.0	3.0	55	90
20	60.0	10.0	6.0	3.0	150	50
21	42.5	15.0	10.5	2.0	104	110
22	60.0	20.0	15.0	1.0	133	230
23	42.5	15.0	19.5	2.0	20	310
24	42.5	5.0	10.5	2.0	160	60
25	25.0	20.0	6.0	1.0	80	98
26	77.5	15.0	10.5	2.0	78	169
27	42.5	25.0	10.5	2.0	56	100
28	42.5	15.0	10.5	2.0	103	109
29	25.0	10.0	6.0	3.0	256	80
30	25.0	10.0	15.0	3.0	138	200

2.2.1.4. Batch adsorption experiments

The batch adsorption experiments were carried out in a 100 mL borosilicate beaker, and the experimental parameters are presented in **Table 2.3**. Adsorption experiment was done by adding 100 mg of adsorbents into 50 mL of Pb (II) and Cu (II) solutions separately using an incubated shaker at 150 rpm (solid/liquid ratio: 0.002 g/mL). The parameters, such as initial concentrations of Pb (II) and Cu (II) taken as 50 mg/L, contact time ranged from 0 to 300 min, and temperatures of the solution were varied from 25 °C to 55 °C. The effects of TiO_2 nanoparticles content on adsorption capability of the adsorbents for the elimination of heavy metals were investigated. The effects of pH on the elimination of Pb (II) and Cu (II) ions were studied within the range of 1 to 9 at 35 °C for 5 h agitation period. The effects of the contact time were also investigated by altering the time using a constant temperature of 35 °C.

Table 2.3 Batch adsorption parameters

Initial conc., (mg/L)	Adsorbent dose, (mg)	Shaker speed, (rpm)	pH	Contact time, (min)	Temp. (^oC)
50	100	150	1,2,3, 4,5, 6,7,8, 9	0, 30, 60, 90, 120, 150, 180, 210, 240, 270, 300	25, 35, 45, 55

The adsorbent phase concentrations after equilibrium, q (mg/g), were calculated using the well-known equation as:

$$q_e = \frac{(C_o - C_e)V}{M} \quad \textbf{(2.1)}$$

The percentage of removal is calculated as Eq. **(2.1)**

$$R(\%) = \frac{(C_o - C_e)}{C_o} \times 100 \quad \textbf{(2.2)}$$

Where q_e is the adsorbent phase concentration after equilibrium in mg of adsorbate per g of adsorbent; V is the volume of the liquid in the solution (L); C_0 and C_e are the initial and the equilibrium concentrations of heavy metal ions in the liquid phase (mg/L), respectively; and M is the mass of adsorbent (g). Regeneration of adsorbent was done by rapidly washing the

adsorbents with HNO_3 (1M) and then rinsed using deionized water for three times, followed by drying in a vacuum oven at 50 ºC for 24 h. **[3]**.

2.2.2. Phase Inversion Method

2.2.2.1. Preparation of CA, CA-PEG, and CA-PVP membranes

Phase inversion technique using immersion precipitation was used for the fabrication of asymmetric ultrafiltration membrane from cellulose acetate polymer. Initially 10.5 wt. % of CA powder was dissolved in acetone: DMAc (70/30 wt. %) and DMF separately with continuous magnetic stirring at room temperature (28±2 ºC). Particular attention was given to acetone and DMAc where the two solvent properties were then mixed to attain enhanced CA solubility due to a synergistic effect, and we have selected the mixture ratio according to the literature. On the other hand, DMF was selected due to its good solvent nature for CA where it avoids rapid evaporation of the solution **[92, 99]**. After getting a uniform solution of the CA/solvent, a fixed amount of each additive (5 wt. %) was added and stirred continuously at least for 1 day until the solution was fully dissolved, and finally, homogeneous casting solution was obtained. The amount of polymer and additives were chosen based on the literature **[53, 56]**. Membranes with different composition were designated as, CA0, CA1, CA2, CA3, CA4, and CA5. **Table 2.4** shows the solution casting compositions of polymeric additives with CA.

The membrane preparation process is shown in **Fig. 2.2**. The casting solution was stirred overnight using a magnetic stirrer at room temperature. After that, a homogeneous solution of solvent, polymer, and the additives were attained and kept for 24 h at room temperature. Consequently, the casting solutions were poured consistently on a glass sheet with the help of a casting knife keeping an allowance of roughly 0.25 mm between the knife and the glass plate. Then, the resultant films were exposed to air for about 30 s earlier to soaking in the coagulation bath containing DI water at room temperature.

Table 2.4 Compositions and viscosity of the casting solution of polymeric additives with CA

Membrane	CA wt.%	PEG wt.%	PVP wt.%	Ac: DMAc (70/30 wt. %)	DMF wt. %	Viscosity (mPa.s)
CA0	10.5	-	-	89.5	-	1680
CA1	10.5	5	-	84.5	-	1780
CA2	10.5	-	5	84.5	-	1720
CA3	10.5	-	-	-	89.5	1850
CA4	10.5	5	-	-	84.5	1920
CA5	10.5	-	5	-	84.5	1970

In the coagulation bath, the cast solution turned from transparent to white color and the thin film detached from the glass plate. The membrane sheets were kept for 30 min in the coagulation bath. After that, the fabricated membranes were reserved in DI water beakers until use. Finally, the membrane sheet was cut into a circular disc to put in the filtration cell for pure water and BSA filtration experiments.

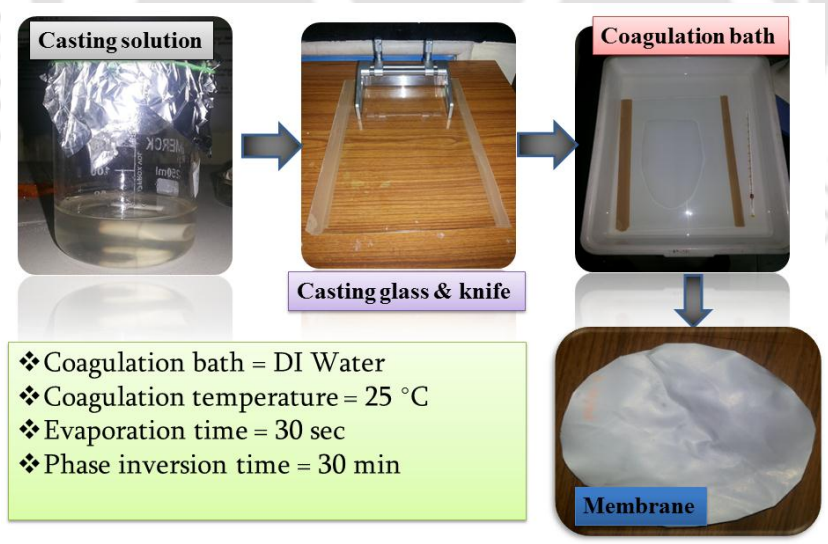

Fig. 2.2 Membrane preparation process

During the preparation of phase inverted membranes using immersion precipitation process, a ternary and multicomponent system were used. In ternary system, scheme consisting of a solvent, a polymer, and a non-solvent was applied where the non-solvent and solvent are

miscible. On the other hand, the multicomponent system (polymer/solvent/non-solvent/additive) was also investigated. In immersion precipitation, a homogenous mixture of the solvent and polymer are cast to a thin film on the glass plate and then immersed in a non-solvent (water in this case) bath. As seen in **Fig.2.3**, the non-solvent (water) starts to diffuse into the cast film *(J_1)*, and the solvent diffuses into the coagulation bath *(J_2)*. After a specified time, the exchange of non-solvent and solvent has continued until the solution becomes thermodynamically unstable and liquid-liquid de-mixing occurs. Finally, a polymeric film is obtained with an asymmetric structure.

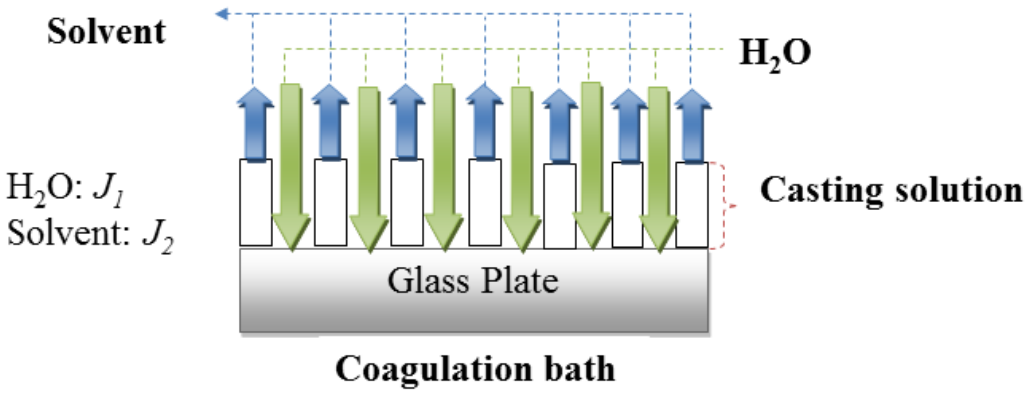

Fig. 2.3 Schematic representation of casting film and coagulation bath interface: solvent *(J_2)* and non-solvent *(J_1)*

2.2.2.2. Preparation of CA−PEG –TiO_2 membrane

Phase inversion technique by immersion precipitation was used for fabrication of asymmetric UF membrane from cellulose acetate polymer. Initially, uniform solutions of CA in Acetone/DMAc (70/30; v/v) were prepared under continuous magnetic stirring at room temperature (28 ±2 ºC). The casting solution was stirred overnight using a magnetic stirrer at room temperature. After that, the solutions containing CA, solvents and the additives (PEG and TiO_2 NPs) became homogeneous, and they were kept at room temperature for one day to avoid air bubbles. Subsequently, the casting solution was poured consistently on a glass sheet and carefully cast using a casting knife keeping a gap of roughly about 0.25 mm between the knife and glass plate. The resultant films were exposed to air for approximately 30 s earlier to immersing to the coagulation bath comprising of DI water at room temperature. In the

coagulation bath, the cast solution turned from transparent to white color for membranes CA and CA-PEG. On the other hand, the milky color for CA-TiO_2 and CA-PEG-TiO_2 membranes was changed to white, and all the thin films were detached from the glass plate.The membrane sheets were kept for 30 min in the coagulation bath. After that, the prepared membranes were put in DI water-filled beakers until use. Lastly, the membrane films were cut into circular discs to put in the membrane cell for UF experiments. The membranes with different composition are designated as, M_1, M_2, M_3 and M_4 (i.e. CA, CA-TiO_2, CA-PEG-TiO_2, and CA-PEG, respectively). **Table 2.5** shows the solution casting compositions of CA, PEG and TiO_2 nanoparticles. The flow diagram for membrane preparation process is presented in **Fig. 2.4**. The amounts of CA, PEG and TiO_2 NPs, were selected based on the previous works **[53, 100].**

Table 2.5 Solution compositions and viscosity of the casting solution: CA, PEG and TiO_2 nanoparticles

Membrane	**CA (wt. %)**	**TiO_2 (wt. %)**	**PEG (wt. %)**	**AC:DMAc (70:30; v/v)**	**Viscosity (mPa.s)**
M_1	10.5	-	-	89.5	1680
M_2	10.5	2	-	87.5	3180
M_3	10.5	2	4	83.5	1850
M_4	10.5	-	4	85.5	1781

The flow diagram for membrane preparation process is presented in **Fig. 2.4.**

2.2.2.3. Preparation of CA-PVP–TiO_2 membrane

All the asymmetric ultrafiltration membranes from cellulose acetate polymer presented in this study were fabricated using phase-inversion technique by immersion precipitation. Initially of CA polymer was uniformly dissolved in Acetone/DMAc (70/30) to prepare homogeneous solution under continuous magnetic stirring at room-temperature. After getting a uniform solution of the CA/solvent, a quantified amount of PVP additive (i.e. 4 wt. %) was added and stirred continuously at least for 1 day until the solution was fully dissolved, and finally, homogeneous casting solution was obtained.

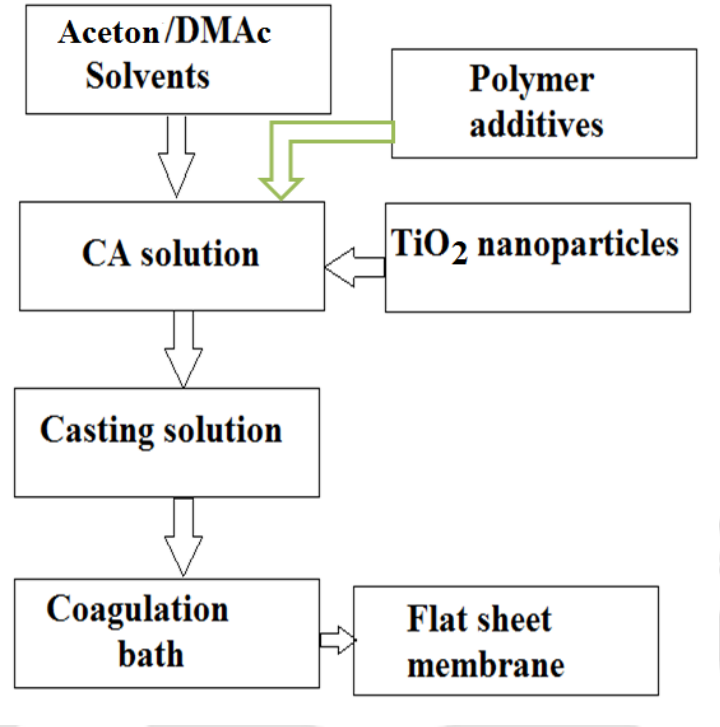

Fig. 2.4 Flow diagram of the preparation method of flat sheet membranes.

Then 2 wt. % TiO_2 NPs was added and well dispersed for another 24 hours to form a homogeneous composite casting solution (i.e. CA-PVP-TiO_2) and also entrapped into the polymer matrix due to the high viscosity of the polymer solution. Finally, the resultant polymer solutions were kept for 24 hours in order to remove all of the bubbles before casting was done. Thus, the membranes with different composition were designated as, CA, CAT, CATP, and CAP. **Table 2.6** shows the solution casting compositions CA, PVP additive, and TiO_2 nanoparticles. The membrane preparation process is presented in flow diagram below **(Fig. 2.5)**. The casting solution was poured consistently on a glass sheet with the help of a casting knife maintaining a clearance of approximately 0.25 mm between the knife and the glass plate. The resulting films were then exposed to air for about 30 s earlier to immersing into the coagulation bath containing distilled water at room temperature. In the coagulation bath, the cast solution turned from transparent to white color for membranes CA and CA-PVP.

Table 2.6 Solution compositions and viscosity of the casting solution: CA, PVP additive, and TiO_2 nanoparticles

Membrane	CA	PVP	TiO_2	Acetone/DMAc	Viscosity
	wt.%	wt.%	wt.%	(70/30 wt. %)	(mPa.s)
CA	10.5	-	-	89.5	1020
CAT	10.5	-	2	87.5	2080
CATP	10.5	4	2	83.5	1790
CAP	10.5	4	-	85.5	1680

On the other hand, the milky colors for CA-TiO_2 and CA-PVP-TiO_2 membranes were changed to white, and all the thin films were detached from the glass plate. The membrane sheets were kept for 30 min in the coagulation bath. After that, the prepared membrane sheets were kept in deionized water bottles until use.

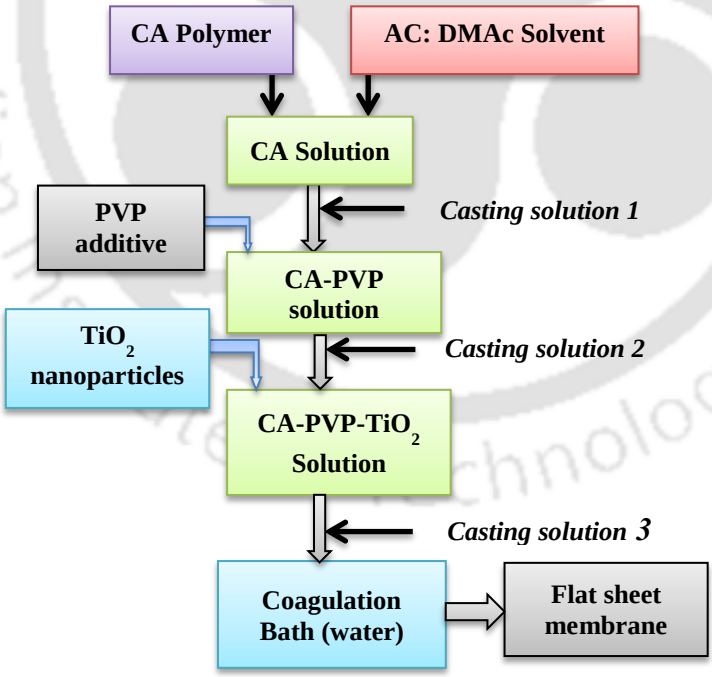

Fig. 2.5 A flow diagram for the preparation process of flat sheet membranes

2.2.3. Physical blending process

2.2.3.1. Preparation of amine-modified TiO_2

The amine-modified TiO_2 (i.e. Ti-EDA, Ti-HMTA and Ti-TEPA) were prepared by impregnation of the amines into the NPs. Briefly, 3.0 mL of each amine was dissolved in 30 mL of deionized water and stirred for about 0.5 h using magnetic stirrer. After that, 3.0 g of TiO_2 was added to the solution and stirred for 6 h. Thus, the amine-modified TiO_2 NPs were then dried in a hot air oven at 70°C for 2 h and consequently kept in a capped vial until use. The composition of amine modified TiO_2 NPs is presented in **Table 2.7**.

Table 2.7 Composition of amine modified TiO_2 nanoparticles

Sample	TiO_2 (g)	EDA (mL)	HMTA (mL)	TEPA (mL)	DI Water (mL)
Ti-EDA	3	3	0	0	30
Ti-HMTA	3	0	3	0	30
Ti-TEPA	3	0	0	3	30

2.2.3.2. Preparation of CA/U-Ti, CA/Ti-EDA, CA/Ti-HMTA, and CA/Ti-TEPA membranes

Phase inversion technique by immersion precipitation was used for fabricating asymmetric ultrafiltration membranes. Firstly, uniform solutions of CA in acetone/DMAc (70/30; v/v) were prepared under continuous magnetic stirring at room-temperature (28 ±2 ºC). After getting a uniform solution of the CA/solvent, a fixed amount of PEG additive (3 wt. %) was added and stirred continuously at least for 24 hours until the solution was fully dissolved and a homogeneous casting solution was obtained. Finally, 2 wt. % unmodified (U-TiO_2) and modified (M- TiO_2) nanoparticles were added separately and well dispersed for another one day to form a homogeneous composite solution. Therefore, the membranes with different

composition were designated as, CA/U-Ti, CA/Ti-HMTA, CA/Ti-EDA, and CA/Ti-TEPA. **Table 2.8** shows the solution casting compositions of all the prepared membranes.

Table 2.8 Solution compositions of the casting solution: CA, PEG, U-TiO_2 and M-TiO_2 nanoparticles

Membrane	**CA (%)**	**U-TiO_2 (%)**	**M-TiO_2 (%)**	**PEG (%)**	**Ac: DMAc (70:30; v/v)(Wt. %)**
CA/U-Ti	10.5	2	-	3	84.5
CA/Ti-EDA	10.5	-	2	3	84.5
CA/Ti-HMTA	10.5	-	2	3	84.5
CA/Ti-TEPA	10.5	-	2	3	84.5

2.2.4. Grafting and amination process

2.2.4.1. Synthesis of CA-g-PMMA and CA-g-PMMA_TEPA

Cellulose acetate powder was washed using methanol and deionized water, respectively, for three times and then was vacuum dried at 60 ºC for 12 h before use. As seen in the schematic of the graft copolymerization process (**Fig. 2.6)**, the graft copolymerization of MMA onto CA took place using a three necked round bottom reactor vessel with magnetic stirrer inside the aqueous solution. For graft copolymerization, 8.0 g of CA was added into the reactor vessel comprising 100 mL of an aqueous solution of 0.006 mol/L of CS in 0.4 M sulfuric acid. After that, the reaction mixture was purged using N_2 gas approximately for 30 min prior to addition a 25 mL of 0.08 mol/L MMA monomer to start graft copolymerization. Consequently, the aqueous solution was stirred continuously at a constant rate (250 rpm) to avoid the influence of stirring on the degree of grafting copolymerization. A condenser was connected to ensure that any solvent or aqueous solution vapor cools, and drips back down into the chamber containing the solid sample. Finally, the polymerization reaction was stopped with the addition of a 5.0 wt. % hydroquinone solution at a fixed time of reaction and the mixture was discharged into a mixture of water and methanol (1:1), and the grafted CA powder was separated.

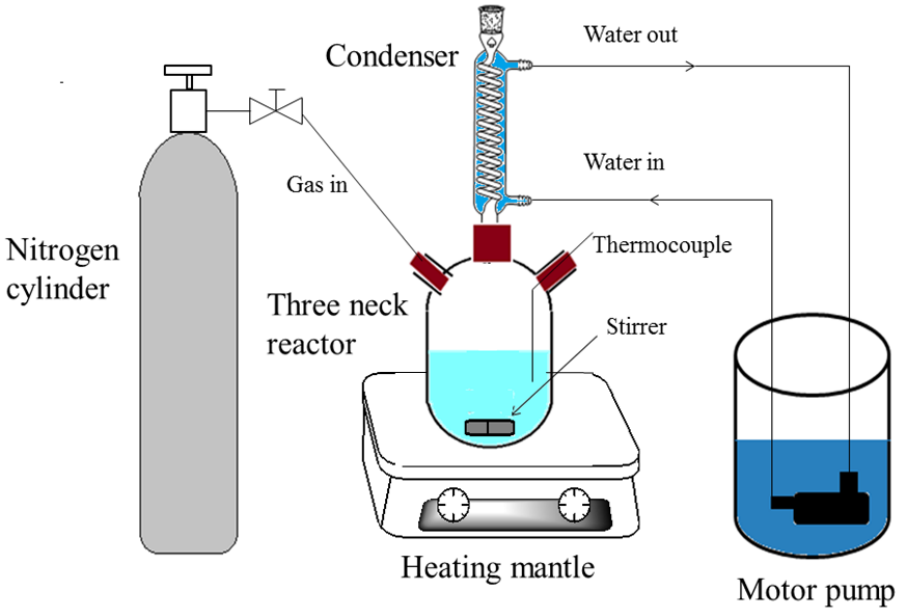

Fig. 2.6 Schematic of the graft copolymerization process

The polymerization reaction was conducted at different temperatures (i.e. 25, 45, 60, and 70 ºC) in an oil-bath using heating magnetic stirrer. The pH of the polymerization reaction was adjusted at 2.0 before the reaction was started. On the other hand, the duration of the copolymerization was varied from 2 h to 8 h to investigate its effect on the reaction. The contents of the reactor were stirred continuously throughout the reaction period to avoid the homopolymer precipitation on the substrate surfaces. The grafted samples were quickly taken out after the desired polymerization time from the reactor vessel and washed repetitively using methanol and deionized water. **Table 2.9** presents the amount of CS and MMA; the variation of time and temperature on the polymerization reaction. To remove all the unreacted MMA monomer, its low MW PMMA homopolymer, and the impurities precipitated along with grafted CA powder, the PMMA grafted cellulose acetate (CA-g-PMMA) samples were Soxhlet extracted using methanol/ acetone (1:1) for 24 h and repeatedly washed using deionized water. Consequently, the grafted CA powders were dried using vacuum drier at 60 °C.

Table 2.9 The variation of time and temperature on the polymerization reaction

Reaction	CS, mmol/L	MMA, mmol/L	Time, h	Temperature, ºC
G-1	8	6	2	25
G-2	8	6	2	60
G-3	8	6	6	45
G-4	8	6	6	70
G-5	8	6	8	25
G-6	8	6	8	60

The percentage of the graft was calculated by the percent increase in weight as follows**[101]**:

$$Gp(\%) = \left[\left(\frac{W_g - W_{ug}}{W_{ug}} \right) \times 100 \right] \quad \textbf{(2.3)}$$

Where, W_g (g) and W_{ug} (g) are the weight of the grafted and the un-grafted cellulose acetate samples, respectively.

During the amination process, 6 g of CA-g-PMMA sample was dispersed in 250 mL DMF/water aqueous solution, and finally, 10 % vol/vol. TEPA in DI (20 mL TEPA in 200 mL of DI) was introduced through the ring opening reaction of the methyl groups of the copolymer by reacting with 99 % TEPA in DMF/water aqueous solution at 70 ºC for approximately 8 h. Thus, the resultant product (i.e. CA-g-PMMA_TEPA) was filtered and washed using methanol and deionized water following drying in vacuum at 50 ºC.

The weight gain percentage *(W_{gp})* of the aminated samples were calculated using the following equation.

$$Wgp(\%) = \left[\left(\frac{W_f - W_i}{W_i} \right) \times 100 \right] \quad \textbf{(2.4)}$$

Where, W_f (g) and W_i (g) are the weight of the aminated sample and the initial weight of the grafted CA, respectively.

2.2.4.2. Preparation of Un-g-CA, CA-g-PMMA, and CA-g-PMMA_TEPA membranes

Phase inversion technique by immersion precipitation was used for fabricating asymmetric ultrafiltration membrane from modified and unmodified cellulose acetate polymer. Initially, uniform solutions of the modified and unmodified CA in acetone/DMAc (70/30; v/v) were prepared under continuous magnetic stirring at room-temperature (28 ±2 ºC). After getting a uniform solution, a fixed amount of PEG additive (3 wt. %) was added and stirred continuously at least for 24 h until the solution was fully dissolved and a homogeneous casting solution was obtained. Finally, 2 wt. % TiO_2 nanoparticles were added separately and well dispersed for another one day to form a homogeneous composite solution. PEG additive and TiO_2 NPs were added to enhance the porosity, hydrophilicity, thermal/chemical stability, and antifouling properties of the membrane as already explained in previous studies elsewhere **[102, 103]**. Therefore, the membranes with different composition were designated as, CA, CA-g-PMMA, and CA-g-PMMA-TEPA. **Table 2.10** shows the solution casting compositions of all the prepared membranes.

Table 2.10 Solution casting compositions of all the prepared membranes

Membrane	**CA** wt. %	**TiO_2** wt. %	**PEG** wt. %	**AC:DMAc** (70:30; v/v)
Un-g-CA	10.5	2	3	84.5
CA-g-PMMA	10.5	2	3	84.5
CA-g-PMMA_TEPA	10.5	2	3	84.5

2.3. Characterization Methods

2.3.1. Physicochemical Characterization

2.3.1.1. Pure water flux and hydraulic permeability

In this study, a 400 mL stirred batch cell experimental set-up was used for the permeability experiments, which is presented schematically in **Fig. 2.7**. This experimental set up comprised of (1) a pressure source to supply the pressure required for the filtration experiment; (2) feed tank where the feed is collected; (3) filtration cell, (4) membrane piece, and (5) permeate collector after membrane filtration. Membranes with the circular shape of 7×10^{-2} m diameter and with an effective filtration area of 3.848×10^{-3} m^2 were employed for this experiment. Compaction studies of each of the prepared membranes were done using deionized water for 2 h using a fixed pressure of 300 kPa and PWFs were recorded with 10 min interval. The membrane compaction factors *(CF)* were found by calculating the ratio of initial PWF (J_{wi}) to steady state PWF (J_{wf}). PWF results were calculated using the following equation:

$$J_W = \left[\frac{Q}{(A\times\Delta t)}\right] \quad \textbf{(2.5)}$$

Where, J_w is PWF (L/m^2 h), Q is the volume of water permeated (L), A is the effective membrane area (m^2), and Δt is permeation time (h). Thus, PWFs were evaluated by passing deionized (DI) water through the membranes. PWF values at different operating pressures (ΔP) (ranging from 100 to 300kPa) were recorded. The hydraulic permeability (P_m) (L/m^2h kPa) of the membranes was calculated from the inverse slope of J_w versus ΔP plot. The calculations for the hydraulic permeability were done as follows:

$$P_m = \left(\frac{J_W}{\Delta P}\right) \quad \textbf{(2.6)}$$

The resistances (R_m) of the prepared membranes were calculated according to Darcy's law (**Eq. (2.7)**):

$$R_m = \left[\frac{\Delta P}{(\mu \times J_W)} \right] \quad \textbf{(2.7)}$$

Where μ is the water viscosity (8.9×10^{-4}) (Pa. s)

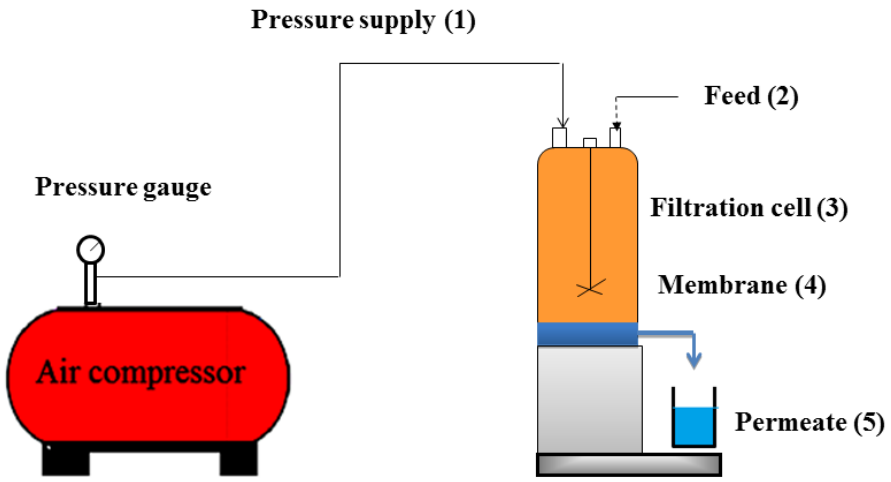

Fig. 2.7. Schematic diagram of the batch cell ultrafiltration set-up

2.3.1.2. Membrane porosity measurements

To study the membranes porosity results, two parameters were applied namely, equilibrium water content (EWC) and membrane porosity (ε). The ε plays a significant role in the permeability and rejection nature of the membrane. On the other hand, the EWC and ε were evaluated using a simple gravimetric method, where each membrane samples (2.5×2.5 square cm) were immersed in DI water beakers for a specified period. Then, the samples were dabbed with dry filter paper and weighed immediately (W_w). Finally, the membranes were kept inside vacuum atmosphere for 24 h at 50 ºC. The final dry weights of the samples (W_D) have taken again. The membrane porosities were calculated by dividing the volume of the pores by the total volume of the membrane. Therefore, the results are found using the following equation**[104, 105]**,

$$\varepsilon(\%) = \left\{ \frac{\left[\frac{(W_W - W_D)}{\rho_W} \right]}{\left[\frac{(W_W - W_D)}{\rho_W} \right] + \left(\frac{W_D}{\rho_P} \right)} \times 100 \right\} \quad \textbf{(2.8)}$$

Where W_W is the wet membrane weight (g), W_D is the dry membrane weight (g), ρ_W is the pure water density at working condition (g cm^{-3}), and ρ_p is the polymer density (g cm^{-3}).

EWC results were calculated using the subsequent equation **[44, 49]**,

$$EWC(\%) = \left\{ \left[\frac{(W_W - W_D)}{W_W} \right] \times 100 \right\} \quad \textbf{(2.9)}$$

The average values of EWC and membrane porosity were taken after measuring of five different samples to reduce the error of the balancing measurement.

2.3.1.3. Membrane fouling and rejection experiments

Membrane fouling experimentations were done using a stirred batch cell specified before to investigate the effect of PEG and PVP additives and effect of the two solvents on BSA rejection and permeate fluxes of the fabricated membranes. The BSA solution (1 g L^{-1}) was prepared using deionized water as a solvent. The pH of the BSA solutions was kept at 7.9. The flux values were calculated using Eq. **(2.3)** and the %age rejection of BSA solutions was evaluated by the next equation:

$$R_{BSA}(\%) = \left\{ \left[1 - \left(\frac{C_p}{C_f} \right) \right] \times 100 \right\} \quad \textbf{(2.10)}$$

Where, C_f and C_p are the BSA concentrations (mg L^{-1}) on the feed side and the permeate side, respectively. The ultrafiltration experiments for BSA solution was achieved through all prepared membranes at an operating pressure of 150 kPa. After that, the permeates were collected using a measuring container at a constant interval of time (20 min) to calculate flux values and the length of each filtration test was for 2 h. Finally, the permeate concentration of BSA solution was evaluated by using UV–vis spectrophotometer (Thermo Fisher Scientific, UV2300, India) at a

wavelength of 278 nm. After filtration of BSA solutions, fouled membranes were soaked in DI water and rinsed for 30 min, and the water flux of the membranes was measured. These experimentations were repeated for three times, and the graphs including error bars are presented. To investigate the anti-fouling properties of the prepared membranes, the flux losses due to irreversible fouling *(F_{ir})*, reversible fouling *(F_r)*, and total fouling *(F_t)* of all the experiments were calculated using the following equations, respectively **[106, 107]**.

$$F_{ir} = \left[\frac{\left(J_{Wi} - J_{Wf} \right)}{J_{Wi}} \right] \quad \textbf{(2.11)}$$

$$F_r = \left[\frac{\left(J_{Wf} - J_B \right)}{J_{Wi}} \right] \quad \textbf{(2.12)}$$

$$F_t = \left[1 - \left(\frac{J_B}{J_{Wi}} \right) \right] \quad \textbf{(2.13)}$$

Where the fouling resistant capacity of the prepared membranes was evaluated using normalized flux ratio (NFR) as shown in **Eq. (2.14).**

$$NFR(\%) = \left[\left(\frac{J_{Wf}}{J_{Wi}} \right) \times 100 \right] \quad \textbf{(2.14)}$$

Where J_{Wf} is the flux of the membrane after fouling (2 h) and J_{Wi} is the flux of the membrane found at the start of the fouling stage. Normally, greater NFR value (next to 1) indicates better anti-fouling nature of the membranes.

2.3.1.4. Average pore radius determination

Image J software and water filtration velocity method were employed to determine the average pore size of the membranes and the results were calculated at constant operating pressure (250 kPa).Water filtration velocity method was employed to determine the average pore size of the membranes, and the results were calculated at constant operating pressure (300 kPa). Membrane average pore radius *(r_m)* is considered as an approximation of true pore size, and it

denotes the average pore radius throughout the membrane's thickness (ζ). Average pore radius can be estimated by using the Guerout–Elford–Ferry equation **[105, 108],**

$$r_m = \sqrt{\left[\frac{(2.9-1.75\times\varepsilon)(8\times\mu\times\zeta\times Q_W)}{(\varepsilon\times A_m\times\Delta P)}\right]} \qquad \textbf{(2.15)}$$

Where μ is the water viscosity (8.9×10^{-4}) in Pa. s, Q_W is the water flow ($m^3\ s^{-1}$), and ΔP is the operating pressure (0.3 MPa).

2.3.1.5. Chromium removal performances

Ultrafiltration experimentations were done in the stirred ultrafiltiration batch cell to investigate the performances of prepared membranes' on the rejection and permeate flux Cr (VI) ions. The flux values and the rejection of Cr (VI) ions were evaluated by the following equations, respectively.

$$J_{Cr} = \left[\frac{Q}{(A\times\Delta t)}\right] \qquad \textbf{(2.16)}$$

$$R_{Cr}(\%) = \left[\left(1-\frac{C_p}{C_f}\right)\times100\right] \qquad \textbf{(2.17)}$$

Where, C_p and C_f are the concentrations (ppm) in the permeate side and the feed side, respectively. Subsequently, all the required solutions were prepared with analytical reagents and deionized water. 2.9 g of 99% K_2CrO_4 was dissolved in deionized water of 1.0 L volumetric flask up to the mark to obtain 1000 ppm of Cr (VI) stock solution. Synthetic samples of Cr (VI) with different concentrations (i.e. 10, 30, 50, 70, and 100 ppm) were prepared from this stock solution by appropriate dilutions. The pH of the Cr (VI) ion solutions was kept at 3.5 and 7. The pH values of the prepared solutions were adjusted using 1 N of HCl and NaOH. Deionized water (DI) was used throughout this experimentation to avoid side reactions and contamination of the solution. The initial and final concentrations of Cr (VI) ions before and after ultrafiltration process were determined by using an Atomic Absorption Spectrophotometer (AA240FS, USA).

The analytical wavelength for Cr (VI) was fixed at 357.9 nm. These experiments were repeated for three times. The washing experiments of the adsorbed/deposited Cr (VI) ions in the membranes were performed usinig a 2.5 g/L KCl solution for four times, and the membranes were rinsed to a neutral condition by using DI water.

2.3.1.6. HA Ultrafiltration and regeneration performance

Ultrafiltration experimentations were done in the stirred ultrafiltiration batch cell to investigate the performances of prepared membranes on the removal and permeate flux of HA solution. The flux values were calculated using **Eq. (2.15)** and the removal efficiencies of HA molecules were evaluated by **Eq.(2.18)**.

$$J_{HA} = \left[\frac{Q}{(A \times \Delta t)} \right] \qquad \textbf{(2.18)}$$

$$\mathrm{R}_{HA}(\%) = \left[1 - \left(\frac{C_p}{C_f} \right) \times 100 \right] \qquad \textbf{(2.19)}$$

Where, C_p and C_f are the concentrations (mg L^{-1}) in the permeate side and the feed side, respectively. The ultrafiltration experiments for HA solution was achieved through all prepared membranes at an operating pressure of 150 kPa. After that, the permeates were collected in a measuring container at a constant interval of time inorder to calculate flux values and the length of each filtration test was 2 h. A 1000 ppm stock solution of HA was prepared by dissolving 1 g HA in to100 ml DI water following by the addition of 900 ml DI water. This solution was stirred for 6 h at 200 rpm then filtered through a filter paper. The pH values of the prepared solutions were adjusted using 1 N of HCl and NaOH. Finally, the permeate concentration of HA solution was evaluated by using UV–vis spectrophotometer (Thermo fisher scientific, UV2300, India) at a wavelength of 254 nm. Later filtration of HA solutions, fouled membranes were cleaning with 0.05 M NaOH solution followed by rinsing using DI water for 30 min and the DI water fluxes of the tested membranes were measured.

2.3.2. Instrumental Characterization

2.3.2.1. Field emission scanning electron microscopy (FESEM)

Morphological studies of the electro-spun and phase inverted membranes were done using a high-resolution field emission scanning electron microscopy (FESEM, ZEISS, USA), which provides visual information of the topographic view besides the cross-sectional structure of the membrane. The elemental composition analysis was done by using high energy electrons of the energy dispersive X-ray spectroscopy (EDS, ZEISS, USA). For both the analyses, a gold coating for the samples was done using a high-resolution sputter coater, Quorum, to protect the membranes from charging during the image analysis. Finally, the pieces of the membranes were attached to a plate holder using double-sided adhesive carbon tape in a horizontal position.

2.3.2.2. Thermo gravimetric analysis (TGA)

The thermal degradation analysis was conducted by thermo-microbalance (Thermo gravimetric Analyzer) (TG 209 F1 Libra®, Germany). The TGA results were found from 30 to 800 ºC using nitrogen gas where the flow rate was kept as 40 mL/min at a heating rate of 10 ºC/min. All the membranes were loaded into a platinum sample holding pan. The graphs were plotted as weight loss (%) vs. temperatures (ºC).

2.3.2.3. Nuclear Magnetic Resonance (NMR) analysis

^{1}H NMR spectra were recorded on a 600 MHz Nuclear Magnetic Resonance (NMR) Spectrometer (Bruker, Japan). All the samples (20 mg) were dissolved in DMSO-d6. Each solution was placed in a 5 mm NMR glass tube (WILMAD-Lab Glass Co., USA).

2.3.2.4. ATR-FTIR Spectroscopy analysis

The chemical structures of the all the samples were characterized by using attenuated total reflectance Fourier transform infrared (ATR-FTIR) spectrophotometer (IR affinity-1, SHIMADZU, Japan). Each spectrum was acquired in transmittance mode by an accumulation of 40 scans through resolutions of 4 cm^{-1}, and the wave number was ranged from 500 to 4000 cm^{-1}.

2.3.2.5. Zeta potential (ζ) analysis

Zeta potential (ζ) results of the all the samples were measured by dynamic and electrophoretic light scattering (Delsa Nano-C, Beck-man Coulter, Switzerland). 10 mg of sample was dissolved in 40 mL water and then placed in the ultrasonic bath for 20 min at pH ranging from 1 to 10.

2.3.2.6. Water contact angle (WCA) measurements

The hydrophilicity natures of all the prepared membranes were evaluated from the contact angle measurements. The contact angle (CA) measurements of the prepared membranes were conducted on a contact angle measuring instrument (Kruss, advance drop shape analysis, Germany). Deionized water was used as the probe liquid in all the measurements using the sessile drop method. To minimize the experimental error, the contact angle was measured at five random locations for each membrane sample. To avoid the membrane surface contamination due to surface active substances, the samples were washed using DI water and later dried and stored in a vacuum desiccator for 24 h before water contact angle measurements. Water droplet volume about 2 μL at 0.16 mL/min was dropped on the dried flat membrane surface from a microsyringe with a stainless steel needle at room-temperature conditions. As the temperature increases the amount of water vapor in the air needed for saturation increases. If the air is not humidified, the water drops formed for measurements will evaporate and hence the obtained contact angle may vary from the actual one. For this reason, the humidity was increased by placing water filled containers in the heat enclosure.

2.3.2.7. X-ray diffractometer (XRD)

X-ray diffraction patterns of the electro-spun membranes, membrane textural properties, were recorded using an X-ray diffract meter (BRUKER, D_8 advance, USA) working at 40 KV /50mA with radiation of Cu Kα.

2.3.2.8. Leica microscope

The thickness of the electro-spun membranes was measured by Leica microscope (Leica DM 2500M, Germany).

2.3.2.9. Atomic force microscopy (AFM)

The Atomic force microscopy (AFM) (Agilent, Model 5500 series, USA) was employed to examine the smoothness of the electro-spun membrane surfaces and top surface morphology in the size of 5 μm×5 μm.

2.3.2.10. Transmission electron microscopy (TEM)

The particle size and microstructural information of U-TiO_2 (commercial) and M-TiO_2 NPs were characterized by using transmission electron microscopy (TEM, JEOL, JEM 2100, USA) at 210 kV. First, the TiO_2 nanoparticle sample was prepared by dispersing in distilled water (500 mg/L) and then poured on a carbon tape covered plate. Finally, the sample was dried at room temperature and ready for TEM analysis.

2.3.2.11. Brunauer-Emmet-Teller (BET) isotherm

The specific surface areas of the electro-spun membranes were analyzed using N_2 adsorption-desorption isotherm measurements in Quantachrome® ASiQwin™, USA by using Brunauer-Emmet-Teller (BET) isotherm model.

2.3.2.12. Atomic Absorption Spectrophotometer (AAS)

The initial and final concentrations of Pb (II) and Cu (II) ions before and after equilibrium adsorption were determined by using an Atomic Absorption Spectrophotometer (AA240FS, USA). The analytical wavelengths were fixed at 217.0 and 324.7 nm for Pb (II) and Cu (II) ions, respectively. The initial and final concentrations of Cr (VI) ions before and after ultrafiltration process were determined by using an Atomic Absorption Spectrophotometer (AA240FS, USA). The analytical wavelength for Cr (VI) was fixed at 357.9 nm.

2.3.2.13. UV–vis Spectrophotometer (UV-2600)

To examine the interaction between the adsorbent and the heavy metal ions and to evaluate the Ti leaching tendency, their UV–vis absorbance was determined using a Shimadzu UV–vis Spectrophotometer (UV-2600, Japan) over a wavelength of 250–600 nm.

The permeate concentration of HA solution was evaluated by using UV–vis spectrophotometer (Thermo fisher scientific, UV2300, India) at a wavelength of 254 nm. BSA solution was

evaluated by using UV–vis spectrophotometer (Thermo Fisher Scientific, UV2300, India) at a wavelength of 278 nm.

Chapter 3

Preparation, characterization, and application of electro spun composite membranes

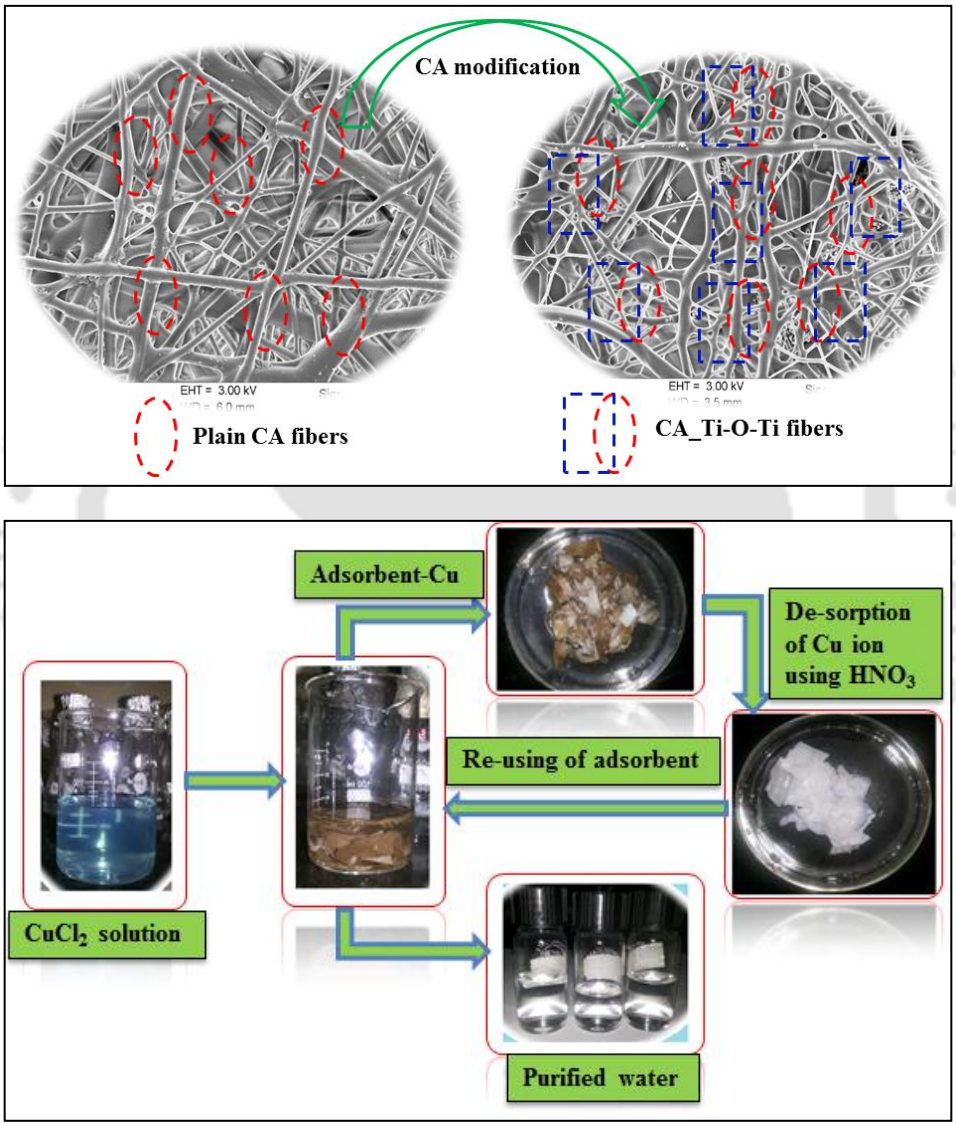

Chapter 3: Preparation, characterization, and application of electro spun composite membranes

In this chapter, an empirical investigation into the impacts of time duration, voltage supply, concentration, and flow rate on the membrane average fiber diameter and surface pore size distribution was done using response surface methodology (RSM) based on central compact design (CCD) are presented. In addition, the effect of glutaraldehyde on membrane crosslinking was also assessed for further studies.

Secondly, hybrid membranes from cellulose acetate (CA) and titanium oxide (TiO_2) nanoparticles (NPs) were fabricated using a novel electro-spinning technique and evaluated as an adsorbent for the elimination of lead and copper metal ions. The impact of TiO_2 NPs contents on the electro-spun membranes matrix was studied in detailed. The impacts of various adsorption parameters, namely, pH, the amount of TiO_2 nanoparticles, contact time, temperature, and kinetics of metal uptake were investigated using batch adsorption experiments. The model isotherms, such as Dubinin–Radushkevich (D-R), Freundlich, and Langmuir were used to analyze the adsorption equilibrium data. Both pseudo first-order and pseudo second order were preferred for kinetic model study.

These works are published in the following Journals

[1] Kibrom Alebel Gebru, Chandan Das "Removal of Pb (II) and Cu (II) ions from wastewater using electrospun cellulose acetate/ titanium oxide (TiO_2) membrane as adsorbent", ***Journal of Water Process Engineering 16 (2017) 1–13***

[2] Kibrom Alebel Gebru, Chandan Das "Cellulose acetate−modified−Titanium dioxide (TiO_2) nanoparticles electro-spun composite membranes: Fabrication and characterization", ***Journal of The Institution of Engineers, Article in press, 2017***

[3] Kibrom Alebel Gebru, Chandan Das "Response surface optimization of electro-spun polyvinyl alcohol nano-fiber membrane process parameters and its characterization", ***Journal of Membrane and Separation Technology, 5 (2016), 140-156***

3.1. Preliminary investigation of electro-spinning process parameters

An empirical exploration into the effects of time duration, voltage supply, concentration, and flow rate on the membrane average fiber diameter and surface pore size distribution was done using response surface methodology (RSM) based on central compact design (CCD). The average fiber diameter and average surface pore diameter of the membrane (i.e. 110 nm and 130 nm, respectively) were obtained at optimum input parameters of 45 min, 10 wt. %, 12 kV and 1.0 mL/h for the time duration, concentration, voltage supply, and flow rate, respectively. The optimization study showed that the predicted versus actual values of both membrane fiber diameter and surface pore diameter are at $R^2 = 0.96$.

In addition, the effect of glutaraldehyde on membrane crosslinking was also assessed for further studies. The results from FESEM images of the fabricated PVA nanofiber membranes using the optimized parameters revealed that the membranes showed smooth morphological structures, without formation of beads. From this study, we have observed that the membrane average fiber diameter and surface pore diameter can be controlled by varying the electro-spinning parameters and can be utilized for waste water treatment application.

3.1.1. Results and discussion

3.1.1.1. Statistical analysis (ANOVA) and Response Surface of electro-spinning parameters

The statistical analyses of the electro-spinning parameters were performed using design expert software. ANOVA test was employed to perform the statistical tests for significance of model, individual model terms and lack of fit. It is obvious that a significant model is needed and "Prob. > F" values less than 0.05 shows significance of the model and the individual model terms. The ANOVA results for both fiber diameter (FD) distribution and surface pore diameter (SPD) distribution were analyzed. In both cases, the lack-of-fit test values were insignificant, which are desired as we need a model that fits.

3.1.1.2. Membrane fiber diameter

The relationship between electro-spinning process factors (i.e. time duration, voltage supply, and concentration and flow rate) and the expected responses (i.e. membrane fiber diameter and membrane surface pore diameter) are plotted graphically after mathematical analysis of the experimental data. **Fig. 3.1** shows the three-dimensional response surfaces for membrane fiber diameter. As already observed from these figures, the factors involved in the membrane electro-spinning process exhibited non-linear effects on the membrane fiber diameter. The highest membrane average fiber diameter (i.e. 256 nm) was obtained at 25 min, 10 kV, 15 wt. % and 3 mL/h (run 29) of time duration, voltage supply, polymer concentration and flow rate, respectively. On the other hand, the lowest membrane average fiber diameter (i.e. 20 nm) was obtained at 42.5 min, 15 kV, 19.5 wt. % and 2 mL/h (run 23). As clearly showed in the three-dimensional plots (i.e. **Fig. 3.1a, b, c, d and e**), the membrane fiber diameter exhibited a decreasing trend from 140.6 nm to 72.9 nm as the voltage supply raised from 10 kV to 20 kV, where the polymer concentrations and flow rates were kept at 10.5 wt. % and 2 mL/h. On the other hand, As observed from the experimental results, continuous fibrous structures were obtained for 6 wt. % PVA aqueous solution concentrations, where the fibers contained many twists, branches and were highly interconnected. At higher concentrations, the cross-sections of the fibers were spherical, but once the concentration of the solution was increased above 19.5 wt. %, the fiber diameter and inters fiber spacing was increased, and there was a slow change from circular to flat ribbon-like structure of the fibers **[8, 9]**. On the other hand, when the PVA concentration was lowered below 6 wt. %, the formation of large beads and non-uniform entanglement of fibers was observed. This result may be accredited to an increasing in the surface tension and/or concentration of the polymer solution **[109]**. At relatively high voltage supply (15 kV), as the polymer concentration was raised from 6 wt. % to 8.25 wt. %, the average fiber diameter of the membrane was increased from 72.9 nm to 114 nm. Further increasing the concentration above 8.25 wt. %, the average fiber diameters seem to have a slight difference. Even though the average fiber diameter is expected to increase with increasing the polymer concentration, in this case, the high voltage supply seems to control the spinning of fibers with large diameters. The analysis of variance and regression model for the four model terms are presented in **Table 3.1** where the model F-value of 22.63 implies the model is significant. There is only a 0.01% chance that a "Model F-Value" this large could occur due to noise. As observed

from the results the model terms such as A, B, C, D, AB, AC, AD, BD, CD, C^2, D^2 are significant, where their Prob. > F" values are below 0.05. Moreover, the voltage supply seems to be a highly significant factor when compared with other significant input factors (time duration, concentration and flow rate). Values greater than 0.10 indicate that the model terms are not significant. The "Lack of Fit F-value" of 1.07 implies the Lack of Fit is not significant relative to the pure error. There is a 50.12% chance that a "Lack of Fit F-value" this large could occur due to noise. Non-significant lack of fit is good that we want the model to fit. The following equation is the final equation in terms of coded factors which is developed using central composite design to designate the curvatures around the optimal point.

$$FD = \begin{pmatrix} 95-11.08\,(A)-28\,(B)-8.83\,(C)+7.92\,(D)+16.88\,(A\times B)+15.88\,(A\times C)-13.75\,(A\times D) \\ +2.63\,(B\times C)-22\,(B\times D)-24.5\,(C\times D)+1.75\,(A^2)+2.88\,(B^2)-15.88\,(C^2)+15.12\,(D^2) \end{pmatrix} \quad \textbf{(3.1)}$$

The reliability of regression models for membrane fiber diameter was described on the basis of high values of R^2 (0.96), which shows that this model is well fitted to the experimental values. On the other hand, the "Pred R-Squared" of 0.80 is in reasonable agreement with the "Adj R-Squared" of 0.91. "Adeq Precision" measures the signal to noise ratio, and a ratio greater than 4 is desirable, where this model's ratio of 22.5 indicates an adequate signal.

Table 3.1 Analysis of variance (ANOVA) for respective response surface quadratic models

Source	Fiber diameter (nm)		Surface pore diameter (nm)	
	p-value Prob > F	F Value	p-value Prob > F	F Value
Model	< 0.0001	22.63	< 0.0001	27.15
A: time duration	0.0023	13.36	0.1265	2.62
B: voltage supply	< 0.0001	85.26	0.0109	8.43
C: Concentration	0.0107	8.49	< 0.0001	25.13
D: flow rate	0.0197	6.82	0.1051	2.98
AB	0.0004	20.64	0.4661	0.56
AC	0.0007	18.27	0.7281	0.13
AD	0.0021	13.71	0.0518	4.46
BC	0.4905	0.50	0.0122	8.11
BD	< 0.0001	35.09	0.0058	10.34
CD	< 0.0001	43.52	0.0003	21.70
A^2	0.5465	0.38	< 0.0001	53.27
B^2	0.3269	1.03	0.0452	4.77
C^2	< 0.0001	31.32	< 0.0001	36.75
D^2	< 0.0001	28.43	0.0004	20.39
Lack of fit	0.5012	1.07	0.0592	4.35

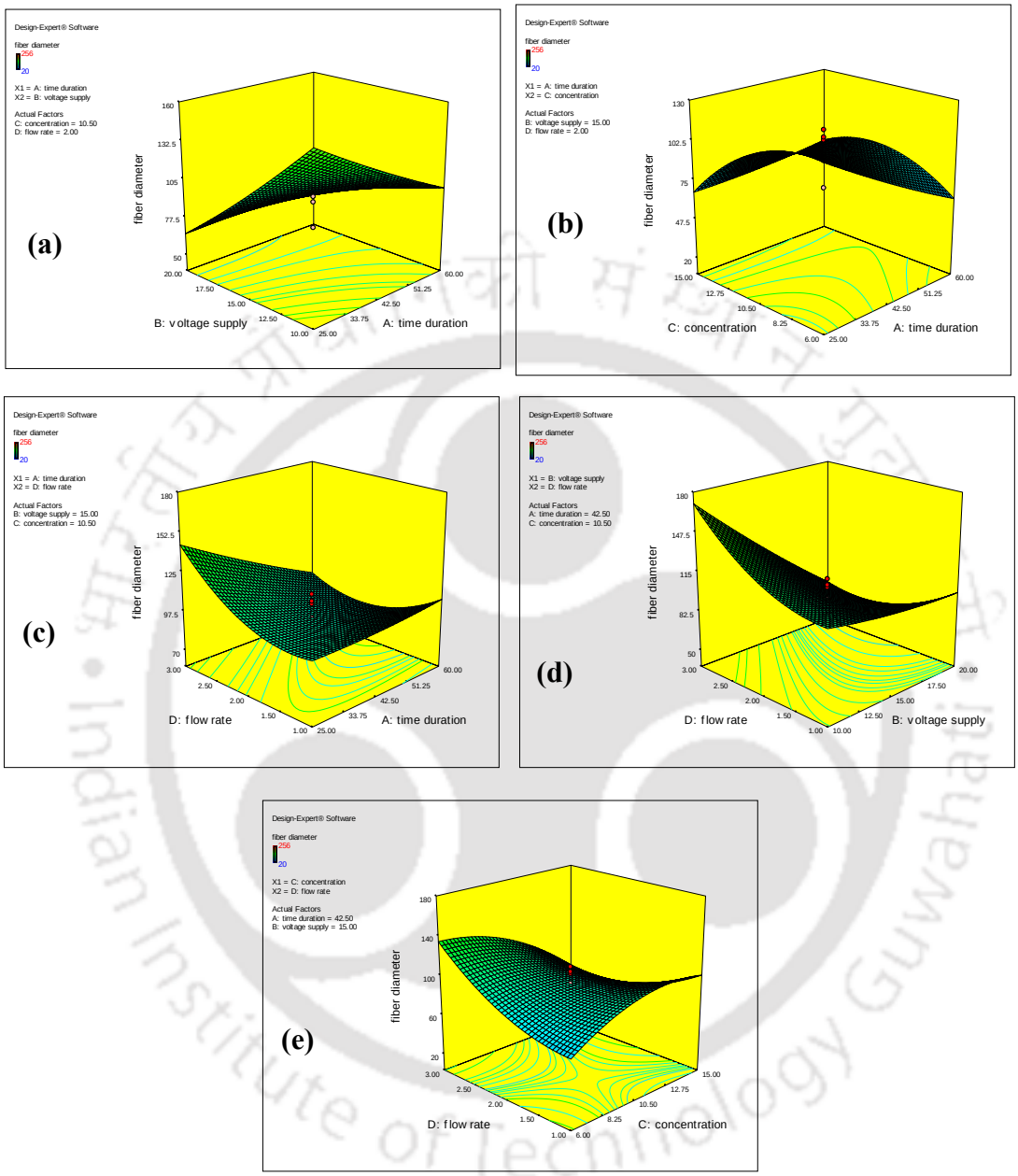

Fig. 3.1 Three-dimensional Response surface plot of (a) voltage supply and time duration, (b) concentration and time duration, (c) flow rate and time duration, (d) flow rate and voltage supply, and (e) flow rate and concentration for membrane fiber diameter

3.1.1.3. Membrane surface pore diameter

The three-dimensional response surface plots, which show the impact of input factors (i.e. time duration, concentration, and voltage supply and flow rate) on membrane surface pore diameter are presented in **Fig. 3.2**. The maximum average membrane surface pore diameter of 310 nm was attained at a time duration of 42.5 min, voltage supply of 15 kV, a concentration of 19.5 wt. % and flow rate of 2 mL/h (run 23) whereas the minimum average membrane surface pore diameter of 50 nm were achieved at a time duration of 60 min, voltage supply of 10 kV, a concentration of 6 wt. % and flow rate of 3 mL/h (run 20). These results indicate that the concentration seems to have a greater contribution to the variation in membrane surface pore diameter (**Fig. 3.2 (b) and (d)**). On the other hand, as shown from **Fig. 3.2 (a)**, the average surface pore diameter was decreased from 142 nm to 115 nm as the deposition time was increased from 25 to 51 min. These results can be explained due to the entanglement of fibers as the electro-spinning time duration was increased. However, when the deposition time duration further increases beyond 51 min, the surface pore diameter showed a slightly increasing trend. At maximum polymer concentration of 19.5 wt. % (Run 23), it is observed that the surface pore diameter is high (310 nm), compared to the membranes prepared from less polymer concentration of (10.5) (Run 28), where the surface pore diameter was 100 nm. This incident is due to the increase in fiber diameter of the membrane, as the concentration of the solution was increased. The Model F-value of 27.15 implies the model is significant. There is only a 0.01% chance that a "Model F-Value" this large could occur due to noise. Values of "Prob > F" less than 0.05 indicate model terms are significant. In this case, B, C, BC, BD, CD, A^2, B^2, C^2, D^2 are significant model terms. Values greater than 0.10 indicate the model terms are not significant. The "Lack of Fit F-value" of 4.35 implies there is a 5.92% chance that a "Lack of Fit F-value" this large could occur due to noise. The following equation is the final equation in terms of coded factors which is developed using central composite design to designate the curvatures around the optimal point.

$$SPD = \begin{pmatrix} 107.33+11.29\,(B)+57.4\,(C)-10.06\,(A\times D)+13.56\,(B\times C)+15.31\,(B\times D) \\ +22.19\,(C\times D)+26.55\,(A^2)-7.95\,(B^2)+22.05\,(C^2)+16.43\,(D^2) \end{pmatrix} \quad \textbf{(3.2)}$$

The reliability of regression models for membrane surface pore diameter was described on the basis of high values of R^2 (0.96), which shows that this model is well fitted to the experimental values. On the other hand, the "Pred R-Squared" of 0.80 is in reasonable agreement with the "Adj R-Squared" of 0.93. "Adeq Precision" measures the signal to noise ratio. A ratio greater than 4 is desirable, and the ratio of 19.7 in this model indicates an adequate signal.

3.1.1.4. Model Verification on the Basis of Statistical Analysis

The effects of the interactions among the input electro-spinning parameters were examined by using RSM optimization technique. This optimization tool is useful in investigating the effect of a binary combination of two input factors. The plots of the interaction between the input parameters are presented in **Fig. (3.3)** and **(3.4)** for fiber diameters and surface pore diameter, respectively. As clearly observed from **Fig. 3.3**, all the interaction plots exhibited non-parallel curvatures. From these results, it is suggested a strong interaction between the variables (i.e. AB, AC, AD, BD, and CD) for membrane fiber diameters. As presented in **Table 3.1**, BD and CD seemed to be highly significant model terms. Therefore, from this study, it can be suggested that the effect of voltage supply and concentration are highly significant input parameters for average fiber diameter of the membrane.

It is clearly seen from **Fig. 3.4** that the interactions of all the input factors (i.e. time duration, voltage supply, concentration and flow rate) have a significant effect on the surface pore diameter distribution. The interaction plots showed non-parallel curvatures, and it is suggested that there is strong interaction between the variables (i.e. AD, BC, BD and CD) for membrane surface pore diameters. As shown in **Table 3.1**, BD and CD seemed to be highly significant model terms when compared with the other model terms. In this case, the most significant factors are voltage supply and concentration. On the other hand, the effects of the interactions of time duration and flow rate with the other parameters on the surface pore diameter of the e-PVA membranes are investigated. This model suggested that the flow rate and time duration are more significant when they are in combination with other parameters than alone.

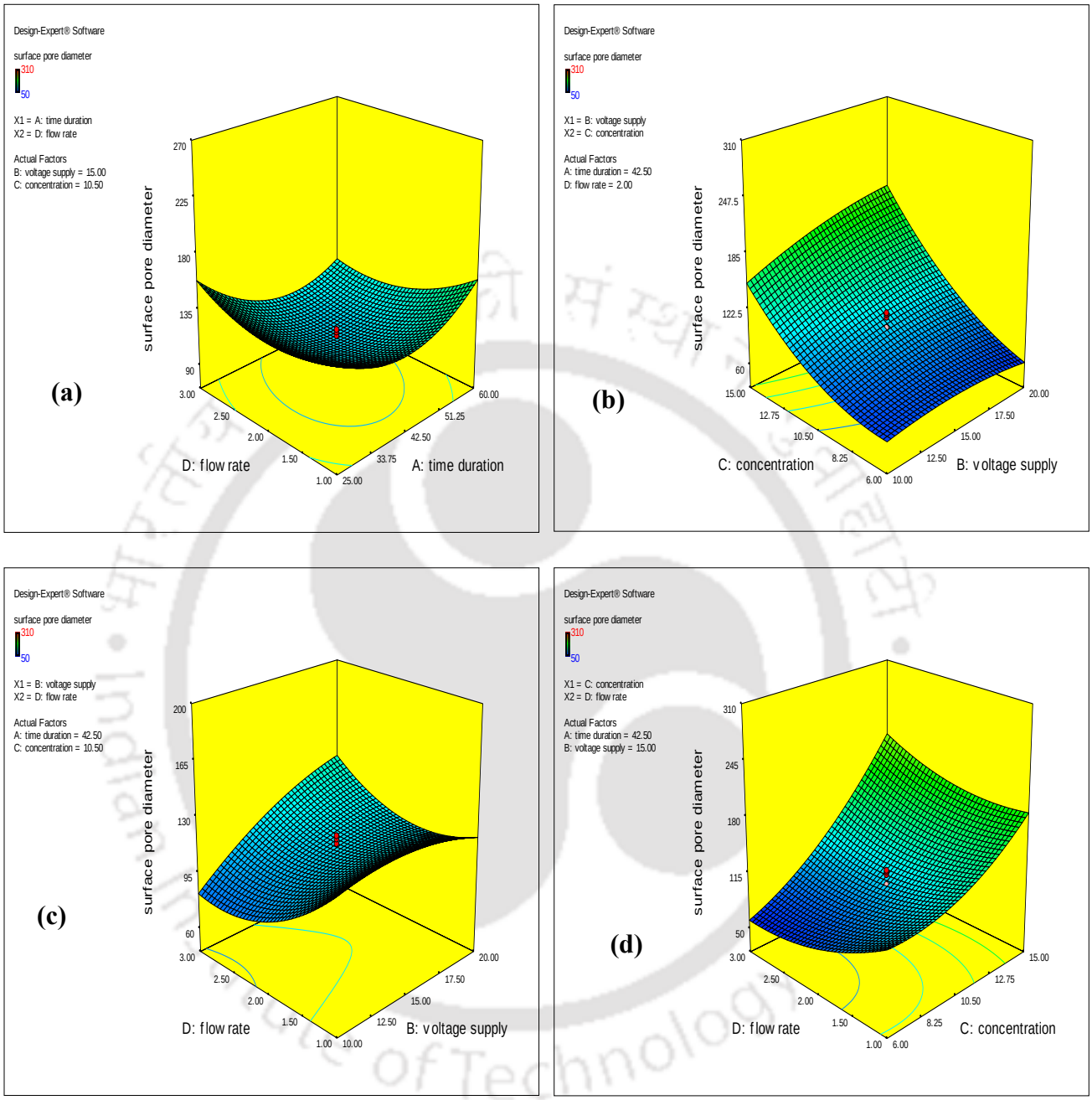

Fig. 3.2 Three-dimensional Response surface plot of (a) flow rate and time duration, (b) concentration and voltage supply, (c) flow rate and voltage supply, and (d) flow rate and concentration for membrane surface pore diameter

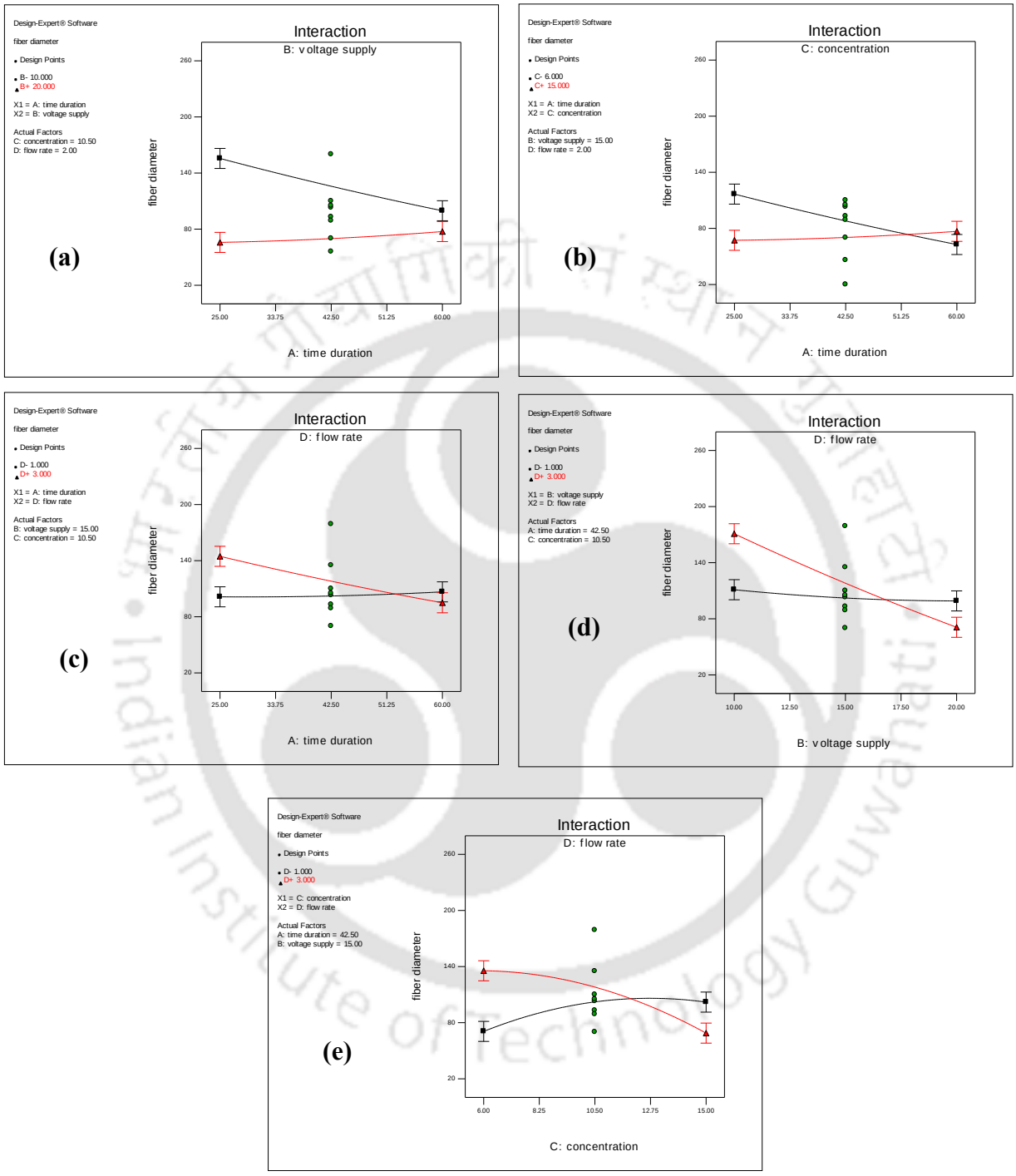

Fig. 3.3 The interaction plots of (a) time duration and voltage supply; (b) time duration and concentration; (c) time duration and flow rate;(d) flow rate and voltage supply; and (e) flow rate and concentration for membrane fiber diameter

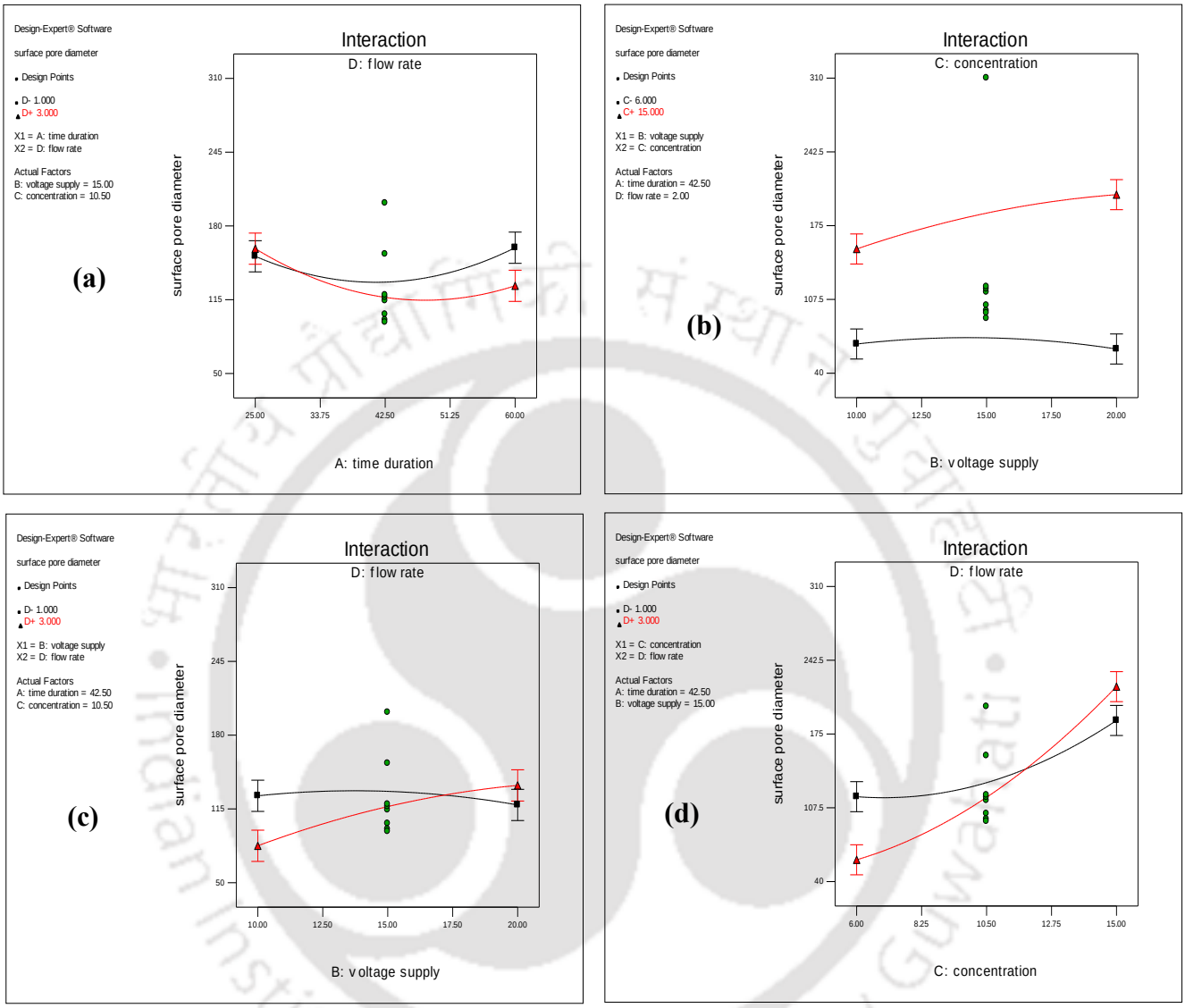

Fig. 3.4 The interaction plots of (a) time duration and flow rate; (b) voltage supply and concentration; (c) voltage supply and flow rate; and (d) flow rate and concentration for membrane surface pore diameter.

Fig. 3.5 shows the actual versus predicted value plots where the predicted values attained from regression model were compared with the experimental values to check the reliability and suitability of the empirical model for individual responses. Therefore, the comparison between predicted and actual values for membrane fiber diameter and membrane surface pore diameters are presented in **Fig. 3.5 (a)** and **(d),** respectively. As clearly shown from the figures, that all the design points are distributed near the straight line, where the points above the straight line are

over-estimated and below the straight line are under-estimated. Based on these results we can conclude that the estimated models are acceptable and there are no violations of constant variance assumptions. Furthermore, according to the data, the empirical model attained from CCD can be used as a predictor for the optimization of the four input parameters to achieve a required average fiber diameter and surface pore diameter depending on the application interest.

Fig. 3.5 (b) and **(e)** show the normal probability plot of residuals for fiber diameter and surface pore size, respectively. The plots in **Fig. 3.5 (b)** and **(e)** ensured that no abnormality signal of the experimental results was observed. The falling of the residual points on a straight line suggests that the errors are normally distributed. On the other hand, **Fig. 3.5 (c)** and **(f)** show the plots of the residuals versus predicted responses for the membrane fiber diameter and membrane surface pore diameter, respectively. The random scattering of all experimental data points across the horizontal line of residuals suggests that the projected models are suitable.

3.1.1.5. Optimization Study

The investigation of the optimized input parameters (electro-spinning parameters) was done through a desirability function (D) for two responses using Eq. **3.3 [110]**. The optimum time duration, concentration, voltage supply and flow rate for preparation of the electro-spun membrane predicted from all responses with a high or low limit of inputs can be satisfied with the desirability function (D).

$$D = \left[\prod_{i=1}^{N} d_i^{r_i}\right]^{1/\sum r_i} \qquad \textbf{(3.3)}$$

Where D is the desirability function, N is the number of responses, r_i refers to the significance of a particular response, and d_i indicates the partial desirability function for specific responses. The desirability plot presented in **Fig. 3.6** confirms that the desirable time duration, concentration, voltage supply and flow rate are 43.48 min, 10.67 kV, 10.89 wt. % and 1.01 mL/h, respectively, which gave optimized average fiber diameter of 110 nm and average surface pore diameter of 120 nm. The prediction of desirable input variables is also confirmed with the optimized input variables calculated from central composite design (listed in **Table 3.2**)

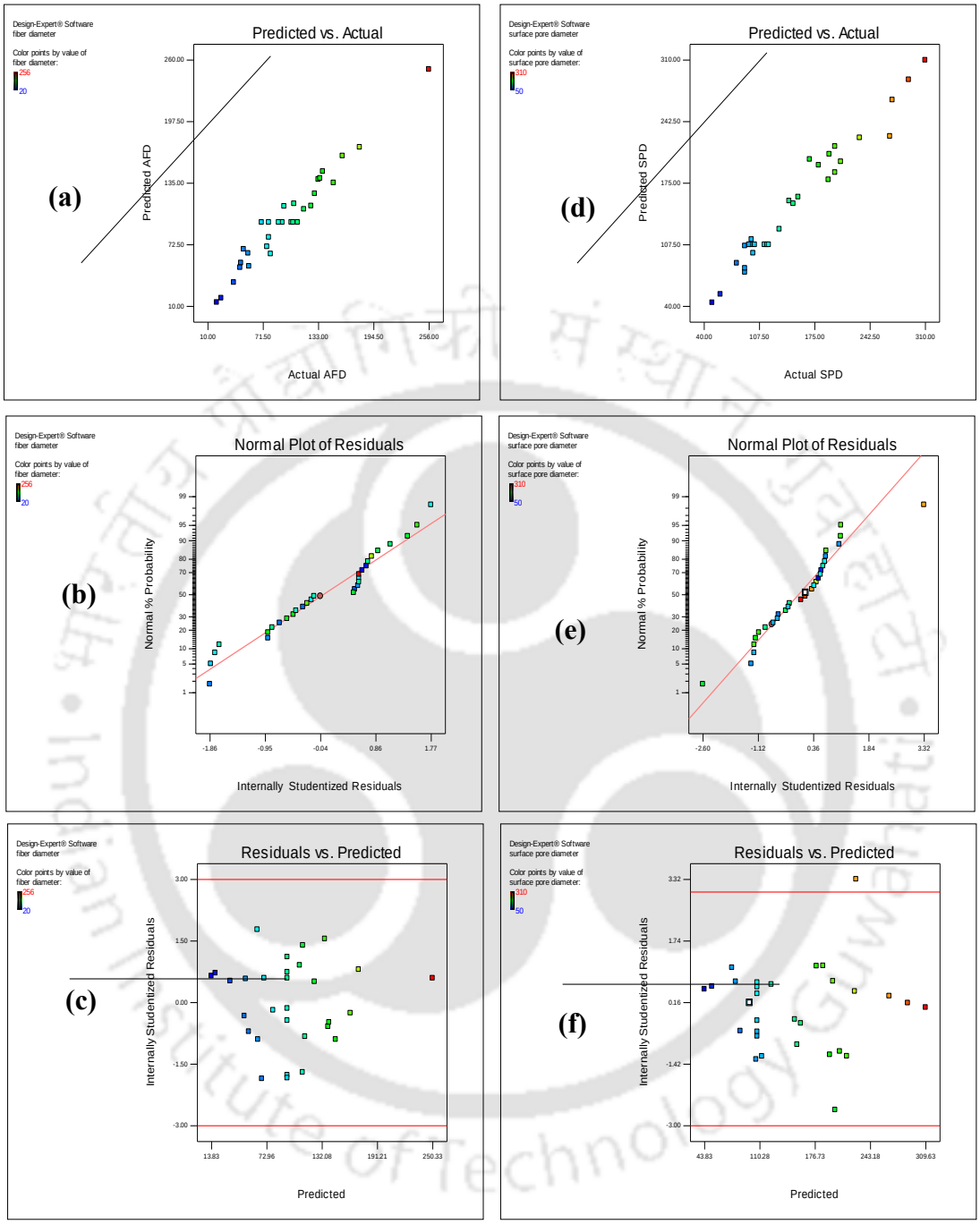

Fig. 3.5 Plots of predicted versus actual values of membrane (a) fiber diameter (R^2 = 0.96) and (d) surface pore diameter (R^2 = 0.96); Normal probability plot of residual (b) membrane fiber diameter and (e) membrane surface pore diameter; Plot of residual vs. predicted of (c) membrane fiber diameter and (f) membrane surface pore diameter.

Table 3.2 Optimized input variables calculated from CCD

No.	Factor 1: A, Time duration (min)	Factor 2: B, Voltage supply (kV)	Factor 3: C, Concentration (wt. %)	Factor 4: D, Flow rate, (mL/h)	Response 1: Fiber diameter (nm)	Response 1: Surface pore diameter (nm)	Desirability	Remarks
1	34.00	12.13	10.26	1.10	110	130	1.00	
2	40.82	11.32	11.41	1.12	110	130	1.00	
3	38.68	11.57	11.48	1.17	110	130	1.00	
4	**44.11**	**10.59**	**11.03**	**1.02**	**110**	**130**	**1.00**	**Selected**
5	46.33	10.14	11.41	1.07	110	130	1.00	
6	43.48	10.67	10.89	1.01	110	130	1.00	

This optimization study shows that, the desirability value of the model is D = 1.00.

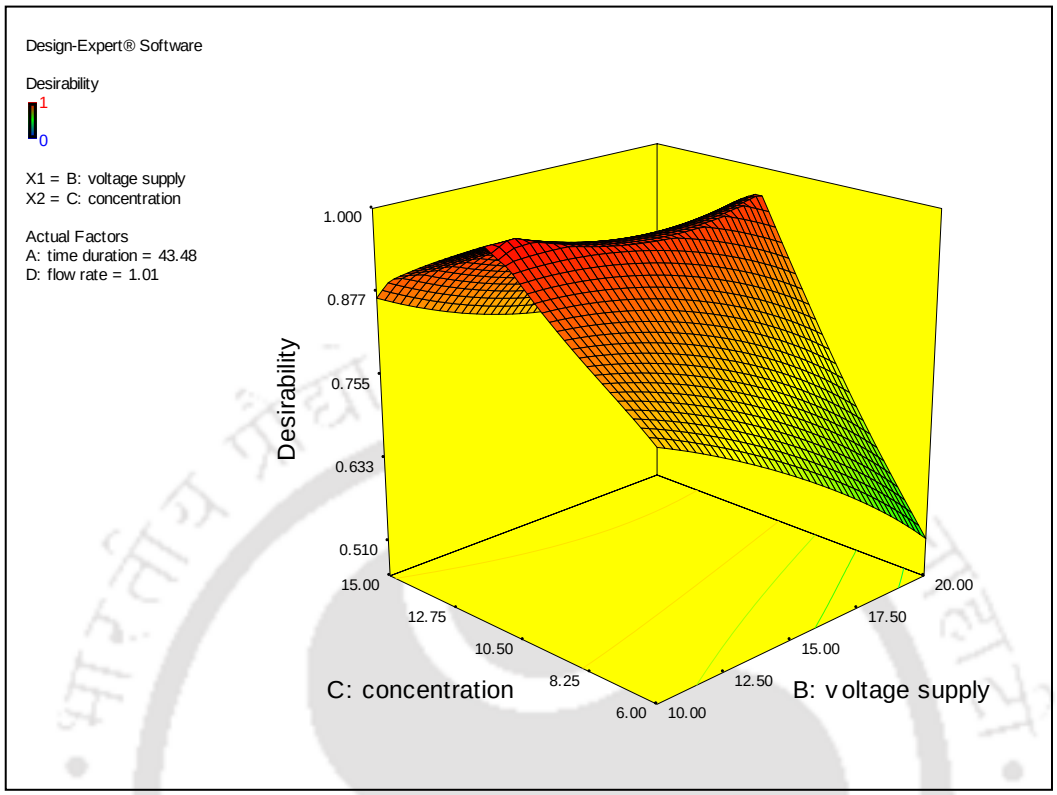

Fig. 3.6 Response surface plot of desirability operating region: voltage supply and concentration of 10.67 kV and 10.89 wt. %, respectively.

This study draws the conclusions of an empirical exploration into the effects of time duration, voltage supply, concentration and flow rate (while the distance and collector rotating speed were kept constant) on fiber diameter and surface pore size distribution during the preparation of e-PVA membranes. Therefore, 10 wt. % aqueous PVA solutions were chosen as the optimized solution concentration; an applied voltage of 12 KV was selected throughout the process, and the feed rate was 1.0 mL/h by means of a 50 mL syringe using a needle of 0.4 mm internal diameter. For further investigation on the effect of time duration, membranes were prepared at 25, 35, 45 and 60 min. The conductivity, surface tension and viscosity values of the PVA solution were 0.079 mS cm^{-1}, 73.7 mN/m, 0.299 Pa.s, respectively.

3.1.1.6. Morphological study (FESEM)

The FESEM images of the electro-spun PVA fibers obtained with 10 wt. % for different electro-spinning durations are shown in **Fig. 3.7**. Fabricated PVA nanofiber membranes showed

a smooth morphological structure, without developing beads. The fiber diameter distributions and surface pore diameters of the membranes were measured using Image J software from FESEM images. We have measured more than 100 fibers of each membrane sample using Image J software to get the average fiber diameter. As shown from **Fig. 3.7 (a_2, b_2, c_2, d_2),** the fiber diameter results indicated that diameters between 78 and 276 nm for 25 min **(a_2);** between 81 and 190 nm for 35 min **(b_2)**; between 59 and 160 for 45 min **(c_2)** and between 37 and 199 nm for 60 min **(d_2).** The average fiber diameters were varied as 124, 117, 100 and 88 nm for samples designated as M_x (x=25, 35, 45, 60 min), respectively. It can be seen from FESEM images presented in **Fig. 3.7 (a_1, b_1, c_1, d_1)** that the slight decrease in average fiber diameter can be related to increasing in ambient temperature during the electro-spinning duration. If the electro-spinning duration of the surrounding electric field delays, the surrounding temperature may increase due to increase in an electron temperature because of collision between the charges. Therefore, increasing temperature has the effect of decreasing the viscosities of the polymeric solutions, increasing solvent evaporation rate, and also may cause a high degree of polymer solubility within the solvent. As a result of these effects, the columbic forces would be able to affect the surface tension of the solution greatly and apply a larger stretching force within the solution causing in the fabrication of thinner fibers. Therefore the effect of the electro-spinning duration alone on the fiber diameter distribution is not highly significant when compared with other parameters like concentration and voltage supply. Due to this reason, the distribution of fiber diameters of the four different samples deposited at 25, 35, 45, and 60 min indicated similar distribution. These results show a similar agreement with statistical analysis of this study. The electro-spinning method is an effective technique to produce nano meter range fibers and nanofibrous membranes with high porosity within nano to micrometer range pores **[26]**. The membrane surface pore size distribution was examined using image J software from the FESEM images.

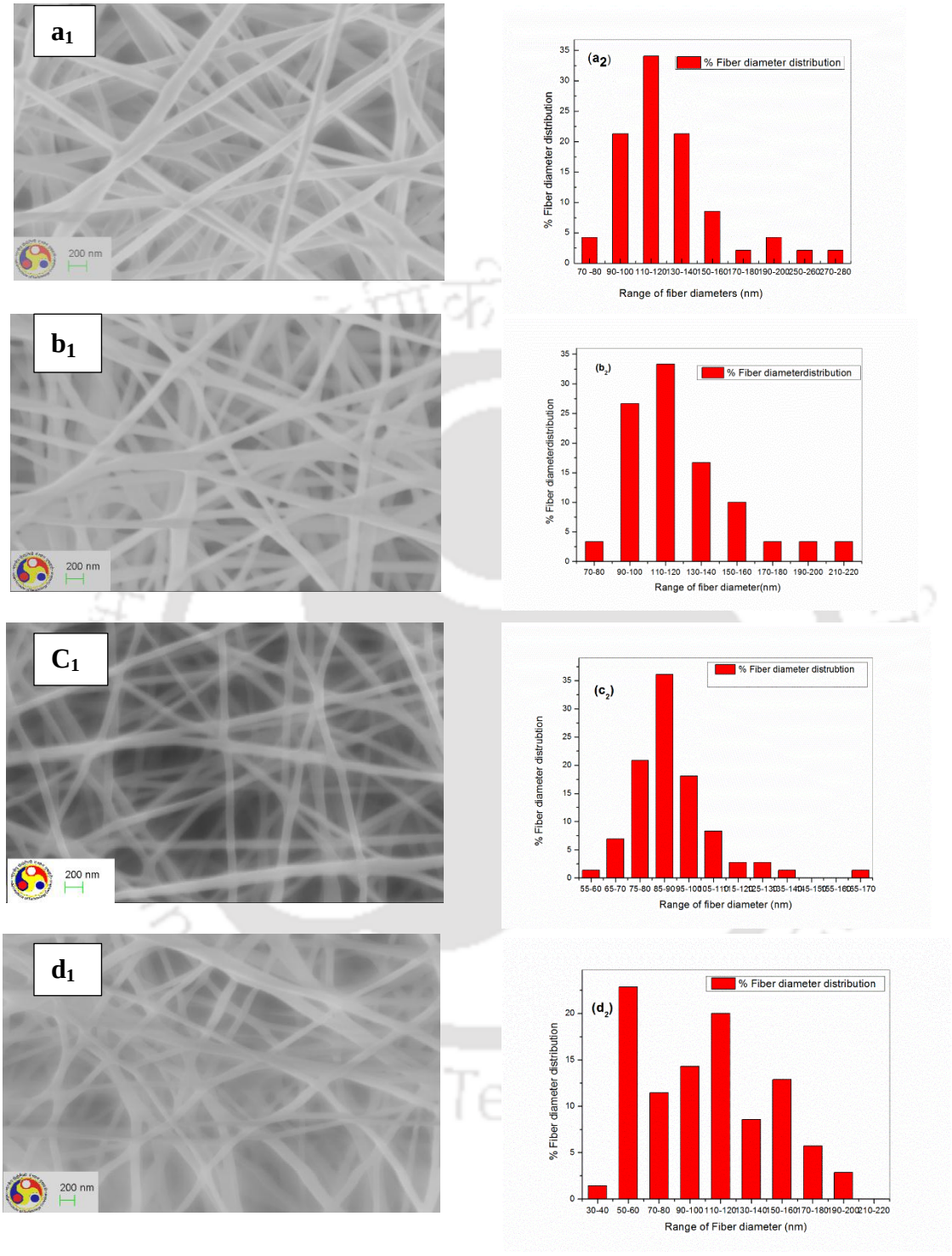

Fig. 3.7 FESEM images of the ePVA fibers and their corresponding fiber diameter distribution at different process time, (a_1, a_2) 25 min, (b_1, b_2) 35 min, (c_1, c_2) 45 min and (d_1, d_2) 60 min.

The pore size distributions are presented in **Fig. 3.8** As shown from the results that the surface pore size of the electro-spun PVA membranes, increased as the electro-spinning duration time decreased. This result can be explained due to the fact that increasing the electro-spinning duration means that we are allowing more fibers to be collected on the collector plate and the entanglements of the fibers were practically increased. In other words, more fiber layers were formed by increasing electro-spinning duration, where the surface pore was reduced due to the entanglements of the fibers layer-on-layer. Thus, the average surface pore diameters are measured as 72.1, 129.7, 149.4 and 160.9 nm for 60, 45, 35, and 25 min electro-spinning duration, respectively. All the membranes fall into ultrafiltration/microfiltration ranges. The decreasing of the average surface pore size is due to an increasing in the number of entangled fibers over and over as the electro-spinning duration increases from 25 to 60 min. Therefore, due to the increase in entanglement of these fibers, there is a possibility of formation of a narrower net-like structure which leads to the decrease of surface pore diameters of the membranes. As already discussed earlier, a slight decrease in average fiber diameter was observed. However, the effect of the fiber diameter variation on the surface pore diameter was insignificant when compared with the effect of the entanglement of the fibers as the electro-spinning duration was increased. On the other hand, the thickness of the membranes has increased as the electro-spinning duration increases. The thickness measurement of the nanofiber membranes was performed using Lieca microscope as shown in **Fig. S 3.1** in the appendix. The images revealed that the thickness of the membranes increased from 20 to 38 μm for increasing electro-spinning duration from 25 to 60 min, respectively, in which the surface pore size is inversely proportional to membrane thickness. **[4]** But, the depth/flowing channel of the membrane pore is expected to increase with increasing thickness.

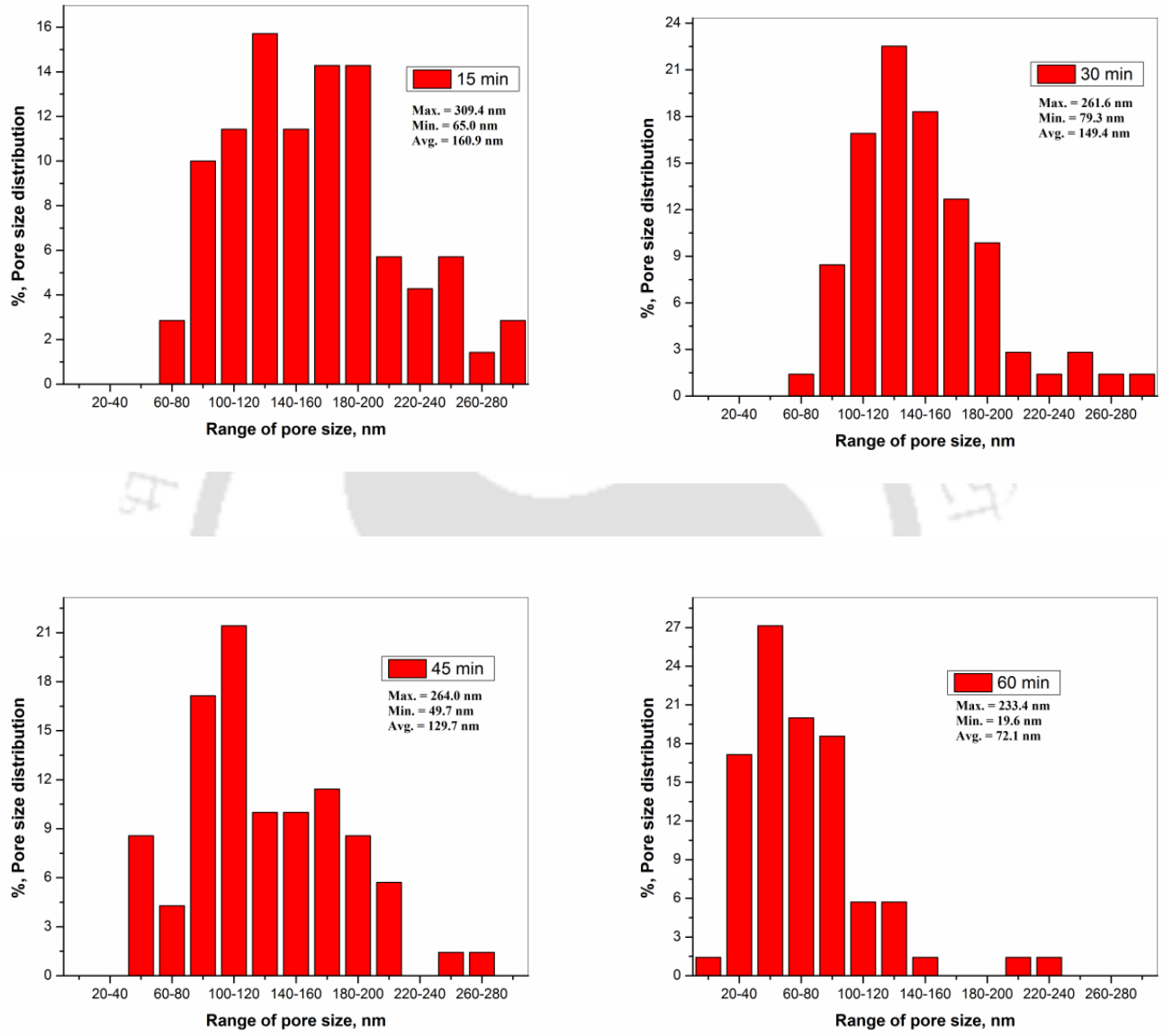

Fig. 3.8 % Surface pore size diameter distribution of e-PVA membranes obtained at different electro-spinning duration, 25 min, 35 min, 45 min and 60 min

The effect of independent variables on the responses was compared with the reported literature. However, the investigation of the effect of the independent variables on the surface pore diameter has been carried out in this study for the first time. **Mohaddeseh et al., 2015** conducted a study which presents the findings of an empirical investigation into the effect of flow rate, voltage, distance and collector rotating speed on diameter distribution during the fabrication of ferrofluid/PVA structure magnetic nanofibers. The procedure commenced with screening the electrospinning process. The ANOVA revealed that the two factors of flow rate and voltage have a significant impact on the response. The $(\text{flow rate})^2$ and $(\text{voltage})^2$ make a second order contribution to the response. The acquired second order regression model is reasonably adequate and can be used for prediction within the limits of the factors investigated. The minimum diameter for fabricated nanofibers was 240 nm with the condition of 0.25 ml/h for flow rate and 45 kV for applied voltage while the distance and rotating speed kept constant at 8 cm and 1500 rps, respectively. On the other hand, Yordem et al., 2008 have studied the predictions of the empirical models and contour plots on electrospinning of polyacrylonitrile/DMF system. Their study suggests the following conclusions:

- Applied voltage was found to be an insignificant factor when the concentration level was high. That is, control of fiber diameter in micrometer scale may be provided by concentration alone. However, voltage was found to be an eminent parameter, depending on the concentration and collector distance levels, and this observation demonstrates the interactive effects of the parameters.
- Collector distance, as well as both voltage and concentration were found to be significant in nano-scale fiber production. The collector distance may be increased in favor of reducing the fiber diameter.
- The fiber diameter and the coefficient of variation are negatively correlated. Scatter of the diameter of nanoscale fiber mats is predicted to be high.
- The domain of potential nano-scale fiber was predicted to be in low concentration and voltage ranges (8–10% and 10–20 kV, respectively, for PAN/DMF with molecular weight of about 75,000 g/mol due to Mark-Houwink equation).

3.1.2. Summary

This study draws the conclusions of an empirical exploration using RSM method into the effects of time duration, voltage supply, concentration and flow rate (while the distance and collector rotating speed were kept constant) on fiber diameter and surface pore size distribution during the preparation of e-PVA membranes. Therefore, 10 wt. % aqueous PVA solutions were chosen as the optimized solution concentration; an applied voltage of 12 KV was selected throughout the process, and the feed rate was 1.0 mL/h by means of a 50 mL syringe using needle of 0.4 mm internal diameter. For further investigation on the effect of time duration, membranes were prepared at 25, 35, 45 and 60 min. Electro-spun PVA nanofiber membranes were successfully prepared at selected electro-spinning duration, crosslinked with glutaraldehyde and characterized. The average fiber diameters varied slightly between 88 to 124 nm when electro-spinning duration was varied. The surface pore size of the electro-spun PVA membranes, increased as the electro-spinning duration time decreased. Thus the average surface pore diameters are measured as 72.1, 129.7, 149.4 and 160.9 nm for 60, 45, 35, and 25 min electro-spinning duration, respectively. All the membranes fall into ultrafiltration/microfiltration ranges. In addition, no change in surface pore size and fiber diameter after cross-linking was observed. However, crosslinking led to uniform arrangement of the fibers and increased network rigidity. The FESEM results agreed with the FTIR and TGA results in that the cross linker glutaraldehyde has reacted properly and confirmed the formation of an acetal-bridge. This study showed that membrane properties could be controlled by varying the electro-spinning duration along with other process and solution parameters. However, future studies will be needed to fully investigate the performance characteristics of the electro-spun PVA membranes for its flux, permeability and fouling performances studies.

3.2. Preparation and characterization of CA_TiO_2 electro-spun composite membranes

Hybrid membranes from cellulose acetate (CA) and titanium oxide (TiO_2) nanoparticles (NPs) were fabricated using electro-spinning technique. The impact of TiO_2 NPs contents on the electro-spun membranes matrix was studied in detail. All these characterization results indicated that TiO_2 NPs were uniformly distributed on the CA electro-spun membrane's matrix. The Addition of TiO_2 NPs caused a formation of largely interconnected fiber networks which in turn have a positive effect on the enhancement of the membrane's mechanical strength, thermal stability, pore structures and permeability/flux property. As the amount of TiO_2 addition was raised from 0 to 6.5 wt. %, the entanglements of the fibers and the spider-net like network among fibers were increased. The water uptake ability of all the membranes after the introduction of TiO_2 was increased with time, and this result was attributed to the hydrophilicity nature of these membranes. Pure water permeation experiments were conducted using CA_TiO_2 hybrid membranes, and high pure water flux values were obtained at very low transmembrane pressures without affecting the hydrophilic nature of the membrane. The initial sharp decrease in pure water flux for CA membrane was significantly improved due to the introduction of TiO_2 NPs in the membrane matrix.

3.2.1. Results and discussion

3.2.1.1. Solution composition

The main aim of this study was to fabricate cellulose acetate_TiO_2 hybrid membranes using electro-spinning technique. Organic–inorganic hybrid membranes are prepared using mixing inorganic oxide with the polymeric solution. Present researchers have paid attention to TiO_2 NPs because of its stable mechanical strength, less costly and high potential for various applications. Furthermore, TiO_2 NPs can improve the hydrophilic nature of various polymers to enhance flux and decline fouling problems which are significant factors in water and wastewater treatments **[60]**. In this study, a mixture of acetone and dimethylacetamide (DMAc) was chosen as cellulose acetate solvent during electro-spinning. To get the optimum electro-spun membrane

with good morphological structures, four different concentrations (25, 20, 15, 13.5 Wt. %) of cellulose acetate were prepared and 13.5 wt. % was selected for the next experiment. Cellulose acetate solutions were prepared by uniformly dissolving in 2:1 ratio of acetone/DMAc **[92]**. Subsequently, different amounts of TiO_2 NPs were added to the cellulose acetate to enhance the physical and mechanical property of cellulose acetate. Therefore, different amounts (0, 1.0, 2.5, 4.5 and 6.5 wt. %) of TiO_2 NPs were dispersed in 13.5 wt. % solution of CA. The mixed solution was stirred for 4 h at 200 rpm speed and sonicated for 3 h to ensure the optimum distributions of the TiO_2 NPs in the CA solution.

Table 3.3 Solution compositions of CA_TiO_2 membranes

Membrane	**CA (wt. %)**	**TiO_2 (wt. %)**	**Acetone/DMAc (wt. %)**
M_1	13.5	0	86.5
M_2	13.5	1.0	85.5
M_3	13.5	2.5	84.0
M_4	13.5	4.5	82.0
M_5	13.5	6.5	80.0

3.2.1.2. CA, CA_TiO_2 membrane fabrication

During the electro-spinning of 20 and 25 wt. % solutions of CA, difficulty of getting uniform bending instability was observed, and no enough fibers were deposited due to the interruption of the spinning process due to the development of beads at the tip of the needle. On the other hand, uniform bending instability and the continued deposition of fibers was observed as the solution concentration was reduced to 13.5 and 15 wt. % of CA throughout the electro-spinning process. Finally, 13.5 wt. % solution of CA was selected as optimized solution, and the membrane from this solution was fabricated at process parameters of an electric field of 14 KV, solution feed rate of 2 mL/h and the needle tip to collector plate distance was kept as 100 mm.

As seen from **Fig. 3.9 (a)**, the CA fibrous membrane has shown sticky-cotton or sponge-like structure, shown by the rectangular shape, which was explained as a poor physical property where the fibers do not adhere to each other **[111].** For this reason, we have chosen TiO_2 as additive to the CA membranes in order to improve their morphological properties. Then, the prepared hybrid solution (CA_TiO_2) was put into the electro-spinning setup for the fabrication of CA_TiO_2 hybrid membranes. It was clearly observed that due to the addition of TiO_2, the sticky-cotton or sponge-like structure of the CA membrane was totally turned to smooth and tightened up membrane structure as shown in **Fig. 2 (b)**.

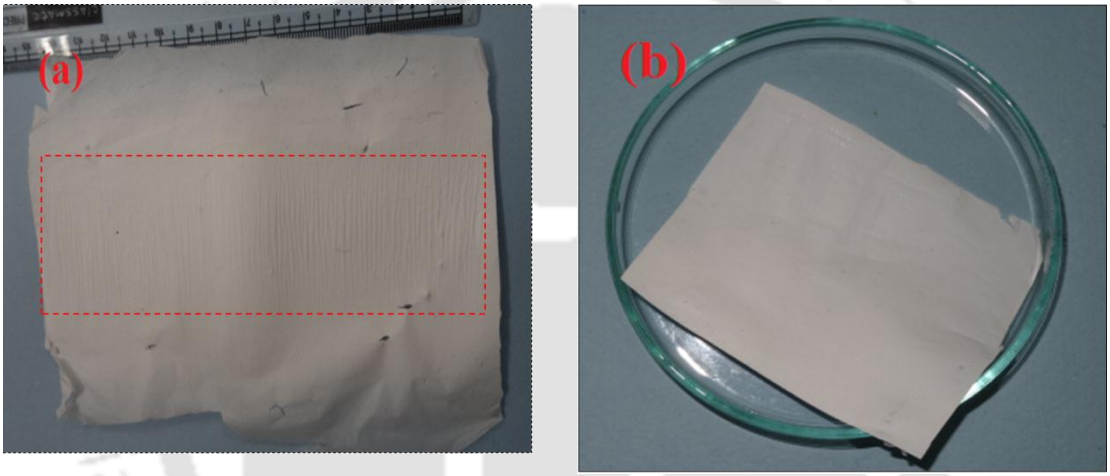

Fig. 3.9. Images of (a) fabricated CA membrane and (b) CA_TiO_2 hybrid membrane.

3.2.1.3. Study of TiO_2 Nanoparticles

As clearly shown in **Fig. 3.10**, the size of TiO_2 was determined by transmission electron microscopy (TEM). The TiO_2 appeared in the form of spots. To measure the size of each nanoparticle, Image J software was used, and their size was ranging from 16 to 72 nm. The average particles size was approximately 29.8 nm.

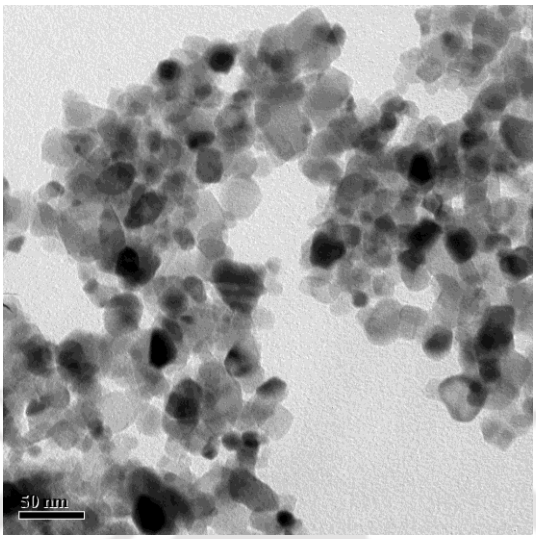

Fig. 3.10. TEM image of commercial TiO_2 nanoparticles

3.2.1.4. Surface charge study

The outer surface zeta potential (ζ) values of the solutions of CA and CA_TiO_2 and TiO_2 at pH of 7 are presented in **Table 3.4.** The solution composition for CA membrane (M_1) had a negative outer surface ζ value (-5.10 mV) due to the dissociation of carboxylic groups present in the cellulose acetate chains and molecular structure **[112].** The outer surface ζ values of the solution compositions for M_2, M_3 and M_4 were -4.13 mV, -2.95 mV and -1.74 mV, respectively. However, with further increasing the amount of TiO_2 blended with CA solution, a high positive ζ value was attained reaching a value of +16.19 mV at 6.5 wt. % of TiO_2. These results confirm that the positively charged characteristics of hybrid membranes were enhanced with increasing the amount of TiO_2 with in the CA solution. On the other hand, the ζ value of the pure TiO_2 nanoparticles was positive (+33.4 mV) at pH=7. The limitations particularly the oxygen vacancies on the surface morphology and structure of the nanoparticles could be introduced, and this may change the electronic structure of the nanoparticles **[113]**. Furthermore, water molecules can occupy the oxygen vacancies and produce adsorbed –OH groups, which indicated that the nanoparticles were positively charged. Nevertheless, the outer surface ζ values for the hybrid membranes containing TiO_2 were negative at the studied pH value (1.0 wt. %, 2.5 wt. % and 4.5 wt. % of TiO_2).

Table 3.4 Zeta potential values: Solution of CA and CA_TiO_2, and TiO_2

Samples	**M_1**	**M_2**	**M_3**	**M_4**	**M_5**	**TiO_2**
Zeta potential (mV)	-5.10	-4.13	-2.95	-1.74	+16.19	+33.4

3.2.1.5. Membrane morphological study

The FESEM images of the electro-spun CA and CA_TiO_2 hybrid membranes, which are designated as M_1, M_2, M_3, M_4 and M_5 are shown in **Fig. 3.11 (a_1, b_1, c_1, d_1, e_1)**. The electro-spun membranes with good morphological structures which have smooth fibers and uniform fiber entanglements were fabricated successfully. The FESEM images were taken to evaluate the impact of TiO_2 on the electro-spun hybrid membranes morphological structures. According to these images, increasing TiO_2 content on cellulose acetate caused the formation of largely interconnected fiber networks which may have good effect on the enhancement of the membranes strength and membrane pore structures. When the addition of TiO_2 amount was increased from 0 to 6.5 wt. %, the entanglements of the fibers and the network between the fibers were increased. However for higher amount of TiO_2 (4.5 and 6.5 wt. %), large amount of agglomerations were observed on the membrane's top layer, and some of the fibers turned from a round shape to flat shape **(Fig. 3.11 d_1, e_1)**. Therefore M_2 and M_3 were chosen as best hybrid membranes with their optimized morphological structures. The elemental results of the electro-spun membranes are shown from the EDS images in **Fig. 3.11 (a_2, b_2, c_2, d_2, e_1)**. The EDS image clearly confirmed that the existence of the TiO_2 NPs on the fibers within the membrane matrix. When the TiO_2 percentage increases from 0 to 6.5 wt. %, the composition of titanium atom increased from 0 to 10 wt. %. As shown in **Fig. 3.11 (a_2),** only oxygen and carbon atoms were detected in CA membrane. The EDS mapping also revealed that an even dispersion of TiO_2 was observed in the membrane matrix. Both the FESEM and EDS studies revealed that the fabricated membrane has good morphological structures with a uniform distribution of TiO_2.

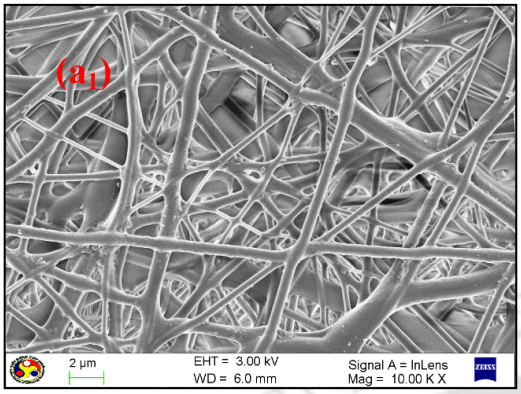

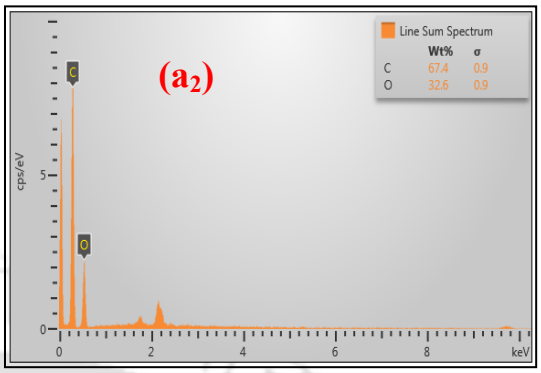

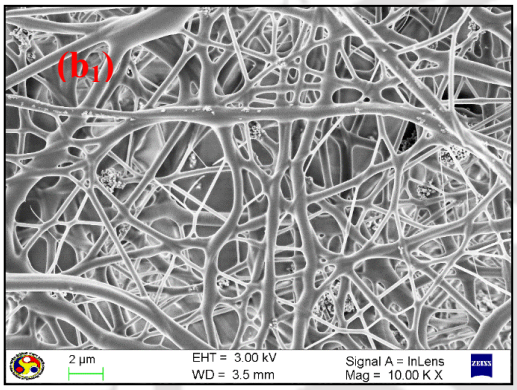

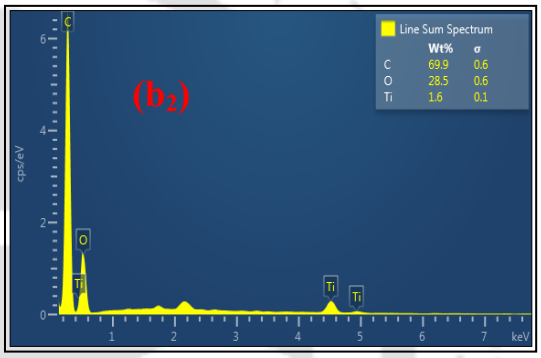

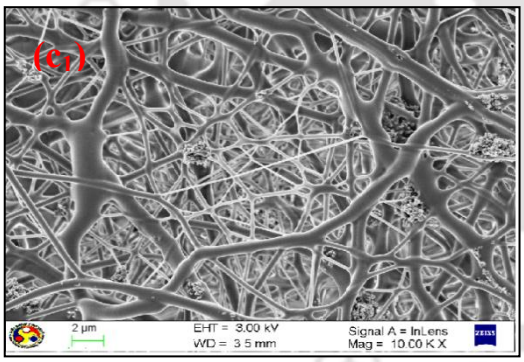

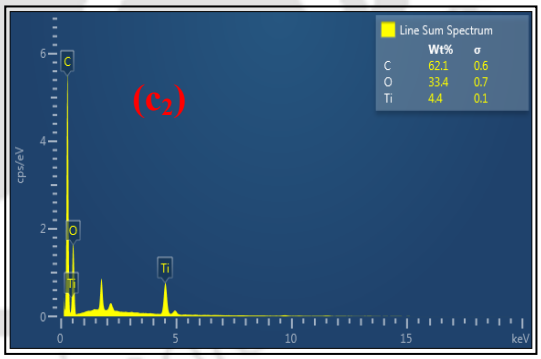

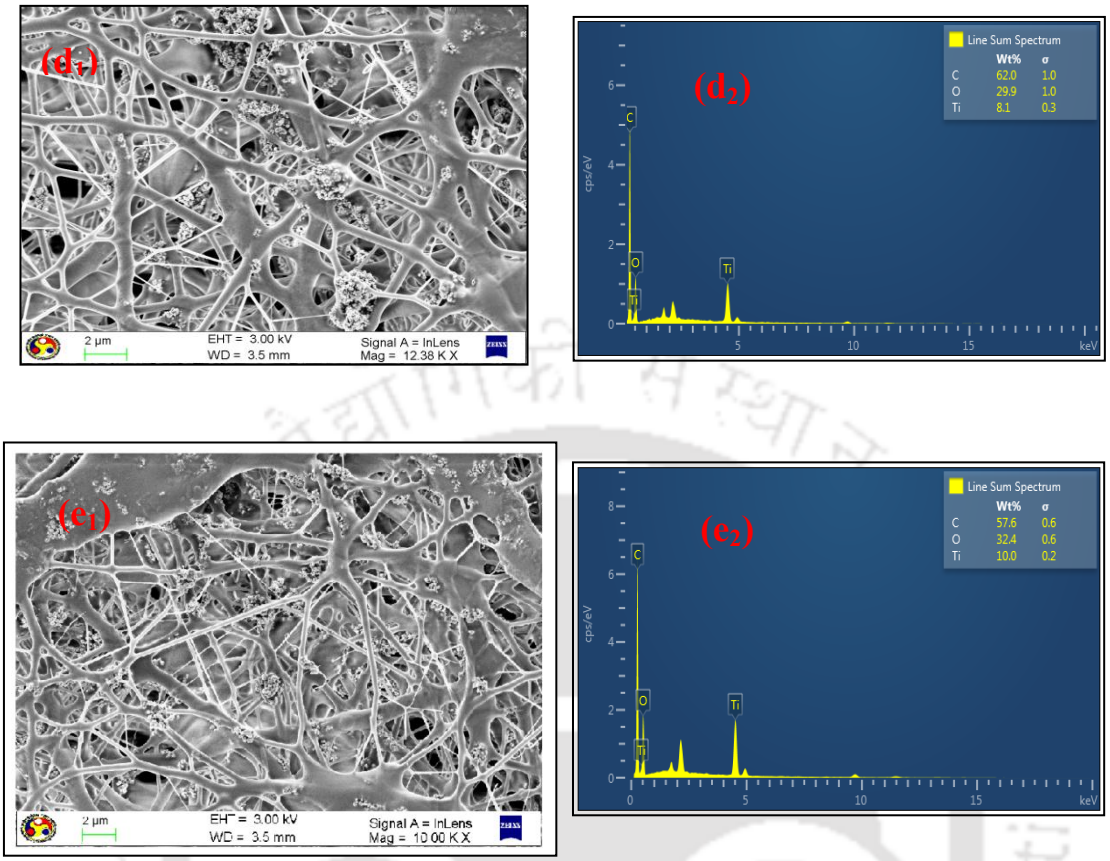

Fig. 3.11 FESEM and EDS images of CA, CA_TiO_2 electro-spun fibers M_1 (a_1, a_2), M_2 (b_1, b_2), M_3 (c_1, c_2), M_4 (d_1, d_2) and M_5 (e_1, e_2).

The fiber diameter and surface pore diameter distributions of the electro-spun membranes were studied from the FESEM images using Image J software. The fiber diameter distributions of all the membranes are shown in **Fig. 3.12.** An average fiber diameter was examined by measuring around 600 fibers. From these measurements, the average fiber diameter was found to be 0.43 µm. From the whole fiber diameter measurements, the minimum and maximum fiber diameters were found to be 0.06 µm and 1.2 µm, respectively. The effect of the increasing TiO_2 on the fiber diameters of the membrane was also investigated. A uniform decline in average fiber diameter was confirmed as the content of TiO_2 increases. This uniform decrease in average fiber diameter can be explained as some CA chains may be broken due to the ionization of the solution as the distribution of TiO_2 was further increased, as will be discussed in detail later in this section. As shown in **Fig. 3.12 (M_1 to M_5)**, most of the fiber diameters are laid in the range

of 0.35 to 0.8 µm; large number of the fibers for M_3 have found in the range of 0.15 to 0.8 µm; the largest number of fibers for both M_4 and M_5 were found within the range of 0.15 to 0.3 µm; and the average fiber diameters for M_1, M_2 and M_3 were 0.6, 0.55 and 0.5 µm, respectively. On the other hand, the average fiber diameters for M_4 and M_5 were found to be 0.4 µm and 0.3 µm, respectively, (defective fibers were excluded). Therefore, the impact of the TiO_2 on the fiber diameters of the hybrid membranes was evidently observed from this study.

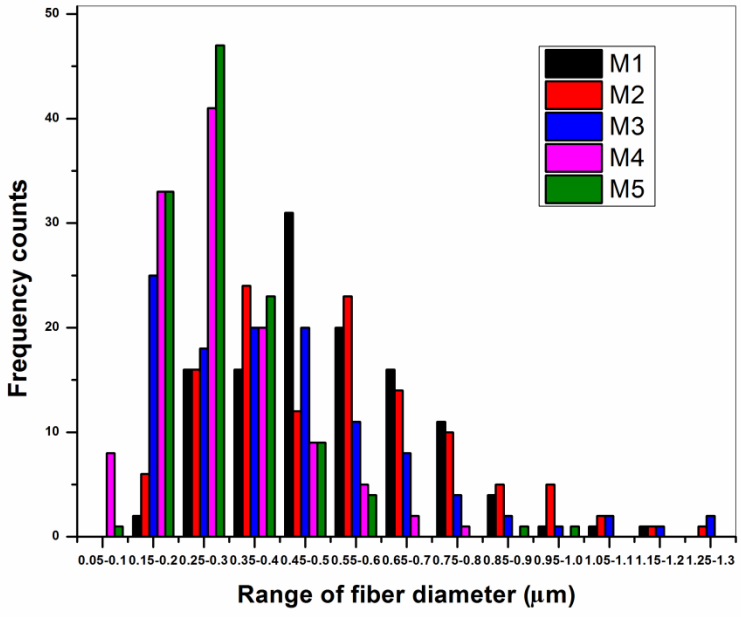

Fig. 3.12 Fiber diameter distribution of CA (M_1) and CA_TiO_2 electro-spun fibers (M_2, M_3, M_4 and M_5).

Surface pore size distributions of the CA and CA_TiO_2 membranes were examined using image J software from the FESEM images and are presented in **Fig. 3.13**. 100 surface pores of each membrane sample were measured. The results showed that the surface pore size of the electro-spun hybrid membranes decreases as the content of the TiO_2 increase. For example, the average surface pore diameters are measured as 0.85, 0.79, 0.70, 0.54 and 0.48 µm for M_1, M_2, M_3, M_4 and M_5, respectively. Normally, all the membranes fall into microfiltration ranges. The decreasing of the average surface pore size is due to an increasing in the TiO_2 to the membrane matrix. From the FESEM image analysis, it was indicated that the cellulose acetate matrix comprises less spider-net like network, but, with increasing the TiO_2 content, the spider-net like structure or fiber networks were highly interconnected to each other. The spider-net like network structure development was mainly because of the improved ionization of the polymeric solution

in the presence of TiO_2 during electro-spinning, and similar results were reported by **[114]**. Thus, the acidic CA solution may be further ionized when the TiO_2 were added, which was also confirmed by pH measurement. The pH of the CA solution (6) was increased to neutral (7) for CA_TiO_2 solution. Under a neutral condition, electro-spun CA_TiO_2 solution results in a significant reduction in surface pore diameter compared to those obtained in an acidic condition of cellulose acetate (CA) membranes, due to the increase in complex fiber network. The uniform dispersion of TiO_2 can reduce the power of the inter-molecular hydrogen bonds among polymeric species, by tending ions to travel freely and subsequently, the conductivity was raised. The additional uniform desperation of TiO_2 on the membrane matrix can further raise the number of ions in the electro-spinning solutions. An additional increase of ions can cause the splitting-up of sub-fibers from the main fiber jets and solidification with TiO_2 in the form of a spider net-like structure. The surface hydroxyl group and acetate group part of the ionic species of CA were suggested to hold TiO_2 on the surfaces of fibrous membranes. The ionized species of the polymer and TiO_2 (Ti^{4+}) were linked either using hydrogen-bonding **[115]** or using the development of complexes within polymeric ligands initiated by the lone-pair of electrons in cellulose acetate. But, further increasing the amount of TiO_2 (4.5 and 6.5 wt. %) NPs caused the formation of thick and flat fibers on some parts of the CA_TiO_2 hybrid membranes. This can be explained due to the fact that, with increasing the quantity of TiO_2, the CA_TiO_2 was turned into a more viscous solution, which might grow the columbic force required to overcome the surface tension for erupting the electro-spinning jet, resulting in large agglomeration, thicker and flat fibers with having rough surfaces.

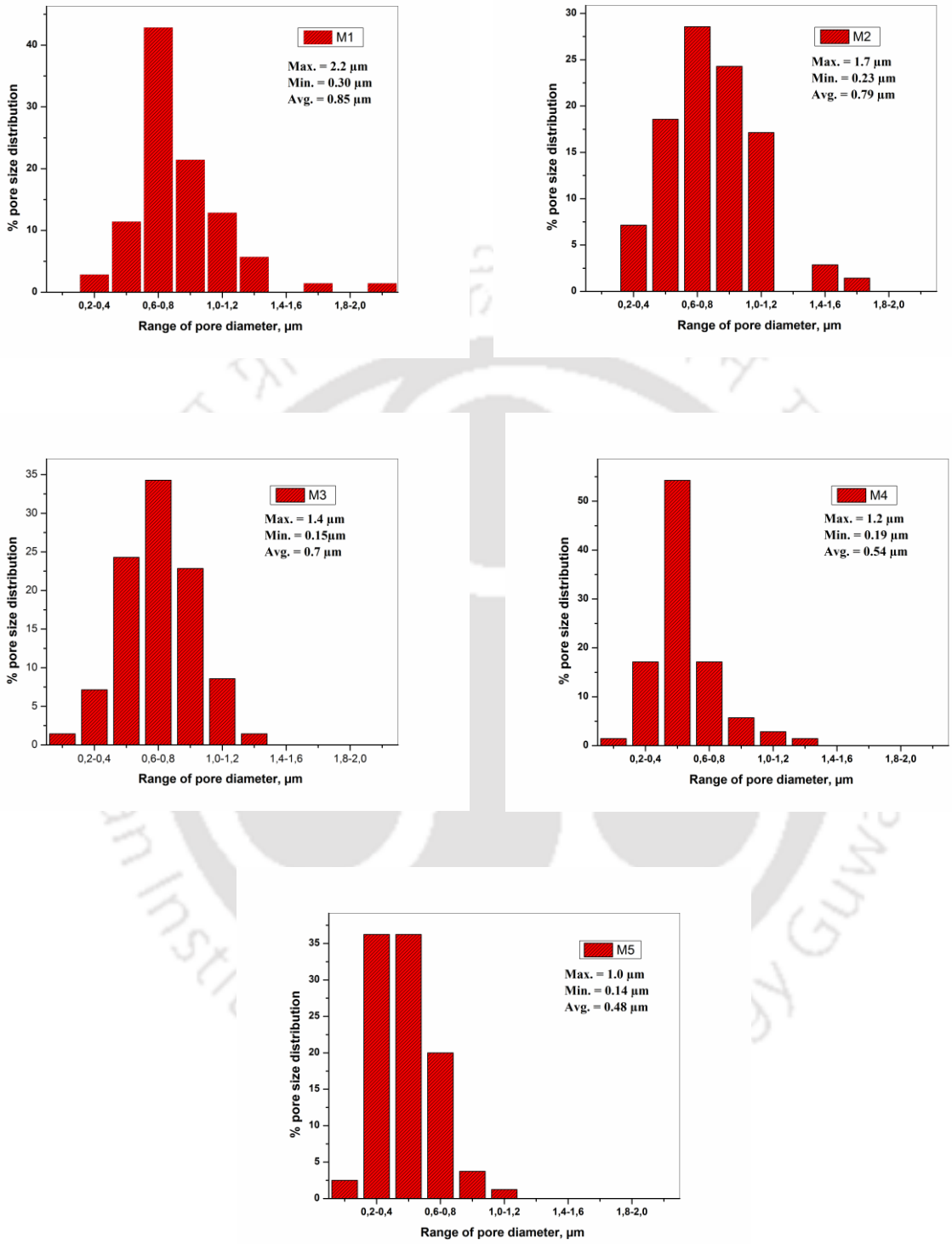

Fig. 3.13. % Surface pore size diameter distribution of CA_TiO_2 membranes (M_1, M_2, M_3, M_4 and M_5)

3.2.1.5. Membrane crystallinity analysis

Crystallinity analysis was carried out using X-Ray diffraction. The X-ray diffraction patterns of CA, CA_TiO_2 electro-spun hybrid membranes and TiO_2 are presented in **Fig. 3.14**. The patterns of TiO_2 were presented as 2θ= 48.06º, 37.86º, 25.41º, matching with brookite, rutile and anatase, respectively, where these are characteristics of crystalline peaks **[116]**. According to these results, it was indicated that the TiO_2 are largely comprised of anatase. Among the three types, anatase has an excellent stability, adsorption capacity, antifouling characters and hydrophilic nature, which are the important characteristics of filtration and adsorbent membranes. In addition, this is suitable for membrane modification **[48]**. As seen in **Fig. 3.14**, the wide peak observed below 2θ = 20° for pure CA membrane **(M_1)**, corresponds to the semi-crystalline arrangement of cellulose acetate membrane **[117]**. For the CA_TiO_2 hybrid membrane **(M_2)** only one crystalline characteristic peak is observed at 2θ of 24.15° and as the TiO_2 content increases, the CA_TiO_2 hybrid membranes (M_3, M_4 and M_5) showed characteristic of three crystalline peaks at 2θ = 24.06º, 37.85º, 48.15º which are similar with the TiO_2 characteristic peaks including the semi-crystalline peak of CA. However, 2θ was slightly shifted for the main peak of TiO_2 NPs as shown in **Fig. 3.14 (M_2-M_5)**. This slight shift of TiO_2 peaks in electro-spun CA_TiO_2 hybrid membranes is may be due to the interactions between cellulose acetate and TiO_2 **[118]**. The strong and sharp characteristic peaks in the hybrid membranes indicate the good crystallinity of the fabricated membrane.

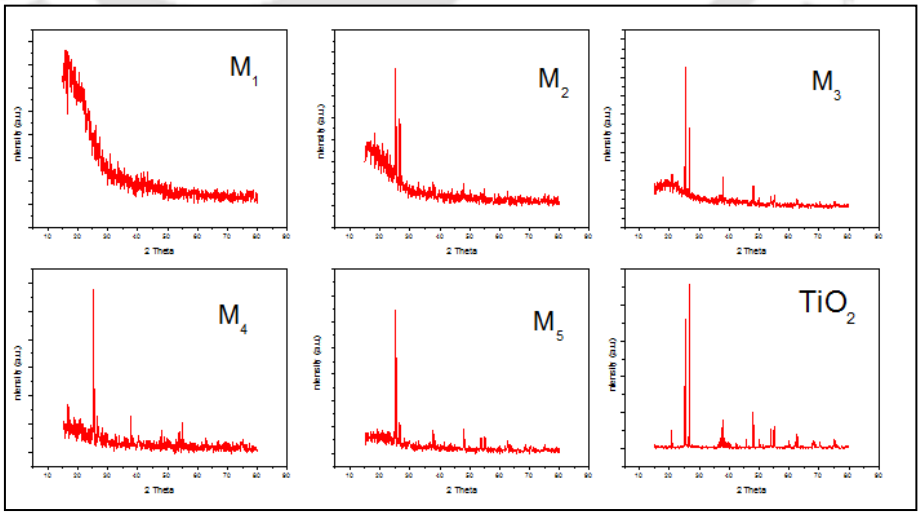

Fig. 3.14 X-ray diffraction patterns of TiO_2 nanoparticle, CA and CA_TiO_2 electro-spun

membranes (M_1, M_2, M_3, M_4 and M_5).

3.2.1.6. Surface roughness study

The Surface roughness study of the prepared membranes was conducted using atomic force microscopy (AFM). The three-dimensional surface AFM images of electrospun CA and CA_TiO_2 hybrid membrane are shown in **Fig. 3.15.** The AFM analysis software was used to examine the membrane roughness parameters within a scanning area of 5 µm×5 µm. The mean value of the Z value *(R_a)*, the root mean square of the Z value (Rms *(R_q)*) and the mean difference in the height between five highest peaks and five valleys *(R_{max})* were evaluated. It was confirmed that all the roughness parameters of electrospun CA membrane (M_1) were higher than the

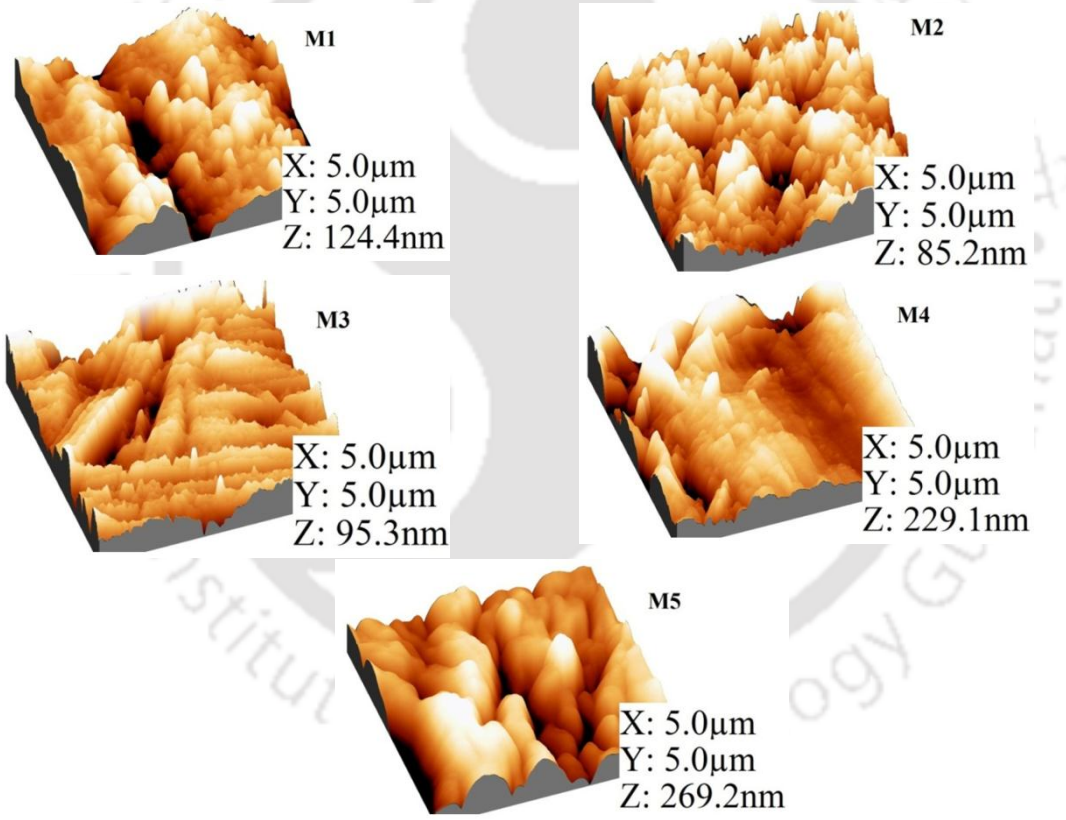

Fig. 3.15 Three-dimensional AFM images of CA (M_1) and CA_TiO_2 (M_2, M_3, M_4 and M_5) electro-spun membranes.

electrospun CA_TiO_2 (M_2) membranes.

As the content of the TiO_2 NPs on CA was raised from 0 to 2.5 wt. %, the membranes roughness also declined from 124.4 nm (M_1) to 95.3 nm (M_3). It might be considered that the uniform distribution of TiO_2 NPs within the matrix of the electrospun membranes made the membrane to have denser skins, in which the rough and cotton like structure of CA membrane was changed into a smoother surface. However, as the TiO_2 NPs content increased to 4.5 and 6.5 %, the roughness for M_4 and M_5 **(Fig. 3.15)** was increased largely to 229.1 and 269.2 nm, respectively, which may be due to the high agglomeration of TiO_2 NPs on the membrane's matrix as already seen in **Fig. 3.11(d_1** and **e_1)**. Membranes with smoother surface have found to have better anti-fouling ability and good permeability properties. The membranes fouling tendency could rise, and the flux property would decline as the roughness of the membrane increases due to pollutants collecting on the valleys and peaks of the irregular membrane surface **[60, 119]**.

3.2.1.7. Thermal stability analysis

The thermo gravimetric analysis (TGA) was used to study the thermal analysis of **(a)** pure CA and **(b-e)** CA_TiO_2 hybrid membranes as shown in **Fig. 3.16.** In addition to a slight change in decomposition temperatures, the weight losses of the membrane samples were found to be 97, 91, 85, 76, and 69 % for M_1, M_2, M_3, M_4, and M_5, respectively. The weight loss decreased uniformly with increasing TiO_2 amount in the hybrid membrane, and additional heat was transferred to the TiO_2 in the membrane throughout the analysis. The residual mass of CA_TiO_2 membrane is higher than that of TiO_2 free membranes where the degradation amount for the CA membrane was improved by the addition of TiO_2 nanoparticles. Thus, the delay in decomposition was due to the slight enhancement of CA_TiO_2 membrane's decomposition temperature (T_d). This result is may be due to the increase in rigidity of the polymer chain due to the interaction between CA and TiO_2 NPs, which improves the energy of CA chain from simple breaking down. This interaction between CA chains and TiO_2 NPs was suggested, due to the hydrogen or covalent bonds. Similar results were reported by **[48, 115]**. The results confirmed that the TiO_2 NPs were evenly distributed in the electro-spun membrane fibers. This good compatibility between the CA and TiO_2 NPs was suggested due to the possible coordination

bond of Ti^{4+} and acetate group and the possible hydrogen bond formation among the surface hydroxyl groups and acetate groups of CA **[48]**. Furthermore, the strong interaction between TiO_2 NPs and the CA chains could avoid TiO_2 NPs from being leached easily from membrane matrix. The results revealed that deposition of TiO_2 NPs into CA matrix had improved the rigidity of the polymer chain, which is significant property to increase the mechanical strength and thermal stability of the membranes. Also, EDS images of M_2–M_5 confirmed uniform distribution of TiO_2 NPs in the matrixes of the electro-spun fibrous membranes, regardless of the large amount of TiO_2 NPs agglomeration for M_4 and M_5.

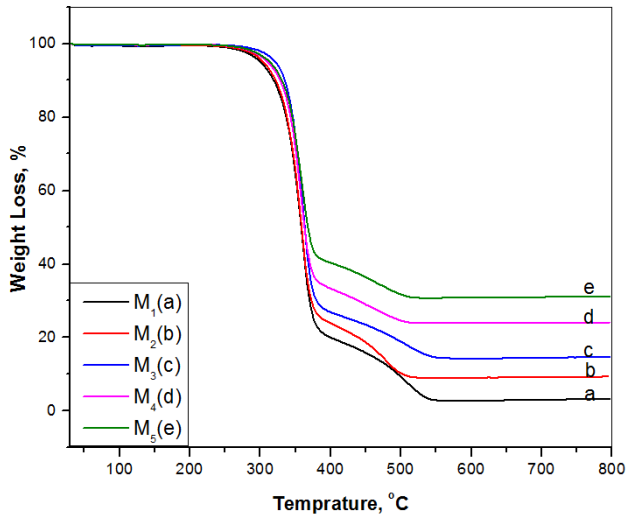

Fig. 3.16. TGA Analysis of (a) cellulose acetate and (b, c, d and e) cellulose acetate_TiO_2 hybrid membranes.

3.2.2. Summary

In this study, a cellulose acetate (CA) _titanium oxide (TiO_2) hybrid membrane was fabricated by using electro-spinning technique. The CA_TiO_2 hybrid membranes showed a structure resembling the pure CA membrane. However, the spider-net like network between the fiber structures were improved due to the NPs deposition on the surface of membrane fibers.The effect of TiO_2 contents on the electro-spun membrane matrix was studied in detailed. The characterization studies confirmed the existence of nanoparticles in the CA electro-spun membrane matrix and the pure CA membrane was modified successfully. The outer surface ζ

values of the solution compositions for M_1, M_2, M_3, M_4, M_5 and TiO_2 were -5.10 mV, -4.13 mV, -2.95 mV, -1.74 mV, +16.19 mV, and +33.4 mV, respectively. The positively charged characteristics of hybrid membranes were enhanced with increasing the amount of TiO_2 with in the CA solution. The roughness surface observed for electrospun CA membrane (M_1) was enhanced when the content of the TiO_2 NPs on CA was raised from 0 to 1.0 wt. % and 2.5 wt. % (M_2 and M_3, respectively). The weight losses of the membrane samples were found to be 97, 91, 85, 76, and 69 % for M_1, M_2, M_3, M_4, and M_5, respectively, and the degradation amount for the CA membrane was improved by the addition of TiO_2 nanoparticles. This modified CA_TiO_2 hybrid membrane will be used for water treatment applications. However, future studies will be needed to fully investigate the performance characteristics of CA-TiO_2 hybrid membranes for specific applications.

3.3. Removal of Pb (II) and Cu (II) ions from wastewater using composite electrospun cellulose acetate/ titanium oxide (TiO_2) adsorbent

Electrospun cellulose acetate (CA) / titanium oxide (TiO_2) adsorbents were prepared using the electrospinning technique. The adsorbents were analyzed using Brunauer–Emmett–Teller (BET) surface area analyses, Fourier transform infrared (FTIR) spectroscopy, field emission scanning electron microscopy (FESEM), and Energy dispersive X-ray spectroscopy (EDS) characterization methods. The impacts of various adsorption parameters, namely, pH, the amount of TiO_2 nanoparticles, contact time, temperature, and kinetics of metal uptake were investigated using batch adsorption experiments. The highest removal capacities of Pb (II) and Cu (II) after 300 min using CA/TiO_2 adsorbent at 35 °C were estimated as 25 mg/g and 23 mg/g at pH of 5.2 and 5.8, respectively. The model isotherms, such as Dubinin–Radushkevich (D-R), Freundlich, and Langmuir were used to analyze the adsorption equilibrium data. Comparing the regression values (R^2), the Langmuir model isotherm was well fitted than D-R and Freundlich isotherms with the adsorption equilibrium data for both metals. In general, pseudo-first-order and pseudo- second order are preferred for kinetic models. Pseudo-second order kinetic equation was well fitted to the adsorption experimental data for both lead and copper ions. The removal efficiencies didn't change significantly when four adsorption–desorption experimental cycles were conducted.

3.3.1. Results and Discussion

This section is divided into three subsections as a characterization of adsorbents, adsorption study, and kinetic study.

3.3.1.1. Morphology and diameter distributions

In this work, electrospun adsorbents with smooth morphological structures (which have smooth fibers and uniform fiber entanglements) were fabricated using the electrospinning technique. As clearly shown from the FESEM images **(Fig. 3.17)**, increasing TiO_2 content on cellulose acetate caused the formation of largely interconnected fiber networks. When the addition of TiO_2 amount was increased from 0 to 2.5 wt. %, the entanglements of the fibers and the network between the fibers were increased. But for the higher amount of TiO_2 (i.e. 4.5 and 6.5 wt. %), some agglomerations were observed on the adsorbent top layer, and some of the fibers turned from a round shape to flat shape. Although the composition and solvents used in this study are different, similar results were reported by **[117]** on the effects of TiO_2 NPs during the preparation of CA/TiO_2 composite adsorbents.

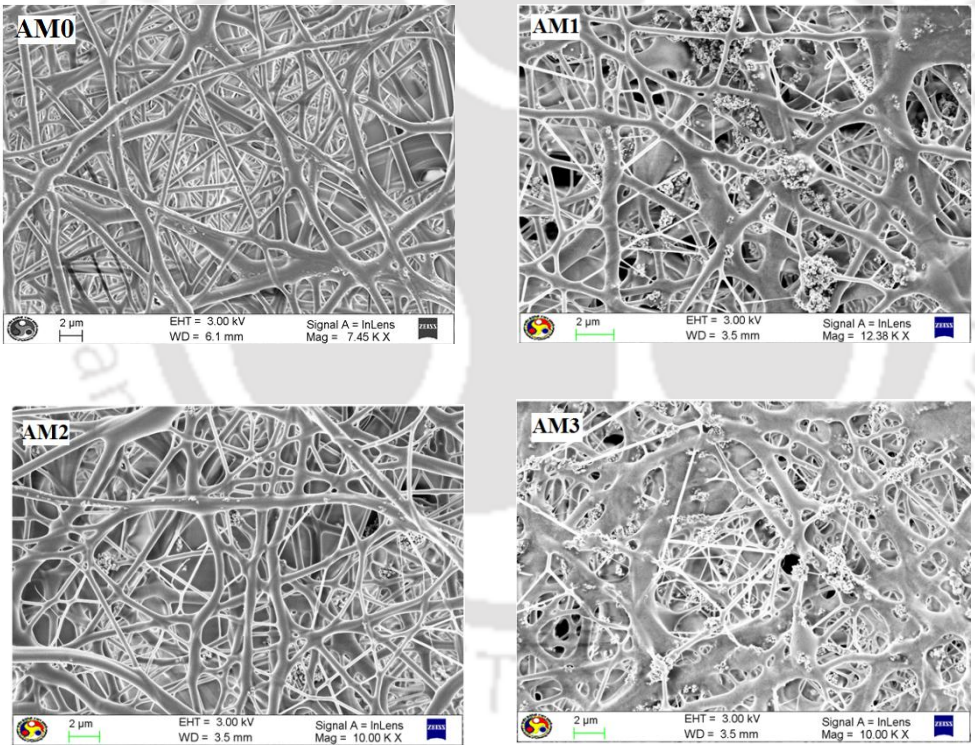

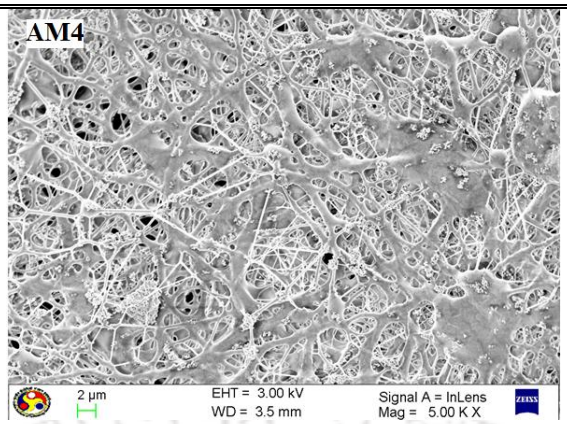

Fig.3.17. FESEM images of electrospun adsorbents (AM0, AM1, AM2, AM3, and AM4).

As seen from **Table 3.5** the addition of TiO_2 NPs improved the porosity of the plain adsorbent. An increase in porosity for CA/TiO_2 is because of the uniform network formation within the matrix of the adsorbent after the introduction of the TiO_2 NPs and the hydrophilic nature of the adsorbent, in which the TiO_2 NPs are known as hydrophilicity enhancer. And it is also believed that the occurrence of TiO_2 NPs creates the spaces within the adsorbent matrix by separating the CA chains which lead to the improvement of the adsorbent porosity. However, on the addition of higher TiO_2 NPs (i.e. 4.5 and 6.5 wt. %), the porosity value was observed to decrease. This result is due to the agglomeration of the NPs in the matrix of the adsorbent as clearly seen from the FESEM images **(Fig.3.17)**. In this study, AM2 was chosen as best composite adsorbent due to its improved specific surface area, porosity, and overall best morphological structures.

Table 3.5 Effect of TiO_2 content on adsorbent porosity and specific surface area

Adsorbent	**CA content (wt. %)**	**TiO_2 (wt. %)**	**Solvent (wt. %)**	**Porosity, ε (%)**	**Specific surface area (m^2/g)**
AM0	13.5	0	86.5	57.2	30.2
AM1	13.5	1.0	85.5	80.1	38.5
AM2	13.5	2.5	84.0	85.9	48.5
AM3	13.5	4.5	82.0	72.9	19.9
AM4	13.5	6.5	80.0	69.0	12.5

3.3.1.2. Textural properties of the adsorbent

The textural properties (crystallinity) analysis was carried out using X-Ray diffraction. The X-ray diffraction patterns of AM0, AM1, AM2, AM3, and AM4 electrospun adsorbents and TiO_2 NPs are presented in **Fig. 3.18.** The patterns of TiO_2 NPs were presented as 2θ= 48.06º, 37.86º, 25.41º, matching with brookite, rutile, and anatase, respectively, where these are characteristics of crystalline peaks **[116]**. According to these results, it was indicated that the TiO_2 NPs are largely comprised of anatase. As seen in **Fig. 3.18**, the wide peak observed below 2θ = 20° for AM0, corresponds to the semi-crystalline arrangement of cellulose acetate **[117].** For AM1 only one crystalline characteristic peak is observed at 2θ of 24.15°, and as the TiO_2 NPs content increases, the AM2, AM3, and AM4 showed a characteristic of three crystalline peaks at 2θ = 24.06º, 37.85º, 48.15º which are similar with the TiO_2 NPs characteristic peaks including the semi-crystalline peak of cellulose acetate. However, 2θ was slightly shifted for the main peak of TiO_2 NPs as shown in **Fig. 3.18** (AM1, AM2, AM3, and AM4). This slight shift of TiO_2 peaks is may be due to the interactions between cellulose acetate and TiO_2 NPs **[118]**. The strong and sharp characteristic peaks in the adsorbents indicate that the strong textural properties of the fabricated adsorbents which are an important property of the mechanical strength of adsorbents.

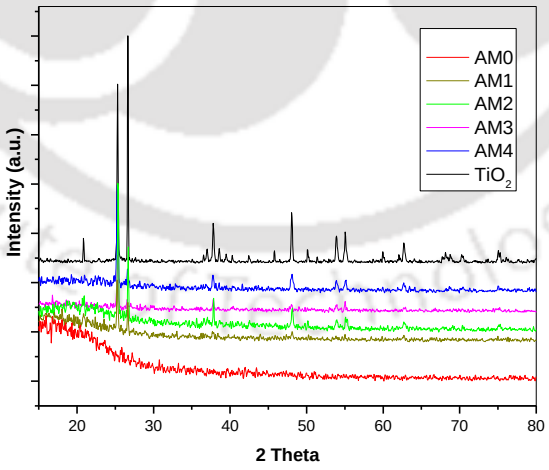

Fig. 3.18. X-ray diffraction patterns of the TiO_2 nanoparticle, electrospun adsorbents (AM0, AM1, AM2, AM3, and AM4).

3.3.1.3. Infrared spectroscopy analysis

To investigate the chemical structure of the samples, the FTIR analysis was done. Therefore, the functional groups of TiO_2 nanoparticles, electrospun CA and CA/TiO_2 adsorbents were characterized. **Fig. 3.19** shows the FTIR bands for TiO_2 nanoparticles, CA and CA/TiO_2 adsorbents. The broad peak at 3490 cm^{-1} matches to the surface hydroxyl stretching and the peak at 1750 cm^{-1} corresponds to the vibrations of −OH bonds on the surfaces of TiO_2 nanoparticles **[71]**. In the spectra of pure CA, the broadband detected at 3456 cm^{-1} corresponded to −OH stretching because of the strong hydrogen bond of intermolecular and intra-molecular kinds. The characteristic band of 2900 cm^{-1} attributed to the C−H stretching **[120]**. The patterns of the C–H bending bands in the region 890 cm^{-1} are likewise characteristics of the aromatic replacement patterns in CA. For the TiO_2 nanoparticles and CA/TiO_2 adsorbents, a new broadband around 600–800 cm^{-1} appeared, which is attributed to the Ti−O−Ti band **[121]**. This result shows that TiO_2 nanoparticles are successfully introduced to the cellulose acetate adsorbent matrix. In addition to this, some small peaks were disappeared after the introduction of TiO_2 nanoparticles.

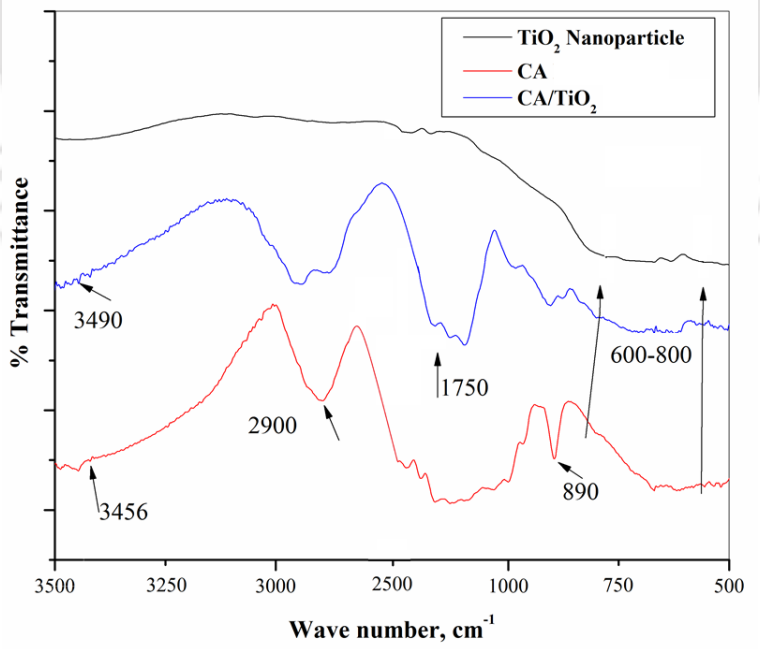

Fig. 3.19. FTIR spectra of CA, TiO_2, and CA/TiO_2 adsorbents.

3.3.1.4. Specific surface area analysis

The nitrogen adsorption-desorption analysis was done for TiO_2 nanoparticles alone and CA/TiO_2 adsorbent with various TiO_2 doses. The adsorbents designated as AM0, AM1, AM2, AM3, and AM4, the amount of TiO_2 nanoparticles in the cellulose acetate matrix were varied as 0, 1.0, 2.5, 4.5 and 6.5 wt. %, respectively. Adsorption isotherm graphs were plotted as the volume of molecules adsorbed on solid surfaces versus partial pressures (P/P_o) at a constant temperature. Relative pressure is defined as the ratio of actual gas pressure (P) to the saturated vapor pressure of adsorbate (P_0) at a specific temperature. As observed from **Fig. 3.20**, the results indicate that all the isotherm graphs are of type II, which is a characteristic of mesoporous structure. In the case of the isotherm graphs for nanoporous materials, these desorption curves retrace the adsorption curves. But, for macroporous and mesoporous materials, these desorption curves do not repeat the adsorption curves causing in a wide loop **(Fig. 3.20).** In adsorption study, the specific surface area of the adsorbent is the most important factor **[122]**. In the BET analysis, the effects of TiO_2 nanoparticles on the specific surface areas of the adsorbents were observed. As shown in **Table 3.5,** the specific surface area of TiO_2 nanoparticles powder (i.e. 59.9 m^2g^{-1}) is higher than those of the adsorbents. The specific surface area of the adsorbent increased from 30.2 m^2g^{-1} to 48.5 m^2g^{-1} as the amounts of TiO_2 nanoparticles in the adsorbent matrix were increased from 0 to 2.5 wt. %, respectively. An additional increase of TiO_2 nanoparticles indicated a decline in specific surface area of AM3 and AM4 (i.e. 19.9 m^2g^{-1} and 12.5 m^2g^{-1}, respectively). This result is suggested due to an increase in agglomeration of the nanoparticles on the top layer and inside the channel of the adsorbent matrix. As already depicted from the morphological structures of the CA/TiO_2 adsorbents in the FESEM analysis **(Fig. 3.17)**, further increasing the amount of TiO_2 nanoparticles caused the formation of thick and flat fibers in some parts of the CA/TiO_2 adsorbent which could decrease the porosity of the adsorbent. The specific surface area of TiO_2 nanoparticles is greater than CA/TiO_2 as some of the vacant spaces of the nanoparticles were occupied by CA chains during the production of CA/TiO_2 adsorbents. The main advantage of using films in the adsorption process is that it can be easily recovered without difficulty. Where reusing of powder or particulate adsorbent nanoparticles has been challenging **[66]**. Throughout this study, AM2 was selected as the best adsorbent because of its enhanced specific surface area **(Table 3.5),** but for comparison, all the adsorbents were tested for their adsorption capacity.

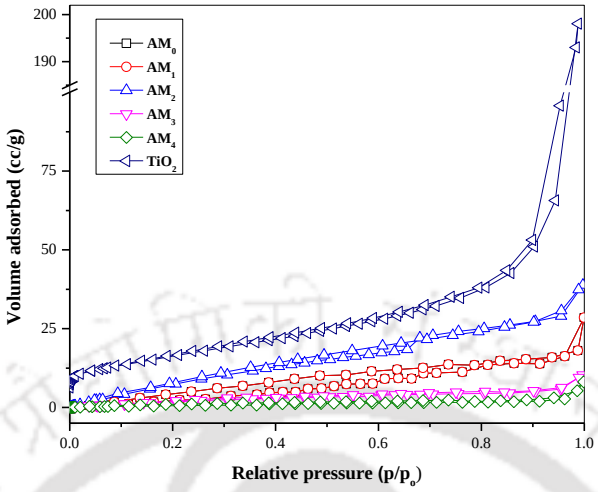

Fig. 3.20 Adsorption-desorption isotherm graph of adsorbents (TiO_2 nanoparticles and AM0, AM1, AM2, AM3, AM4)

3.3.1.5. Energy dispersive X-ray analysis

The EDS characterization was used to study the elemental composition analysis of the adsorbents. The FESEM and EDS images of the AM2 (i.e. (a_1, a_2), (b_1, b_2), (c_3, c_2), (d_1, d_2) and (e_1, e_2) for pre-adsorption, after adsorption of Pb (II), after adsorption of Cu (II), after desorption of Pb (II), and after desorption of Cu (II), respectively) adsorbents before adsorption, after adsorption and after desorption of heavy metal ions are presented in **Fig. 3.21.** The images were clearly able to evaluate the efficiency of the CA/TiO_2 adsorbents. As can be seen in **Fig. 3.21 (a_1),** there is no deposition of metal ions on the surface of the adsorbent matrixes as this image was taken before metal adsorption analysis. During the EDS elemental analysis **(Fig. 3.21 (a_1))**, Pb and Cu elements were not detected at all. On the other hand, deposition/occurrence of lead and copper ions was clearly observed in **Fig. 3.21 (b_1), (c_1)** after adsorption experiment. As discussed previously, the adsorbent had smooth morphological properties; it had a satisfactory surface area and porosity. Due to these favorable properties of the adsorbent, the metal ions were easily captured onto the surface of the fiber matrix within the adsorbents. The lea3.21 **(Fig. 5 (b_2))** and copper **(Fig. 3.21 (c_2))** elements were detected in the EDS analysis, which in turn confirmed the presence of the metal ions on the fibers of the matrix of the adsorbent. The FESEM images in **Fig. 3.21 (b_1), (c_1),** depicted the development of adsorbent-metal complex

ions on the surface of the adsorbent as clearly explains later. Accordingly, the FESEM results agreed with the experimental analysis, in which these adsorbents have shown high adsorption efficiencies for both the heavy metal ions. In the case of the desorption process, it is evidently shown from **Fig. 3.21 (d_1)** and **(e_1),** that the metal ions were desorbed successfully and a free fiber network was observed, unlike that of adsorbents morphological structures before desorption study. The elemental analysis strongly supported these results, where elements of Pb and Cu were not detected **(Fig. 3.21 (d_2), (e_2))**.

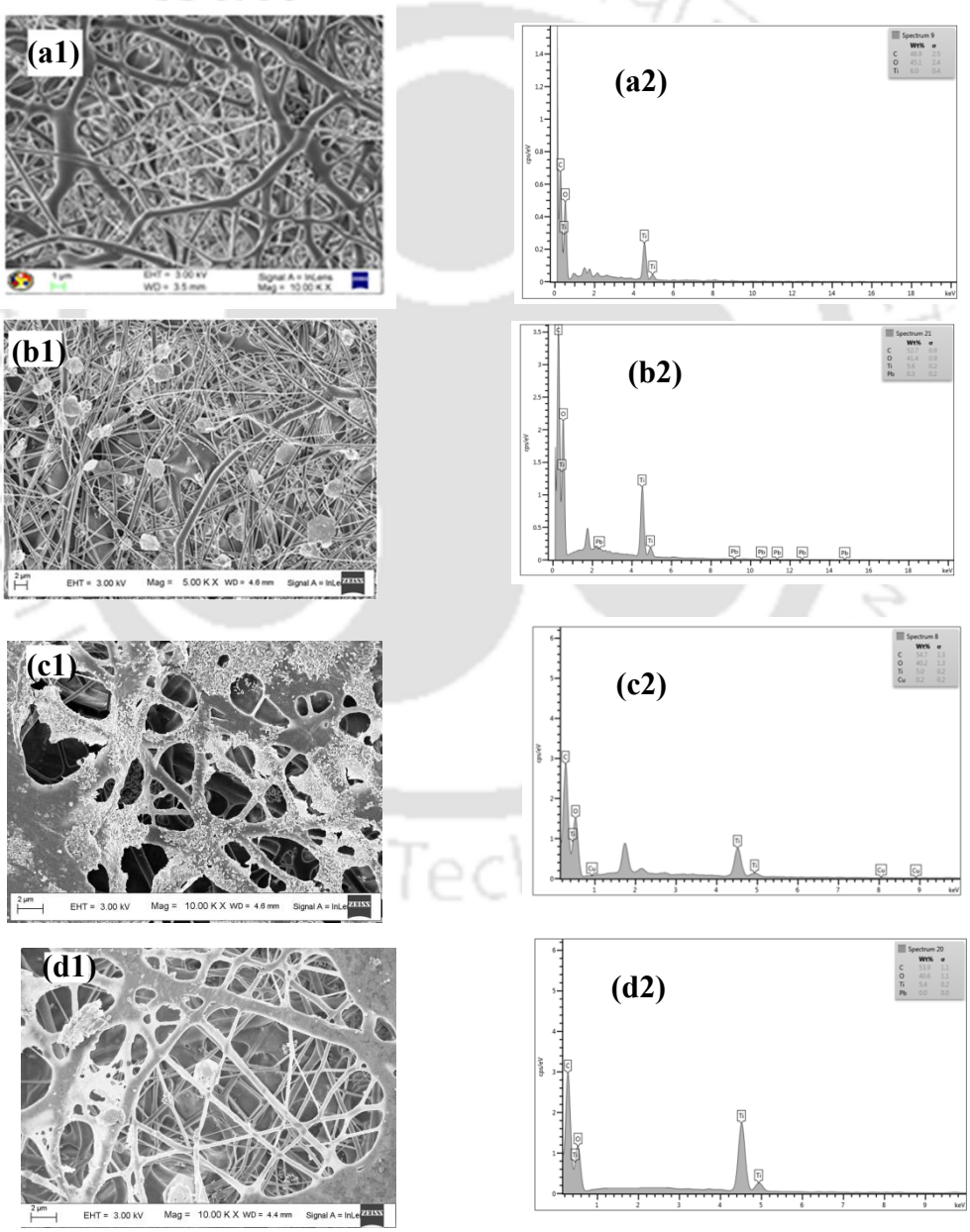

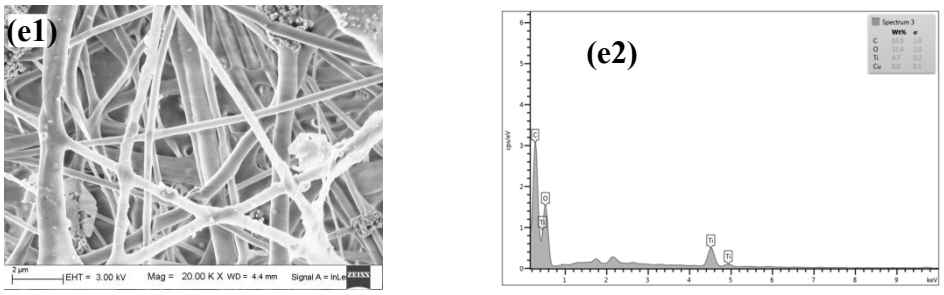

Fig. 3.21 FESEM and EDS images of (a_1, a_2) AM2 adsorbent, (b_1, b_2) after adsorption of Pb (II), (c_1, c_2) after adsorption of Cu (II), (d_1, d_2) after desorption of Pb (II), (e_1, e_2) after desorption of Cu (II).

3.3.1.6. Adsorption Study

Effect of contact time and temperature

The study of the effects of contact period of the synthetic solution and solid phase adsorbent is one of the significant factors for effective use of the adsorbent for practical applications in water treatments **[3, 69]**. The samples were shaken in an incubated shaker at 150 rpm for different times (30 to 300 min) with a known dosage of adsorbent at of 35 ^{o}C. The results of kinetic studies for the adsorption of heavy metal ions, Pb (II) and Cu (II) onto CA/TiO_2 are presented in **Fig. 3.22.** The concentration of copper and lead decreases rapidly within 30 min and the final concentrations of copper and lead ions after 5 h contact time were 0.15 mg/L and 0.55 mg/L, respectively. It is known that firstly all active area on the adsorbent surfaces had empty spaces and the concentration of the solution was high. When contact time was increased, the available active area on the adsorbent was decreased, and rate of adsorption was found to decrease slowly. Consequently, 5 h, contact time was chosen for all the equilibrium studies.

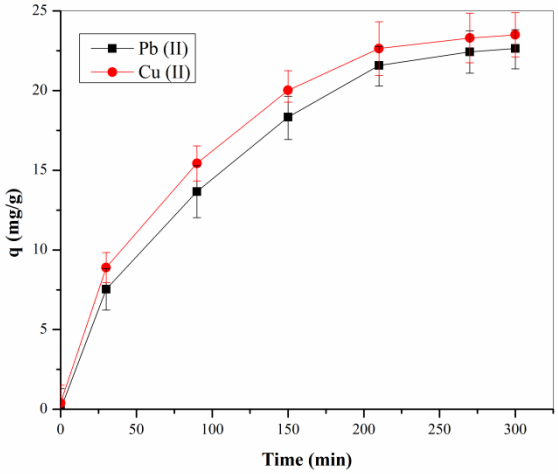

Fig. 3.22. Effect of contact time on the Pb (II) and Cu (II) ions adsorption onto CA/TiO_2 adsorbent.

Adsorption experiments were furthermore studied at different temperatures (25 ^{o}C to 55 ^{o}C). **Fig. 3.23** shows that Cu (II) ion removal efficiency rises quickly with rising temperature from 25 ^{o}C (84 %) to 35 ^{o}C and then maximum removal efficiency was attained (> 98%). This rise is because of the stepping up of some sluggish adsorption stages or because of the formation of a new empty active area on the surface of adsorbents. The removal efficiency of Pb (II) ion was almost similar for all the temperatures (> 99%), may be because of the adsorption of Pb (II) ion using CA/TiO_2 adsorbent is favorable at the given temperatures. Increasing of temperature hardly influenced the amount adsorbed ions at equilibrium, which shows that variation in temperature had less effect on adsorption of Pb (II) ions.

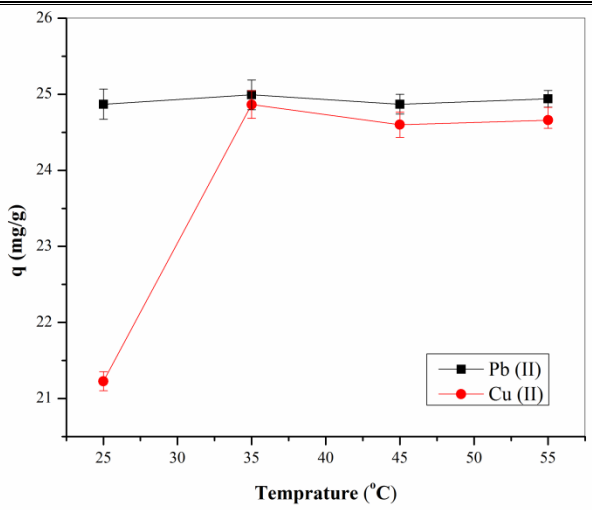

Fig. 3.23. Effect of temperature on the Pb (II) and Cu (II) ions adsorption onto CA/TiO_2 adsorbent.

Effect of pH

To study the adsorption capacity of the adsorbents, the initial pH value of the solution is an important factor. Therefore, optimization of the pH value is required. The procedure of cation exchanges among adsorbent surface, and the heavy metal cations comprising solutions are greatly dependent on the pH values of the intermediate. Therefore, the adsorptions of Pb (II) and Cu (II) were investigated at various pH values alternating from highly acidic to neutral (pH=1.0 to 7.0). For comparison purpose, the adsorbent was tested at pH of 8 and 9. The influence of pH on the adsorption efficiency of metals is presented in **Fig. 3.24 (a)**. The adsorption occurred slightly at low pH values (up to pH= 1.0 to 3.0), beyond this pH level (between 3.0 and 5.0), the quantity of lead and copper ions adsorption on the CA/TiO_2 adsorbent was improved. With further increasing the pH level of the solutions, the adsorption develops significantly and maximizes at pH of 5.2 and 5.8 for both lead and copper ions, respectively. As the pH rises beyond 7, the TiO_2 surface −OH groups suggested making the adsorbent surface more negatively charged. These results were confirmed by analyzing the zeta potential (ζ) values of the solids, and the results are presented in **Fig. 3.24 (b)**. As clearly observed from the figure, at low pH (1-3) values, the surface of the adsorbent had positive charges. However, as the pH values were raised beyond 3, the surfaces of the solids were negative. High negative ζ values were attained

with further increase in the pH values to 8 and 9. These results are accredited to an increase in the amount of –OH groups in the solid barrier due to alkaline nature of the solutions. Accordingly, the metal ions with positive charges easily interact with the adsorbent surface. This condition helps to continue the adsorption process of the adsorbent since the competitions among H^+, and heavy metal ions are reduced **[71, 123]**. Kim et al. **[123]** have suggested that the monodentate inner-sphere-type surface complexation is the possible mechanism of the elimination of Pb (II) ions by using TiO_2. The possible mechanisms for copper and lead in this study are suggested as:

$$Ti{-}OH + Pb^{2+} \leftrightarrow Ti - O - Pb^{+} + H^{+} \quad \textbf{(3.4)}$$

$$Ti{-}OH + Cu^{2+} \leftrightarrow Ti - O - Cu^{+} + H^{+} \quad \textbf{(3.5)}$$

However, upon further increase in the pH level of the solution, an acceptable removal of metal ions was observed. At high pH (alkaline solutions), the metal cations start to react with hydroxide ions to form metal hydroxide and get precipitated **[124]**. Since the adsorbent used for this study was highly porous, the heavy metal hydroxide precipitates can easily be adsorbed or captured on the surface as well as a depth channel of the adsorbent. Precipitation of each copper and lead ions in their solution as hydroxides was starting to rise at higher pH values (i.e. >7) **[125].**

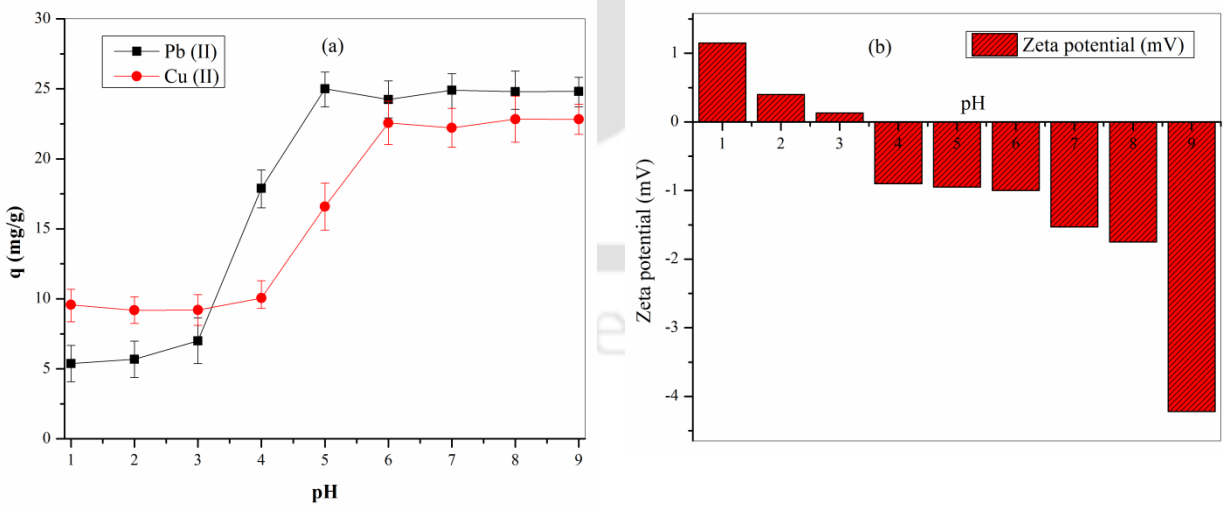

Fig. 3.24. Effect of pH (a) on the Pb (II) and Cu (II) ions adsorption onto CA/TiO_2 adsorbent and (b) on zeta potential values of the adsorbent

Effect of TiO_2 amount

The effect of TiO_2 content percentage on adsorption capacities or removal efficiencies of copper and lead ions onto CA/TiO_2 adsorbent was investigated. The adsorbents with various quantities of TiO_2 nanoparticles (0, 1.0, 2.5, 4.5 and 6.5 wt. %) are designated as AM0, AM1, AM2, AM3, and AM4, respectively. The removal efficiency of lead and copper ions by using CA/TiO_2 adsorbents are shown in **Fig. 3.25**. As presented in **Fig. 3.25**, the adsorption capacity of Pb (II) and Cu (II) ions rise with the increase of TiO_2 nanoparticles from 0 to 2.5 wt. %. This rise is because of the improved specific surface area of the adsorbent (as discussed in **Section 3.3.1.4.)**. An additional increase in TiO_2 amounts caused a reduction in the removal efficiency of the adsorbent. In the case of the Pb (II) ion, the removal efficiency of all the adsorbents showed a higher removal percentage, though the slight decrease was observed for TiO_2 contents of 4.5 and 6.5 wt. %. Because of the accumulation and thickening of TiO_2 nanoparticles, this decrease in removal efficiency for both metal ions is observed which in turn diminishes the existing specific surface area and porosity of the adsorbent. Moreover, the agglomeration of nanoparticles causes difficulty to the Pb (II) and Cu (II) ions to diffuse within the internal and surface pores of the adsorbent matrix. As shown in **Fig. 3.25,** maximum removal of 99.7 % and 98.9 % were attained for lead and copper ions, respectively, by using AM2 (2.5 wt. % of TiO_2 nanoparticles). Whereas 86.3 % removal efficiency for Pb (II) at pH ranging from 4.5-5.0, adsorbent dose 0.5 g/L, initial concentration 30 mg/L and equilibrium time 90 min was reported by **[126]** and less selectivity for Cu (II) ion at pH of 3.4, initial concentration 50 mg/L and adsorbent dose 2 g/L was reported by **[127]**. (Adsorption capacities of Pb(II) and Cu(II) for some adsorbents reported in the literature is presented in **Table 3.6)**. Comparatively, for the CA adsorbents without TiO_2, the corresponding removal efficiencies are 65.7 % and 70.5 % for Cu (II) and Pb (II), respectively, thereby confirming the efficiency of TiO_2 nanoparticles to enhance heavy metal adsorption.

Table 3.6 Adsorption capacities of Pb (II) and Cu (II) for some adsorbents reported in the literature

Adsorbent	Adsorption capacity (mg/g)		
	Pb (II)	**Cu(II)**	**Refs.**
CA/TiO_2	25.0	23.0	**Present study**
CA/PMMA	-	3.0	**[2]**
Cellulose/chitin	<19.0	19.2	**[128, 129]**
CA/zeolite	-	28.6	**[1]**
Sawdust	3.8	-	**[33]**

Therefore, CA/TiO_2 (2.5 wt. % of TiO_2) adsorbents were chosen for the next step of the adsorption study in which this result agreed with the theoretical conclusion of BET surface area analysis (**Section 3.3.1.4.**).

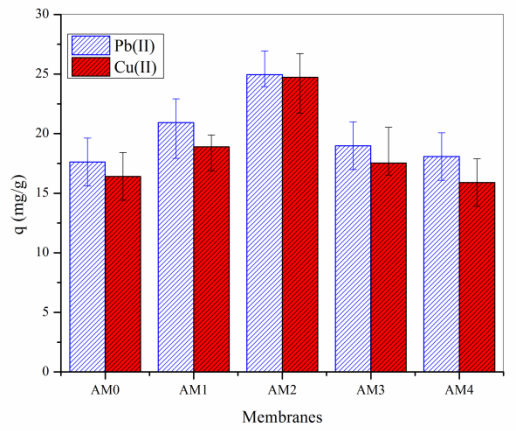

Fig. 3.25. Effect of TiO_2 nanoparticles amount on removal efficiency of Pb (II) and Cu (II) ions

3.3.1.7. Adsorption isotherms

For this work, three well-known adsorption models, viz., Freundlich, Langmuir **[130, 131]** and Dubinin–Radushkevich (D–R) **[131]** were investigated to analyze the equilibrium data of Pb (II) and Cu (II) metal ions. In Langmuir model, the adsorption mechanism is based on the physical phenomenon in which the highest adsorption capacity involves of a mono-layer adsorption, where the energy of adsorption is constant; the surface is energetically uniform, and no interaction between neighboring adsorbed molecules. Therefore, the heat of adsorption is constant through the fractional superficial coverage. All adsorptions occur by the same

mechanism and result in the same adsorbed structure.The general equation of the Langmuir isotherm is **[132]:**

$$q_e = \left[\frac{q_{\max} b C_e}{(1 + b C_e)} \right] \quad \textbf{(3.6)}$$

The linear form **Eq. (3.6)** can be written as:

$$\frac{C_e}{q_e} = \left(\frac{1}{q_{\max} b} + \frac{C_e}{q_{\max}} \right) \quad \textbf{(3.7)}$$

Where C_e (mg/L) is the equilibrium metal ion concentration; q_e (mg/g) is the amount of heavy metal ions adsorbed per unit mass of adsorbent (mg/g) at equilibrium; q_{max} (mg/g) is the highest quantity of the metal ions per unit mass of adsorbents to develop a complete mono-layer, and b (L mg^{-1}) is the Langmuir constant related to the affinity of binding sites.

The Freundlich equation has been commonly used for isothermal adsorption and is dependent on a heterogeneous surface adsorption. It was derived empirically in 1912, and it is defined by the following equation **[130]:**

$$q_e(x/m) = \left[K_f \left(C_e \right)^{\frac{1}{n}} \right] \quad \textbf{(3.8)}$$

The linear form can be written as:

$$\log q_e = \left[\log K_f + \frac{1}{n} (\log C_e) \right] \quad \textbf{(3.9)}$$

Where *x/m* is the weight of contaminants adsorbed per unit weight of adsorbents (mg/g), n and K_f (mg/g) $(mg/L)^n$ are the intensity parameter and Freundlich capacity factor of the adsorbent, respectively. The adsorption isotherms data of Pb (II) and Cu (II) were generated at pH of 5.2 and 5.8, respectively, for 300 min using 100 mg of CA/TiO_2 (AM2) adsorbent at 35 °C. The results of adsorption model from linear plots are given in **Fig 3.26.** All the parameters were computed by using the three isotherm model equations and the R^2 values **(Table 3.7)** for Freundlich (a), Langmuir (b) and D-R (c) isotherms were compared. The results from Freundlich isotherm revealed that the *1/n* values for both metals were not laid between 0 and 1. This result clearly indicates that the adsorptions of various metal ions using CA/TiO_2 adsorbents were not favorable for Freundlich. Therefore, by looking at the R^2 values **(Table 3.7)** of the Freundlich (R^2 > 0.85, 0.91), Langmuir (R^2 > 0.98, 0.99), and D-R (R^2 > 0.44, 0.52) models, the Langmuir

isotherms model was well-fitted with the experimental data of both metal ions (Cu (II) and Pb (II), respectively) as compared to D–R and Freundlich isotherm models. The Langmuir isotherm model applicability for CA/TiO_2−metal ion adsorption process suggests that the monolayer adsorption condition exists in the experimental condition.

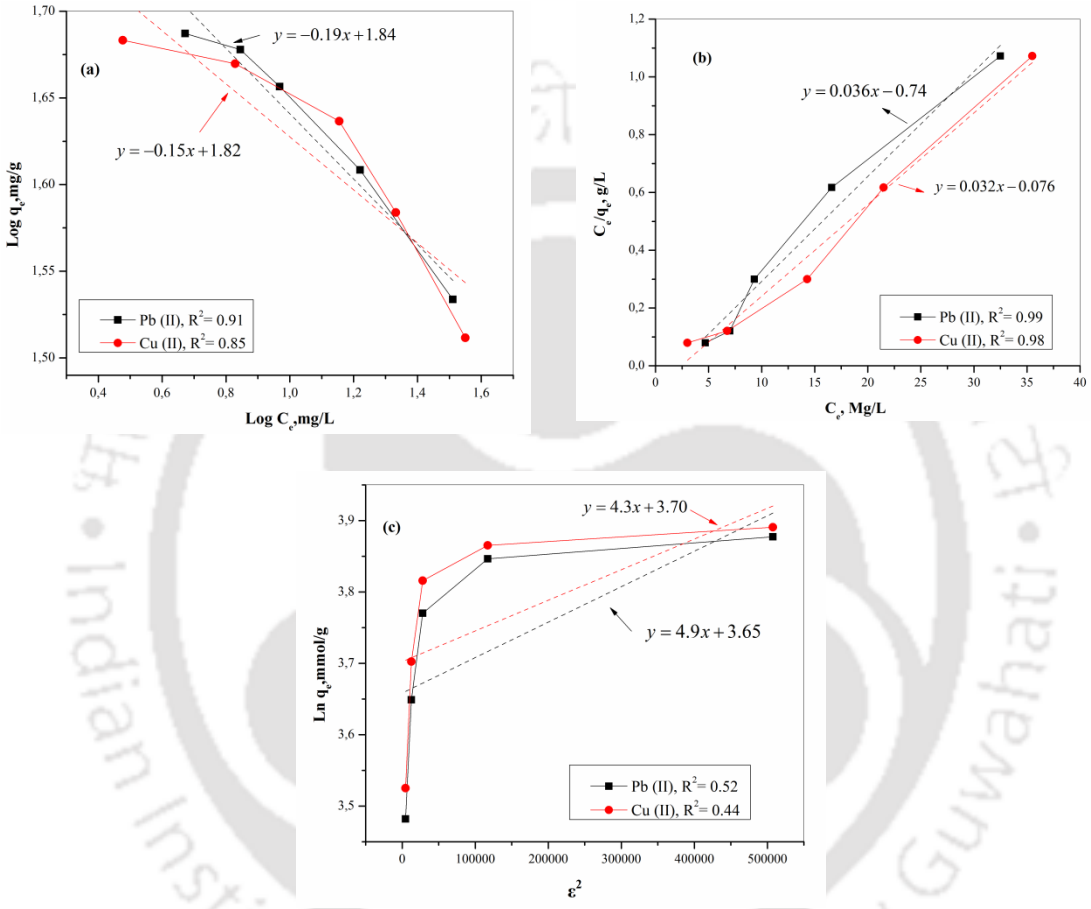

Fig. 3.26. Adsorption model: (a) Freundlich (b) Langmuir (c) D-R plots for copper and lead adsorption onto the adsorbent.

The D–R adsorption model is more general than the Langmuir model and is used to show the adsorption method through a Gaussian energy distribution on a heterogeneous surface **[131]**. The common form of the D–R isotherm model equation is stated as:

$$q_e = \left[q_{DR} \exp\left(-K_{DR}\varepsilon^2\right) \right] \qquad \textbf{(3.10)}$$

The linear form can be rewritten as:

$$\ln q_e = \left[\ln q_{DR} + \left(-K_{DR}\varepsilon^2\right)\right] \quad \textbf{(3.11)}$$

Where q_e is the quantity of metals adsorbed on the adsorbent surface per unit mass of adsorbents (mmol g^{-1}); q_{DR} is the highest adsorption capacity (mmol g^{-1}); ε is the polanyi potential (ε = RT ln(1 + 1/*Ce*)); K_{DR} is the activity coefficient associated with adsorption free energy ($mol^2\ J^{-2}$); T is the absolute temperature (K), and *R* is the gas constant (8.314 J $mol^{-1}\ K^{-1}$). A fixed volume of adsorption space near to the adsorbent surface and the presence of an adsorption capacity of these sites are assumed by the Polanyi adsorption theory.

Table 3.7 The three isotherms model parameters for metal adsorption onto CA/TiO_2 adsorbent

Metal ion	**Freundlich isotherm**		**Langmuir isotherm**		**D-R isotherm**	
	K_f,(mg/g)(mg/L)^n	R^2	$q_{max,}$ mg/g	R^2	q_{DR}, mmol/g	R^2
Pb (II)	6.12	0.91	31.9	0.99	38.55	0.52
Cu (II)	5.90	0.85	31.4	0.98	38.75	0.44

The results of four phases of adsorption and desorption of copper and lead metal ions onto the CA/TiO_2 adsorbents were examined. As shown in **Fig. 3.27 (a),** the adsorption efficiencies of the adsorbents for those heavy metal ions were slightly declined with increasing adsorption desorption phases. This slight decreasing in adsorption capacity of the adsorbent might be because of losing a certain functional-groups and/or Ti leaching of the adsorbents through the acid cleavages, and some of the adsorbent pores may be blocked. However, as seen from **Fig. 3.27 (b)** the TiO_2 leaching tendency due to the acid cleavage during the desorption process was negligible. There were no obvious characteristic peaks for the AM2 adsorbent before adsorption took place. Nevertheless, after the adsorption of those heavy metals onto the adsorbent absorption peaks were observed at about 323 nm and 327 nm for Pb (II) and Cu (II) ions, respectively. This confirms the formation of adsorbent metal ion complexion due to an efficient adsorption. The absorption peak for TiO_2 NPs was observed for all the samples at around 385 nm. On the other hand, no metal ion peaks were observed after the desorption process using HNO_3 acid and similar graphs with the AM2 adsorbent were detected. Therefore, the outcomes indicated that the CA/TiO_2 adsorbents could repeatedly be recycled without showing substantial damage in adsorption efficiency. The decreasing in the adsorption

efficiencies was not significant when compared with the control. Moreover, the FESEM images in **Fig. 3.21 d_1** and **e_1** confirmed that the morphological structure of the adsorbent was not disturbed during the recycling procedure.

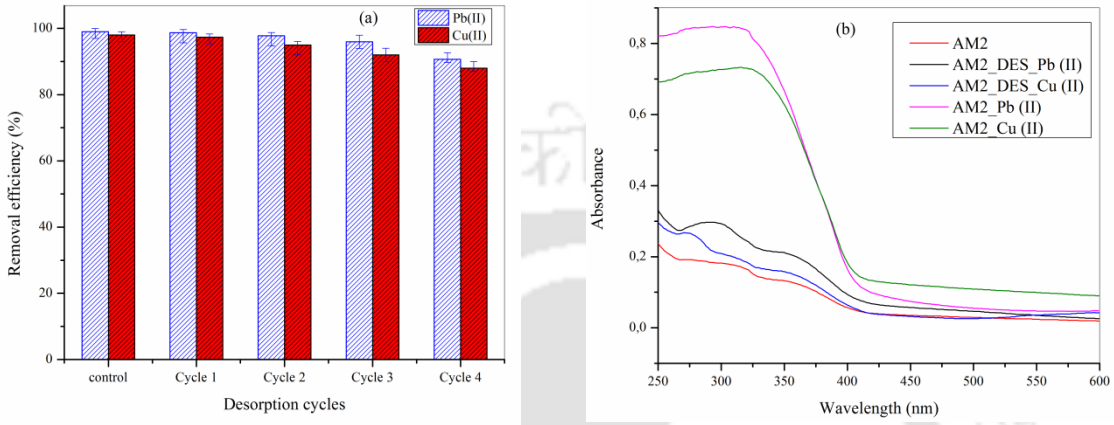

Fig. 3.27 (a) Adsorption-desorption cycles, (b) UV–vis absorption spectra of before and after adsorption and after desorption of AM2 adsorbent

3.3.1.8. Adsorption kinetics

Adsorption kinetics study is one of the most vital parameters of the adsorption study. Because the mechanisms of the adsorption processes can be modeled by using kinetic models **[133]**. Therefore, the experimental results were analyzed using the two kinetic models called pseudo- first-order and pseudo- second-order using the kinetic equations as follows **[134-136]**:

Pseudo- first-order:

$$q_t = q_e(1-\exp(-k_1 t)) \qquad \textbf{(3.12)}$$

The linear form of first order kinetic can be rewritten as:

$$\log(q_e - q_t) = \left[\log q_e - \left(\frac{k_1}{2.303}\right)t\right] \qquad \textbf{(3.13)}$$

Where, q_e and q_t (mg/g) are the adsorption capacities at equilibrium time and at time t, respectively; k_1 (min^{-1}) is the pseudo- first-order model rate constant. The constant of the pseudo-first-order kinetic model was found using a linear regression of $log\ (q_e - q_t)$ versus t, and the results are presented in **Table 3.8**.

Pseudo- second-order:

$$q_t = \left[\frac{k_2 q_e^2 q_t}{(1 + k_2 q_e t)} \right] \quad \textbf{(3.14)}$$

The linear form of second-order kinetic can be written as:

$$\frac{t}{q_t} = \left(\frac{1}{k_2 q_e^2} + \frac{t}{q_e} \right) \quad \textbf{(3.15)}$$

Where k_2 (g/ mg min^{-1}) is the second-order adsorption rate constant. The plots of t/q_t versus t were employed to calculate the constants of the pseudo- second-order kinetic model. The graphs for both kinetic models are shown in **Fig. 3.28 (a** and **b)** and the pseudo- second-order kinetic model parameters are given in **Table 3.8**. As indicated in **Table 3.8**, the pseudo- second-order equation fitted-well with the experimental data of both copper (R^2 = 0.99) and lead (R^2 = 0.99). Since the CA/TiO_2 adsorbents employed in this experiment have relatively high equilibrium adsorption, the adsorption could be very fast and thus the equilibrium time may be short. Due to this short equilibrium time together with high adsorption capacity, a high degree of affinity between the metal ions and the CA/TiO_2 adsorbents is indicated. On the other hand, the pseudo-first-order kinetic model fitted the experimental results poorly.

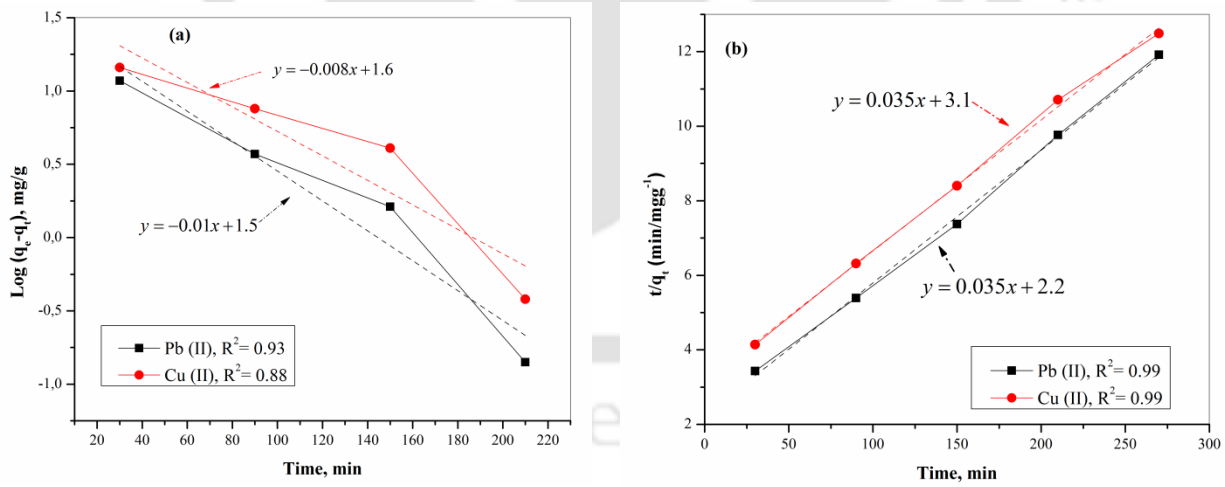

Fig. 3.28. Adsorption kinetics: (a) Pseudo- first-order and (b) Pseudo- second-order plots for copper and lead adsorption onto the adsorbent.

Table 3.8 Kinetic parameters of metal adsorption onto the CA/TiO_2 adsorbent

Metal ion	q_{exp}	Pseudo--first-order model			Pseudo--second-order model		
	(mg/g)	q_e (mg/g)	k_1 (min^{-1})	R^2	q_e (mg/g)	k_2 (g/mg min)	R^2
Pb (II)	20.5	5.40	0.0362	0.93	28.09	0.00057	0.99
Cu (II)	22	4.75	0.0193	0.88	33.11	0.00026	0.99

3.3.2. Summary

The characterization and adsorption study of the CA/TiO_2 adsorbent were done successfully in this work.

- The specific surface areas of the adsorbent were increased from 30.2 to 48.47 m^2g^{-1} as the amounts of TiO_2 nanoparticles in the adsorbent matrix were increased from 0 to 2.5 wt. %.
- The highest removal efficiencies of lead and copper ions with CA/TiO_2 adsorbent were estimated to be 99.7 % and 98.9 % under the optimized conditions of TiO_2 amounts (2.5 wt. %), pH (5.2 for Pb (II) and 5.8 for Cu (II), respectively), agitation period (5 h), adsorbent dosage (2 g/L) and temperature (35 °C).
- The Langmuir isotherm (R^2 >0. 98 for copper and > 0.99 for lead) model was well fitted to the equilibrium data of both metal ions than D–R and Freundlich isotherms.
- The adsorption experimental data agreed perfectly with the pseudo- second-order kinetic equation where the regression coefficients were greater than 99 % (R^2 > 0.99) for both copper and lead ions.
- Repeated adsorption–desorption experiments after four phases revealed that CA/TiO_2 adsorbent showed high elimination capacity for copper and lead ions. The CA/TiO_2 adsorbent provided in this study can be employed for the applied treatment of heavy metal contaminated water.

Chapter 4

Preparation, characterization, and application of phase inverted cellulose acetate membranes

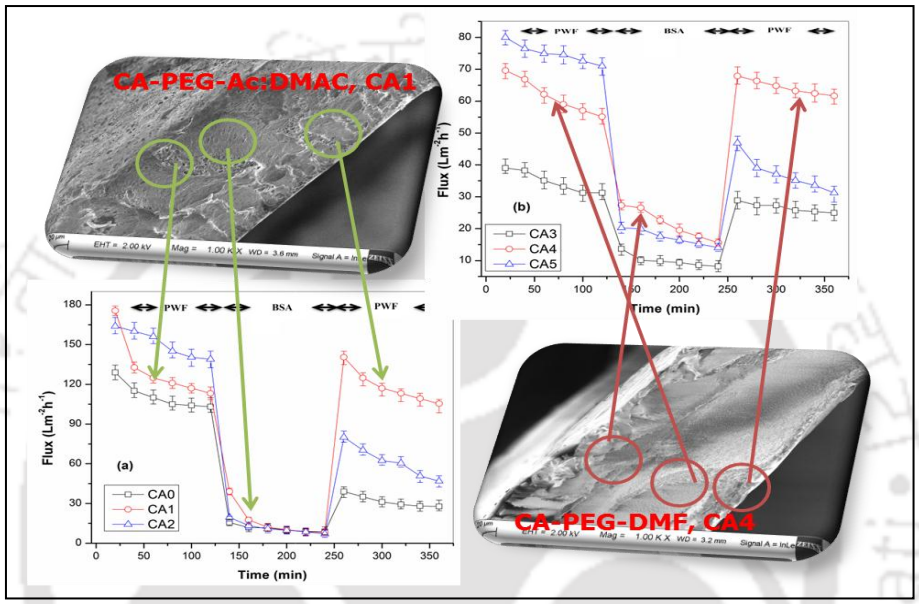

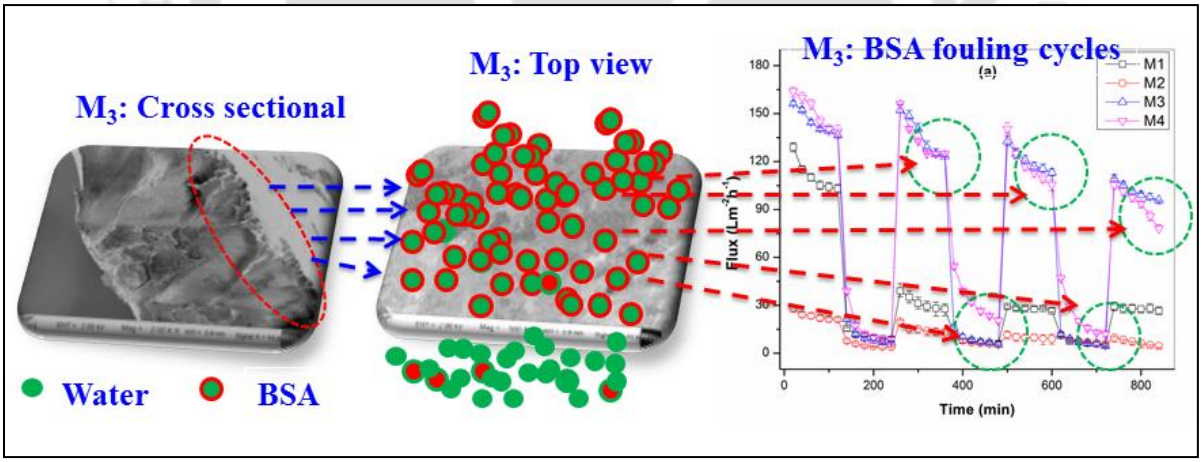

Chapter 4: Preparation, characterization, and application of phase inverted membranes

This chapter presents the investigation on the effects of additives and solvents in the characteristics and performances of cellulose acetate (CA) ultrafiltration membranes. The effects of two different hydrophilic additives and two solvents on the membrane morphological structure, permeability property and anti-fouling performances of cellulose acetate (CA) ultrafiltration membranes were investigated. During the phase-inversion process polyethylene glycol (PEG) and polyvinyl pyrrolidone (PVP) were used as additives; and acetone (Ac): N, N-Dimethylacetamide (DMAc) and N, N-Dimethylformamide (DMF) were used as solvents. The experimental studies of fouling/rinsing cycles, rejection, and permeate fluxes were used to investigate the effect of PEG and PVP additives and effect of the two solvents on the fabricated membranes using bovine serum albumin (BSA) as a model protein.

Secondly, Modified cellulose acetate (CA) membranes were prepared by dissolving the polymers in a mixture of acetone (AC) and N, N-dimethylacetamide (DMAc) (70:30) solvent. Effects of PEG additive and TiO_2 NPs on the preparation of phase-inverted CA ultrafiltration membrane were investigated in terms of morphology, equilibrium water content (EWC), pure water flux (PWF), hydraulic resistance, thermal stability, water contact angle (WCA) and anti-fouling performance.

Thirdly, fouling resistant ultrafiltration membranes based on the blends of PVP, TiO_2 nanoparticles and cellulose acetate, CA-PVP-TiO_2 (CATP), for removal of bovine serum albumin (BSA) were prepared by using phase inversion process. BSA protein removal efficiency, anti-fouling performance, and recycling potential of the UF membranes were investigated.

These works are published in the following journals

1. Kibrom Alebel Gebru, Chandan Das "Effects of solubility parameter differences among PEG, PVP and CA on the preparation of ultrafiltration membranes: Impacts of solvents and additives on morphology, permeability and fouling performances", ***Chinese Journal of Chemical Engineering, DOI: 10.1016/j.cjche.2016.11.017***

2. Kibrom Alebel Gebru, Chandan Das "Preparation and characterization of phase inversion CA –PEG-TiO_2 membranes: Effect of PEG and TiO_2 nanoparticles on the permeability properties and anti-fouling performance", ***Journal of Membrane Science and Research, 3 (2017) 90-101***

3. Kibrom Alebel Gebru, Chandan Das, "Removal of bovine serum albumin from wastewater using fouling resistant ultrafiltration membranes based on the blends of cellulose acetate, and PVP-TiO_2 nanoparticles", ***Journal of Environmental Management, 200 (2017) 283-294***

4.1. Effects of solubility parameter differences among PEG, PVP and CA on the preparation of ultrafiltration membranes: Impacts of solvents and additives on morphology, permeability and fouling performances

The effects of two different hydrophilic additives and two solvents on the membrane morphological structure, permeability property and anti-fouling performances of cellulose acetate (CA) ultrafiltration membranes were investigated. During the phase-inversion process cellulose acetate was selected as membrane forming polymer; polyethylene glycol (PEG) and polyvinyl pyrrolidone (PVP) were used as additives; acetone (Ac): N, N-Dimethylacetamide (DMAc) and N, N-Dimethylformamide (DMF) were used as solvents; and deionized (DI) water was used in the coagulation bath. All the prepared membranes were characterized in terms of hydraulic permeability (Pm), membrane resistance, average pore radius, and hydrophilicity. The top surface and cross-sectional view of the prepared membranes were also observed by using field emission scanning electron microscopy. Membrane fouling and rejection experimentations were done using a stirred batch-cell filtration set-up. The experimental studies of fouling/rinsing cycles, rejection, and permeate fluxes were used to investigate the effect of PEG and PVP additives and effect of the two solvents on the fabricated membranes using bovine serum albumin (BSA) as a model protein.

4.1.1. Results and discussion

4.1.1.1. Morphological study

The FESEM images of (a) top layer surface view and (b) the cross-sectional view of the prepared membranes by dissolving the polymer and additives in two different solvents (DMF and Ac: DMAc) are presented in **Fig. 4.1**. As clearly shown from the figures, the prepared membranes are asymmetric in structures comprising a porous sublayer and a dense top layer for all types of the membranes (i.e. for CA/DMF and CA/Ac: DMAc). The sublayer portion of the membranes without additives (CA0 and CA3) seems to have finger-like voids as well as macro-

void structures. According to the literature, there are so many parameters, such as evaporation step **[137]** and coagulation bath temperature (CBT) **[53]** that allow to the development of macro-voids during membrane formation using immersion precipitation process. The development of macro-voids happen under rapid precipitation condition, and the precipitations are quicker at higher coagulation temperatures. In the current study, the coagulation bath temperature and evaporation step (i.e. before immersion) are fixed to 25ºC and 30 s, respectively, during the preparation of all the membranes. Another important factor which affects the formation or suppression of macro-voids is the type of de-mixing which occurred during the phase separation process. Furthermore, the instantaneous de-mixing and the delayed de-mixing depends on the mutual affinity of the non-solvent and solvent in the ternary system **[40]**. The solvents used in this study (DMF and Ac: DMAc) have a high mutual affinity with water. Therefore, apparently, the formation of the finger-like voids and macro-voids in the sublayer of the membranes without additives is due to the instantaneous de-mixing. On the other hand, when the polymeric additives are added to the ternary (polymer/solvent/non-solvent) system the formations of macro-voids are suppressed for membrane prepared using PEG (i.e. CA1 and CA4). However, for membranes prepared using PVP the formation of some macro-voids are still maintained (i.e. CA2 and CA5). However, the formation of microporous structures was observed for both the additives. In a quaternary system (polymer/solvent/non-solvent/additive), nevertheless, the exchange process of water and solvent between the coagulation bath and the casting solution taking place right upon immersing is considerably faster than the separation of the two polymers. However, after some instants of immersion process, polymer-polymer movement may occur. This is because of the separation of the two polymers (membrane forming and additive) that involves the movement of one polymer with respect to the other **[138]**. Therefore, a binary phase arises from the phase separation, where one involves of the CA (i.e. membrane-forming polymer), Ac: DMAc/DMF (i.e. solvents) and non-solvent (i.e. water) and the second contains the polymer additives (i.e. PEG or PVP), solvents (i.e. Ac: DMAc or DMF) and non-solvent (i.e. water). The membrane forming polymer and additives have a driving force to separate completely into a CA-rich and a PEG-rich or PVP-rich phase. Consequently, the type of de-mixing process is this case can be influenced by the diffusion/movement of the two polymers on each other. Therefore, this phenomenon should be slow compared to the diffusion of solvent and non-solvent in the polymer

solution. To maintain this, a polymeric additive with a certain minimum molecular weight in the system is required **[139]**.

Effect of additives

The introduction of hydrophilic additives which are soluble in the non-solvent (i.e. water) with high affinity to the solvents and low affinity to the membrane forming polymer, tends to increase the thermodynamic instability of the casting film which further leads to instantaneous de-mixing to occur in the coagulation bath. This result encourages the development of macro-voids in the membrane structure. On the other hand, the presence of the polymeric additives increases the concentration/viscosity of the casting solution which may diminish the diffusional exchange rate of the solvent and non-solvent during the membrane formation process. Consequently, this may hinder the instantaneous liquid-liquid de-mixing process which suppresses the development of macro-voids **[50, 53, 140]**. It is evidently clear from the figures that the finger-like voids in the sublayer are considerably reduced with the adding of polymeric additives (PEG and PVP) for both solvents. Particularly, for CA/Ac: DMAc/PEG scheme (CA1) and CA/DMF/PEG (CA4), the membranes are found to have almost macro-void free cross-sectional structures. On the other hand, the CA/Ac: DMAc/PVP system (CA2) and CA/DMF/PVP system (CA5) membranes showed the development of some finger-like and macro-voids. These results lead to the conclusion, although the instantaneous de-mixing is yet continued, the effect of those additives has considerable part on the suppression or development of macro-voids. The FESEM images of the top view of all the prepared membranes are presented in **Fig. 4.1 (a)**. Some of the open pore structures developed in the membranes are formed by nucleation and development of the polymer-lean phase in the metastable area between the bi-nodal and the spinodal curve **[139, 141]**. Nevertheless, the top layer structure of the ultrafiltration membrane frequently doesn't reveal an open pore structures and not a completely uniform gel-layer, which is stated as a nodular structure. The development of nodular structures can't be described by nucleation of the polymer lean part. It is also not common that nucleation of the polymer-rich part happens because this only occurs at initially low polymer concentrations, below the critical point. A possible explanation for the formation of a nodular structure on the top surface of the membranes could be due to the spinodal de-mixing because the diffusion process throughout the development of the top layer is faster for the homogenous system to

develop greatly unstable and crosses the spinodal curvature **[43, 139]**. The top surface with improved inter-connected pores structures is observed more prominently in the case of PEG (i.e. CA1) which is attained because of the spinodal decomposition. Therefore, the inter-connected pores may be regarded as a continuous CA-lean (PEG-rich) phase tangled by a constant CA- rich (PEG-lean) phase which produces membrane with a uniform matrix. On the other hand, in the case of PVP (CA2), a non-uniform pore structure was observed. However, the remaining membrane surfaces (i.e. CA0, CA3, CA4, and CA5) depicted dense top surface structures.

Effect of solvents

The effects of solvent: non-solvent and solvent: polymer interactions are also very important parameters on the final morphological structures of the membranes. Therefore, the tendency of mixing of the solvent with non-solvent, the degree of swelling of the pure polymer in the non-solvent and the solubility of the membrane forming polymer in the solvent should be considered during the investigation of the effect of different parameters on the final structure of the membranes. From the FESEM images, **Fig 3.4 (b)**, it is clearly observed that the macro-void formation in the CA/DMF system is greater than Ac: DMAc system. This can be due to the transition from instantaneous to delayed onset of de-mixing attained by changing the type of solvents**[44, 138]**, which is also complemented by the diminishing of development of macro-voids. The miscibility of the solvent: non-solvent mixture, employed for the preparation of the membranes, has a significant effect on the final structure of the membrane **[141].** According to Reuvers et al. **[142]**, the delay time for the onset of liquid-liquid de-mixing increases with decreasing the tendency of mixing solvent with the non-solvent. The current observations are completely in agreement with these explanations that the absence or less macro-voids formation in the case of Ac: DMAc/CA system is due to the delayed onset of de-mixing. On the other hand, development of macro-voids or finger-like cavities is observed for DMF/CA systems. These results are because DMF has greater tendency of miscibility with water than that of Ac/DMAc and therefore the instantaneous de-mixing occurs which is responsible for the formation of macro-voids. The effect of these solvents can be explained from another point of view that the top layer thickness of the cross-sectional views depicted a visible difference. Therefore, the delayed and instantaneous de-mixing processes can affect the top layer surface of the finally prepared membrane. In this case, the membrane formed from DMF/CA system gives membranes

with relatively lesser top layer thickness than the membranes prepared using AC: DMAc/CA system. However, the total thickness of the AC: DMAc/CA membranes are lesser than DMF-CA system membranes as seen from **Table 4.1**. It is clear that a thicker top layer is due to the delayed onset de-mixing during the phase separation. One point which should be clarified here is that the delayed de-mixing, in this case, is not extended delayed de-mixing. Normally, if the delayed de-mixing is extended, the polymer film thickness will decrease considerably which may cause a decrease in the porosity of the sublayer membranes **[142]**. This result may further prevent the formation of interconnected pore structures which in turn can form membranes with homogenous and with dense layer structure. However, for the membrane prepared from Ac: DMAc/CA system (CA0, CA1, and CA2) the pores in the sublayer are interconnected due to the development of aggregates associated with the gelation of sublayer. Therefore, the resistance of the sublayer of these membranes is much lower than that of membranes could prepare from extended delayed de-mixing (dense membranes).

4.1.1.2. Pure water flux and hydraulic permeability

Effect of additives

The study of compaction factor (CF) is very important to understand the pore structures of the membranes specifically the membrane sublayer structure. Membranes with high CF implies that they are highly compacted which may, in turn, indicate the availability of a large number of macro-voids or finger-like arrangements in the membrane's sublayer structure. Therefore, the impacts of compaction time on PWF of the prepared membranes are depicted in **Fig. 4.2**. All the membranes prepared using both solvents (Ac: DMAc and DMF), and both additives (PEG and PVP) are presented in **Fig. 4.2(a) and (c)**, respectively. The PWF of all the membranes was observed to decline slowly with time because of the compaction, and finally, the steady state fluxes were reached after 80 min. This gradual decrease in PWF results can be explained due to the compaction of pore walls (attain a uniform and denser structures) causing the pore size and the flux to decrease **[40]**.

(a) **(b)**

CA0

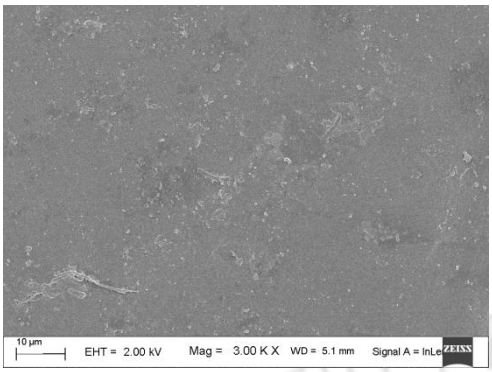

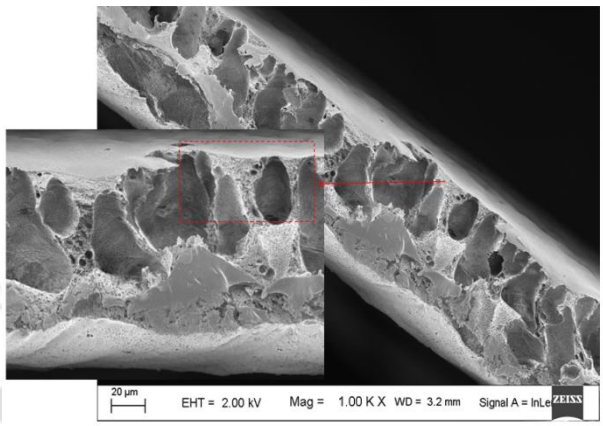

CA1

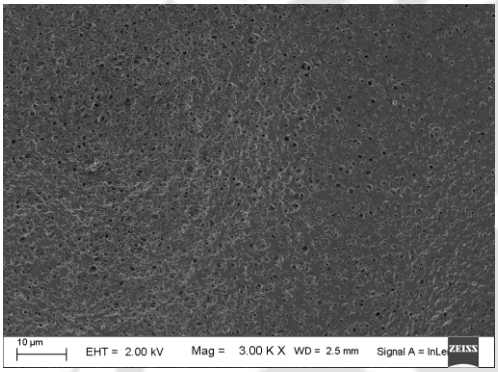

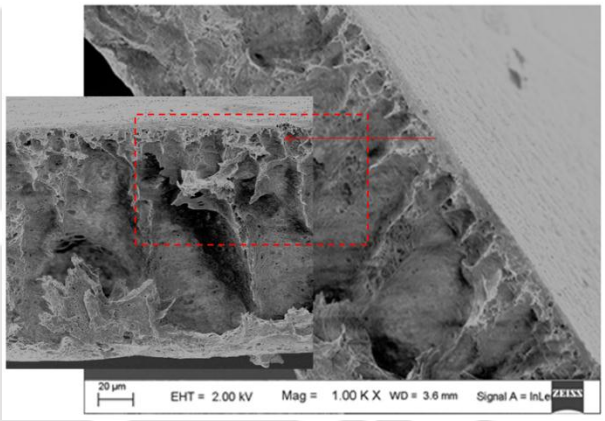

CA2

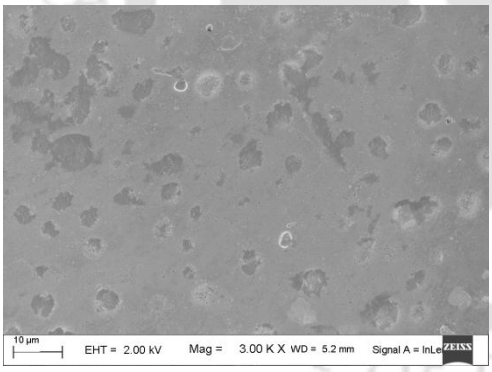

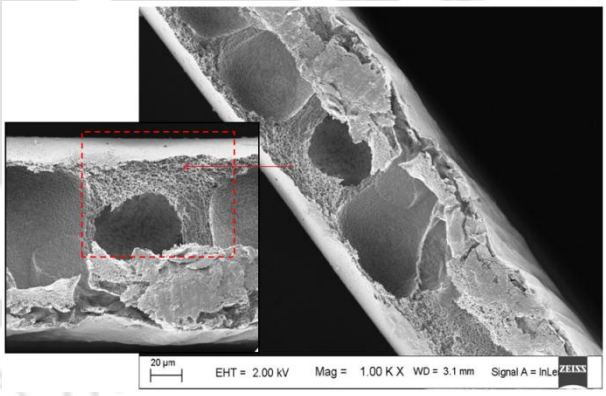

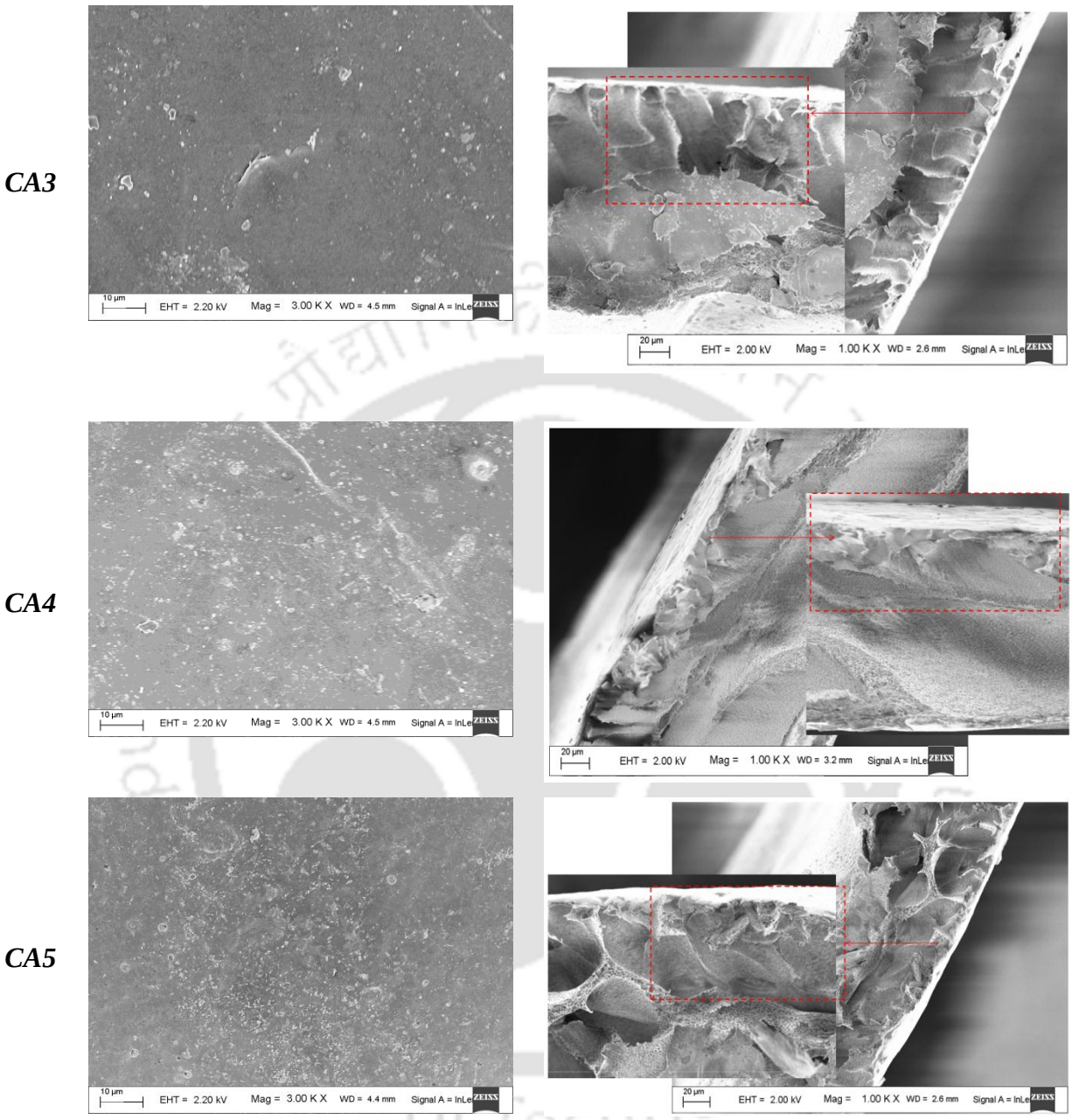

Fig. 4.1. (a) Top surface and (b) cross-sectional FESEM images of CA membranes with different additives and solvents

Therefore it is important to investigate the effect of additives on the compaction process, where the effects of the additives were significantly noticed from this study. Another point which is observed from this study was that the membranes without additives showed lesser PWF than

membranes with additives for both the solvents. This result is apparent that the introduction of hydrophilic additives to the membrane casting solution makes the membrane porous and more hydrophilic **[143]**. The result evidently shows that the introduction of PEG and PVP impact the development of porous structure in the membrane, where the permeability properties of the ultrafiltration membranes were significantly affected **[144, 145]**. Moreover, the whole removal of polymeric additive from the membrane-forming polymeric medium may not be achieved during the phase separation process in the coagulation bath and even after rinsing with DI water. Consequently, the residual additives (i.e. PEG and PVP), are forced to remain within the membrane matrix permanently, thus, forming more hydrophilic membrane **[145-148]**. In the current study, due to the introduction of the hydrophilic additives, a small quantity of PVP and PEG may permanently stay entangled in the membrane's matrix. These results can improve the hydrophilic nature of the CA membranes (**Fig. 4.3)**. Therefore, the polymeric additives can play an important role in the formation of porous membrane with improving its hydrophilic nature which is again directly related to its water permeability performance. Comparing both the additives, the membranes with PVP gained higher flux than membranes with PEG for both solvents. It is clearly explained from the FESEM images **(Fig. 4.1)** that the membranes formed using PVP additive (i.e. CA2 and CA5) showed the development of greater macro-voids when compared with membranes formed using PEG additive (CA1 and CA4). The decrease in water flux for membranes prepared from casting solutions containing PEG additive is due to the development of a denser top layer as the phase separation is delayed. These results are also supported by the porosity and pore size measurements reported in **Table 4.2**, where it clearly shows that a relatively lower affinity of PEG to the membrane forming polymer interferes the de-mixing process and prevents the formation of large pores. Therefore, regardless of the effect of solvents, the membranes with PVP additive are more porous than the membranes with PEG additive, which influences their water flux performance.

Effect of solvents

To develop the membrane skin layer with sharp polymeric concentration difference (lower concentration at the lowest surface and a higher concentration at the upper surface) should be attained. The polymeric concentration difference will be made because of the solvent evaporation before the immersion and due to the immersion of the casting solution into the non-

solvent. Therefore, the investigation of the effects of organic solvents on preparation of membranes by phase-separation is an important matter **[149]**. On the other hand, the membrane characteristics, which are evidently interrelated to the membrane morphological structures, can be strongly impacted due to the level of interaction between the membrane forming polymers and solvents during the preparation of solution casting. An additional interesting point is that the residual solvents in the membrane after completing the phase separation may also alter the final membrane properties **[150]**. Normally, the morphological structure variation of the membranes can be associated with the solvent and polymer interaction. In a solvent and polymer interaction scheme, three kinds of interactions viz. polymer: polymer, polymer: solvent and solvent: non-solvent are applied. When we use good polymer solvents, the degree of polymer stretching reaches to its highest level, and more favorable polymer/solvent interactions can occur **[151, 152]**. Furthermore, the affinity between the solvent and polymer can be predicted by presenting the "solubility parameter", δ, which is described as the square root of the cohesive energy density and expresses the strengths of attractive forces among the molecules. Solvent: polymer interaction in a polymer solution has been estimated based on the solubility parameter difference (Δ) between polymer and solvent as already clearly mentioned by Hansen **[153]**. The Hansen solubility parameters of the solvents, additives, and polymer used in this study with their boiling points are presented in **Table 4.1**. According to Hansen, the permanent dipole–dipole interactions (δ_p), dispersive (δ_d) and hydrogen bonding forces (δ_h) should be taken into consideration. Consequently, the solubility parameters (δ) can be calculated as follows **[153]**:

$$\delta^2 = (\delta_d^2 + \delta_p^2 + \delta_h^2) \qquad \textbf{(4.1)}$$

The Hansen solubility parameter differences (Δ) among the solvents and the membrane forming polymers were computed using the following equation:

$$\Delta = \sqrt{[(\delta_{P,d} - \delta_{S,d})^2 + (\delta_{P,p} - \delta_{S,p})^2 + (\delta_{P,h} - \delta_{S,h})^2]} \qquad \textbf{(4.2)}$$

Where, *S* and *P* denote the solvent and polymer respectively; and *p*, *d*, and *h* represent for polar, dispersive, and hydrogen bonding elements of Hansen solubility parameter. The polymer-solvent interaction parameter is inversely proportional with Hansen solubility parameters (Δ), i.e. the smaller the difference between the solubility parameters of polymer and solvent, the stronger the

polymer–solvent interaction. The results of the solubility parameter difference are listed in **Table 4.1** and show that the *Δs* of the solvents are in decreasing order (i.e. DMF < DMAc < Acetone). Therefore, the solvent: polymer interaction of the three solvents increases in the order of DMF > DMAc > Acetone. From these results, it can be suggested that a relatively strong hydrogen bonding interaction happened between remaining DMF and CA when compared with CA/Ac/DMAc. Therefore, the strong interaction between DMF and CA was suggested during the preparation of solution casting process for membrane forming.

Table 4.1 Hansen solubility parameters for selected solvents, non-solvent, additives and cellulose acetate **[150, 154]**

Polymer/solvent	δ_d**(MPa$^{1/2}$)**	δ_p**(MPa$^{1/2}$)**	δ_h**(MPa$^{1/2}$)**	δ**(MPa$^{1/2}$)**	Δ	**Boiling point (◦C)**
DMF	17.4	13.7	11.3	24.9	1.6	153
DMAc	16.8	11.5	10.2	22.8	2.3	165
Acetone	15.5	10.4	7.0	19.9	5.6	56
Cellulose acetate	18.6	12.7	11.0	25	-	-
PVP [a]	16.06	12.13	8.75	23.86	-	-
PEG [b]	16.8	10.2	8.6	21.45	-	-
Water	15.6	16.0	42.3	47.8	-	100

a **[155]**, *b* **[156]**

The effect of solvents on the PWF was also observed clearly from this study. Membranes prepared using Ac: DMAc (CA0, CA1, and CA2) showed higher fluxes than membrane fabricated with DMF (CA3, CA4, and CA5) regardless of the effect of additives. Moreover, the initial sharp decrease in PWF for CA/DMF membranes was significantly improved for CA/Ac:DMAc membranes. This result is evidently related to the effect of solvent on the morphological/ sublayer structures of the membranes. All the membranes prepared with CA/DMF system depicted large flux decline due to non-uniform sublayer pore structures. The percentage flux declines were found to be as 89 %, 72 % and 75 % for CA3, CA4, and CA5, respectively. Secondly, the formation of larger macro-voids due to an instantaneous de-mixing may have resulted in the formation of non-uniform pore distributions within the membrane matrix. However, for the membranes prepared from CA/Ac:DMAc system, the percentage flux decline

for CA0, CA1, and CA2 were 34 %, 32 % and 33 %, respectively. Unlike the CA/DMF membranes, the uniformly interconnected pore structures of the sublayer with uniform pore distribution of CA/Ac:DMAc membranes showed better permeability characterstics. The difference in flux between the CA-DMF and CA-Ac:DMAc membranes can also be associated with the effect of the solvents on the hydrophilicity nature of the membrane. As it is believed that there are some residual solvents within the final membrane matrix **[150, 157]**, they may affect the water flux performance of the membrane. Guan et al. **[150]** also reported that the membranes with DMAc solvent showed a higher hydrophilic nature than membranes with DMF. Similar results were found in our study. Regardless of the effects the polymeric additives the CA/AC: DMAc showed more hydrophilicity nature than the CA/DMF membranes. It is clearly shown from the membranes prepared without additives (i.e. CA0 and CA3). The effects of the residual solvents are not significant as compared to the effect of additives. However, it is believed to have some influences on the membrane performance. **Table 4.2** presents the compaction factor and hydraulic characteristics of all prepared membranes. It was observed that for both CA/Ac:DMAc and CA/DMF membranes, the CF decreases with introduction of the additives. However, for membranes prepared using both solvents the CF for CA/PEG was less than CA/PVP. This can be described that an introduction of additive into the membrane forming solutions may suppress or increase formation of macro-voids in the membrane sublayer based on the type of additive and solvent **[138]**. In the current study, for both the solvents less formation of macro-voids was observed for CA/PEG than CA/PVP. Due to these reasons, membranes with PVP additives have resulted in highly porous sublayer structure because of the occurrence of more numbers of macro-voids for both the solvents. These results are also depicted from the FESEM images (**Fig. 4.** The effects of polymer additives and solvents on PWF at different operating pressures are presented in **Fig. 4.3(b) and (d)**. The results of PWF for all the membranes were increased almost uniformly with increasing in an operating pressure from 100 to 300 kPa. It is also shown that the PWF for all the CA/DMF membranes is lesser than that of CA/Ac: DMAc membranes. Nevertheless, of the effect of the solvent, the membranes with PVP additives showed higher PWF than that of membranes with PEG additives for both the solvents. These results are in good agreement with the conclusions of the compaction study in **Fig. 4.3(a, c)**. The hydraulic resistance (R_m) of CA/DMF membranes was greater than that of CA/AC: DMAc membranes.

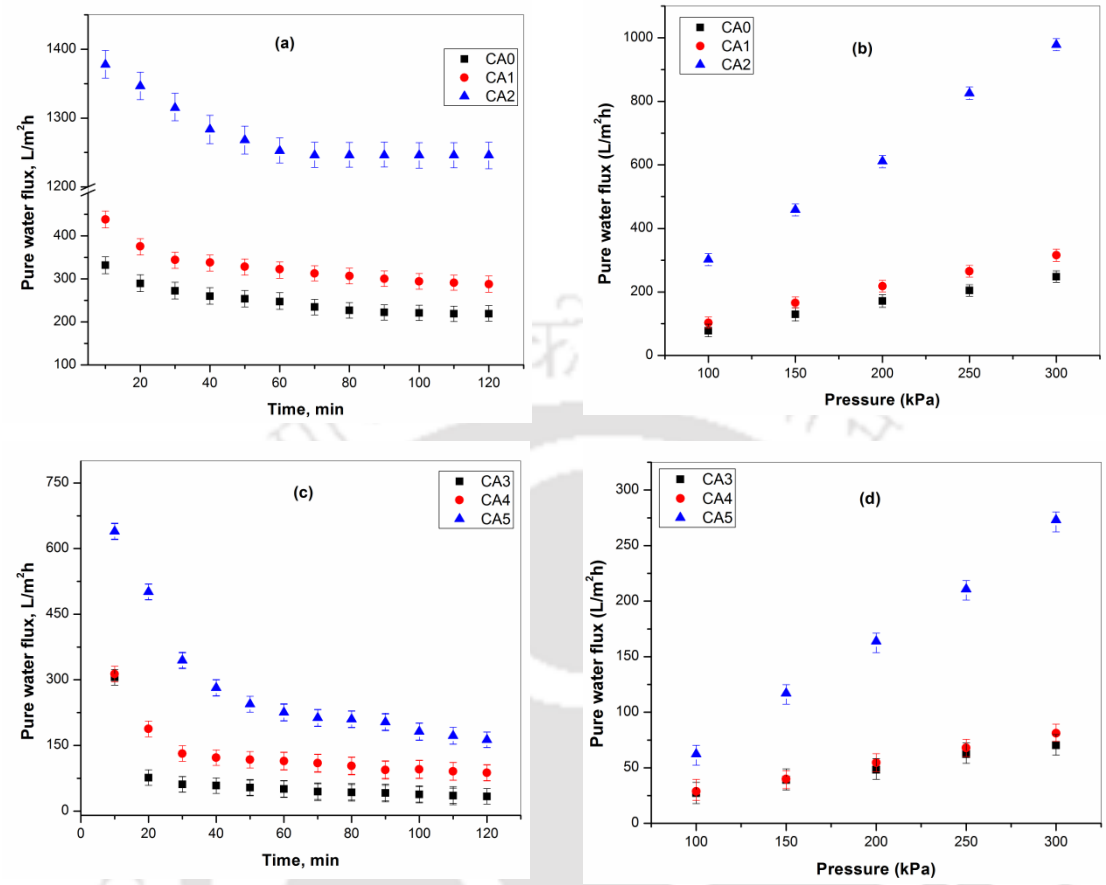

Fig. 4.2. (a, c) PWF profile during compaction study and (b, d) effect of operating pressure on PWF

Table 4.2 Compaction factor, hydraulic characteristics, EWC and porosity of all prepared membranes at 300 kPa

Membrane	***CF***	P_m (L/m^2hkPa)	R_m $(\times 10^{-10} m^{-1})$	J_w (L/m^2h)	***EWC*** ***(%)***	ε ***(%)***	r_m (nm)	**Thickness** μm
CA-0	1.5±0.5	0.8	1.1	248	79	83	14.4	72.9±15
CA-1	1.3±0.6	1.1	0.9	316	84	87	23.6	119.9±10
CA-2	1.4±0.5	3.3	0.8	978	86	89	28.9	116.4±11
CA-3	4.0±0.2	0.2	3.5	70	75	80	12.7	186.2±8
CA-4	2.5±0.3	0.3	1.9	81	82	85	13.9	166.5±9
CA-5	3.3±0.4	0.9	1.6	273	83	86	22.4	172.0±8

In addition, the R_m for the membranes without additives was higher than all the membranes with additives for both solvents. On the other hand, the R_m for CA/PEG was higher than that of CA/PVP for both the solvents. Therefore, an increase in hydraulic resistance and decrease in flux with varying additives and solvents may be accredited to the decline in pore size during compaction. In general, both the additive namely, PVP and PEG are more hydrophilic than the CA polymer. Therefore the CA membranes with these additives showed improved flux results. Comparing the two additives the CA/PVP showed higher flux and lower R_m than membrane of CA/PEG. These results can be explained because of higher solubility and diffusivity of PVP than PEG, where most of the PVP can be washed out more easily and quickly (as compared to PEG) with the non-solvent (i.e. water) during the membrane fabrication period **[50]**. This result may also be explained due to the formation some macro-voids because of the rapid penetration of non-solvent at certain weak spots in the top layer of the membrane; the PVP rich phase might act as the weak spots during the precipitation process and result in the development of macro-voids **[57]**. As a result, the suppressed sublayers of the PEG membranes are possible to give additional resistances to water permeability than PVP membranes resulting in low flux. The effects of additives as a pore former as well as hydrophilicity enhancer were also investigated, and the porosity and EWC results were calculated using **Eq. (2.6 and 2.7)**. The wettability of the membranes was studied by measuring the water contact angle and the drop age, defined as the duration of the water droplet on the surface of the membrane and spreading and/or permeating through the membrane cross-section **[158]**. The variation of water contact angle of all the prepared membranes is presented in **Fig. 4.3 (a)**. The images of the water droplets with a volume of about 2 µL at 0.16 mL/min on the membrane surface after 60 s are shown in **Fig. 4.3 (b)**. CA1, CA2, CA4, and CA5 membranes have taken about 15 s, 10 s, 25 s, and 20 s, respectively, and show best water wettability, where most parts of the membrane surface were almost completely wetted and smaller spread radius of the water drops on the top side of the membrane were observed after 60 s. On the other hand, CA0 and CA3 membranes have taken about 34 s and 36 s to initiate the surface wetting and big water drops spread radius on the top side of the membrane were observed after 60 s (**Fig. 4.3b**). If smaller water drop spread radius wetting area between top and bottom surface and on the top membrane side is observed, it means a better water permeability. As clearly observed form the graph the contact angle results of the pristine CA0 and CA3 membranes show water contact angle about 61.3±1.6º and 64.1±1.5º,

respectively. In contrast, after the introduction of hydrophilic additives, all the CA1, CA2, CA4, and CA5 membranes showed greatly reduced water contact angle results (i.e. 43.3±2.2º, 35.1±3.1º, 49.6±1.8º, and 47.6±2.0º, respectively). Membranes having smaller contact angle results are considered as more hydrophilic membranes. Therefore, an increase in the hydrophilicity, EWC, and porosity of the membrane after adding of additives is due to the pore-forming and hydrophilicity properties of PEG and PVP. Besides, as already discussed above using different solvents also influenced the hydrophilicity, EWC, and porosity of the membrane in some way. Thus, the CA/Ac: DMAc membranes showed better hydrophilicity nature than that of CA/DMF membranes irrespective of the effect of additives. Moreover, it is confirmed that all the membranes are in ultrafiltration range as seen from the pore radius (r_m) measurement results in **Table 3.3**.

4.1.1.3. Membrane fouling and rejection experiments

Membrane fouling is defined as the deposition of retained particles colloids, macromolecules, salts, etc. at the membrane surface, pore mouth or pore wall causing flux decline. Fouling can be caused by broadly three kinds of substances: organic (macromolecules, biological substances like protein, enzyme, etc.), inorganic (metal hydroxides, calcium salts, etc.), and particulates. Proteins are strongly adsorbed on hydrophobic or less hydrophilic surfaces but less on hydrophilic surfaces **[40, 159]**. In this study, the fouling and rejection experiments of all the membranes were done in the ultrafiltration stirred batch cell to examine the consequence of PVP and PEG additives and effect of DMF and Ac: DMAc solvents on BSA rejection and permeate flux. The concentration of bovine serum albumin (BSA) protein and pH of the solutions were kept at (1 g L^{-1}) and at 7.9, respectively, using deionized water as solvent. To examine the fouling performance of the prepared membranes, three steps BSA filtration processes were done. The flux results of pure water and BSA solutions of the prepared membranes are presented in **Fig. 4.4**.

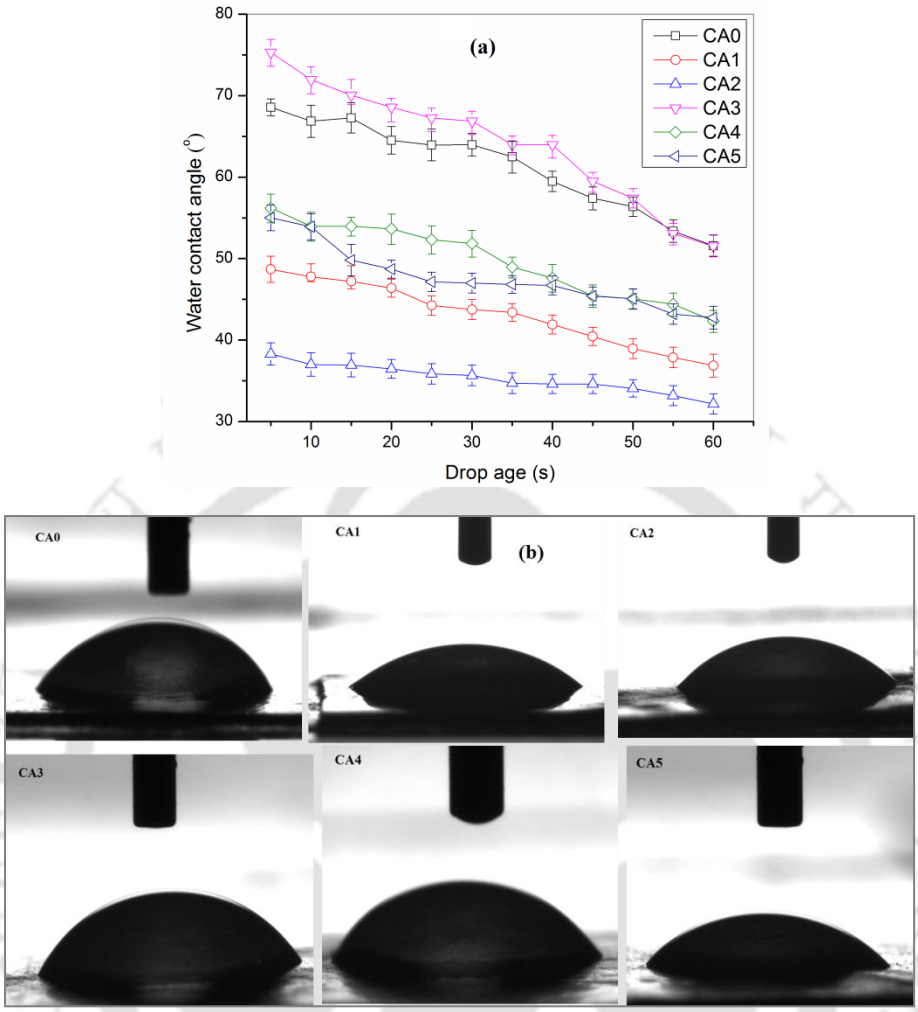

Fig. 4.3. (a) Water contact angle values and (b) images of water droplets of the prepared membranes. (Water droplet volume is about 2 µL at 0.16 mL/min)

Effect of additives and solvents

It is clear that the fouling and rejection behavior of the ultrafiltration membranes are strongly dependent on morphological structures of the membrane (i.e. both top layer and sublayer). The effects of additives have their potential role on the variation in morphological structure of the membranes. Therefore, the introduction PVP and PEG into the membrane matrix observed to influence the flux and BSA rejection performance of the prepared membranes. The fluxes and rejections of protein in ultrafiltration membrane can be described using the theory of resultant pore narrowing and protein adsorption; due to electrostatic and hydrophobic interaction

between BSA molecule and the membrane's surface **[160].** Regardless of the effect of solvent, the effect of PEG and PVP were clearly observed from the fouling experiments. Therefore, the fouling experiment results of CA/Ac: DMAc membrane system and CA/DMF membrane system are presented in **Fig.4.4. (a)** and **(b),** respectively. The results showed that initially the CA/PVP membranes showed higher PWF fluxes than the CA/PEG membranes for both the solvents. However, a relatively higher BSA fluxes results were observed for CA/PEG membranes. It is clear from the results that the membranes without additives (i.e. CA0 and CA3) showed less PWF as well as the BSA fluxes due to their less hydrophilic nature and less pore formation. The improvement of pure water and BSA fluxes for membranes with additives (i.e. CA1, CA2, CA4, and CA5) were attributed to the pore-forming effect and hydrophilic nature of PEG and PVP additives. On the other hand, the whole removal of additives may not be attained from the matrix of the membrane **[73]**.

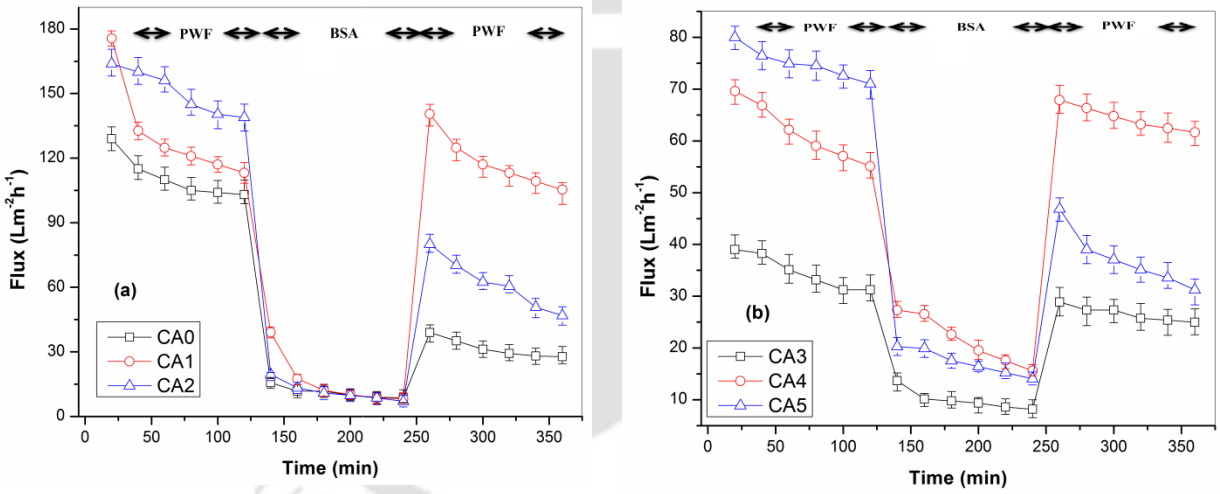

Fig.4.4. Permeate flux versus filtration time for (a) CA/Ac: DMAc and (b) CA/DMF membranes: effect of solvents and additives on fouling performance (25 ºC, 150 kPa)

As clearly depicted from **Fig. 4.4**, in the second BSA filtration operation (for 2 h), it is observed that with increasing time, the BSA fluxes gradually decreases for both CA/DMF and CA/Ac: DMAc membranes. The decrease in BSA fluxes with increasing time could be due to susceptible pore blocking of the membranes because of BSA protein adsorption and deposition on membrane surface, where the effect of concentration polarization was reduced by using a high

molecular weight of BSA (66 kDa) molecules and rigorous stirring (200 rpm) on the surface of the membrane. Moreover, the rapid drop in the primary fluxes are realized, and the ending fluxes are slowly dropped which is credited to the porosity loss of the membrane due to an interior adsorption of BSA protein which further leads to pore blocking. After membrane cleaning operation, the third step pure water filtration operation result showed that greater relative fluxes were recovered for both CA/PEG and CA/PVP membranes for both solvents. Normally, the orders of flux recovery ratios for the examined membranes were consistent with their hydrophilic and porosity nature. Thus, the additive-free membrane is more likely to prone to pore-blockage and fouling because of protein adsorption than the membrane with additives. In the literature, it is mentioned that both PEG and PVP **[161]** have the potential to minimize membrane fouling due to protein adsorption. Moreover, the PEG among various polymers is believed to be an excellent material to resist nonspecific protein adsorption contact with the surfaces due to the hydrated, neutral, highly mobile, and flexible chains since they provide maximum entropic repulsion between the proteins and surfaces **[162, 163]**. Therefore, the anti-fouling capacity of CA/PEG membranes was better than that of CA/PVP membranes irrespective of the effect of the solvents. The desorption of the adsorbed BSA proteins was performed by soaking the samples in DI water for 2 h and followed by rinsing using DI water. Moreover, the PWFs of CA-PEG-DMF and CA-PEG-Ac: DMAc were slightly increased after desorption of the BSA by washing the membranes for 2 h. Such phenomenon is not common in the conventional trends for fouling ultrafiltration experiments. These results could be caused by the inherent interactions between foulant (BSA), and PEG additive entangled in the membrane matrixes and the membrane top layer **[164-166]**. It was also confirmed that PEG could efficiently avoid the irreversible adsorption of the protein on the surfaces. Therefore, due to the hydrophobic interaction between PEG and BSA, the proteins might be wrapped by PEG chains, forming a protective layer **[163]**. Membrane fouling consists of reversible and irreversible fouling. In the case of reversible fouling deposited protein could be eliminated easily using hydraulic cleaning (i.e. back washing and cross flushing) **[167]**. Conversely, the irreversible fouling occurs due to an irreversible adsorption of proteins which can only be removed using chemical cleaning **[168].** To further examine the anti-fouling properties of the prepared membranes and to study the effect of additives, the flux losses viz. total fouling *(F_t)*, reversible fouling *(F_r)* and irreversible fouling *(F_{ir})* were calculated, and the results are presented in **Table 4.3**. From these results, it can be shown that the F_{ir} for the

CA/PEG membranes is less than CA/PVP membranes. However, the reversible fouling *(F_r)* for CA/PEG membranes are higher than CA/PVP membranes. This may be credited due to extra BSA protein buildup on membrane surfaces because of the better BSA rejection. In spite of the greater reversible fouling, total fouling *(F_t)* of CA/PEG membranes showed lesser results than CA/PVP membranes due to the decreasing of irreversible fouling. From this result, it can be suggested that the fouling resistances, particularly resistances due to irreversible fouling, of CA/PVP membranes are significantly higher than CA/PEG membranes irrespective of the solvent effects.

Table 4.3 Fouling study data of the prepared membranes

Membrane	J_{w1} (L/m^2 h)	J_{Bs} (L/m^2 h)	J_{w2} (L/m^2 h)	F_t $(1-\frac{J_B}{J_{Wi}})$	F_r $(\frac{J_{Wi}-J_{Wf}}{J_{Wi}})$	F_{ir} $(\frac{J_{Wf}-J_B}{J_{Wi}})$	NFR $(\frac{J_{Wf}}{J_{Wi}})$
CA0	111	15.9	76.7	0.86	0.55	0.31	0.69
CA1	130.7	21.5	118.4	0.84	0.74	0.09	0.91
CA2	150.7	17.2	81.8	0.89	0.43	0.46	0.54
CA3	34.7	10.0	26.6	0.71	0.48	0.23	0.76
CA4	64.6	11.5	61.4	0.82	0.77	0.05	0.95
CA5	75	11.1	37.1	0.85	0.35	0.51	0.49

The effect of solvents on the membrane morphological structures and PWFs were already explained in detailed in previous discussions (**Sections 4.1.1.2.**). Therefore, from these experiments, it was clearly observed that both the PWF and BSA flux of CA/Ac: DMAc membranes (**Fig. 4.2a)** are higher than the CA/DMF membranes (**Fig. 4.2b**). Similarly, the BSA protein rejection of CA/Ac: DMAc membranes are higher than of CA/DMF membranes irrespective of the effects of additives.

4.1.1.4. Rejection performance

The rejection performances of the prepared membranes are showed in **Fig. 4.5**. The maximum BSA rejection results for CA/Ac:DMAc and CA/DMF system (i.e. 94.4 % and 82.9 % rejections were attained for CA0 and CA3 membranes, respectively). These results can be explained due to the additive free membranes have less porous structures, where a better resistance to protein molecules was observed. On the other hand, the higher BSA rejection (91.9 % and 69.9 %) for CA/PEG (i.e. CA1 and CA4) membranes than CA/PVP (CA2 and CA5) membranes (77.9 % and 60.7 %), respectively, were achieved irrespective of the effect of the solvents. The characteristic of the BSA rejection can be described using the protein adsorption phenomenon as we have already explained above. The increase in BSA rejection for CA/PEG membranes is understood to be an indicator of substantial protein adsorption inside and on the membrane surfaces. Therefore, the surface depositions of BSA proteins provide an extra hindrance to solute transportation. Another reason for CA/PEG membranes to have higher rejections than CA/PVP membranes may be due to the adsorption of protein on pore-wall of CA/PVP membrane has lesser influence on pore-narrowing because of their highly porous structure and higher macro-voids. However, the rejection result for CA3 is higher than CA2 but less than CA0 and CA1 membranes. This result can be explained due to high resistance capacity of the membranes without additives having less porous properties. The high rejections and comparatively lower fluxes of CA/PEG membranes than CA/PVP for both the solvents can be assumed from the morphological study. The reasonably dense asymmetrical layer possibly describes the enhancement in the rejection rate whereas the sublayer with inhibited macro-voids gives resistance ensuing in moderately lower fluxes and higher BSA rejections. From the above discussions, it is clear that the type of additives and type of solvents showed significant effects on the membrane flux and BSA rejection performances. The results attained in this specific study seem to be reasonably fascinating that the membranes with PEG additives gained higher rejection results and moderate fluxes. On the other hand, the membranes prepared using Ac: DMAc solvent showed better characteristics (i.e. hydrophilicity, flux and rejection) than the membranes prepared using DMF as solvent.

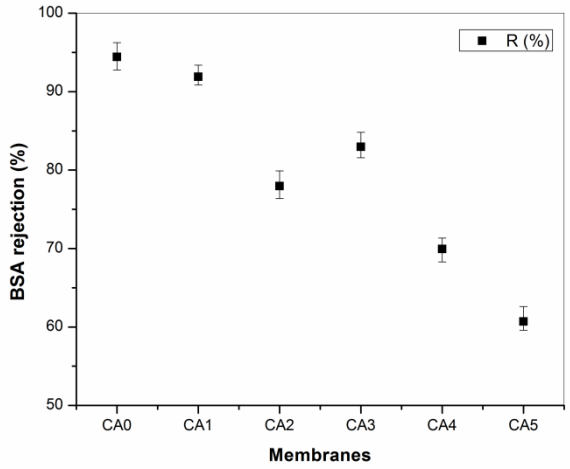

Fig.4.5. Rejection performance of different CA membranes: effect of solvents and additives (25 ºC, 150 kPa).

4.1.2. Summary

Phase inverted CA membranes were prepared from casting solutions comprising of two different solvents, namely Ac: DMAc and DMF individually using immersion precipitation process. Two different hydrophilic additives viz. PEG and PVP were used as membrane pore formers and hydrophilic enhancers. The effects of additives and solvents on the morphological structures (i.e. top surface and a cross-sectional structure of the membranes) were studied in detail. The permeability properties of the prepared membranes using different additives and solvents were also estimated using CF, hydraulic permeability, hydraulic resistance, hydrophilicity, porosity, EWC, PWF, and BSA rejection performance. The outcomes from this study presented the following concluding points:

- The membranes prepared using PVP additive showed the development of greater macro-voids and finger-like structure when compared with membranes formed using PEG additive.
- The introduction of hydrophilic additives to the membrane casting solution makes the membrane highly porous and more hydrophilic where the permeability properties of the CA ultrafiltration membrane were significantly influenced.

- The difference in flux between the CA/DMF and CA/Ac: DMAc membranes are associated with the effect of the solvents on the hydrophilic nature of the membrane. As it is believed that there are some residual solvents within the final membrane matrix.
- The fouling resistances, particularly resistances due to irreversible fouling, of CA/PVP membranes are significantly higher than CA/PEG membranes irrespective of the solvent effects.
- Higher BSA rejection and relatively moderate flux of CA/PEG membranes than CA/PVP for both the solvents were obtained, and the comparatively dense asymmetric layer of CA/PEG membrane possibly describes the enhancement in the rejection rate whereas the sublayer with inhibited macro-voids gives resistance resulting in moderately lower fluxes and higher BSA rejections.

4.2. Preparation and characterization of CA−PEG−TiO_2 membranes: Effect of PEG and TiO_2 on morphology, flux and fouling performance

Modified cellulose acetate (CA) membranes were prepared by dissolving the polymers in a mixture of acetone (AC) and N, N-dimethylacetamide (DMAc) (70:30) solvent and deionized (DI) water were used in the coagulation bath. The introduction of polyethylene glycol (PEG) additive and TiO_2 nanoparticles (NPs) into the casting solution have changed the structures of the resulting membranes during the phase inversion process. Effects of PEG additive and TiO_2 NPs on the preparation of phase-inverted CA ultrafiltration membrane were investigated in terms of morphology, equilibrium water content (EWC), pure water flux (PWF), hydraulic resistance, thermal stability, water contact angle (WCA) and anti-fouling performance. Improvements in average pore size, porosity, thermal stability, and hydrophilicity nature of the CA membranes were detected after the introduction of PEG and TiO2 simultaneously to the polymer matrix. Thermo gravimetric analysis (TGA) results confirmed that the interaction between TiO_2 and the degradation temperature of the CA membrane were significantly improved. The anti-fouling performance and the flux recovery potential of the membranes were investigated using bovine serum albumin (BSA) protein. M3 (CA-PEG-TiO_2) membrane (10.5 Wt. % CA: 4 Wt. % PEG: 2 Wt. % TiO_2) exhibited highest BSA flux result and normalized flux recovery ratios (NFR) for the three fouling cycles.

4.2.1. Results and discussion

4.2.1.1. Morphological study

The FESEM analysis is an important method to study the membrane morphological structure and qualitative information about surface and cross-sectional morphology of the membranes to be achieved. The top layer surface view, the cross-sectional view, and elemental analysis results of the prepared membranes by dissolving the polymer and additives in AC: DMAc are presented in the FESEM and EDS images (i.e., **Fig. 4.6(a), (b)** and **(c)** respectively).

As evidently revealed from the figures, the synthesized membranes are asymmetric in structure involving a dense top layer and a porous sub-layer for all types of membranes. For additional information, the mapping or distributions of the elements within the matrix of the prepared membranes are presented in **Fig. 4.6(d)**. PEG polymer and TiO_2 nanoparticle were added to the membrane forming polymer (i.e. CA) as an additive to examine their impacts on the morphological structures, thermal stability and anti-fouling performance of the synthesized membranes. As evidently revealed from the figures, the synthesized membranes are asymmetric in structure involving a dense top-layer and a porous sub-layer for all types of membranes. The sub-layer portion of the membranes without additives (M_1) appears to have finger-like voids as well as macro-void structures.

Effect of PEG additive and TiO_2 NPs

The sub-layer portion of the M_1 membrane appears to have finger-like voids as well as macro-void structures. Generally, the development of macro-voids happens under rapid precipitation condition, and the precipitations are quicker at high coagulation temperature **[53]**. In the present study, the coagulation bath temperature and evaporation time (i.e. before immersion) were fixed to 25±2 ºC and 30 s, respectively, during the preparation of all the membranes. An additional significant factor which can affect the formation or suppression of macro-voids is the type of de-mixing occurred during the phase separation process, where, the instantaneous de-mixing and the delayed de-mixing depend on the mutual affinity of the solvent and non-solvent in the ternary system **[40]**. In solvent and polymer interaction scheme, three kinds of interactions viz. polymer: polymer, polymer: solvent and solvent: non-solvent is applied. If good polymer solvents are used, the degree of polymer stretching reaches to its highest level, and more favorable polymer/solvent interactions can occur. The solvents used in this study (i.e. AC: DMAc) have high mutual affinity with water **[150].** Thus, apparently, the development of the finger-like voids and macro-voids in the sub-layer of the M_1 (additive free) membrane is due to the instantaneous de-mixing. In this case, the CA (additive free) stretches to its highest level where there is a maximum interaction between the CA and AC: DMAc which tends to instantaneous de-mixing condition to happen. On the other hand, after adding the PEG and TiO_2 to the ternary (polymer/solvent/non-solvent) system, the developments of macro-voids are suppressed significantly (i.e. M_2, M_3 and M_4). The presence of the polymeric additives and

TiO_2 NPs can increase the concentration/viscosity of the casting solution which may diminish the diffusional exchange rate of the solvent and non-solvent during the membrane formation process. Accordingly, this may hamper the instantaneous liquid-liquid de-mixing process which suppresses the development of macro-voids **[140]**. However, for membranes prepared using PEG and TiO_2 nanoparticles (M_3) and without TiO_2 nanoparticles (M_4), the formation of micro-voids (microporous structure, which is important for the porosity of membrane) was observed. It is clear that the pore forming properties of PEG polymer has played the key role in the development of porous sublayer. A quaternary system (polymer/solvent/non-solvent/additive) of the phase separation involves de-mixing of the entangled polymers. In this quaternary system, two phases occur from the phase separation; one involves CA (i.e. membrane forming polymer), AC: DMAc (i.e. solvent) and non-solvent; the second contains the additive (i.e. PEG), AC: DMAc and non-solvent. The membrane forming polymer and additive have a dynamic strength to be completely separated to CA-rich and PEG-rich phases. Consequently, the type of de-mixing process can also be decided by the diffusion of these polymers in respect of each other. On the other hand, the addition of TiO_2 to the membrane formation system has its influence on the de-mixing process. However, almost macro-void free cross-sectional structures were observed for the M_4 system. From these results, it can be concluded that although the instantaneous de-mixing is still continued, the effect of the PEG has a substantial role in the suppression of the finger-like structure and macro-voids which occurred for the M_1 membrane. The presence of the polymeric additive increases the concentration/viscosity of the casting solution which may diminish the diffusional exchange rate of the solvent and non-solvent during the membrane formation process. Consequently, this may hinder the instantaneous liquid-liquid de-mixing process which suppresses the development of macro-voids **[53]**. On the other hand, the comparatively low affinity of PEG to the solvents may take additional time to reach the top surface allowing the polymeric molecule to get sufficient time to accumulate and re-arrange and subsequently developing a relatively thicker and denser top layer. The open pore structures developed in the membranes are formed by nucleation and development of the polymer-lean phase in the metastable area between the bi-nodal and the spinodal curve **[139, 141]**. A possible explanation for the formation of a nodular structure on the top surface of the membranes could be due to the spinodal de-mixing because the diffusion process throughout the development of the top-layer is faster for the homogenous system to become highly unstable and crosses the

spinodal curve **[139]**. In the present study, the top surface with some open pores structures is observed more prominently in the case of PEG (i.e. M_3 and M_4) which is attained because of the spinodal decomposition. Therefore the inter-connected pores may be accounted as a constant CA-lean/ PEG-rich phase entwined by a continuous CA- rich/ PEG-lean phase which is responsible for developing the uniform matrix of the membrane **[169]**. On the other hand, in the case of M_1 and M_2 membranes, no open pore structure was detected, where a less porous top surface structure was observed instead. On the other hand, It is evident from these figures that the finger-like structures and macro-voids are suppressed after adding TiO_2 (M_2 and M_3) regardless of the effect of PEG for M_3 membrane. However, the M_2 membrane seems to have less microporous cross-sectional structures. These results are also confirmed by the porosity study (**Table 4.4**) where the M_2 membrane shown relatively lowest porosity than the other membranes. The introduction of both PEG and TiO_2 played an important role in the improvement of the membrane hydrophilicity and porosity. The porosity, EWC and pore radius results of the prepared membranes are calculated using **Eq. (2.6, 2.7 and 2.13)**. The membrane average pore radius *(r_m)* is considered as an approximation of true pore size and the results are 23.6 nm, 15.6 nm, 35 nm and 31.4 nm for M_1, M_2, M_3 and M_4, respectively. Moreover, these lowest pore radius for M_2 membrane were attributed to aggregation of some of the TiO_2 on the surface of the membrane pores. It can also be seen from the top surface view of M_2 presented in **Fig. 4.6a.** Adding of TiO_2 NPs to the polymeric solution can increase its viscosity. Therefore, the particles leaching problem is lesser, and subsequently, the pore forming effect of NPs can be declined in the case where the high viscosity of a solution hampers the development of pores and causes the porosity of the membrane to decrease **[170]**. To minimize the influence of thickness shrinkage of the polymer-phase due to the accumulation of NPs, in the present study, TiO_2 NPs having low concentration (i.e. 2 wt. %) was selected **[171]**. It may be worthy to mention here that the addition of NPs in the polymeric membrane may decrease or increase its viscosity depending on various parameters, such as concentration of additive, and ligand stabilizer **[172]**. Due to the introduction of a relatively lower concentration of TiO_2, the finger-like structures, and macro-voids present in M_1 was greatly suppressed and a relatively dense layer with small finger-like structures was observed for M_3 and M_4. The presence of small macro-voids with a little finger-like structure in the case of M_3 and M_4 is assumed to be related to the interference effect of NPs and PEG additive during the phase inversion process. Therefore, due to the interfacial stress

between polymers and NPs, interfacial pores are formed as a result of shrinkage of polymer-phase during the de-mixing process **[173]**. However, the presence of TiO_2 in M_2 diminishes the presence of finger-like structures and a sublayer structure with almost macro-voids free is obtained. These results can be described in terms of NPs agglomeration on the membrane forming polymer matrix during phase inversion process. The occurrence of NPs agglomeration can be mainly caused due to the high surface energy of the NPs, which tend to aggregate for weakening their surface energy to reach a more stable state. Furthermore, NPs agglomeration leads to a non-uniform dispersion of the NPs within the polymer surface and structure. This phenomenon can negatively change the resulting membrane properties such as hydrophilicity and surface roughness **[171]**. However, in the case of M_3, the NPs agglomeration was significantly minimized due to the improved distribution of the NPs because of the introduction PEG additive **[174].**

4.2.1.2. Thermal stability studies

The thermal degradation analyses (i.e. TGA and DTG results) of all the prepared membranes are presented in **Fig. 4.7 (a)** and **(b)**, respectively. The graphs were plotted as weight loss (%) vs. temperatures (ºC). It can be clearly seen from the TGA figure that the decomposition of M_1 shown three steps. The first degradation step of the M_1 membrane was detected between 30 and 60 °C, and the weight loss was about 4.5 %. This degradation is due to the presence of some volatile material or because of the evaporation of absorbed moisture by the sample. During the second degradation step, a high weight loss of around 16.5 % was observed between 60 to 260 °C, which is possibly due to the start of the main thermal breakdown of CA chains. A final degradation step started at 260 °C and ended at 380 °C with a weight loss of 79 % was due to the main degradation and possibly because of the carbonization of the decomposition of the residual materials to ash. The TGA results of the M_1 membrane clearly shown that it could be highly unstable at high temperature and similar results were reported by Zafar et al. and Chatterjee et al. **[175].** The TGA results of the CA membrane with PEG additive and TiO_2 displayed two-step degradation procedures. Therefore, the start of the decomposition step for M_2, M_3 and M_4 were 278 °C, 271 °C and 234 °C, respectively. The observed weight losses are due to the degradation of CA chains because of the pyrolysis of the back-bone of the CA polymer and also followed by de-acetylation of CA **[176].**

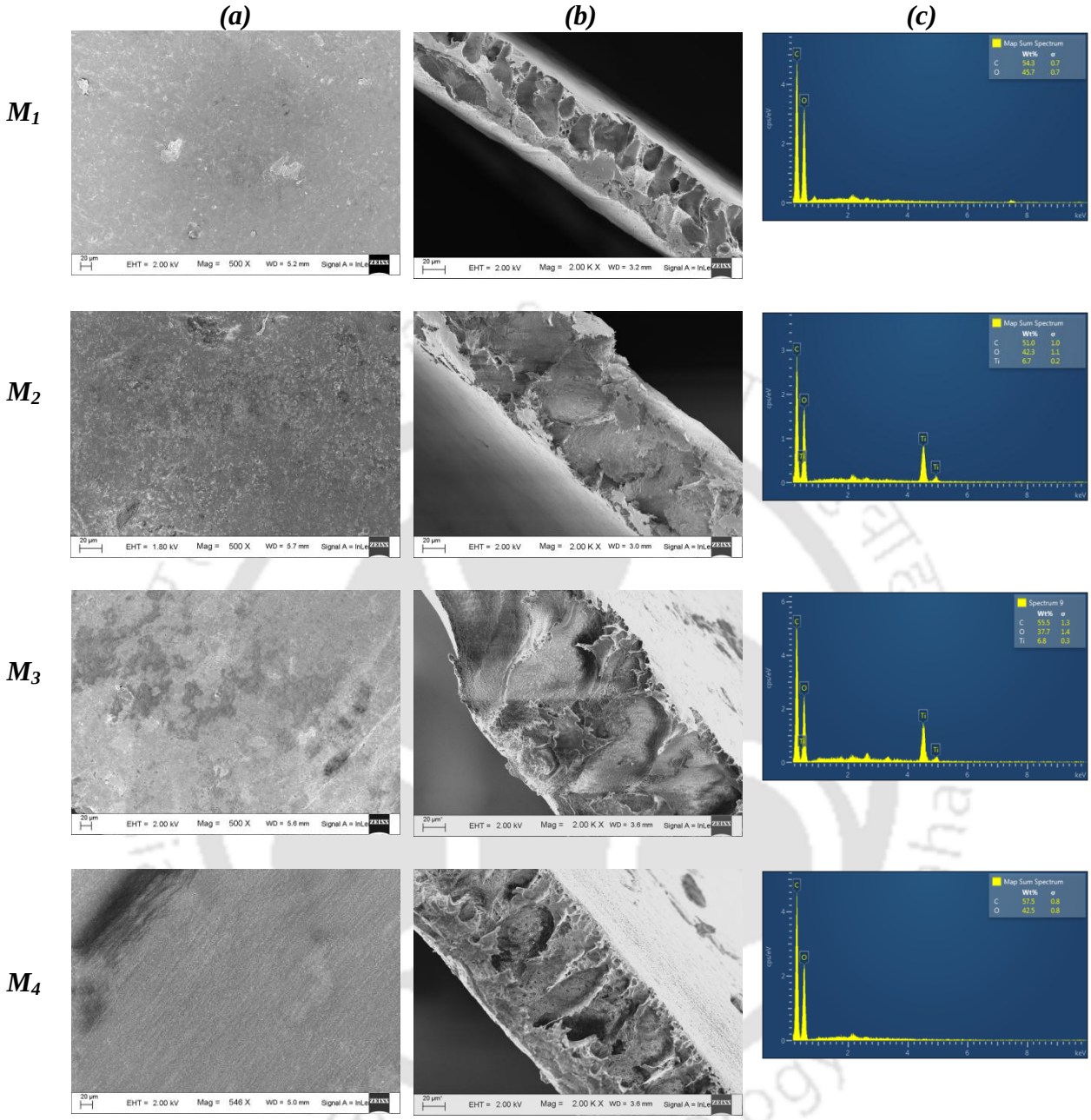

Fig. 4.6. (a) Top surface and (b) cross-sectional FESEM images (c) EDS results of M_1 (CA), M_2 (CA-TiO_2), M_3 (CA-PEG-TiO_2) and M_4 (CA-PEG) membranes

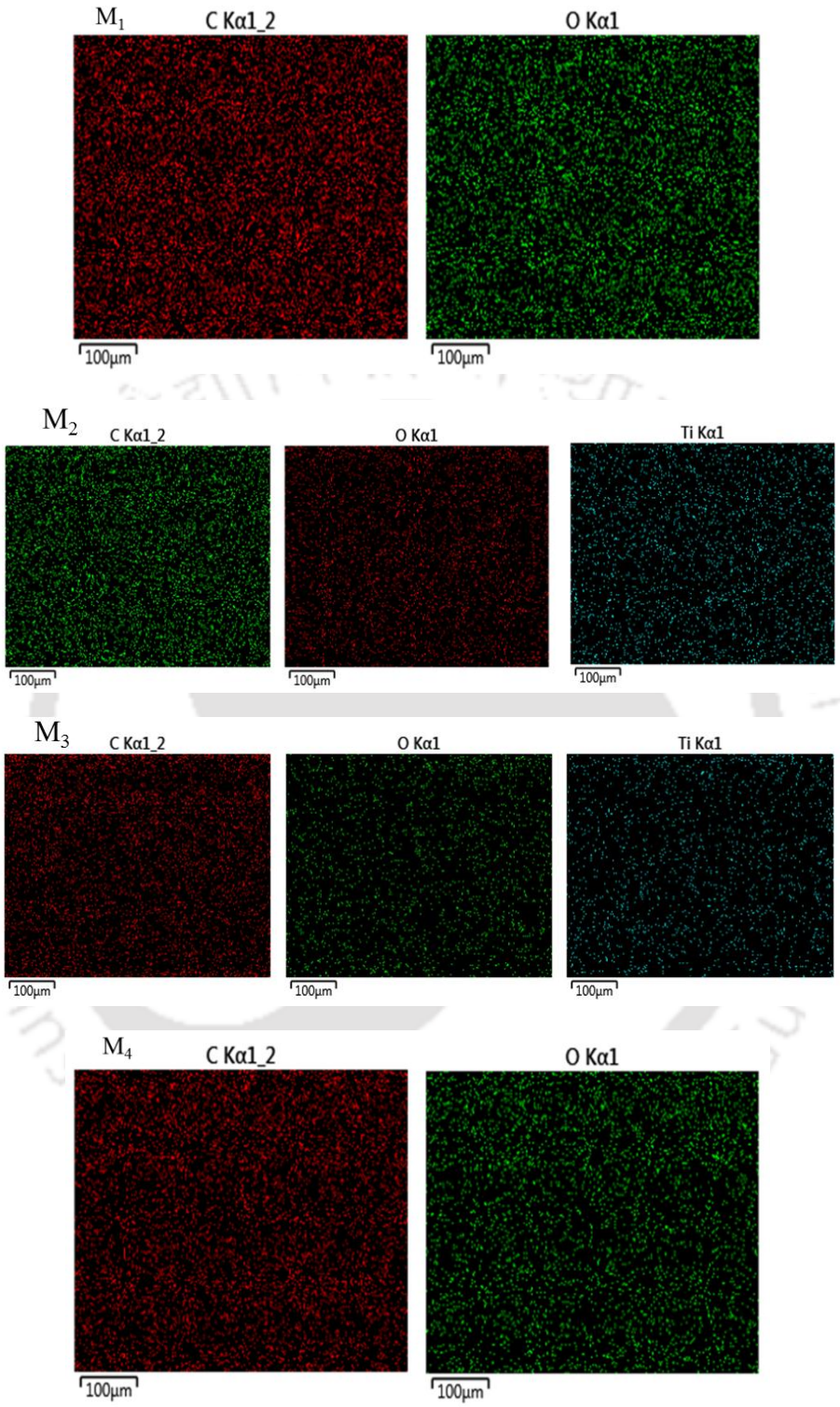

Fig. 4.6. (d) EDS mapping images of CA membranes with PEG and TiO_2 NPs *(continued)*

During the last decomposition step, the degradation temperatures of M_2, M_3 and M_4 are 388 °C, 386 °C and 382 °C signifying the main thermal degradation of the CA chains, whereas the TiO_2 were totally stable until the end of the analysis (i.e. up to 800 °C). From these results, it is clearly noticed that the thermal degradation of M_1 membrane was significantly enhanced due to the addition of PEG and TiO_2. An interesting observation from this study is that the increase in thermal stability after addition of PEG to CA membrane (M_4) is due to the presence of a trace amount of the PEG in the membrane matrix. The improved thermal stability of the M_4 membranes was due to the strong interaction between the CA and PEG in the membrane matrix by creating hydrogen bonds **[177]**. Moreover, the residuals i.e. 0.08 %, 21.9 %, 19.6 % and 7.3 % for M_1, M_2, M_3 and M_4 are consistent with the thermal stability performances of the prepared membranes. Furthermore, the thermal stability of M_3 membrane exhibited higher degradation temperature than the M_4 membrane. This result is attained due to the highly stable nature of TiO_2 at high temperatures and therefore the degradation temperature of the M_4 membrane was significantly improved after addition of TiO_2. On the other hand, the slight improvement in degradation temperature for the M_2 membrane when compared with the M_3 membrane is that the less porous sublayer structure of the membrane is responsible for having strong resistant to heat flow than that of the porous membrane (M_3). In this study, the TGA and DTG plots clearly revealed that the thermal properties of CA membrane were significantly improved after incorporation of PEG and TiO_2 into the CA solution.

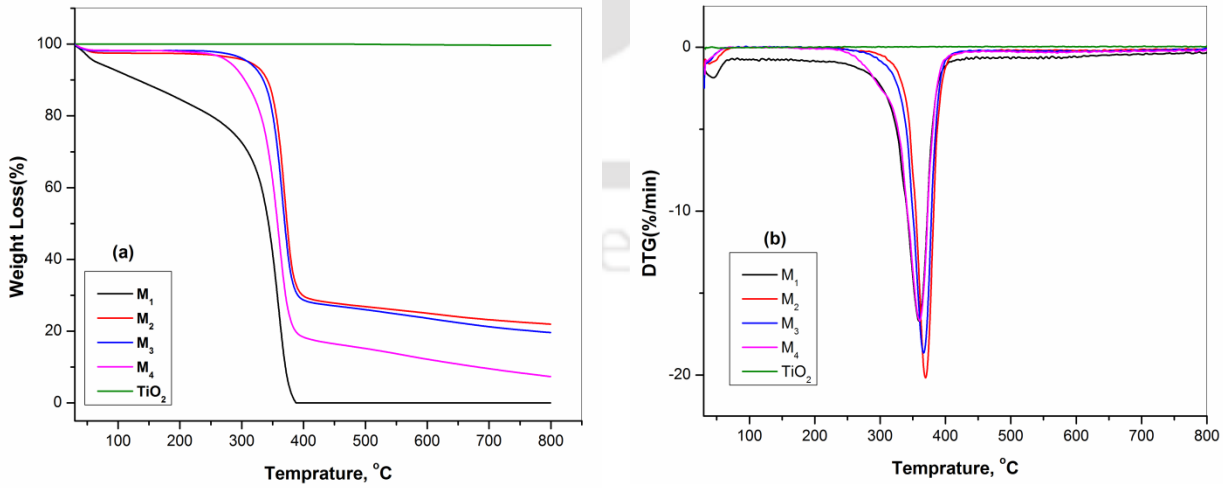

Fig. 4.7 (a) TGA and (b) DTG analysis results of M_1, M_2, M_3, M_4 membranes and TiO_2 NPs.

4.2.1.3. Pure water flux performance

The membranes prepared using CA, CA-TiO_2, CA-PEG-TiO_2 and CA-PEG (M_1, M_2, M_3 and M_4, respectively), using AC: DMAc as solvent were investigated to evaluate the influence of PEG additive and TiO_2 NPs on PWF properties of the membranes. The membranes were characterized in terms of compaction factor, PWF and hydraulic resistance.

Effect of PEG and TiO_2 NPs

Studying of compaction factor (CF) of the prepared membranes is very essential to recognize the morphological structures (i.e. pore arrangements) of the membranes specially the membrane sub-layer configuration. Membranes having high CF indicate that these are highly compacted and show the existence of some defective pores in the membrane sub-layer structure. The compaction factor and hydraulic characteristics of all the prepared membranes are presented in **Table 4.4**. It was observed that the CF of M_2 was greater (i.e. 4.5±0.2) which can also be explained due to the aggregation of NPs on the pore walls of the membrane could further block the pores after compaction. On the other hand, the CFs for the remaining membranes is almost similar except for the M_1 (1.5±0.4) which is slightly lower than M_3 (1.66±0.3) and M_4 (1.52±0.4). This result is achieved due to the existence of more porous structure in case of M_3 and M_4 due to the introduction of PEG additive where some of the pores were compacted after the compaction process. The introduction of additives into the membrane casting solutions may either suppress or increase the formation of macro-voids in the membrane sub-layer based on the type of additive **[138]**. The effects of PEG additive and TiO_2 NPs on PWF at different operating pressures are presented in **Fig. 4.8 (b)**. The results of PWF for all the membranes were increased almost uniformly with increasing in an operating pressure from 100 to 300 kPa. It is also shown that the PWF for membranes without PEG additive (M_1 and M_2) membranes are lesser than that of membranes with PEG additive (M_3 and M_4). Nevertheless, the effect of the PEG additive, the CA-PEG-TiO_2 membrane shown higher pure water flux than that of CA-TiO_2 membrane. These results are in good agreement with the conclusions of the compaction study in **Fig. 4.8 (a)**. The hydraulic resistance *(R_m)*, EWC, average pore radius, porosity and thickness of all the prepared membranes are reported in **Table 4.4.** As seen from these results the hydraulic resistance of M_2 was greater than all the other membranes. This higher resistance of M_2 is because of its less porous nature than the other membranes which can resist the water flux than the other

membranes. Additionally, this result is supported by the average pore radius calculation **(Eq. 2.13)** where the result was 15.6 nm which is again less as compared with the other membranes. In addition, the R_m (m^{-1}) for the membranes without PEG additive (M_1) was higher than that of the membranes with PEG additive. Thus, the increase in hydraulic resistance and decrease in flux results of the membranes without PEG additive are obviously due to the decrease in average pore size and porosity as already explained in the previous sections. The PEG additive is more hydrophilic than the CA polymer. Therefore the membranes with PEG additive displayed improved flux results. As shown in **Table 4.4,** by comparing the two membranes with PEG additive (M_3 and M_4), the CA-PEG-TiO_2 membrane gained slightly higher resistance and higher flux than CA-PEG membrane. These results can be explained because of the CA-PEG-TiO_2 membrane has higher and uniform porous and hydrophilic surface due to the introduction of TiO_2 NPs. On the other hand, as PEG additives were added and the whole additive wouldn't be washed away during the membrane development due to its low solubility and diffusivity, rather it could exist inside the pores and within the membrane matrices. Therefore, the introduction of both PEG additive and TiO_2 NPs at the same time could play an important role in the improvement of the membrane hydrophilicity and porosity simultaneously. The porosity and EWC results of the prepared membranes results are calculated using **Eq. (2.6 and 2.7)** and presented in **Table 4.4.** From the porosity measurement results, it is shown that all the membranes have shown a satisfactory results in the range of 81 to 83.4 %, which is accredited to lower concentration of the membrane forming polymer (10.5 wt. %) as well as due to the addition of PEG additives and TiO_2 NPs together with the type of solvent used and type of de-mixing occurred. Therefore, the high porosity result for CA (additive free) membranes is due the instantaneous de-mixing happened during the phase inversion process as already explained previously. On the other hand, the effect of PEG additive as pore-former and TiO_2 NPs as hydrophilicity enhancer was also accredited to the highest pore sizes and porosity results of the membranes with PEG additive and TiO_2 NPs though a relatively delayed de-mixing was observed. One point which should be clarified here is that the delayed de-mixing, in this case, is not extended delayed de-mixing. Normally, if the delayed de-mixing is extended, the polymer film thickness will decrease considerably which may cause a decrease in the porosity of the sublayer membranes **[142]**. However, the CA-TiO_2 gained the lowest porosity due to the NPs agglomeration phenomenon as explained previously. It can also be seen from the results that an

increase in the EWC of the membrane after addition of PEG additive is because the PEG is known for its hydrophilicity properties.

Table 4.4 Compaction and hydraulic characteristics of those prepared membranes at 250 kPa

Membrane	*CF*	R_m $(\times 10^{-10} m^{-1})$	J_w (L/m^2h)	*EWC* (%)	ε (%)	r_m (nm)	Thickness (μm)
M_1	1.50±0.4	0.90	204.5	77.8±1.5	81.9±2.0	23.6±5	83.5±8.0
M_2	4.50±0.2	4.30	21.1	76.7±2.6	81.0±2.5	15.6±7	102.4±4.2
M_3	1.66±0.3	0.70	530.7	79.5±1.2	83.4±1.8	35.0±3	84.2±6.5
M_4	1.52±0.4	0.67	265.3	79.0±1.4	82.9±1.9	31.4±4	126.9±3.0

The influences of compaction time on pure water flux of the prepared membranes are shown in **Fig. 4.8 (a)**. It is seen from the figure that the PWFs of all the membranes were observed to decrease slowly with increasing time because of the pore compaction and lastly the steady state fluxes were reached approximately after 80 min filtration operation. The gradual decrease in PWF results can be described because the compaction of pore walls attain uniform and denser structures and causing the pore size and the flux to decrease **[40]**. However, large flux decline was depicted for the membranes without additive which is may be due to a non-uniform sublayer pore structures. Consequently, it is crucial to explore the effect of PEG additive on the membranes compaction process, where the effect of the PEG additive was significantly observed from this study. Another important point which is observed during the compaction study was that the membranes without PEG additive (i.e. M_1 and M_2) revealed lower PWFs when compared with the membranes having PEG additive (M_3 and M_4). The PWF values at 250 kPa, for M_3 and M_4, are 530.7 and 265 L/m^2 h, respectively; whereas these values are 204.5 and 21.1 L/m^2 h, respectively, for M_1 and M_2 as presented in **Table 4.4**. It is clear from the results that the introduction of hydrophilic PEG additive to the membrane casting solution helps these membranes to be porous and more hydrophilic **[143]**. The lowest PWF for M_2 can be explained due to the blockage of pores due to aggregation of the TiO_2 NPs inside the membrane matrix. On the other hand, the membranes with PEG additive (M_3) have shown the highest PWF result. This result obviously indicates that the introduction of PEG additive influences the membrane in two

ways: (1) development of pores in the membrane structure and (2) enhancement of the hydrophilic nature of the membrane **[144]**. In the present study, due to the adding of the hydrophilic additive, trace amount of PEG may permanently exist tangled in the membrane matrix. The presence of PEG additive can enhance the hydrophilic nature of the CA membranes. Hence, the PEG additive can play a significant role in the formation of porous membrane with improving its hydrophilic nature which is again directly related to its water permeability performance. Comparing both the membranes with PEG additive (i.e. M_3 and M_4), the CA-PEG-TiO_2 membrane gained higher flux than CA-PEG membrane. These results are also confirmed by the porosity measurements reported in **Table 4.4**, where the presence of the TiO_2 NPs in the CA-PEG-TiO_2 membrane could interference the de-mixing process and help the formation of additional pores. On the other hand, the hydrophilic nature of TiO_2 NPs can also play an important role on the increasing in flux result of CA-PEG-TiO_2 membrane.

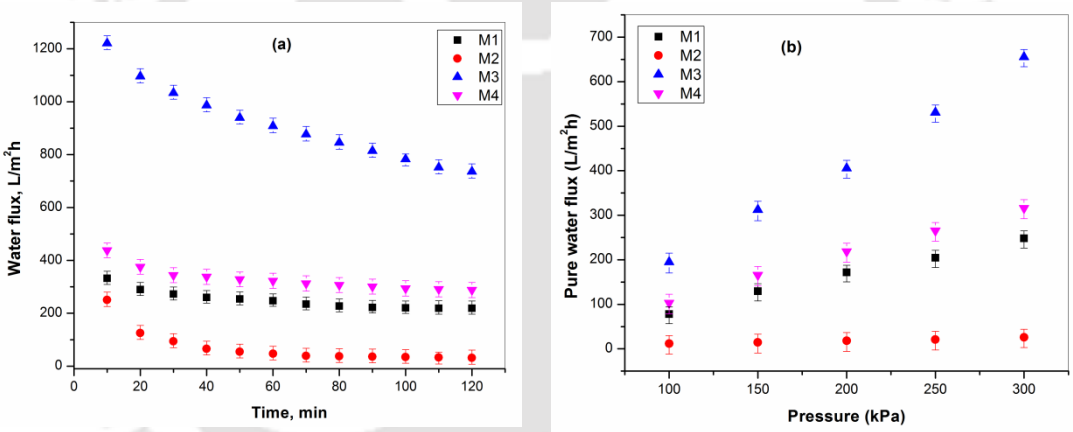

Fig. 4.8. (a) PWF profile during compaction study (at 300 kPa), (b) Effect of transmembrane pressure on PWF

It is well known that the flux properties of the membrane can be influenced by several factors like membrane pore-size, cross-sectional morphology, skin-layer thickness and hydrophilic nature of the membrane. Thus, the PWF of the prepared membranes in this study could be influenced by TiO_2 NPs. The introduction of the TiO_2 NPs can affect the membrane in two ways: (1) due to its hydrophilic nature which could improve the PWF and (2) its effect on the membrane morphological structure would also influence the permeation properties negatively or positively. **Fig. 4.8 (a)** shows the PWF of all the prepared membranes with and without

adding TiO_2 NPs. As TiO_2 is more hydrophilic than CA, the water has higher affinity for TiO_2, and therefore, PWF should increase in CA-TiO_2 membrane (M_2). But, it can be seen from the figure that the pure water flux value for M_2 shown the lowest result. Because the addition of TiO_2 NPs to the membrane forming polymer has caused pore blockage and pore failure in the membrane matrix due to the accumulation of the NPs **[171]**. Another important point which should be noted is that the hydrophilic nature of the CA membrane has its effect on the PWF of the membrane without additive (M_1) so that it has shown better flux result than the CA-TiO_2 (M_2) due to the aggregation of the TiO_2 NPs on to CA matrix. On the other hand, membranes prepared from CA-PEG-TiO_2 resulted in highest flux values. As already explained from the FESEM images, where the presence of PEG additive promotes the formation of porous structure. Thus, the TiO_2 NPs can play their significant role in the enhancement of the hydrophilicity of the membrane with less effect on the porosity of the prepared membrane. It is clear from the porosity (**Table 4.4**) data and the flux result (**Fig. 4.8**) that the membranes with TiO_2 NPs (CA-PEG-TiO_2) gained higher porosity and water flux than the membranes without TiO_2 NPs (CA-PEG). Besides the enhancement of the hydrophilicity and porosity, morphological structure of the CA membranes with TiO_2 NPs may be affected the permeability properties. As TiO_2 NPs have the high affinity to water than the membrane forming polymer, diffusion velocity of non-solvent (i.e. water) into the nascent membrane could be increased with TiO_2 NPs addition during the phase-inversion process. Furthermore, the AC: DMAc (solvent) diffusion velocity from the membrane to non-solvent (water) could also be increased by TiO_2 NPs addition. Based on this fact the interaction between membrane forming polymer and the solvent molecules could be weakened by the hindrance of NPs so that the solvent molecules can be diffused simply from the polymer-matrix to the coagulation bath **[178]**. Consequently, the porosity and pore size of TiO_2 entangled (i.e. CA-PEG-TiO_2) membrane were higher than those of the membranes without TiO_2 NPs (CA-PEG). The effect of PEG as a pore former as well as hydrophilicity enhancer was also accredited.

4.2.1.4. Membrane hydrophilicity and TiO_2 NPs stability

The hydrophilicity of the prepared membranes was studied by measuring the WCA and the drop age, defined as the duration of the water droplet on the surface of the membrane and spreading and/or permeating through the membrane cross-section **[158]**. The difference of WCA of all the prepared membranes is presented in **Fig. 4.9 (a).** The images of the water droplets with

a volume of about 2 µL at 0.16 mL/min on the membrane surface after 60 s are shown in **Fig. 4.9 (b)**. M_3 and M_4 membranes have taken about 15 s, and 25 s, respectively, and show best water wettability, where most parts of the membrane surfaces were almost fully wetted, and smaller spread radius of the water drops on the top side of the membrane were detected after 60 s. On the other hand, M_1 and M_2 membranes have taken about 36 s and 32 s to initiate the surface wetting and big water drops spread radius on the top side of the membrane were observed after 60 s (**Fig. 4.9b**). The smaller the water drop spread radius wetting area between top and bottom surface and on the top membrane side, the better the water permeability is. As clearly observed form the graph, the WCA results of the pristine CA (M_1) membrane displays WCA about 60±1.8º. Conversely, after the introduction of hydrophilic PEG additive and TiO_2 NPs, the M_2, M_3, and M_4 membranes displayed significantly reduced WCA results (i.e. 54.3±2.3º, 42.1±3.4º, and 45±2.0º, respectively). From these results, it is clearly depicted that the contact angle results of the M_1 membrane were significantly reduced after the introduction of PEG and TiO_2 (M_2, M_3 and M_4). Membranes having smaller contact angle results are considered as more hydrophilic membranes. The WCA results of the prepared membranes found after each soaking period are presented in **Fig. 4.9 (c).** The WCA values for M_1 and M_3 and M_4 have remained almost constant (i.e. 58 ±1.3 º, 38 ±3.3 º and 42 ±2.6 º, respectively) with increasing the soaking period in DI water. On the other hand, the WCA value of M_2 was observed to increase significantly from 51.5 ±2.2 º to 54.7 ±2.0 º, where this increase in WCA value can be accredited that the TiO_2 NPs could leach out from matrix of the CA-TiO_2 membrane with increasing the soaking period. Conversely, no significant change in the WCA values was observed in the case of M_3 (CA-PEG-TiO_2) with the soaking period. This interesting result is mainly accredited to the permanent existence of TiO_2 NPs within the membrane matrix, and the stability of the NPs was confirmed. The stability of the NPs within the membrane matrix was occurred mainly due to the introduction of PEG additive which has prevented the leaching of TiO_2 NPs, tending to an insignificant increase in WCA values during the soaking period **[179]**.

4.2.1.5. Fouling and rejection performance study

Membrane fouling can be defined as the deposition of retained particles, colloids, macromolecules and salts, etc. at the membrane surface, pore mouth or pore wall causing flux

decline. Fouling can be caused by broadly three kinds of substances: organic (macromolecules, biological substances like protein, enzyme, etc.), inorganic (metal hydroxides, calcium salts, etc.), and particulates. Proteins are strongly adsorbed on hydrophobic or less hydrophilic surfaces but less on hydrophilic surfaces **[40, 159]**. In this study, the fouling and rejection experiments of all the membranes were conducted using the ultrafiltration stirred batch cell to investigate the effects of PEG additive and TiO_2 NPs on BSA rejection, permeate flux and anti-fouling properties. The concentration of bovine serum albumin (BSA) protein and pH of the solutions were kept constant (1 g L^{-1}) and at 7.0, respectively, during the experiments by dissolving in deionized water. To investigate the anti-fouling performance of the prepared membranes, three cycle ultrafiltration processes were done using BSA as a model protein. The flux results of pure water and BSA solutions of the prepared membranes are presented in **Fig. 4.10 (a)**.

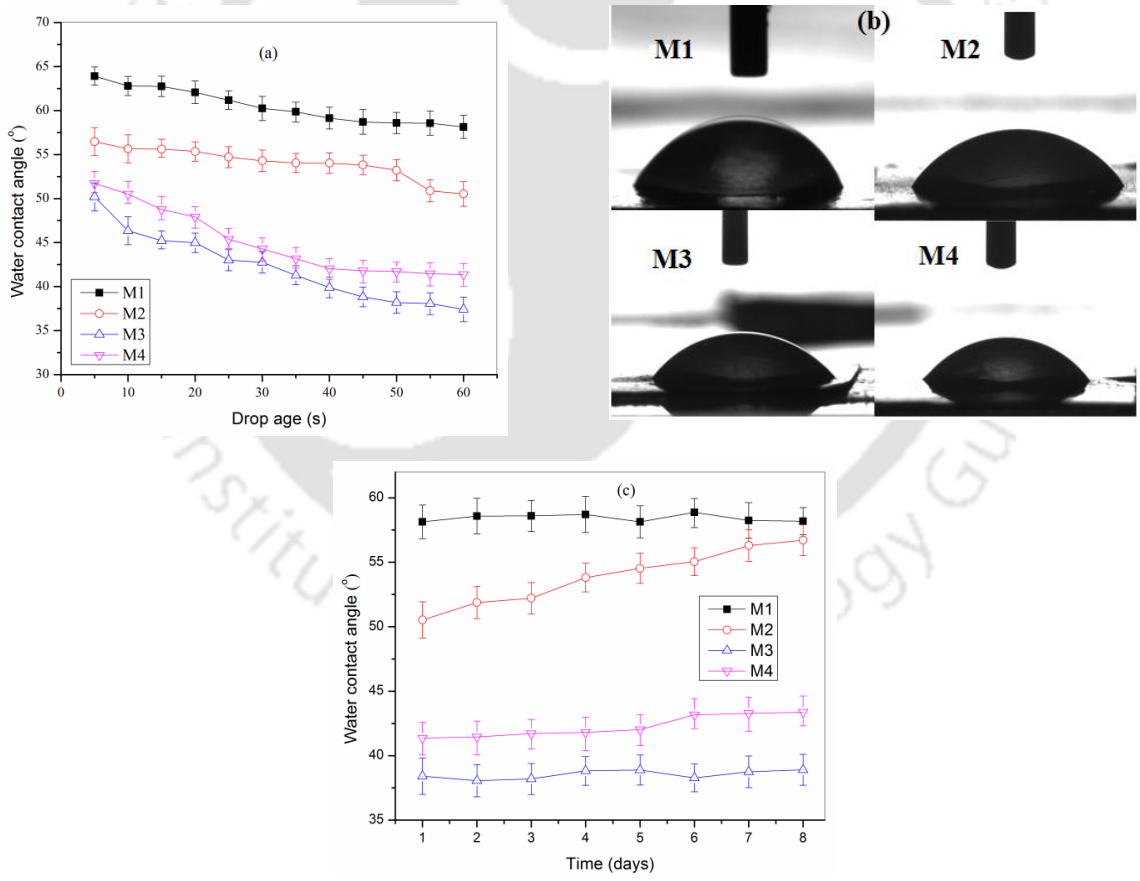

Fig. 4.9. (a) Water contact angle values with different drop ages; (b) images of water droplets of the prepared membranes; and (c) TiO_2 NPs stability study (Water droplet volume is about 2 µL at 0.16 mL/min).

Effect of PEG additive and TiO_2 NPs on fouling

The fouling performances of all the prepared membranes are presented in the **Fig. 4.10 (a).** In this study, the effect of PEG and TiO_2 were evidently detected from the fouling experiments. It is clearly observed from the figure that the PWF and BSA flux results for M_1 and M_2 are less than that of M_3 and M_4. As already explained in previously, these results were attained due to the introduction of PEG and TiO_2 on the membrane matrix in M_3 and M_4 modifies the hydrophilicity and porosity of the membranes. However, the lowest flux results for M_2 were observed because of the less porosity due to the aggregation of the TiO_2 on the membrane surfaces and pore channels of the membrane (**Section 4.2.1.1.**, Morphology study). It is clear from the results that the M_1 and M_2 membranes displayed less PWF as well as the BSA fluxes due to their less hydrophilic nature and less pore formation. The improvement of pure water and BSA fluxes for M_3 and M_4 membranes were attributed to the pore-forming effect and hydrophilic nature of PEG and TiO_2, respectively **[174]**. However, the hydrophilic effect of the TiO_2 in the case of M_2 membrane is dominated by the pore blockage (i.e. less porous membrane). On the other hand, apart from the formation of the porous membrane, a trace amount of PEG may entangle within the membrane matrix permanently, and due to this reason, the hydrophilic nature of the prepared membrane may be enhanced **[73]**. As clearly shown in **Fig. 4.10(a)**, three BSA fouling/rinsing cycles are carried out for a total filtration time of 840 min. Each of the fouling experiments was performed with BSA solution with a concentration of 1 g L^{-1} for 2 h duration, and each rinsing experiments were done with deionized water for 30 min. The decrease in BSA fluxes with increasing time could be due to susceptible pore blocking of the membranes because of BSA protein deposition on membrane surface, where the effect of concentration polarization was reduced by using high molecular weight of BSA (66 kDa) molecules and rigorous stirring (200 rpm) on the surface of the membrane. Moreover, the drop in initial fluxes are realized to be highly noticeable, and the ending fluxes are slowly dropped which are credited to the decreasing in the porosity of the membrane due to an interior deposition of BSA protein which further leads to pore blocking. In the first cycle fouling/rinsing experiment, M_3 displayed the highest flux recovery (i.e. 94.1% of the initial value) with a flux value of 136.3 L m^{-2} h^{-1} at 150 kPa of trans permeable pressure, whereas water flux values of the M_1 and M_2 membranes declined to 31.2 L m^{-2} h^{-1} and 15.3 L m^{-2} h^{-1} respectively, (i.e. 28.6% and 65.7 % of the initial value, respectively). On the other hand, the flux result for M_4 was 134 L m^{-2} h^{-1} with a flux recovery of 88.9 % of the

initial flux value. These results are achieved due to the hydrophilic nature of PEG and TiO_2 which can both minimize severe solute fouling of the membranes. The parameter normalized flux ratio (NFR) with filtration time (2 h) of the membranes operated for three cyles are presented in **Fig. 4.10(b)**. From the figure, it is clearly seen that M_3 exhibited the highest NFR values 94.1%, 88.6% and 84.1 % for cycle 1, cycle 2 and cycle 3, respectively. Moreover, these results indicate that the lowest irreversible flux loss and less BSA deposition on the pore walls as well as on the surface of the membrane consistently during the three cycle operations. However, M_1 and M_2 shown a significant decline in the permeate fluxes to about 28.6 % and 65.7 %, respectively, of the initial flux during the first cycle operation. Moreover, as seen from **Table 4.5**, the irreversible fouling (F_{ir}) results in the first cycle are high enough where their tendency to be fouled would be maximum. To further examine the anti-fouling properties of the prepared membranes and to study the effect of additives, the flux losses viz. total fouling (F_t), reversible fouling (F_r) and irreversible fouling (F_{ir}) were calculated, and the results are presented in **Table 4.5**. On the other hand, the increase in NFR results for M_1 and M_2 during the second and third cycle operations are may be due to the development of a cake layer because of the high irreversible fouling where their flux was too low, and the flux value difference was insignificant. These results are achieved because the porosity and hydrophilicity effect could be played an important role on their anti-fouling and flux properties as already explained in the pure water flux study. Moreover, the NFR results of M_4 are 88.9 %, 88.3 % and 79.1 % for first, second, and third cycle operations, respectively. However, these results are still less than that of M_3 membrane, where it is clear that the introduction of TiO_2 has played a crucial role in the enhancement of hydrophilicity and membrane anti-fouling property. Normally, the orders of flux recoveries for the examined membranes were consistent with their hydrophilicity and porosity nature. Therefore, the PEG free membranes are more likely to prone to pore-blockage and fouling because of protein deposition than those of membranes with PEG. It is mentioned in the literature that the PEG **[161]** has the potential to minimize membrane fouling because of protein deposition **[162]**. In this study, M_3 exhibited better anti-fouling properties in the dynamic fouling process than M_1, M_2 and M_4 membranes. Therefore, the combined effect of PEG and TiO_2 could have played a significant role in a higher resistance towards membrane fouling due to BSA deposition by reducing the hydrophobic interaction between BSA protein and membrane surface. Desorption of the deposited BSA proteins was performed by soaking the samples in water for 30 min. It was

also confirmed that PEG could efficiently avoid the irreversible deposition of the protein on the surfaces. Therefore, due to the hydrophobic interaction between PEG and BSA, the proteins might be wrapped by PEG chains, forming a protective layer in addition to the anti-fouling properties of TiO_2.

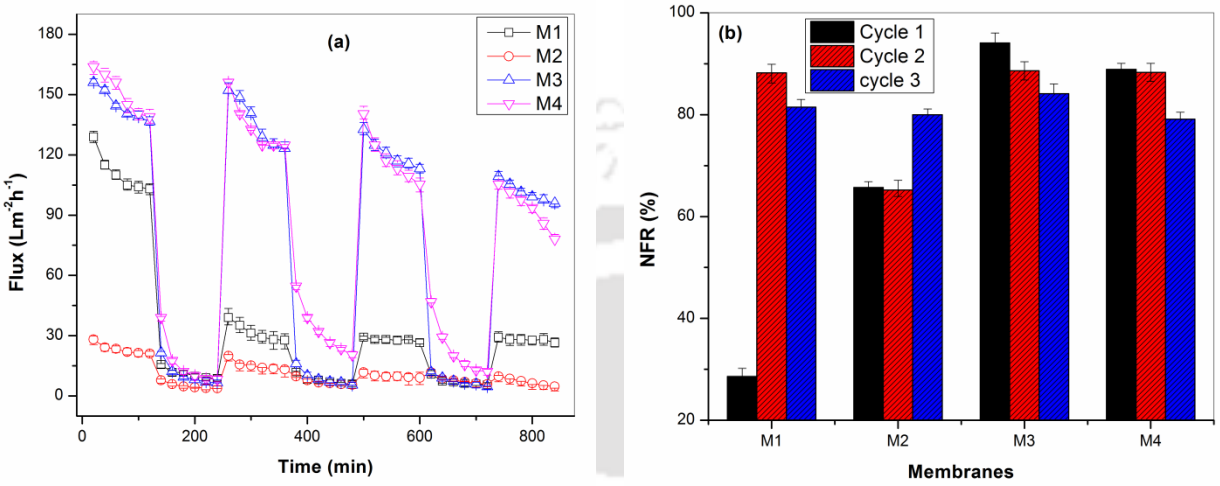

Fig. 4.10 (a) Permeate flux versus filtration time for M_1 (CA), M_2 (CA-TiO_2), M_3 (CA-PEG-TiO_2) and M_4 (CA-PEG) membranes: effect of PEG and TiO_2 NPs on the anti-fouling performance of the membranes (25±2 ºC, 150 kPa), (b) NFR percentage results.

Additional focus was given to the influences of filtration resistance due to concentration polarization for all membranes. The rate of fouling is determined by both the physicochemical properties of the membrane and the hydrodynamic conditions in the membrane device (filtrate flux and bulk mass transfer). In general, membrane fouling is comprised of irreversible and reversible fouling. In the case of reversible fouling, deposited protein could be removed easily using hydraulic cleaning (i.e. back washing and cross flushing). Conversely, the irreversible fouling occurs due to an irreversible adsorption of proteins which can only be removed using chemical cleaning. Therefore the resistances due to concentration polarization were calculated using the resistance in series model Eq. **(3.9).** The total fouling resistance of all the membranes thus was due to both internal membrane fouling (adsorption and deposition) and the formation of a cake/gel layer on the membrane surface. As clearly presented in **Table 4.6**, the results of the fouling resistance due to concentration polarization (R_P) for M_3 are low in the three cycles when compared to the other membranes (i.e. M_1, M_2, and M_4). Therefore, the effect of concentration polarization on the membrane surface was reduced due to the introduction of PEG and TiO_2 simultaneously. These results are consistent with the flux recovery results of the membrane were

the highest values were attained (**Table 4.5**), and it was accredited to the best ant-fouling property of the M_3 membrane as already discussed in the previous sections.

Table 4.5 Results for flux losses caused by total fouling *(F_t)*, reversible fouling *(F_r)* and irreversible fouling *(F_{ir})*, of the three cycles

	First cycle				Second cycle				Third cycle			
Membrane	F_t	F_r	F_{ir}	*NFR*	F_t	F_r	F_{ir}	*NFR*	F_t	F_r	F_{ir}	*NFR*
M_1	0.90	0.21	0.71	28.6	0.75	0.61	0.15	85.2	0.73	0.55	0.19	81.5
M_2	0.78	0.44	0.34	65.7	0.54	0.20	0.35	65.4	0.21	0.01	0.20	80
M_3	0.92	0.87	0.06	94.1	0.93	0.82	0.11	88.6	0.94	0.78	0.16	84.1
M_4	0.89	0.78	0.11	88.9	0.77	0.64	0.12	88.3	0.81	0.60	0.21	79.1

4.2.1.6. Rejection performance

The BSA rejection performances of the prepared membranes are shown in **Fig. 4.11**. The maximum BSA rejection values 98.4 % and 91.6% were attained for M_2 and M_1 membranes, respectively. On the other hand, the rejection results for M_3 and M_4 membranes are 88.9 % and 85.9 %, respectively. It is clearly explained in the morphology analysis section that the PEG free membranes have less porous structures, in which a better resistance to protein molecules was detected. However, the slight increase in BSA rejection for M_3 membrane could be due to the effect of TiO_2 addition to the membrane matrix. The characteristic BSA rejection can be described using the protein deposition/repulsion phenomenon as already explained above. The prepared membranes could become more negatively charged after an introduction of TiO_2 NPs due to more negatively charged carboxylic groups along with –OH and Ti–OH groups present on the surfaces and within the matrices of the membranes **[180]**. Furthermore, as pH 7.0 is far from isoelectric point (IEP=4.9), the BSA protein becomes more negatively charged, and a stronger electrostatic repulsion between BSA and the modified membranes was suggested **[181]**. However, some of the BSA removal characteristic can also be described using the protein deposition phenomenon onto the membrane surface in this pH range which could be accredited to structural interaction. In addition to the electrostatic repulsion phenomena, the highest BSA

removal for M_2 and M_3 membrane was also considered as an indicator of considerable protein removal due to its structural interaction.

Table 4.6 Results for resistances due to the membrane (R_m), fouled layer (R_f) and polarization (R_p) of the three cycles

Membrane	First cycle				Second cycle				Third cycle			
	$\Delta p/\mu J_{bs}$	R_f	R_m	R_p	$\Delta p/\mu J_{bs}$	R_f	R_m	R_p	$\Delta p/\mu J_{bs}$	R_f	R_m	R_p
M_1	7.78	1.37	0.55	3.58	7.79	1.62	0.55	5.61	8.49	1.62	0.55	6.32
M_2	8.73	1.37	2.60	8.05	8.73	3.50	2.06	2.62	7.72	4.99	2.60	2.92
M3	1.86	0.02	0.42	3.37	1.86	0.08	0.40	1.37	2.67	0.18	0.40	2.07
M_4	6.82	0.05	0.40	5.17	6.82	0.11	0.41	6.30	13.6	0.25	0.42	12.9

** All the units are in ($\times 10^{-10} m^{-1}$)*

The BSA removal phenomenon for M_1 and M_4 membranes can be suggested due to a substantial protein deposition inside and on the membrane surfaces. Therefore, the surface depositions of BSA proteins can provide an extra hindrance to solute transportation. The high rejection and comparatively lowest flux of M_2 and M_1 membranes than M_4 and M_3 can also be seen from the morphological study of their cross-section. Moreover, all the experimental results were consistent with the membrane properties and agreed with each other.

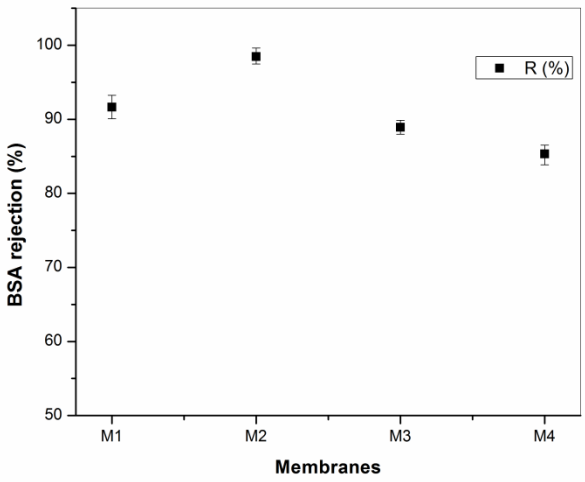

Fig. 4.11 BSA rejection performances of M_1 (CA), M_2 (CA-TiO_2), M_3 (CA-PEG-TiO_2) and M_4 (CA-PEG) membranes: effect of PEG and TiO_2 NPs (25±2 ºC, 150 kPa)

The results presented in this work clearly show that a detailed performance evaluation was done for the prepared ultrafiltration M_3 membrane (i.e. CA-PEG-TiO_2) in this study than the previous studies **[48, 53, 73]**. Therefore, the improved thermal stability and high anti-fouling properties of this membrane will help us to further investigate for specific ultrafiltration applications. Thus, the authors strongly believe that this work will have a substantial contribution to the current state-of-the-art on the modification and enhancement of the properties of conventional cellulose acetate membranes. Future studies will be needed to fully investigate the performance characteristics of CA-PEG-TiO_2 membranes for different ultrafiltration applications.

4.2.2. Summary

In the present work, the effects of PEG and TiO_2 on the preparation of phase inverted CA ultrafiltration membrane blended with TiO_2 (i.e. CA-PEG-TiO_2) were investigated, and the following conclusions were made:

- In the case of M_2 (CA-TiO_2) membrane, some of the TiO_2 observed to be aggregated on the surface of the membrane pores. The NPs agglomeration led to a non-uniform dispersion of the NPs within the polymer surface and structure.

- TiO_2 NPs are highly stable at high temperatures, and the degradation temperature of the M_1 and M_4 were significantly improved after addition of TiO_2. The thermal stability of M_3 exhibited higher degradation temperature than the M_1 and M_4. The slight improvement in degradation temperature for the M_2 due to the less porous sublayer structure and strong resistant to heat flow than that of the porous membrane (M_3).

- The introduction of both PEG additive and TiO_2 NPs at a time play an important role in the improvement of the thermal stability of membrane, hydrophilicity, porosity and antifouling performance simultaneously.

- Membranes without PEG additive (i.e. M_1 and M_2) showed lower PWFs when compared with the membranes having PEG additive (M_3 and M_4). The PWF values at 250 kPa, for M_3 and M_4, are 530.7 and 265 L/m^2 h, respectively; whereas these values are 204.5 and 21.1 L/m^2 h, respectively for M_1 and M_2. The highest PWF was attained for the M_3 (CA-PEG-TiO_2).

- The maximum BSA rejection values 98.4 % and 91.6% were attained for M_2 and M_1 membranes, respectively. The rejection results for M_3 and M_4 membranes are 88.9 % and 85.9 %, respectively. CA-TiO_2 blended with PEG membrane (i.e. M_3) exhibited highest BSA fluxes and flux recovery ratios for the three fouling/rinsing cycles.

4.3. Preparation and characterization of fouling resistant ultrafiltration membranes based on the blends of cellulose acetate and PVP−TiO_2 nanoparticles for removal of bovine serum albumin

The CA-PVP-TiO_2 membranes were prepared by dissolving the polymers in a mixture of acetone (AC) and N, N-dimethylacetamide (DMAc) (70:30) solvent and distilled water were used in the coagulation bath. The introduction of polyvinylpyrrolidone (PVP) additive and TiO_2 nanoparticles (NPs) into the casting solution changed the structure of the resulting membranes during the phase inversion process. The influences of PVP and TiO_2 NPs as an additive on the preparation of phase inversion cellulose acetate (CA) ultrafiltration membrane blended with TiO_2 NPs (CA-PVP-TiO_2) were explored in terms of morphology study, equilibrium water content, hydraulic resistance, permeability performance, and thermal stability. An improvement in average pore size, porosity and hydrophilicity of the CA membranes were detected after the introduction of PVP and TiO_2 NPs to the polymer matrix. The thermo gravimetric analysis (TGA) results confirmed the interaction between TiO_2 NPs and the degradation temperature of the CA membrane were significantly improved. The anti-fouling performance and the recycling potential of the UF membranes were investigated using bovine serum albumin (BSA) as a model protein. It was found that the CAT membrane with PVP additive (i.e. CA-PVP-TiO_2) displayed improved BSA flux permeates and flux recovery ratios for the three fouling/rinsing cycles.

4.3.1. Results and discussion

4.3.1.1. Study of TiO_2 nanoparticles

The size of commercial TiO_2 nanoparticles was determined using transmission electron microscopy (TEM) as presented in **Fig. 4.12** in chapter 3. The TiO_2 nanoparticles appeared in the form of spots. To measure the size of each nanoparticle, Image J software was employed, and their size was ranging from 15 to 71 nm. The average particles size was approximately 29 nm.

4.3.1.2. Morphological study

The top layer surface view, cross-sectional view, EDS images, and maps of the prepared membranes are presented in **Fig. 4.12(a), (b), (c)** and **(d),** respectively. The presence of the TiO_2 NPs within the matrixes of the membranes was confirmed from the EDS results. It is already seen from the figures that all the prepared membranes exhibited asymmetric structure involving of a dense top-layer and a porous sub-layer. However, the sub-layer structure of the CA membrane seems to have finger-like structures and macro-void. It is known that there are several factors that made the finger-like structures and macro-voids to occur during membrane preparation using immersion precipitation method. The effect of solubility parameter differences among organic additives and CA on the morphological structures of the resulting membranes were studied in our previous work **[102]**. The formation or suppression of macro-voids can significantly be influenced by the type of de-mixing occurred during the phase separation process. The instantaneous de-mixing and the delayed de-mixing depend on the mutual affinity of the solvent and non-solvent in the ternary system **[40]**. The occurrence of macro-voids in membranes prepared from ternary systems: (1) membranes without macro-voids can be formed in the case of delayed de-mixing, except when the delay time is very short; (2) membranes with macro-voids can be formed in the case of instantaneous de-mixing, except when the polymer concentration and/or the non-solvent concentration in the casting solution exceed a minimum value **[141]**. Generally, macro-voids formation occurs under rapid precipitation condition, and the precipitation is quicker at higher coagulation temperature **[53]**. In the current study, the coagulation bath temperatures and evaporation step prior to the immersion process were kept at 25 ºC and 30 s, respectively, throughout the membrane preparation process **[50]**.

Effects of PVP and TiO_2 NPs

In general, the addition of organic and/or inorganic additives to the membrane forming polymer can increase the concentration and then the viscosity of the casting solution. This increase in viscosity may, in turn, reduce the diffusional exchange rate of the non-solvent and solvent in the membrane preparation procedure (i.e. phase inversion method) **[53]**. Accordingly, this can delay the instantaneous liquid-liquid de-mixing process to occur and hinders the formation of macro-voids. In solvent and polymer interaction scheme, three kinds of interactions viz. polymer: polymer, polymer: solvent and solvent: non-solvent is applied. If good polymer

solvents are used, the degree of polymer stretching reaches to its highest level, and more favorable polymer/solvent interactions can occur. The solvents used in this study (i.e. AC: DMAc) have high mutual affinity with water **[150].** Thus, evidently, the development of the finger-like voids and macro-voids in the sub-layer of the CA membrane is due to the instantaneous de-mixing **[103].** In this case, the CA stretches to its highest level where there is a maximum interaction between the CA and AC: DMAc which tends to instantaneous de-mixing condition to happen. On the other hand, after adding the PVP and TiO_2 to the ternary (polymer/solvent/non-solvent) system, the developments of finger-like structures are suppressed significantly (i.e. i.e. CAT, CATP and CAP). The presence of the polymeric additives and TiO_2 NPs can increase the concentration/viscosity of the casting solution which may diminish the diffusional exchange rate of the AC: DMAc and water during the membrane formation process. Accordingly, this may hamper the instantaneous liquid-liquid de-mixing process which suppresses the development of finger-like and macro-voids **[182]**. However, the presence of large macro-voids along with micro porous structure in the case of CAP membrane can be explained because of its water soluble behavior, PVP can simply assemble around the water molecule during immersion precipitation process resulted in the development of PVP rich phase **[43]**. On the other hand, the introduction of water (i.e. non-solvent) soluble hydrophilic additive with high affinity to the solvents and low affinity to the membrane forming polymer, tends the thermodynamic instability of the casting solution to increase, which further leads to instantaneous de-mixing to sustain in the coagulation bath. These results, on the other hand, could make the macro-voids to develop in the membrane sub-layer structure **[182]**. In quaternary system two phases arise from the phase separation, one involves of the CA (i.e. membrane forming polymer), AC:DMAc (i.e. solvent) and water (i.e. non-solvent) and the second contains the polymeric additive (i.e. PVP), solvent (i.e. AC:DMAc) and non-solvent (i.e. water). The membrane forming polymer and additive have a driving force to separate completely into a CA-rich and a PVP-rich phase. Accordingly, the type of de-mixing process, in this case, can be influenced by the diffusion/movement of the two polymers on each other. Therefore, this phenomenon should be slow compared to the diffusion of solvent and non-solvent in the polymer solution. To maintain this, a polymeric additive with a certain minimum molecular weight in the system is required **[139]**. On the other hand, the addition of TiO_2 to the membrane formation system has its effect on the de-mixing process. It was evidently observed from the FESEM

images that the fingers-like structures and macro-voids in the membrane sub-layer were significantly reduced after the adding of TiO_2 NPs in CAT and CATP membranes. As shown from the FESEM images the finger-like structures and macro-voids are reduced in the case of CAT and highly suppressed in the case of CATP after adding TiO_2 irrespective of the effect of PVP additive. Nevertheless, the CAT membrane seems to have less micro porous cross-sectional structures with some defect structures. This result can be described due to some of the TiO_2 could be accumulated on the surface and pore walls of the membrane. It is also observed from the top surface image of CAT (**Fig. 4.12a)** that the accumulation of some of the TiO_2 NPs was clearly detected as indicated by the circles. The enhancement of membrane morphological structure occurs with the addition of a small amount of TiO_2 NPs **[170]**. In the current study, the concentration of the TiO_2 NPs was fixed at 2 wt. %. Therefore, the finger-like structures and macro-voids observed in the CA membrane was greatly suppressed, and a relatively dense layer with micro porous structures was observed for CATP. However, minor macro-void and finger-like structures were still detected in the case of CAT membrane, and these results are suggested to be related to the interference effect of NPs during the phase inversion process. Thus, due to the interfacial stress between polymers and NPs, interfacial pores are formed as a result of shrinkage of polymer-phase during the de-mixing process **[173]**. The presence of TiO_2 in CAT diminishes the presence of finger-like structures and a sublayer structure with almost macro-voids free is obtained. These results can be described in terms of NPs agglomeration on the membrane forming polymer matrix during phase inversion process. The occurrence of NPs agglomeration can be mainly caused due to the high surface energy of the NPs, which tend to aggregate for weakening their surface energy to reach a more stable state. Furthermore, NPs agglomeration leads to a non-uniform dispersion of the NPs within the polymer surface and structure. This phenomenon can negatively change the resulting membrane properties such as hydrophilicity and surface roughness **[171].** However, in the case of CATP, the NPs agglomeration was significantly minimized due to the improved distribution of the NPs because of the introduction organic additive **[174].** From these results, it can be concluded that although the instantaneous de-mixing is still sustained, the effect of the PVP and TiO_2 NPs have considerable role on the hindrance of the finger-like structure and macro-voids which was occurred for CA membrane **[182]**. However, the presence of large macro-voids along with micro porous structure in the case of CAP membrane is because of the water soluble behavior of PVP

where it can simply assemble around the water molecule during immersion precipitation process resulted in the development of PVP rich phase **[43]**. Therefore, the developments of macro-voids are as a result of rapid penetration of water at some weak spots in the top-layer. Thus, the PVP rich phase may act as the weak spot in the precipitation process and resulted in the formation of macro-voids **[57]**. As indicated by the rectangular shapes for the CATP and CAP in **Fig 4.12**, the formation of micro porous structures is related to the pore forming nature of PVP. However, the formations of big macro-voids structures in CAP membrane are undesirable, so that they may cause lack of thermal and/or chemical stabilities in the resulted membrane.

4.3.1.3. Thermal stability analysis

It can be clearly seen from TGA and DTG figures (**Fig. 4.13 (a)** and **(b)**, respectively) that the decomposition of CA membrane showed three steps where the graphs were plotted as weight loss (%) vs. temperatures (ºC). The first degradation step of CA membrane was detected between 30 and 260 °C, and the weight loss was about 21%. This degradation is due to the presence of some volatile material or because of the evaporation of absorbed moisture by the sample. During the second degradation step, a maximum weight loss of around 76% was detected between 260 to 380 °C which is because of the main thermal breakdown of CA chain **[183]**. The last degradation step greater than 380 °C was due to the carbonization of the decomposed products to ash. The TGA results of the CA membrane clearly presented that it could not be stable at high temperature and similar results were reported by Zafar et al., **[175]**. On the other hand, the TGA results of the CA membranes with PVP and TiO_2 displayed two-step degradation procedures. Therefore, the first decomposition step for CAT, CATP and CAP are 320 °C, 227 °C, and 208 °C, respectively. These observed weight losses are due to the decomposition of CA chains because of the pyrolysis of the skeleton back-bone of the CA polymer, which is also followed by de-acetylation of CA **[176]**. During the second decomposition step, the degradation temperatures of CAT, CATP, and CAP are 400 °C, 390 °C and 387 °C, respectively, signifying the main thermal degradation of the CA chains, whereas the TiO_2 were highly stable up to 800 °C.

(a) **(b)**

CA

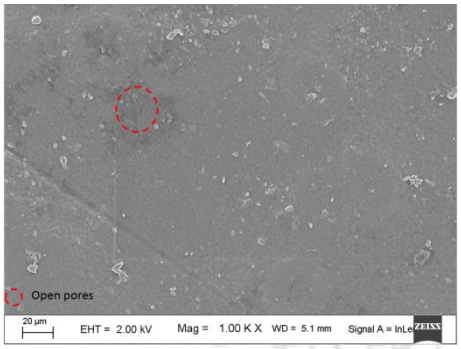

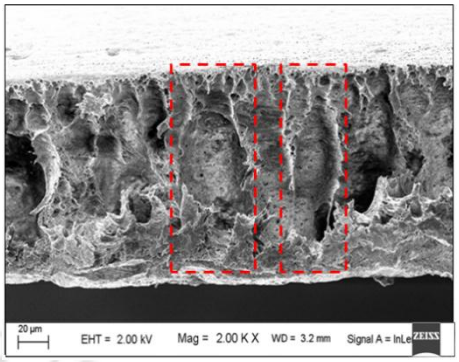

CAT

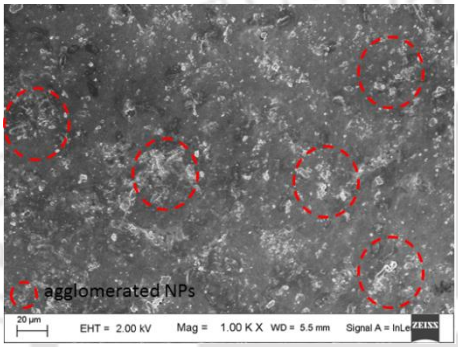

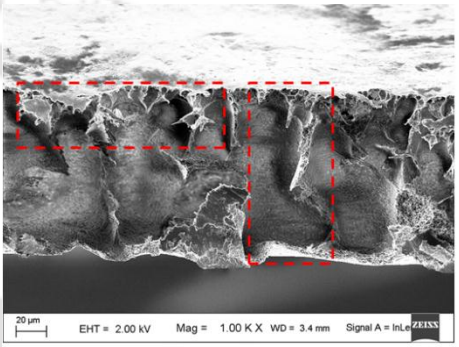

CATP

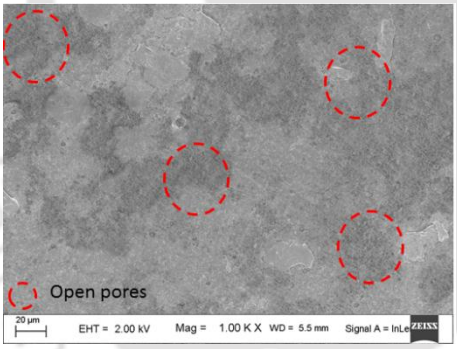

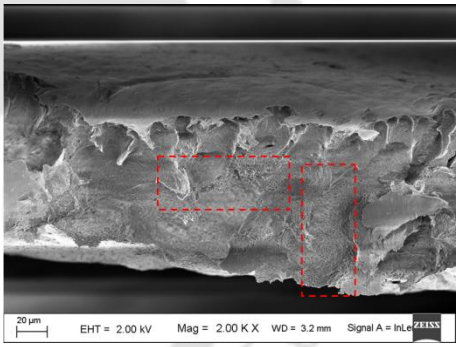

CAP

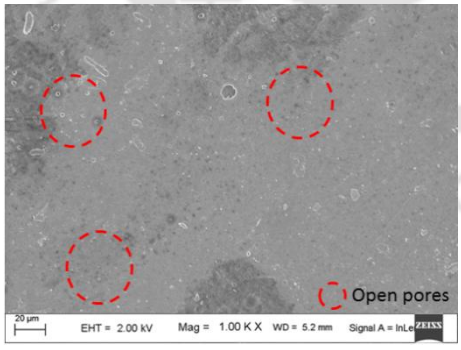

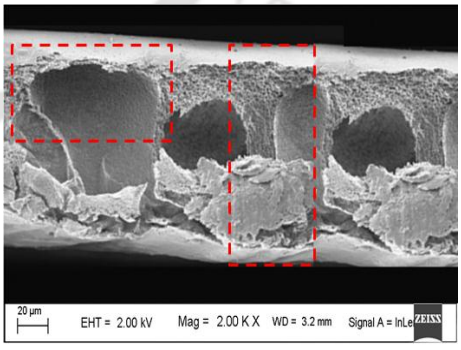

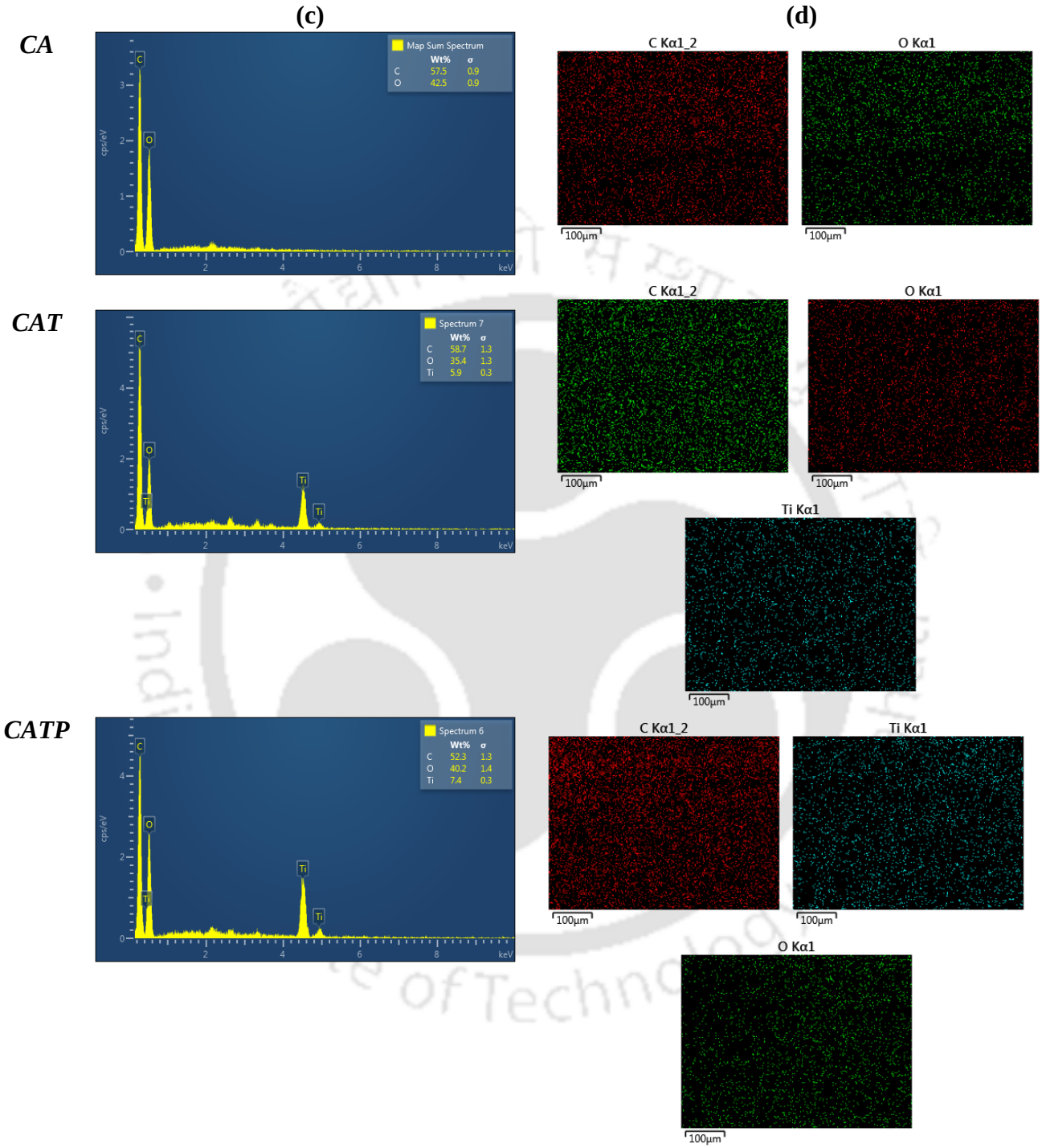

CAP

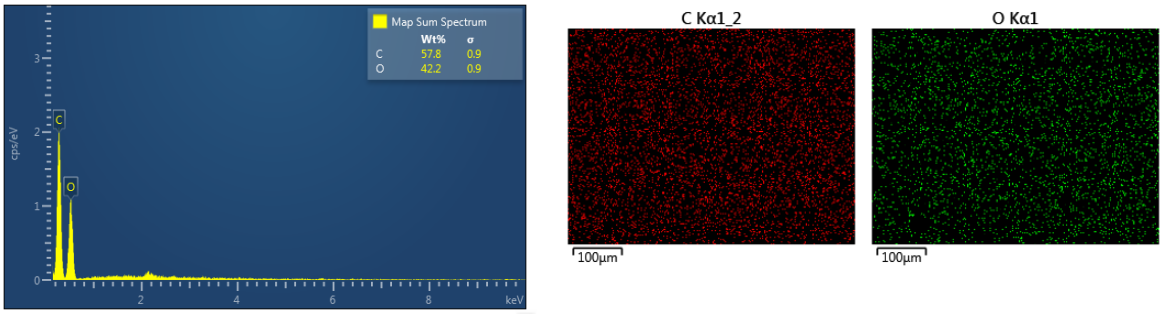

Fig. 4.12. (a) The top surface, (b) cross-sectional, (c) EDS and (d) mapping images of CA, CA with PVP and TiO_2 NPs membranes.

From these results, it is clearly observed that the thermal degradation of CA membrane was significantly enhanced due to the addition of PVP and TiO_2. Another interesting observation from this study is that an increase in thermal stability after addition of PVP to CA membrane (i.e. CAP) is due to the presence of a trace amount of the PVP in the membrane matrix. The improved thermal stability of the CA membranes after addition of PVP was due to the strong interaction between the CA and PVP in the membrane matrix by creating hydrogen bonds **[177]**. Therefore, the improvement of the membrane hydrophilic nature due to the presence of PVP within the membrane matrix in addition to the enhancement of its thermal stability was credited. Furthermore, the thermal stability of CATP membrane exhibited higher degradation temperature than CAP membrane. This result is attained due to the fact that the TiO_2 nanoparticles are highly stable at high temperatures and therefore the degradation temperature of the CAP membrane was significantly improved after addition of TiO_2. On the other hand, the slight improvement in degradation temperature for the CAT membrane when compared with CATP membrane was that the less porous sub-layer structure of the membrane is responsible for have strong resistant to heat flow than that of the porous membrane (i.e. CATP). In this study, the TGA plots have clearly revealed that the thermal properties of CA membrane were significantly improved after incorporation of PVP and TiO_2 into the CA solution.

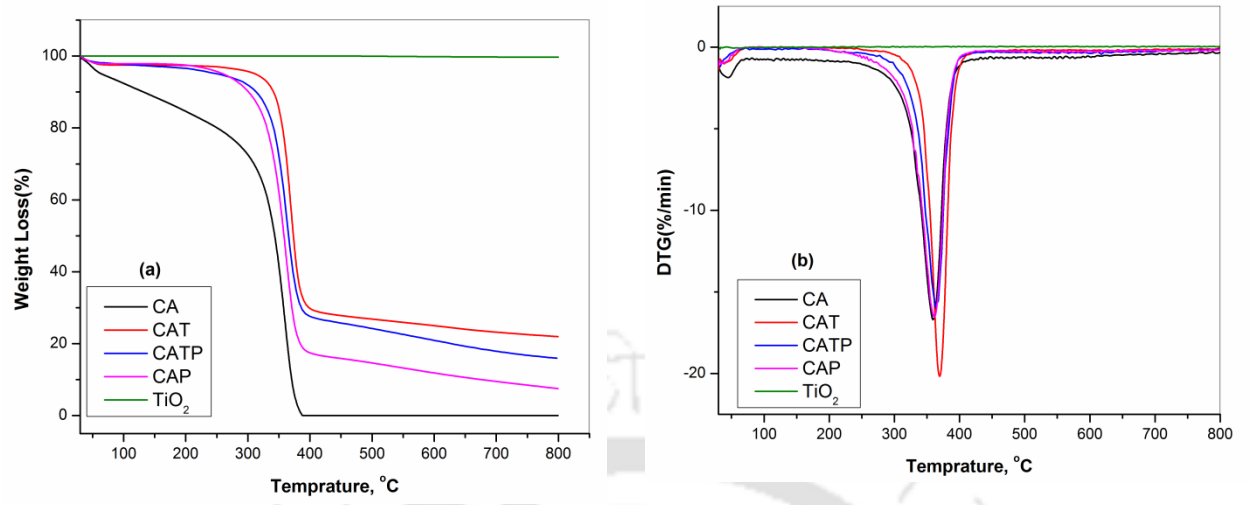

Fig. 4.13. (a) TGA and (b) DTG analysis of all the prepared membranes and TiO_2 nanoparticles.

4.3.1.4. Pure water flux study

Studying of membrane compaction factor (CF) is crucial to investigate the morphological structures, especially the pore arrangements of the membranes and the membrane sub-layer configuration. Membranes having high CF indicates that they are highly compacted which further show the existence of some defect pores in the membrane sub-layer structure **[44]**. Thus, the influences of compaction time on pure water flux of the prepared membranes are showed in **Fig. 4.14(a)**. It is seen from the figure that the PWF results of all the membranes were observed to decrease slowly with increasing time because of the pore compaction and lastly the steady state fluxes were reached approximately after 90 min filtration process. The gradual decrease in PWF results can be described due to the compaction of pore walls attained uniform and denser structures and caused the pore size and the flux to decrease **[40]**.

Effect of PVP and TiO_2 NPs

It is essential to discover the effect of PVP and TiO_2 NPs on the membranes compaction process, where the effects of PVP and TiO_2 were considerably observed from this study. From the compaction study, it was observed that the CA and CAT membranes displayed lower PWF results when compared with the CATP and CAP membranes. As seen from **Table 4.7,** the PWF results at an operating pressure of 300 kPa for CA, CAT, CATP, and CAP are 248 L/m^2 h, 26 L/m^2 h, 416 L/m^2 h, and 978 L/m^2 h, respectively. These results are evident that the introduction

of hydrophilic PVP and TiO_2 NPs to the membrane casting solution made these membranes to be porous and more hydrophilic **[143]**. The lowest PWF for CAT can be explained as the blockage of pores due to aggregation of the TiO_2 inside the membrane matrix. Regardless of the effect of TiO_2 NPs in the case of CATP, the membranes with PVP additive displayed high PWF results. These results clearly indicate that the introduction of hydrophilic additive (i.e. PVP) influences the membrane in two ways: (1) pore forming ability and (2) hydrophilic nature, where the PWF properties of the prepared membranes were significantly improved after the introduction of PVP **[144, 145]**. In the first case, the membrane porosity increased after the introduction of PVP and secondly, the whole removal of PVP additive from the membrane forming polymeric matrix may not be attained during the phase separation process in the coagulation bath and even after rinsing with deionized water **[50]**. Consequently, the trace amounts of PVP additive which are entrapped in the membrane matrix permanently, thus, enhance the membrane hydrophilic property. Comparing CATP and CAP, the membrane without TiO_2 NPs (i.e. CAP) displayed higher flux than CATP membrane. The increase in water flux for membranes prepared from casting solutions CAP membrane is due to the presence of few macro-voids. On the other hand, the CATP showed moderate water flux and where the macro-voids and finger-like structures were significantly suppressed but still with the development of micro porous structures (i.e. important for the porosity of membrane). It is also mentioned in the literature that TiO_2 could considerably increase the porosity of the resulted membrane **[184]**. However, in this study, the influence of TiO_2 on membrane porosity was insignificant as all the prepared membranes exhibited a reasonably high porosity, i.e. greater than 80% except for CAT membrane (i.e. 61.1 %). Generally, adding of TiO_2 NPs alone to the polymeric solution can increase its viscosity. Therefore, the particles leaching problem is lesser, and subsequently, the pore forming effect of NPs can be declined in the case where the high viscosity of a solution hampers the development of pores and causes the porosity of the membrane to decrease **[170].** As clearly seen from the results presented in **Table 4.7**, the introduction of TiO_2 into the CA membrane matrix (i.e. CAT), resulted in water flux decline as membrane average pore size was decreased from 22.2±4.0 nm (i.e. CA) to 14.9±6.0 nm (i.e. CAT). The decrease in average pore size of the membranes after the introduction of TiO_2 was mainly credited to the pore blocking caused by aggregation of TiO_2 on the membrane matrix. In addition to pore blockage, it is also explained that the aggregation of TiO_2 may also cause to reduce the contact area of hydroxyl groups carried by TiO_2 with water

molecules, which could further influence the membrane water permeability properties **[100]**. On the other hand, the introduction of TiO_2 alongside with PVP has shown significant improvement on the average pore size and flux property of the resulted membranes. Thus, it is believed that the presence of hydrophilic PVP can hinder the pore blocking activity of TiO_2 due to its pore forming property as it is easily soluble in the non-solvent (i.e. water) regardless of the presence TiO_2 **[174]**. Though the flux of CAT membrane was expected to increase after the introduction of TiO_2 NPs due to improvement of membrane hydrophilicity **[184]**, membrane pores plugging reduces the influence of hydrophilic nature on the PWF results. Another important point which should be noted is that the hydrophilic nature and higher average pore size of the CA membrane have its effect on the PWF of the membrane, without additive, so that it has shown better flux result than the CAT.

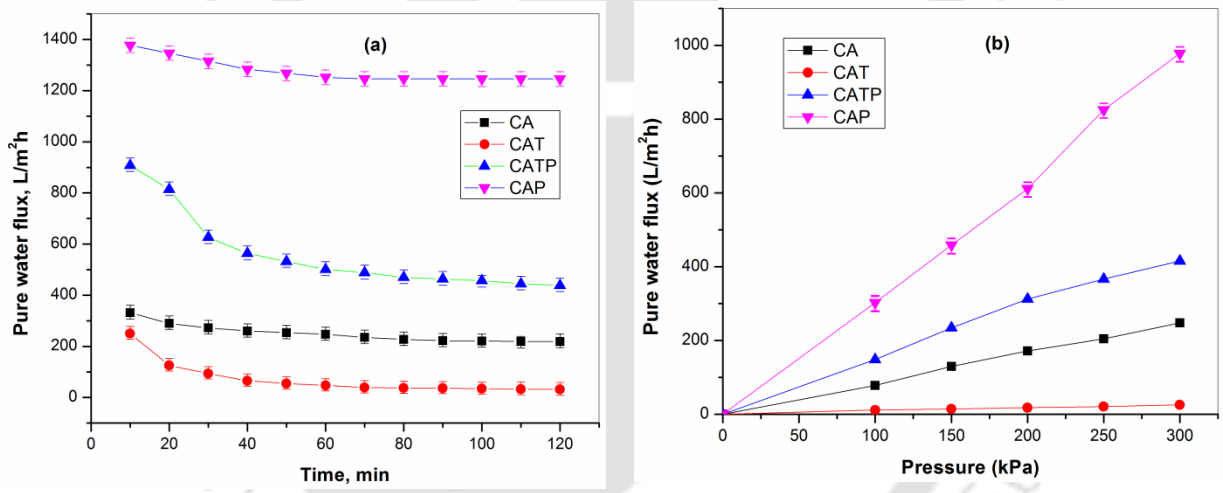

Fig.4.14 (a) PWF profile during compaction study, (b) effect of trans membrane pressure on PWF

The results of compaction factor of all the prepared membranes are presented in **Table 4.7**. As it is observed from the **Table 4.7**, the CF of CAT (i.e. 4.0±0.2) is greater than all of the other membranes. This result can be explained due to the fact that the aggregated TiO_2 on the pore walls and surface of the membrane could further compact and may block the pores after compaction process. On the other hand, the CF results for CA, CATP, and CAP are 1.5±0.4, 1.1±0.4, and 2.1±0.3, respectively. The relatively smaller CF value for CATP was suggested due to the uniformly interconnected pore structures existed in the membrane matrix because of the simultaneous introduction of PVP and TiO_2 NPs **[44].** On the other hand, the effects of PVP and

TiO_2 NPs on PWF at different operating pressures are presented in **Fig.4.14(b)**. The results of PWF for all the membranes were increased almost uniformly with increasing the operating pressure from 100 to 300 kPa. It is also observed that the PWF results for CA and CAT membranes are lower than that of CATP and CAP. As seen from the results of the hydraulic resistance presented in **Table 4.7**, the CAT displayed higher resistance than all the other membranes. This higher resistance is due to the less porous structure of the CAT membrane as compared to the other membranes; in turn, it has a higher tendency to resist the water flux than the other membranes.

Table 4.7 Compaction and hydraulic characteristics of those prepared membranes at 300 kPa

Membrane	***CF***	***R_m***	***J_w***	***EWC***	***ε***	***r_m***	**Thickness**
		($\times 10^{-10} m^{-1}$)	*(L/m^2h)*	*(%)*	***(%)***	(nm)	*μm*
CA	1.5±0.4	0.4	248	76.8±1.6	82.0±2.0	22.2±4.0	71.1±3.0
CAT	4.0±0.2	4.6	26	66.7±2.5	61.1±2.5	14.9±6.0	62.3±7.0
CATP	1.1±0.4	0.3	416	81.8±1.7	85.3±1.8	34.8±3.1	68.7±4.5
CAP	2.1±0.3	0.1	978	83.7±1.3	86.9±1.9	37.9±2.2	70.3±3.2

Moreover, this result is supported by the average pore radius calculation (**Eq. 3.13**). Therefore, the membrane with less average pore radius is more likely to have higher resistance to water flux irrespective of the hydrophilic nature of the membranes. Thus, the increase in hydraulic resistance and decrease in flux with and without PVP is obviously due to the decrease in average pore size and porosity as already explained in the previous sections. The PVP is more hydrophilic than the CA polymer. Therefore, the membranes with PVP have displayed improved flux results. Comparing CATP and CAP membranes, the CAP membrane has shown less resistance and higher flux than CATP membrane. The EWC and porosity results of the prepared membranes results are also calculated using **Eq. (2.6 and 2.7)** and presented in **Table 4.7**. The results from the porosity measurement showed that all the membranes have a satisfactory

porosity in the range of 61.1 to 86.9%, which can be accredited to low concentration of membrane forming polymer (10.5 wt.%); as well as due to the addition of PVP and TiO_2 together with the type of solvent used and type of de-mixing occurred **[185]**. The effect of PVP as a pore former as well as hydrophilicity enhancer was also accredited.

4.3.1.5. Membrane hydrophilicity and TiO_2 NPs stability

The hydrophilicity nature of all the prepared membranes was studied by measuring the WCA and the drop age, defined as the duration of the water droplet on the surface of the membrane and spreading and/or permeating through the membrane cross-section **[158]**. The differences on WCA of all the prepared membranes are presented in **Fig. 4.15 (a)**. The images of the water droplets on the membrane surface after 60 s are shown in **Fig. 4.15 (b)**. As clearly observed form the graph the contact angle results for CA, CAT, CATP, and CAP are 60.5 ±1.3 º, 54.1±2.0 º, 45.4 ±3.2 º, and 47.3±2.8º º, respectively. From these results, it is clearly depicted that the contact angle results of the CA membrane were significantly reduced after the introduction of PVP and TiO_2 (CAT, CATP, and CAP). CATP and CAP membranes have taken about 22 s, and 30 s, respectively, and show best water wettability, where most parts of the membrane surfaces were almost fully wetted, and smaller spread radius of the water drops on the top side of the membrane were detected after 60 s. On the other hand, CA and CAT membranes have taken about 40 s and 32 s to initiate the surface wetting. Big water drops spread radius on the top side of the membrane was observed for CA after 60 s **(Fig. 4.15b).** The smaller the water drop spread radius wetting area between top and bottom surface and on the top membrane side, the better the water permeability is **[158]**. From these results, it is clearly depicted that the contact angle results of the CA membrane were significantly reduced after the introduction of PVP and TiO_2 (CAT, CATP, and CAP). Membranes having smaller contact angle results are considered as more hydrophilic membranes **[171]**. On the other hand, the stability of the TiO_2 NPs incorporated within the matrix of the modified membranes was studied qualitatively. All the prepared membranes were soaked in DI water for 12 days at room temperature (25 ± 2 ºC). The WCA values of all the membranes were done and the TiO_2 leaching tendency during each soaking period was evaluated **[179]**. The WCA results of the prepared membranes found after each soaking period are presented in **Fig. 4.15 (c).** The WCA values for CA, CATP and CAP have remained almost constant (i.e. 58.5 ±1.5 º, 42.6 ±3.0 º and 44.5 ±2.7 º, respectively) with

increasing the soaking period in DI water. On the other hand, the WCA value of CAT was observed to increase from 50.5 ±2.9 º to 58.6 ±2.2 º, where this increase in WCA value can be attributed that the TiO_2 NPs could leach out from matrix of the CA-TiO_2 membrane with increasing the soaking period. Conversely, no significant change in the WCA values was observed in the case of CATP with the soaking period. This interesting result is mainly accredited to the permanent existence of TiO_2 NPs within the membrane matrix, and the stability of the NPs was confirmed. The stability of the NPs within the membrane matrix was occurred mainly due to the introduction of organic additive which has prevented the leaching of TiO_2 NPs, tending to an insignificant variation in WCA values during the soaking period **[179]**.

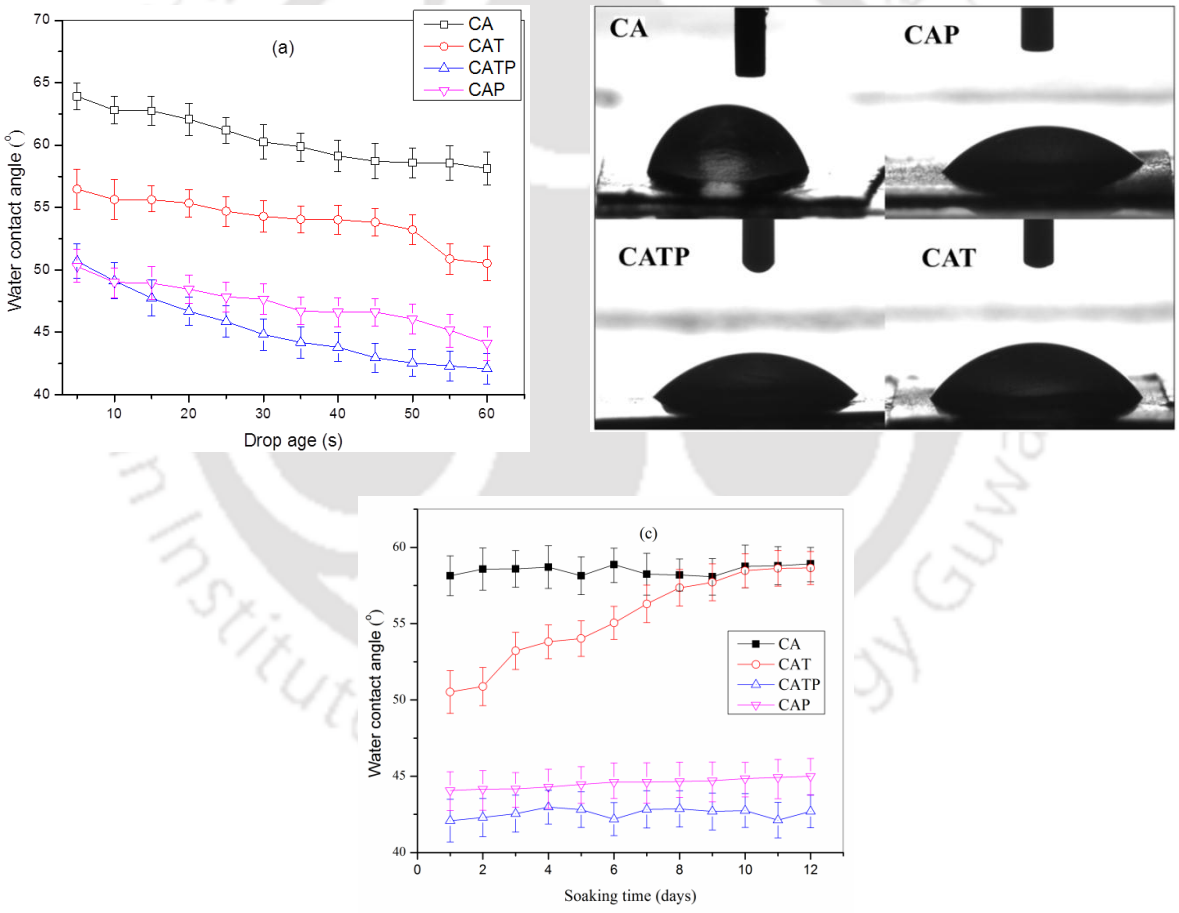

Fig. 4.15. (a) Water contact angle values with different drop ages; (b) images of water droplets of the prepared membranes; and (c) TiO_2 NPs stability study

4.3.1.6. Membrane fouling experiments

Fouling can be caused by broadly three kinds of substances: organic (macromolecules, biological substances like protein, enzyme, etc.), inorganic (metal hydroxides, calcium salts, etc.), and particulates. Proteins are strongly adsorbed on hydrophobic or less hydrophilic surfaces but less on hydrophilic surfaces **[159]**.Therefore, to investigate the BSA removal and anti-fouling performance of the prepared membranes, three cycle filtration processes were done. The flux results of pure water and BSA solutions of the prepared membranes are presented in **Fig. 4.16** and the effects of PVP and TiO_2 are investigated.

4.3.1.7. Membrane anti-fouling performance

The fouling of membranes due to BSA protein in ultrafiltration can be described using the theory of repulsion, adsorption of protein, and resultant pore-narrowing, due to electrostatic and hydrophobic interaction between the protein molecule and the membrane surface **[160].** The fouling performances of all the prepared membranes are presented in the **Fig. 4.16.** It is clear that the fouling and removal performance of the ultrafiltration membranes are strongly dependent on morphology of the membrane (i.e. both top-layer and sub-layer). As already discussed above the effects of PVP and TiO_2 have significant role in modifying the morphological structure of the membranes. Consequently, the introduction of both PVP and TiO_2 into the matrix of the CA membrane appeared to influence the flux and BSA rejection performance of the prepared membranes. The effect of PVP and TiO_2 were clearly noticed from the fouling/rinsing experiments. The flux results in **Fig. 4.16** have evidently displayed that the PWF (i.e. J_{W0}, J_{W1}, J_{W2}, and J_{W3}) and BSA flux (i.e. J_{B0}, J_{B1} and J_{B2}) results for CATP and CAP are higher than that of CA and CAT. The results for PWF are already discussed in **Section 4.3.1.4.** After completion of the PWF tests, the BSA filtration process was continued. To further investigate the fouling performance, the membranes were cleaned after BSA solution ultrafiltration, and the pure water flux of the cleaned membranes was measured. As clearly shown from the results, the membranes without PVP again have displayed low BSA flux results as well as PWF due to their less hydrophilic and pore formation nature.The enhancement of pure water and BSA fluxes for membranes for CATP and CAP were accredited to the pore-forming effect and hydrophilic nature of PVP and TiO_2 **[174]**. Nevertheless, the hydrophilic effect of the TiO_2 in case of CAT membrane is dominated by the pore blockage (i.e. less porous membrane). As clearly presented in

Fig. 4.16, we have carried out three BSA fouling/rinsing cycles for a total filtration time of 840 min. Each of the fouling experiments was performed with BSA solution with a concentration of 1 g L^{-1} for 2 h duration, and each rinsing experiments were done with deionized water for 30 min. A decrease in BSA fluxes with increasing time could be due to susceptible pore blocking of the membranes because of BSA protein adsorption and deposition on membrane surface, where the effect of concentration polarization was reduced by using high molecular weight of BSA (66 kDa) molecules and rigorous stirring (200 rpm) on the surface of the membrane **[73]**. Furthermore, the initial flux drops are realized to be more noticeable and ending fluxes are slowly dropped which is accredited to the loss of porosity of the membrane due to an interior adsorption of BSA protein which further leads to pore blocking. In the first cycle of fouling/rinsing experiment, CATP has displayed the highest flux recovery (i.e. 90 % of the initial value) with a flux value of 108.7 L m^{-2} h^{-1} at 150 kPa, whereas the flux values of the CA and CAT membranes have declined to 31.7 L m^{-2} h^{-1} and 16.4 L m^{-2} h^{-1}, respectively, (i.e. 28.6% and 65.7 % of the initial value, respectively). On the other hand, the flux result for CAP was 61.9 L m^{-2} h^{-1} with a flux recovery of 47.4 % of the initial flux value. The highest flux and recovery ratio for CATP membrane is attributed to the hydrophilic nature of both PVP and TiO_2 NPs and anti-fouling property of TiO_2 loaded within the membrane which could minimize severe solute fouling of the membranes **[60]**.

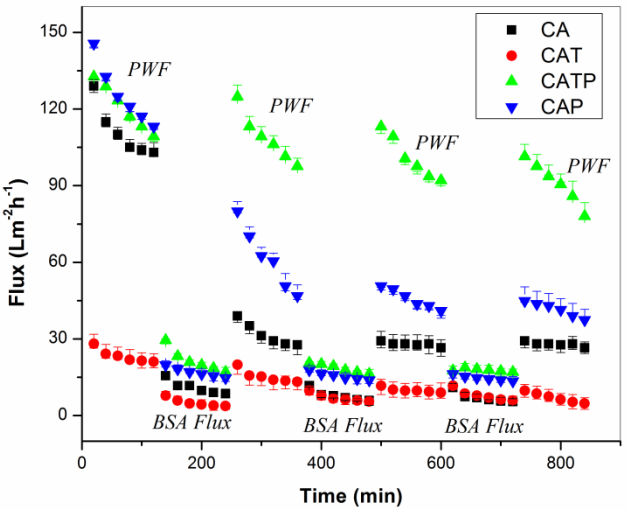

Fig. 4.16. Permeate flux versus filtration time for CA, CAT, CATP and CAP membranes: effect of PVP and TiO_2 NPs on BSA rejection and fouling performance (25 ºC, 150 kPa)

In general, membrane fouling is comprised of irreversible and reversible fouling. In the case of reversible fouling, deposited protein could be removed easily using hydraulic cleaning (i.e. back washing and cross flushing) **[167].** Conversely, the irreversible fouling is caused due to an irreversible adsorption of proteins which can only be removed using chemical cleaning **[168]**. To further examine the anti-fouling properties of the prepared membranes and to study the effect of additives, the flux losses viz. total fouling *(F_t),* reversible fouling *(F_r),* and irreversible fouling *(F_{ir})* were calculated, and the results are presented in **Table 4.8**. An increase in NFR results for CA, CAT, and CAP during the second and third cycle fouling/rinsing operations could be due to the development of the cake layer because of high irreversible fouling where their flux was too low. These results are because the porosity and hydrophilicity of the membrane have played an important role on the ant-ifouling and flux properties as already explained in the pure water flux study. Additionally, relatively consistent NFR results for CATP for first, second, and third cycle operations are attributed to the introduction of TiO_2, and it has played a crucial role in the enhancement of hydrophilicity and membrane anti-fouling property. The surface pore size could also have a complex influence on membrane anti-fouling property **[60]**. It is considered that membranes having larger pore size are possibly prone more seriously to pore-blocking or pore adsorption than those having smaller pore size **[186]**. Hence, membrane with smaller surface pore size and the more hydrophilic surface shows better anti-fouling property. In this study, CATP membrane exhibited better anti-fouling properties in the fouling process than other membranes. Thus, the combined effect of PVP and TiO_2 have played a significant role in a higher resistance towards membrane fouling due to BSA adsorption by reducing the hydrophobic interaction between BSA protein and membrane surface.

4.3.1.8. BSA rejection performance

The BSA rejection performances of the prepared membranes are shown in **Fig. 4.17(a).** The maximum BSA rejection values 96.8 %, and 94.3% were attained for membranes CAT and CATP, respectively. On the other hand, the removal efficiency results for CA and CAP membranes are 80.4 % and 77.9 %, respectively. It is clearly explained in the morphology analysis section that the PVP-free membranes have less porous structures, in which a high resistance to protein molecules was detected.

Table 4.8 Results for flux losses caused by total fouling *(F_t)*, reversible fouling *(F_r)* and irreversible fouling *(F_{ir})*, of the three cycles.

	First cycle				Second cycle				Third cycle			
Membrane	F_t	F_r	F_{ir}	*NFR*	F_t	F_r	F_{ir}	*NFR*	F_t	F_r	F_{ir}	*NFR*
CA	0.9	0.19	0.71	28.6	0.75	0.64	0.12	88.3	0.73	0.51	0.22	77.8
CAT	0.79	0.44	0.34	65.7	0.54	0.20	0.35	65.4	0.21	0.01	0.20	80.0
CATP	0.94	0.84	0.09	90.0	0.95	0.88	0.07	93.0	0.95	0.86	0.09	90.2
CAP	0.91	0.39	053	47.4	0.85	0.59	0.26	74.0	0.80	0.65	0.15	85.2

However, an increase in BSA rejection for CATP and CAT membranes could be explained due to the effect of TiO_2 addition to the membrane matrixes.The prepared membranes could become more negatively charged after an introduction of TiO_2 nanoparticles due to more negatively charged carboxylic groups along with –OH and Ti–OH groups present on the surfaces and matrixes of the membranes **[180]**. On the other hand, as pH 7 is far from isoelectric point (IEP=4.9), the BSA protein becomes more negatively charged, and a stronger electrostatic repulsion between BSA and the modified membranes was suggested **[181]**. However, some of the BSA rejection characteristic can also be described using the protein adsorption phenomenon onto the membrane surface in this pH range which could be accredited to structural interaction **[60]**. In addition to the electrostatic repulsion phenomena, the high BSA rejection for CATP membrane was also considered as an indicator of considerable protein removal due to its structural interaction. On the other hand, the BSA rejection phenomenon for CA and CAP membranes can be suggested due to a substantial protein deposition inside and on the membrane surfaces. Therefore, the surface depositions of BSA proteins can provide an extra hindrance to solute transportation. The high removal and comparatively lowest flux of CAT membrane; the highest removal and improved flux results for CATP membranes after simultaneous introduction of TiO_2 and PVP were attained in this study. All the experiments in this study were performed for three times. Moreover, all the experimental results were consistent with the membrane properties and agreed with each other.

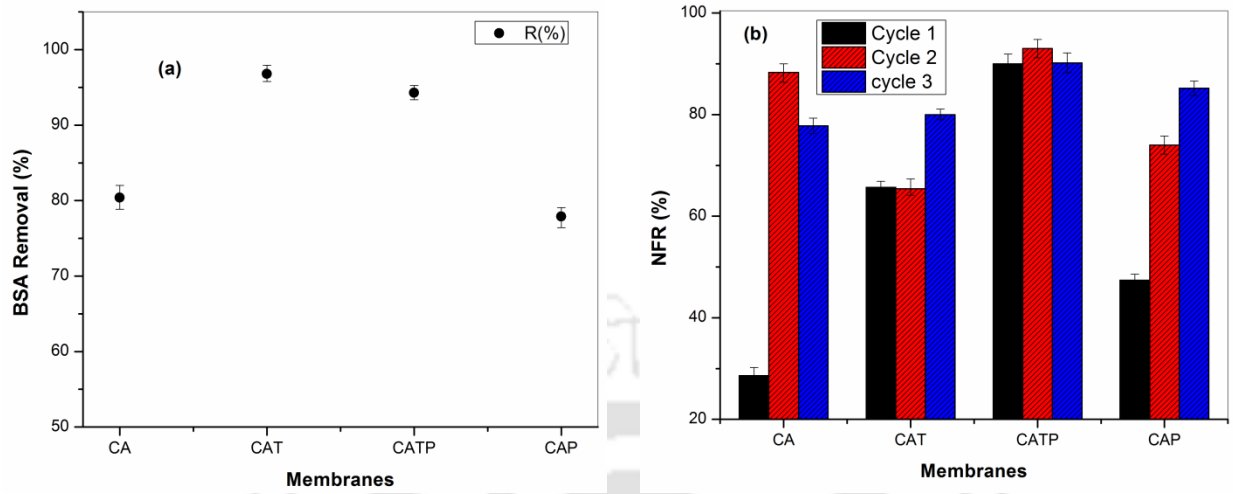

Fig. 4.17. (a) BSA rejection performances and (b) NFR percentage results of the prepared membranes: effect of PVP additive and TiO_2 NPs (25 ºC, 150 kPa).

Fig. 4.17 (b) presents the parameter normalized flux ratio (NFR) with filtration time (2 h) of the membranes operated for three cyles. It is clearly seen in the figure that CATP displayed the highest NFR values 90 %, 93 %, and 90.2 % for cycle 1, cycle 2 and cycle 3, respectively. Furthermore, these results indicate that the lowest irreversible flux loss and less BSA deposition on the pore walls as well as on the surface of the membrane consistently during the three cycle fouling/rinsing operations. However, CA, CAT, and CAP revealed a considerable decline in the BSA and PW fluxes, where the results for NFR are about 28.6 %, 65.7 %, and 47.4%, respectively, of the initial flux during the first cycle operation.

4.3.2. Summary

In the present work, the introductions of PVP and TiO_2 into the casting solution have changed the structure of the resulting membranes during the phase inversion process. The influences of PVP and TiO_2 on the preparation of phase inverted CA ultrafiltration membrane blended with PVP and TiO_2 were explored in terms of morphology study, equilibrium water content, hydrophilicity, hydraulic resistance, permeability performance, and thermal stability.

The BSA removal efficiencies and anti-fouling performances of the membranes were evaluated using ultrafiltration process. Hence, the following conclusions were made:

- After the introduction of PVP and TiO_2 to the ternary (polymer-solvent-non-solvent) system, the formations of finger-like structures and macro-voids were reduced significantly. Nevertheless, for CAP and CATP membranes, the development of micro-voids (i.e. micro porous structure) was observed.

- The introduction NPs alone into the polymer solution have formed aggregation of the NPs within the matrix of the membrane, and a small macro-void and finger-like structure were detected in the case of CAT, and these resulted are suggested to be related to the interference effect of NPs during the phase inversion process.

- The thermal stability of CATP membrane exhibited highest degradation temperature than CA and CAP membranes. This result was attained due to the highly stable nature of TiO_2 NPs at high temperatures.

- The improvement in the average pore size, porosity, and hydrophilic nature of the CA membranes was showed after the introduction of PVP and TiO_2.

- The CAT blended with PVP (i.e. CATP) membrane exhibited improved BSA flux, removal efficiency, and flux recovery ratios for the three fouling/rinsing cycles.

Chapter 5

Modification, characterization, and application of cellulose acetate membranes

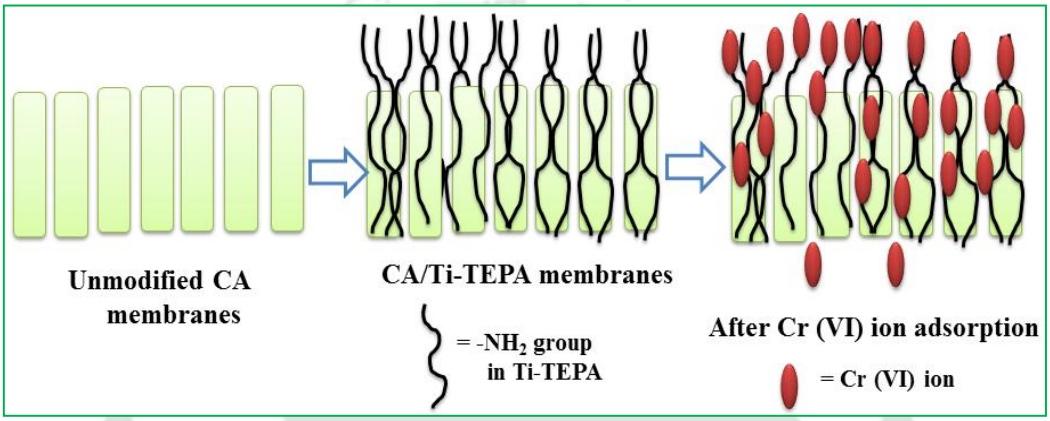

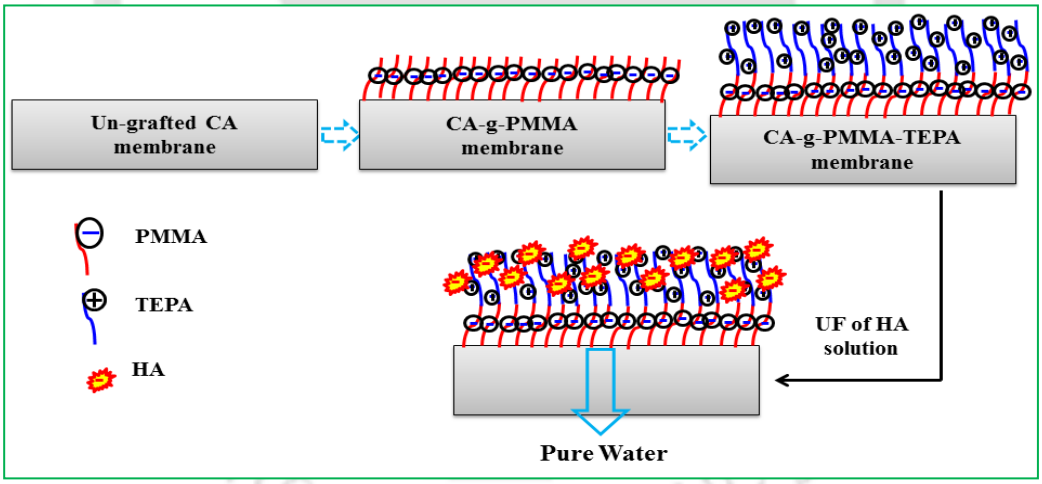

Chapter 5: Modification, characterization and application of cellulose acetate membranes

In this chapter, TiO_2 nanoparticles (NPs) were modified using different amine groups, namely, ethylenediamine (EDA), hexamethylenetetramine (HMTA) and tetra ethylene pentamine (TEPA), using impregnation process. The prepared amine modified TiO_2 composites powders were explored as an additive to fabricate ultrafiltration membranes with enhanced capacity towards the removal of chromium ions from aqueous solution. Membranes were prepared from cellulose acetate (CA) polymer blended with polyethylene glycol (PEG), and amine modified TiO_2 by using phase inversion technique. Fourier transform infrared spectroscopy (FTIR), zeta potential (ζ), thermo gravimetric analysis (TGA), field emission scanning electron microscopy (FESEM), water contact angle (WCA), and atomic absorption spectrophotometer (AAS) studies were done to characterize the membranes in terms of chemical structure, electric charge, thermal stability, morphology, and hydrophilicity properties.

Secondly, Graft copolymerization of cellulose acetate (CA) and poly (methyl methacrylate) (PMMA) was synthesized through free radical polymerization with the presence of cerium sulfate (CS) as an initiator under the nitrogen atmosphere in an aqueous solution. During the grafting reactions, the effect polymerization time and temperature on the grafting were investigated. Furthermore, functionalization of the synthesized product was done using amine group. The results from Nuclear Magnetic Resonance (^1H NMR) spectra and Fourier-transform infrared spectroscopy (ATR-FTIR) confirmed the successful grafting of PMMA on the CA membrane surfaces. Zeta potential (ζ), field emission scanning electron microscopy (FESEM), and atomic absorption spectrophotometer (AAS) studies were done to characterize the membranes in terms of surface charge, morphology, and HA removal percentage, respectively.

These works are communicated in the following journals

1. Kibrom Alebel Gebru, Chandan Das, "Removal of chromium (VI) ions from aqueous solutions by using environmentally friendlier amine-impregnated TiO_2 nanoparticles modified cellulose acetate membranes" ***Chemosphere (Revision Submitted)***
2. Kibrom Alebel Gebru, Chandan Das, "Removal of humic acids using cellulose acetate-g-poly methyl methacrylate (PMMA)-a-tetraethylenepentamine (TEPA) adsorptive membranes" ***Journal of Purification and Separation Technology (Under Review)***
3. Kibrom Alebel Gebru, Chandan Das, "Grafting polymerization of poly methyl methacrylate (PMMA) onto cellulose acetate modified with amine functional groups" ***European Polymers (Submitted)***

5.1. Functionalization and characterization of cellulose acetate membranes for chromium (VI) removal

In this work, TiO_2 nanoparticles (NPs) were modified using tetraethylenepentamine (TEPA), ethylenediamine (EDA), and hexamethylenetetramine (HMTA) amines using impregnation process. The prepared amine modified TiO_2 samples were explored as an additive to fabricate ultrafiltration membranes with enhanced capacity towards the removal of chromium ions from aqueous solution. Modified membranes were prepared from cellulose acetate (CA) polymer blended with polyethylene glycol (PEG) additive, and amine modified TiO_2 by using phase inversion technique. Fourier transform infrared spectroscopy (FTIR), zeta potential (ζ), thermo gravimetric analysis (TGA), field emission scanning electron microscopy (FESEM), water contact angle (WCA), and atomic absorption spectrophotometer (AAS) studies were done to characterize the membranes in terms of chemical structure, electric charge, thermal stability, morphology, hydrophilicity, and removal performance.

The pure water permeability and Cr (VI) ion removal efficiency of the unmodified (i.e. CA/U-Ti) and the amine modified (CA/Ti-HMTA, CA/Ti-EDA, and CA/Ti-TEPA) membranes were dependent on pH and metal ion concentration. Incorporation of amine modified TiO_2 composite to the CA polymer was found to improve the fouling and removal characteristics of the membranes during the chromium ultrafiltration process. The maximum removal efficiency result of Cr (VI) ions at pH of 3.5 using CA/Ti-TEPA membrane was 99.8 %. The washing/regeneration cycle results in this study described as an essential part for prospect industrial applications of the prepared membranes. The maximum Cr (VI) removal results by using CA/Ti-TEPA membrane for four washing/regeneration cycles are 99.6 %, 99.5 %, 98.6 % and, 96.6 %, respectively.

5.1.1. Results and Discussions

5.1.1.1. TEM analysis of U-TiO_2 and M-TiO_2 NPs

The particle size and microstructural information of U-TiO_2 (commercial) and M-TiO_2 nanoparticles were characterized using transmission electron microscopy. First, the nanoparticle samples were prepared by dispersing in DI water (500 mg/L) and then poured on a carbon tape covered plate. Finally, the samples were dried at room temperature and ready for TEM analysis. As clearly shown in **Fig. 5.1,** the TiO_2 NPs appeared in the form of spots. The black spots imbedded on the surface of M-TiO_2 NPs were because of the uniform dispersion of the amines. However, the highly homogeneous dispersion of the black spots was observed prominently for Ti-EDA and Ti-TEPA samples than the Ti-HMTA, which is may be due to the better interaction between the amine groups and TiO_2 NPs during the impregnation process. To measure the size of each nanoparticle, Image J software was employed. The sizes of the nanoparticles were not uniform, and their sizes were ranging from 16 to 100 nm. The average particle sizes were approximately 29.8 nm, 30.1 nm, 29.4, and 32.2 nm for TiO_2, Ti-HMTA, Ti-EDA, and Ti-TEPA, respectively; where no considerable variation in average particle size was detected from this study.

5.1.1.2. ATR-FTIR and zeta potential (ζ) and thermal analysis

As presented in **Fig 5.2 (a)**, in the IR spectrum of Ti-EDA, 3290 (N-H stretch), 1470 (C-H bend), the stretching vibrations of C–H bonds are present at 2953 and 2872 cm^{-1}. The peaks at 1580 and 1309 cm^{-1} are caused by the bending vibration of N–H bonds and stretching vibrations of C–N bonds, respectively. The C−O stretching vibration was observed at 1000 cm^{-1}. In the IR spectrum of Ti-TEPA, the stretching vibrations of C–H bonds are present at 2833 cm^{-1}. The peaks of N–H bonds and C–N bonds are present at 1650 and 1350 cm^{-1}, respectively. Thus, loading of the amines into the pore channels of the TiO_2 nanoparticles have confirmed. The IR transmission spectra of Ti-HMTA reveals that the C−O stretching vibration at 1000 cm^{-1}, the C–H stretching vibration bands at 2984 cm^{-1}, the C–H bend modes at 1454 cm^{-1}, and the IR spectra for C-H rock and C-H wag $(CH_2)_4$ were observed at 1371 $cm^{-1}$and 1236 cm^{-1}, respectively.

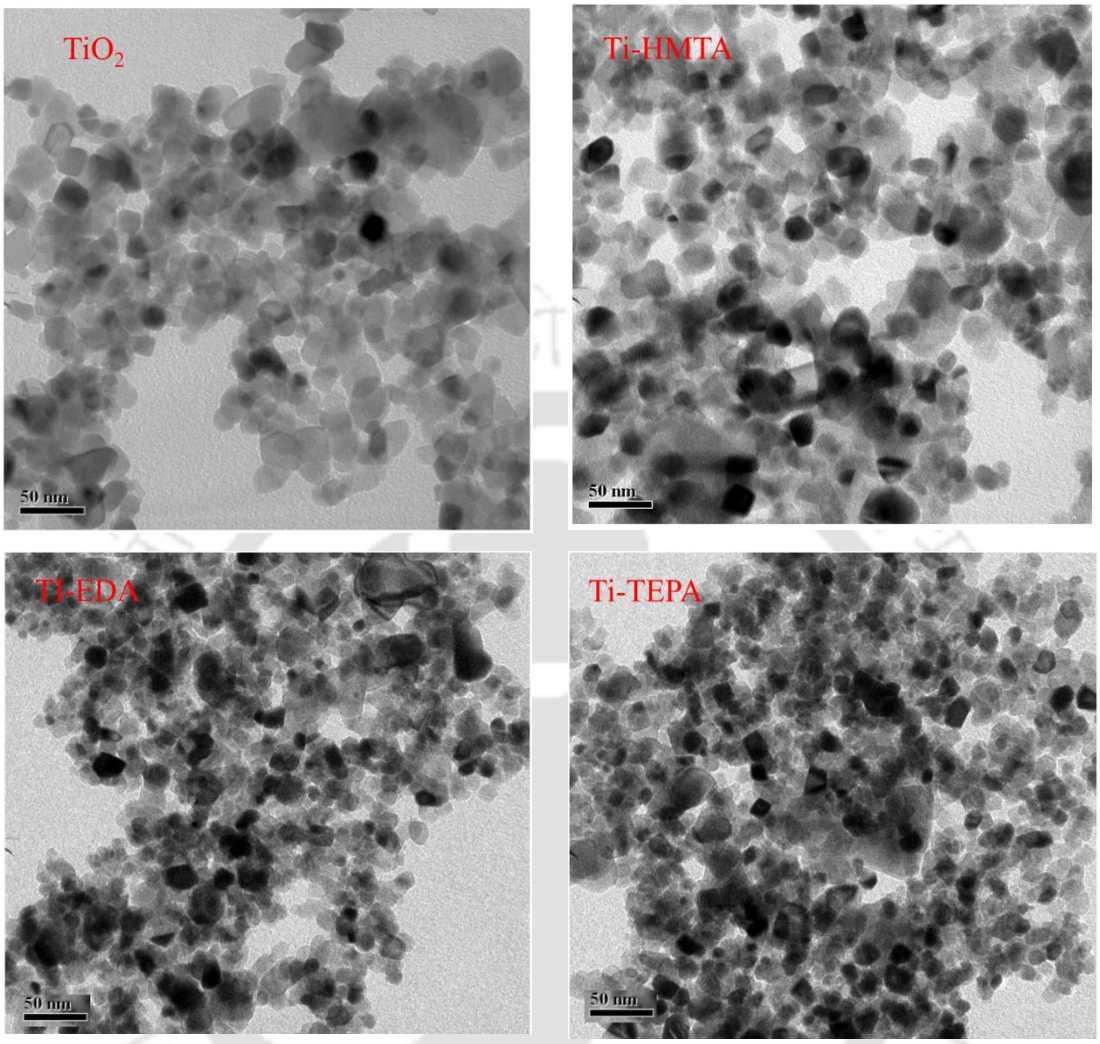

Fig. 5.1. TEM images of U-TiO_2 and M- TiO_2 nanoparticles

The IR spectrum of TiO_2 NPs shows intense broadband in the vicinity of 600 to 800 cm^{-1} attributed to the stretching vibration of Ti–O–Ti as expected for TiO_2 samples. This result, on the other hand, shows the successful interaction between the TiO_2 NPs and the amines. The spectrum for all the samples, except pure TiO_2 NPs, show considerable peaks attributed to O–H group at 3290 cm^{-1}, 3388 cm^{-1}, and 3250 cm^{-1} for Ti-EDA, Ti-HMTA and Ti-TEPA, respectively. This result is due to the sample moisture where the amines can easily absorb moisture than the pure TiO_2 NPs.

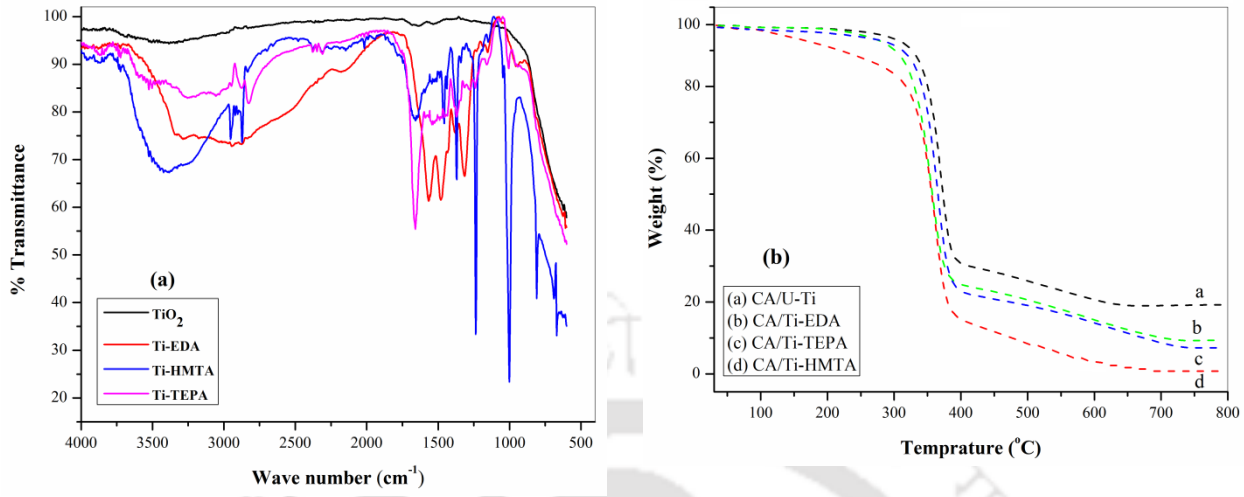

Fig. 5.2. (a) ATR–FTIR results of unmodified TiO_2 and modified TiO_2 NPs; (b) TGA analysis CA/U-Ti, CA/Ti-HMTA, CA/Ti-EDA and CA/Ti-TEPA membranes

The thermal degradation analyses (TGA Graphs) of the prepared membranes before and after impregnation are presented in **Fig. 5.2(b)**. The TGA results of all the prepared membrane displayed two-step degradation procedures. Therefore, the start of the decomposition step for CA/U-Ti, CA/Ti-HMTA, CA/Ti-EDA, and CA/Ti-TEPA membranes are 289 °C, 135 °C, 287 °C, and 286 °C, respectively. The observed weight losses are due to the degradation of CA chains because of the pyrolysis of the back-bone of the CA polymer and also followed by de-acetylation of CA **[176, 183, 187]**. However, the relatively weak thermal stability of CA/Ti-HMTA membrane is an indication of a relatively weak interaction between HMTA and TiO_2, where HMTA has no active groups like, NH_2- or NH-, which can further influence the thermal stability of the membrane. During the last decomposition step, the degradation temperatures of CA/U-Ti, CA/Ti-HMTA, CA/Ti-EDA, and CA/Ti-TEPA are 390 °C, 384 °C, and 388 °C and 389 °C, respectively, signifying the main thermal degradation of the CA chains. From these results, it is shown that all the membranes exhibited satisfactory thermal stability performances except a slight shift in intensity was observed. After the impregnation of the different amines, the second mass loss peak intensities were observed to decrease slightly, which is due to the simultaneous decomposition of the amines and the CA. The improvement in the thermal properties of CA membrane after incorporation of PEG and TiO_2 into the CA solution was elaborated in previous work **[103]**.

Zeta potential (ζ) values of the solutions of unmodified TiO_2 and modified TiO_2 NPs (Ti-HMTA, Ti-EDA, and Ti-TEPA) at pH of 2.0, 3.5, 5.0, 7.0, 8.5, and 10 are presented in **Table 5.1.** The ζ or electrical charge properties of the solid or film polymers influence their characteristics towards the specific applications. Zeta potential analysis is one of the most important methods used to obtain information on the electrical charge properties **[188]**. The unmodified TiO_2 NPs exhibited positive values for pH 2.0, 3.5, 5.0 and 7.0, and negative values for pH 8.5 and 10. On the other hand, the amine-modified samples displayed positive values for pH 2.0, 3.5, 5.0 and negative values for pH 7.0, 8.5 and 10. The high positive ζ values for the modified TiO_2 NPs at pH 2.0, 3.5, and 5.0 is due to the fact that the amines immigrated within the TiO_2 NPs tend to be protonated at lower pH **[189, 190]**. However, the ζ values for Ti-HMTA didn't show significant changes after modification. The amines used in this study have different structures and contents of NH_2-groups. EDA has two NH_2-groups only; TEPA also has two NH_2-groups and three NH-groups, and HMTA has no any NH_2- or NH- group, only N is connected with three CH_2-groups. For this reason, the protonation due to the presence of the amine group is not expected in the case of Ti-HMTA. The ζ value of the unmodified TiO_2 nanoparticles was +3.34 mV at pH of 7.0. The water molecules can occupy the oxygen vacancies and produce adsorbed –OH groups, which indicated that the nanoparticles were positively charged **[113]**. However, with increasing −OH concentration in the solution, adsorption of −OH on the sample increases, causing in substantial ζ change with pH. Therefore, high negative ζ value (i.e. -14.22 and -43.02) at pH of 8.5 and 10 was detected for the unmodified TiO_2 nanoparticles. Moreover, high negative ζ values were attained with further increase in the pH values to 10 for all the amine modified TiO_2 NPs. This result is accredited to an increase in the amount of –OH groups in the solid barrier due to alkaline nature of the solutions **[191]**. The TiO_2 NPs modified with TEPA (Ti-TEPA) displayed higher negative ζ than that of the Ti-HMTA and Ti-EDA, whereas the unmodified TiO_2 NPs showed positive zeta potentials at pH of 7.0. Zeta potential variation as a function of the types of the amines impregnated within the TiO_2 NPs can be explained due to the structure and content of NH_2- or NH- groups. Therefore, the pH dependence of ζ for the modified and unmodified TiO_2 NPs is confirmed from this study.

Table 5.1 Zeta potential (ζ) results of unmodified and modified TiO_2 NPs

	Zeta potential (mV)					
Samples	pH 2.0	pH 3.5	pH 5.0	pH 7.0	pH 8.5	pH 10
TiO_2	+6.23	+4.55	+4.01	+3.34	-14.22	-43.02
Ti-TEPA	+41.02	+40.76	+37.25	-32.62	-36.71	-40.86
Ti-EDA	+28.79	+28.15	+26.32	-15.66	-16.52	-20.35
Ti-HMTA	+6.39	+6.19	+6.01	-4.32	-14.01	-30.28

5.1.1.3. Morphology and hydrophilicity study

The FESEM images of the U-TiO_2 and M-TiO_2 NPs (i.e. Ti-HMTA, Ti-EDA, and Ti-TEPA) are presented in **Fig. 5.3 (a)**. As seen from the figure, the unmodified TiO_2 NPs depicted a flower resembling structures after the amine impregnation process. Thus, a successful modification and interaction of the amines and TiO_2 NPs can be suggested from the TEM **(Fig. 5.1)** and FESEM results. On the other hand, CA/U-TiO_2 and CA/M-TiO_2 casting solutions were prepared, and membranes with different amines (i.e. CA/U-Ti, CA/Ti-HMTA, CA/Ti-EDA, and CA/Ti-TEPA) were fabricated using the immersion precipitation phase inversion technique. The top surface and cross-sectional views of the FESEM images of all the prepared membranes are presented in **Fig. 5.3 (b, c).** It can be seen that all the prepared membranes displayed asymmetric structures with less finger-like macro-voids and a denser top layer. The suppression or the development of finger-like structure and macro-voids during the membrane formation is due to the presence PEG and TiO_2 within the casting solutions. Moreover, the pore forming properties of PEG additive has also played a significant role in the development of porous sub layer structures. Therefore, the finger-like and macro-voids free structures were observed for CA/U-Ti, CA/Ti-HMTA, CA/Ti-EDA, and CA/Ti-TEPA membranes. Comparing CA/U-TiO_2 and (CA/Ti-HMTA, CA/Ti-EDA and CA/Ti-TEPA), it also can be observed that the pore size of CA/U-TiO_2 membranes were slightly decreased after modification. This result was attained because of the adsorption and attachment of the amines within the matrix of the membranes. It can be seen in

Table 5.2 that all the modified membranes had displayed a uniform decrease in pore size, when the type of amines was HMTA, EDA, and TEPA, respectively, and this result can be accredited to the difference in interaction level of the amines with TiO_2 NPs. However, the pore size differences of the membranes are not significant enough to influence on permeation flux, which will be discussed later on.

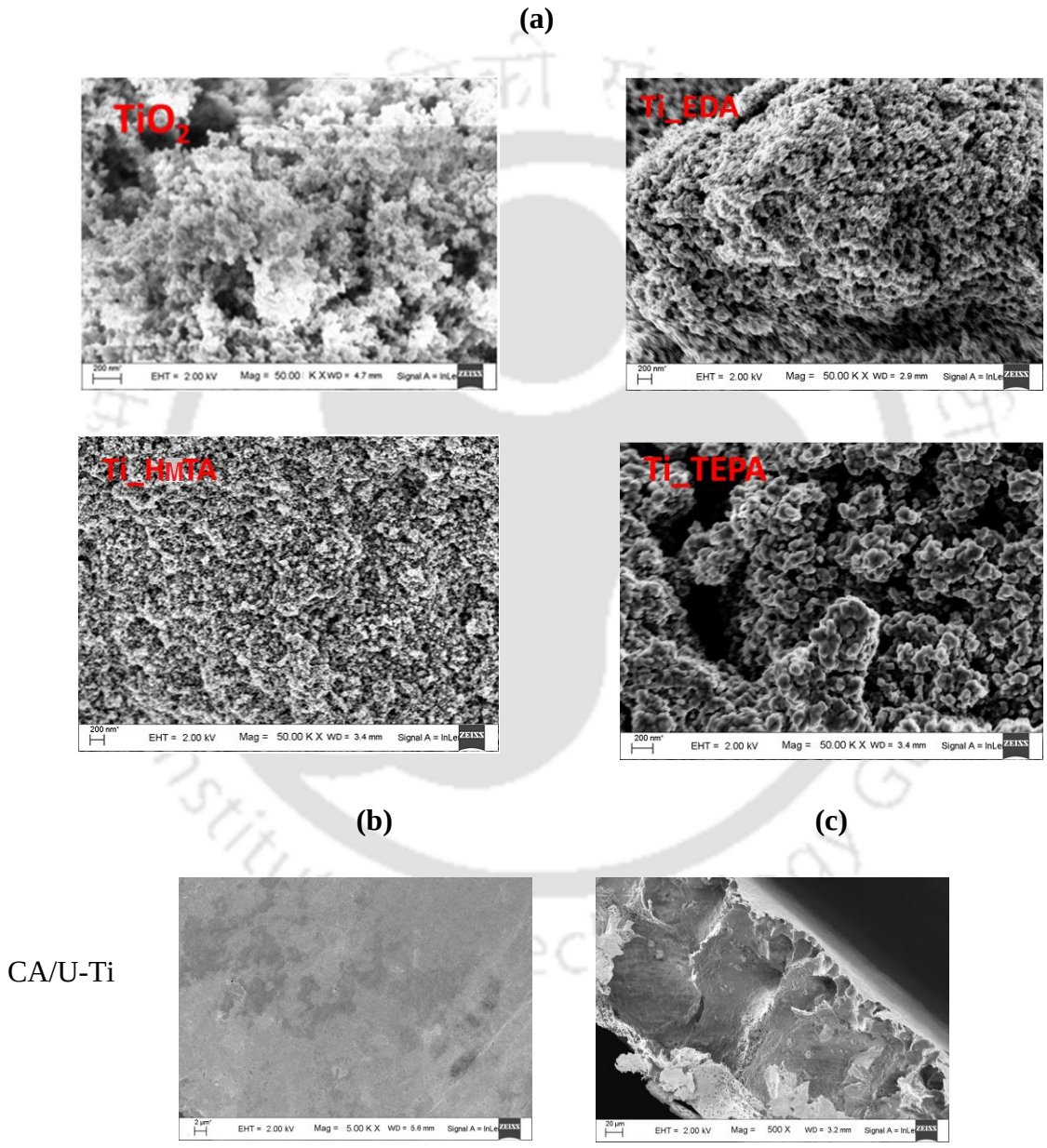

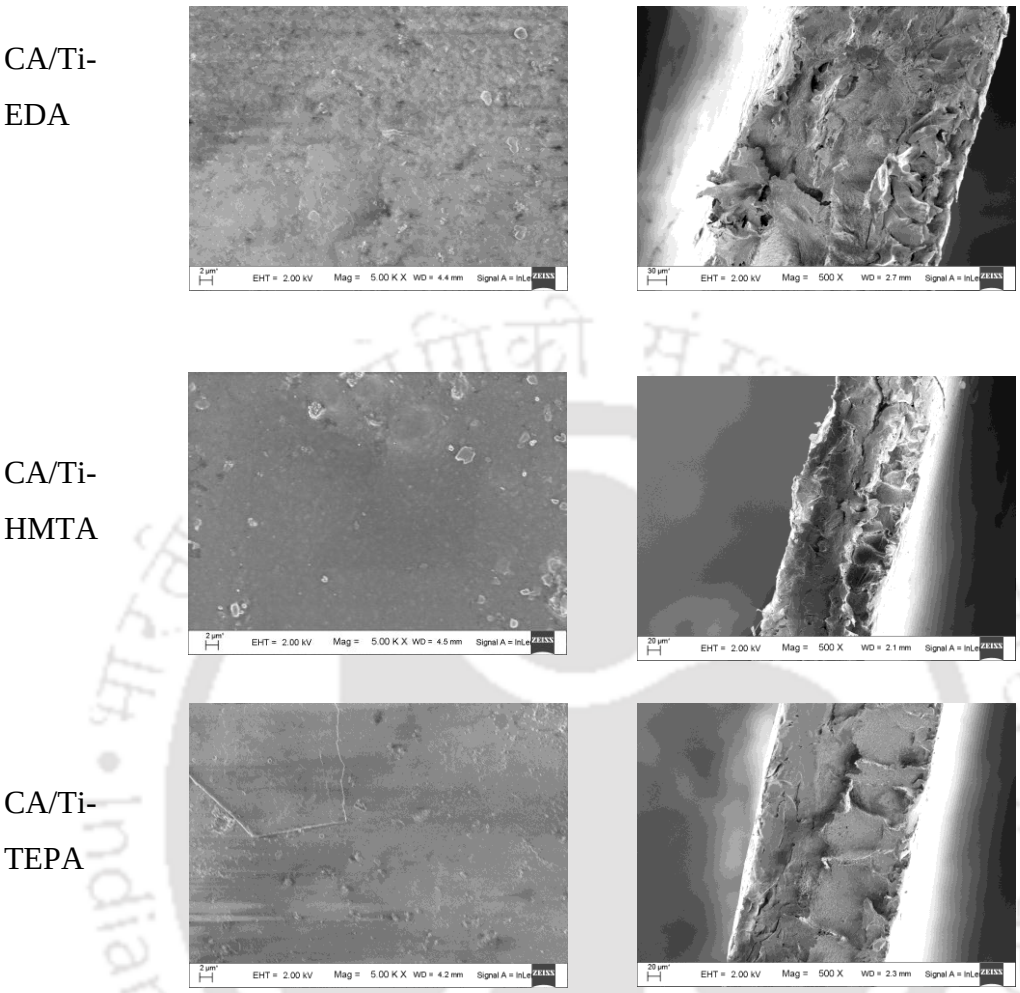

Fig. 5.3. (a) FESEM images of U-TiO_2 and M- TiO_2 powder;(b) Top surface and (c) cross-sectional FESEM images of CA/U-Ti, CA/Ti-HMTA, CA/Ti-EDA and CA/Ti-TEPA membranes

Water contact angle measurement is an effective technique for investigating the hydrophilicity nature of the prepared membranes. The (a) water contact angles values and (b) images of the water drops on the surface of all the prepared membranes are shown in **Fig. 5.4**. Membranes with smaller water contact angle values and higher water permeation rates are considered as hydrophilic **[192]**. As seen from the figure, the water contact angle values of the amine modified membranes were reduced significantly especially for CA/Ti-EDA and CA/Ti-TEPA membranes. The average water contact angle of CA/U-Ti after 60 min was around 55.3°. On the other hand, the average contact angle values of the modified membranes were reduced to

51.3°, 46.6°, and 40.9° for CA/Ti-HMTA, CA/Ti-EDA, and CA/Ti-TEPA, respectively, showing an enhanced surface hydrophilicity. The significant improvement of the hydrophilicity of the CA/Ti-EDA, and CA/Ti-TEPA membranes after impregnation of the amines are that the NH_2-groups are well-known polar groups having high affinity with water and hydrophilic character **[193].** The relatively smallest contact angle value for CA/Ti-TEPA and improved surface hydrophilicity as compared with the other membranes were mainly attributed to the difference in structures and contents of NH_2-groups, where TEPA has two NH_2-groups and three NH-groups.

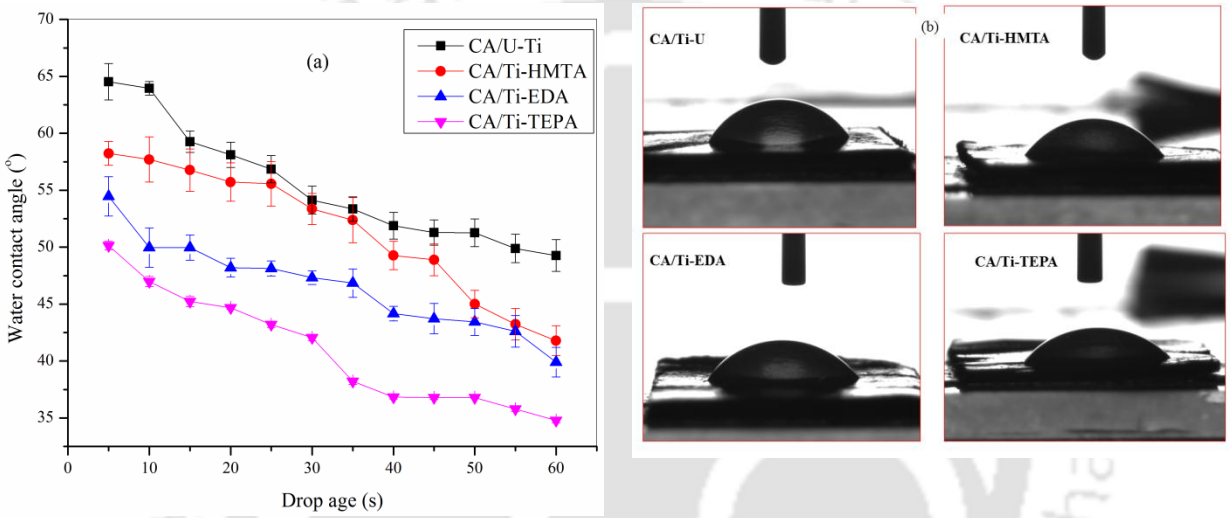

Fig. 5.4. (a) Water contact angle values with different drop ages and (b) images of water droplets of the prepared membranes.

5.1.1.4. PWF performance of membranes

The pure water flux (PWF) results were measured to investigate the influence of the loading of the amine groups in the matrix of the prepared membranes. Therefore, the PWF results and the effect of the operating pressures are presented in **Fig. 5.5** (a) and (b), respectively. As can be seen from the figure, the PWF results of the prepared membranes decreased uniformly with decreasing the amount of functional amines within the matrix of the membranes. These results are attributed to the decreasing hydrophilicity (increasing water contact angle) of the membranes. As clearly presented in **Table 5.2,** the PWF results of CA/U-Ti, CA/Ti-EDA, CA/Ti-HMTA and CA/Ti-TEPA at 250 kPa are 587.8, 649.2, 752.5 and 924.7 Lm^{-2} h^{-1},

respectively. However, the PWF results of all the prepared membranes are appropriate for their efficient use in filtration processes.

Table 5.2 Compaction and hydraulic characteristics of amine modified membranes at 250 kPa.

Membrane	*CF*	R_m ($\times 10^{-10} m^{-1}$)	J_w (L/m^2h)	*EWC* (%)	ε (%)	r_m (nm)	Thickness (μm)
CA/U-Ti	1.50	0.50	587.8	80.1	74.8	27.0	73.5
CA/Ti-HMTA	1.41	0.42	649.2	81.5	73.6	26.5	82.4
CA/Ti-EDA	1.25	0.40	752.2	82.7	72.4	25.7	84.2
CA/Ti-TEPA	1.32	0.35	924.7	84.2	70.2	24.2	86.9

The compaction factor, EWC, porosity, average pore radius, thickness, and hydraulic resistance of all the prepared membranes in this study are presented in **Table 5.2**. Studying of compaction factor (CF) is very important to recognize the morphological structures (i.e. pore arrangements) of the membranes specially the membrane sub layer formation. Membranes with high CF are likely to be highly compacted and may show the existence of some defective pores or macro-voids in the membrane sub layer arrangement. The CF of all the membranes shows similar results. The PWF results of all the membranes were increased almost uniformly with increasing in an operating pressure from 100 to 300 kPa. Thus, the PWF for membranes results were observed to increase uniformly with varying the type of amine group added to the membrane matrix. Hence, the CA/Ti-TEPA membranes have displayed higher PWF than the other membranes due to its best hydrophilic nature. As seen from **Table 5.2,** no significant different was detected in the results of hydraulic resistance, porosity, and the average pore radius of all the prepared membranes. However, a slight increase in average pore size of the membranes with varying the type of amine groups may be accredited to the number of amines involved with in the matrix of the membranes. Therefore, the CA/Ti-TEPA membrane with more number of amine groups showed a slightly lower average pore diameter and porosity which is due to the increase in the number of branched amines within the matrix of the membrane. On the other hand, the slight increase in EWC for CA/Ti-TEPA membrane when compared with other membranes is due to the decrease in water contact angle (higher hydrophilicity value). Moreover,

the hydrophilicity and/or EWC were observed to increase uniformly with increasing the type of amine groups loaded to the membranes (i.e. HMTA, EDA and TEPA). From the porosity measurement results, it is shown that all the membranes have shown a satisfactory results in the range of 70 to 74%, which is accredited to lower concentration of the membrane forming polymer (10.5 wt. %) as well as due to the addition of PEG additives and TiO_2 NPs.

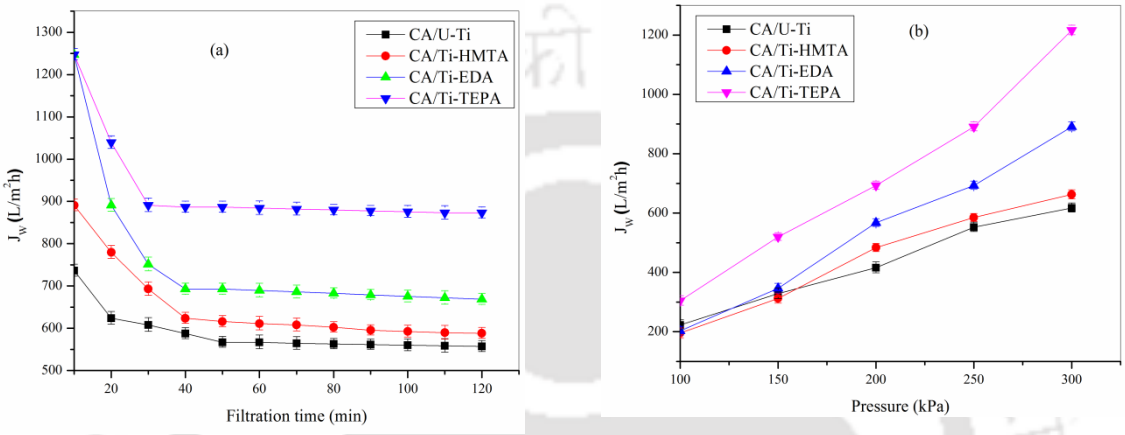

Fig. 5.5 (a) PWF profile during compaction study (at 250 kPa), (b) Effect of pressure on PWF

5.1.1.5. Cr (VI) removal efficiency of membranes

The permeate flux results and efficiency of the prepared membranes for Cr (VI) ions removal was investigated using 10 ppm Cr (VI) solution. On the other hand, to further investigate the influence of pH on Cr (VI) ion removal in the ultrafiltration process using the prepared membranes, the solution pH was kept at 3.5 and 7.0. The flux and removal performance results of CA/U-Ti, CA/Ti-HMTA, CA/Ti-EDA, and CA/Ti-TEPA membranes are presented in **Fig. 5.6**. As seen from the figure, all the membranes have displayed lower Cr (VI) flux values and higher Cr (VI) removal performances at pH 3.5 than at pH 7.0. The membranes which were modified with various amines (HMTA, EDA, and TEPA) have revealed considerably higher removal efficiency for Cr (VI) ions than the unmodified membrane (CA/U-Ti). The improved Cr (VI) ion removal efficiencies of CA/Ti-HMTA, CA/Ti-EDA, and CA/Ti-TEPA were mainly due to the differences in content and structure of the amines within the matrix and pore walls of the membranes. This result approves that the introduction of amines within the matrix of the

membranes indeed enhanced the properties of the membranes towards the removal of Cr (VI) ions. Therefore, the Cr (VI) ion removal for CA/Ti-EDA and CA/Ti-TEPA membranes showed better performances and was assumed because of the electrostatic interaction between the positively charged amines and Cr (VI) anions. Due to the de protonation and protonation of the amine groups impregnated within the CA/Ti-EDA and CA/Ti-TEPA membrane matrixes, the amine-modified membranes could become positively charged at lower pH but not at higher pH values **[190]**. These amine groups impregnated within the membrane matrix can carry out protonation, and the degree of protonation depends on the pH of the solution. These results are confirmed by using zeta potential study as presented in **Table 5.1**. Consequently, the amine functional groups which are impregnated within the membrane matrix have governed the electrostatic interaction between the membrane surface and the chromium ion. Therefore, the protonated amine groups of the modified membranes led to an improved electrostatic attraction between protonated amine groups and the chromium ions at lower pH value **[194]**. It is also mentioned in the literature that although Cr (VI) occurs commonly as anions over the whole pH range the proportions of the Cr (VI) species (i.e. $Cr_2O_7^{2-}$, H_2CrO_4, $HCrO_4^-$ and CrO_4^2) change with pH variation. Aroua et al. **[195]** have conducted speciation profile on Cr(VI), and they have found the following results. $Cr_2O_7^{2-}$ appears at pH 1.0 to 6.0 and disappears at pH 9; on the other hand, H_2CrO_4 (aq.) (a very low concentration) appears only at pH 2.0 and 3.0; $HCrO_4^-$ occurs in low concentration at pH 1.0–8.0 and disappears at pH 10.0; and CrO_4^2 species starts to develop at pH 10 and above. Accordingly, no electrostatic attraction between Cr (VI) and the amine modified membranes was suggested, when Cr (VI) was in the form of H_2CrO_4 and CrO_4^2. On the other hand, the electrostatic attraction exists for both $HCrO_4^-$ and CrO_4^{2-}, though more positively charged amine groups are necessary to attract/adsorb CrO_4^{2-} because of its higher ion valence. Therefore, the variation in ionization degree of the amine modified membranes and the change in Cr (VI) species at various pH caused variation in removal efficiency of the membranes. On the other hand, some of the Cr (VI) ion removal characteristic can also be described using the deposition phenomenon onto the membrane surface in this pH range which could be accredited to structural interaction **[60]**. In addition to the electrostatic interaction phenomena, the Cr (VI) ion removal for the membranes was also considered as an indicator of considerable Cr (VI) ion removal due to its structural interaction. On the other hand, the Cr (VI) ion removal phenomenon for CA/U-Ti and CA/Ti-HMTA membranes can be suggested mainly due to a substantial Cr (VI)

ion deposition inside and on the membrane surfaces due to structural interaction. Therefore, the surface depositions of Cr (VI) ion can provide an extra hindrance to solute transportation. However, lower Cr (VI) ion removal performances were attained in the case of CA/U-Ti and CA/Ti-HMTA membranes. These results are suggested due to the availability of lesser active sites where amine groups are not present, where HMTA has no any NH_2- or NH- group, only N is connected with three CH_2-groups. The amine functional groups loaded within the matrix of the Ti-EDA and Ti-TEPA membranes have lone pair of electrons from nitrogen and mainly act as an active site for the development of the complexion between chromium metal ions and amine groups. The order of the removal/adsorption capacity of the prepared membrane is CA/U-Ti < CA/Ti-HMTA < CA/Ti-EDA < CA/Ti-TEPA. The maximum removal values of the CA/U-Ti, CA/Ti-HMTA, CA/Ti-EDA, and CA/Ti-TEPA membranes at pH 3.5 are 42.2 %, 86.4 %, 93.6 % and 99.8 %, respectively. On the other hand, the Cr (VI) removal values of the membranes at pH 7.0 are 37.1%, 43.3 %, 47.2 %, and 76.2 %, respectively. At pH 7.0, the Cr (VI) ion removal performances of the modified membranes observed to be decreased during the ultrafiltration and these results were essentially due to the low Cr (VI) removal capability of theses membranes at neutral pH. As seen from the zeta potential study in **Table 5.1**, all the modified membranes exhibited negative charges and the removal of Cr (VI) in this case is due to the electrostatic repulsion between Cr (VI) ion and the membrane surfaces charges. On the other hand, due to the lower negative charges for Ti-HMTA and low positive charges for unmodified TiO_2 NPs, lower removal efficiencies were attained. However, higher Cr (VI) removal/repulsion efficiency was observed for Ti-EDA and Ti-TEPA due to the availability of higher negative charges than the other membranes at the neutral pH. As observed from **Fig. 5.6 (c)** and **(d)**, Cr (VI) removal using the amine modified membranes is higher at low pH (3.5) and decreased with increasing the pH of the solution to 7.0. Therefore, at acidic pH the protonated amino groups of the amine impregnated Ti-EDA, and Ti-TEPA membranes have improved the removal/adsorption capabilities of the membranes to Cr (VI) ions. It was clearly observed that the removal of Cr (VI) metal ions by the membranes were in increasing order (i.e. HMTA < EDA < TEPA). This result can be accredited due to an increase in active sites for removal of Cr (VI) metal ions as the content and structure of the amine groups (NH_2- or NH-) within the membranes differs. The difference in removal of Cr (VI) metal ions behavior of the membranes was suggested due to the different electrostatic performance of the negatively charged Cr (VI) ions. Therefore, it was

observed from this study that the pH of the solution was an important parameter that affects removal performances of the prepared membranes. As seen from **Fig. 5.6 (c)** and **(d)**, the removal of Cr (VI) using the prepared membranes was increased with filtration time and the maximum Cr (VI) ion removal was attained after 1h filtration operation. Consequently, pH of 3.5 was considered as a suitable condition for the removal Cr (VI) ion for the modified membranes. Furthermore, comparing all the membranes, the maximum removal of Cr (VI) ion was achieved by CA/Ti-TEPA membrane. The Cr (VI) flux values for all the membranes at pH 3.5 and 7.0 are presented in **Fig. 5.6 (a)** and **(b).** The uniform decrease in Cr (VI) fluxes with increasing time was suggested due to susceptible pore blocking of the membranes because of Cr (VI) ion adsorption and deposition on membrane surface and inner channels of the pores, where the effect of concentration polarization was reduced by rigorous stirring (200 rpm) on the surface of the membrane. On the other hand, flux variation with pH change was observed. At pH of 3.5 low Cr (VI) permeate flux was detected. This result was suggested due to the electrostatic attraction between the positively charged membranes and Cr (VI) ions. Moreover, lower fluxes for CA/Ti-EDA and CA/Ti-TEPA membranes were observed. The $-NH_2$ chains within CA/Ti-EDA and CA/Ti-TEPA membranes have turned into extended arrangement which have formed a narrow effective pore size. On the other hand, at pH of 7.0, the $-NH_2$ chains have changed to collapsed conformation due to the de protonation of the amine groups, which caused large effective pore size and therefore resulted in high Cr (VI) ions flux results for the membranes.

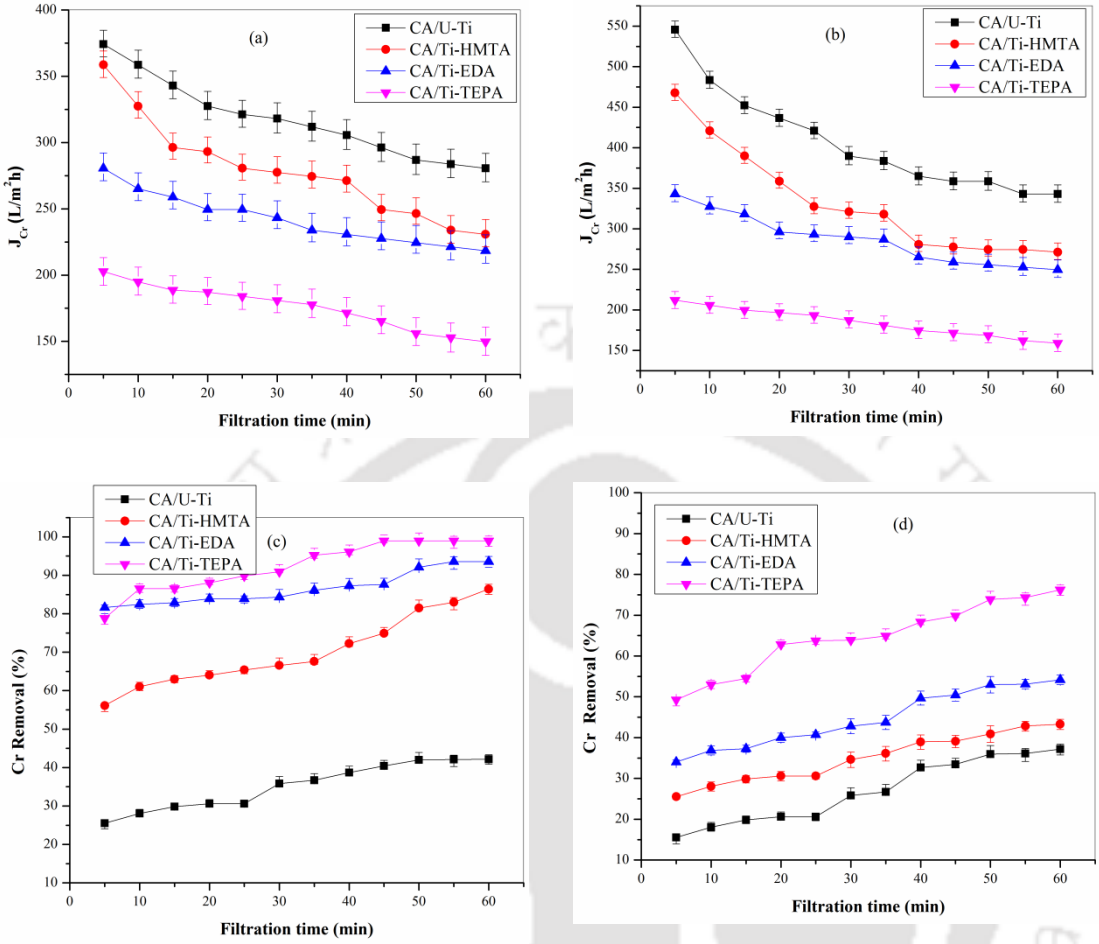

Fig.5.6 Permeate flux of Cr (VI) results of all the prepared membranes at (a) pH=3.5, (b) pH=7 and Cr (VI) removal % at (c) pH=3.5, (d) pH=7 (Cr (VI) concentration= 10 ppm, ΔP=150 kPa, @ 200 rpm)

Furthermore, as explained above the flux results were observed to be dependent on the removal performances of the membranes. The schematic diagram for the impregnation of amine groups and deposition of Cr (VI) ions in ultrafiltration process is presented in **Fig.5.7**.

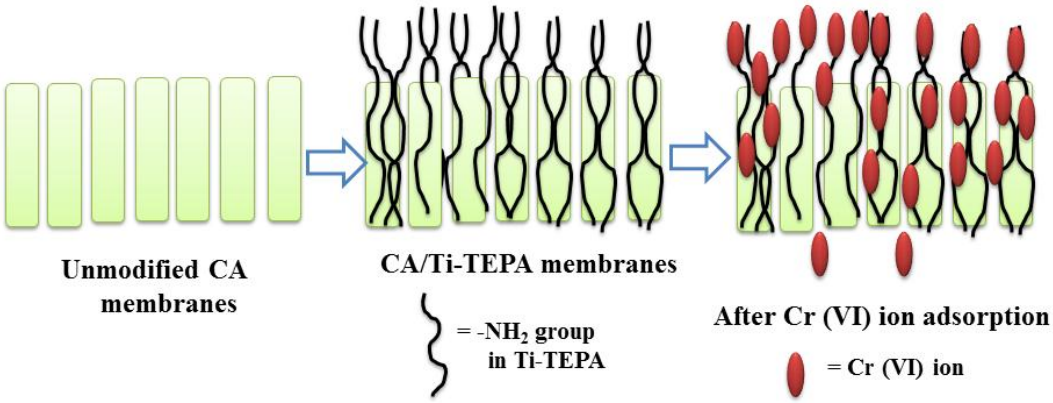

Fig.5.7. Schematic diagram for the impregnated amine groups and deposition of Cr (VI) ions in ultrafiltration process.

5.1.1.6. Effect of Cr (VI) concentration

The removal efficiency of CA/Ti-TEPA membranes for Cr (VI) ions at different initial ion concentration was investigated. Therefore, the removal efficiency of the membranes was found to be concentration dependent. The results of permeate fluxes and removals of chromium ions for various concentrations (i.e. 10, 30, 50, 70, and 100 ppm) with time using CA/Ti-TEPA membrane were investigated and are presented in **Fig. 5.8**. The removals of Cr (VI) ion using CA/Ti-TEPA membranes were observed to be dependent on the feed concentration of the Cr (VI) ion. As clearly depicted in **Fig. 5.8 (c)** and **(d)**, the removal of Cr (VI) ion of the membranes uniformly decreased with increasing the concentration of Cr (VI) ion (from 10 ppm to 100 ppm). This result can be associated with the availability of excess binding sites within the CA/Ti-TEPA membranes for removal of Cr (VI) ion. Therefore, the highest removal of Cr (VI) ion result was attained at low concentration (10 ppm) due to the availability of excess binding sites for Cr (VI) ions removal. The removal/adsorption results for 10 ppm, 30 ppm, 50 ppm, 70 ppm, and , 100 ppm at pH 3.5 are 99.6 %, 98.9 %, 93.6 %, 86.4 %, and 82.2 %, respectively. The flux results of CA/Ti-TEPA for both pH values, on the other hand, were observed to increase uniformly with increasing the concentration of Cr (VI) ions (**Fig. 5.8 a** and **b**). As already discussed in the previous sections, higher removal performances were attained at low pH (3.5) than at high pH (7.0) for all the concentrations. The removal performances of the membrane at pH 7.0 are

presented in **Fig. 5.8 (d)** and the maximum removal results are 80.7 %, 76.2 %, 69.1 %, 58.3 %, and , 52.4 % for 10 ppm, 30 ppm, 50 ppm, 70 ppm, and , 100 ppm, respectively.

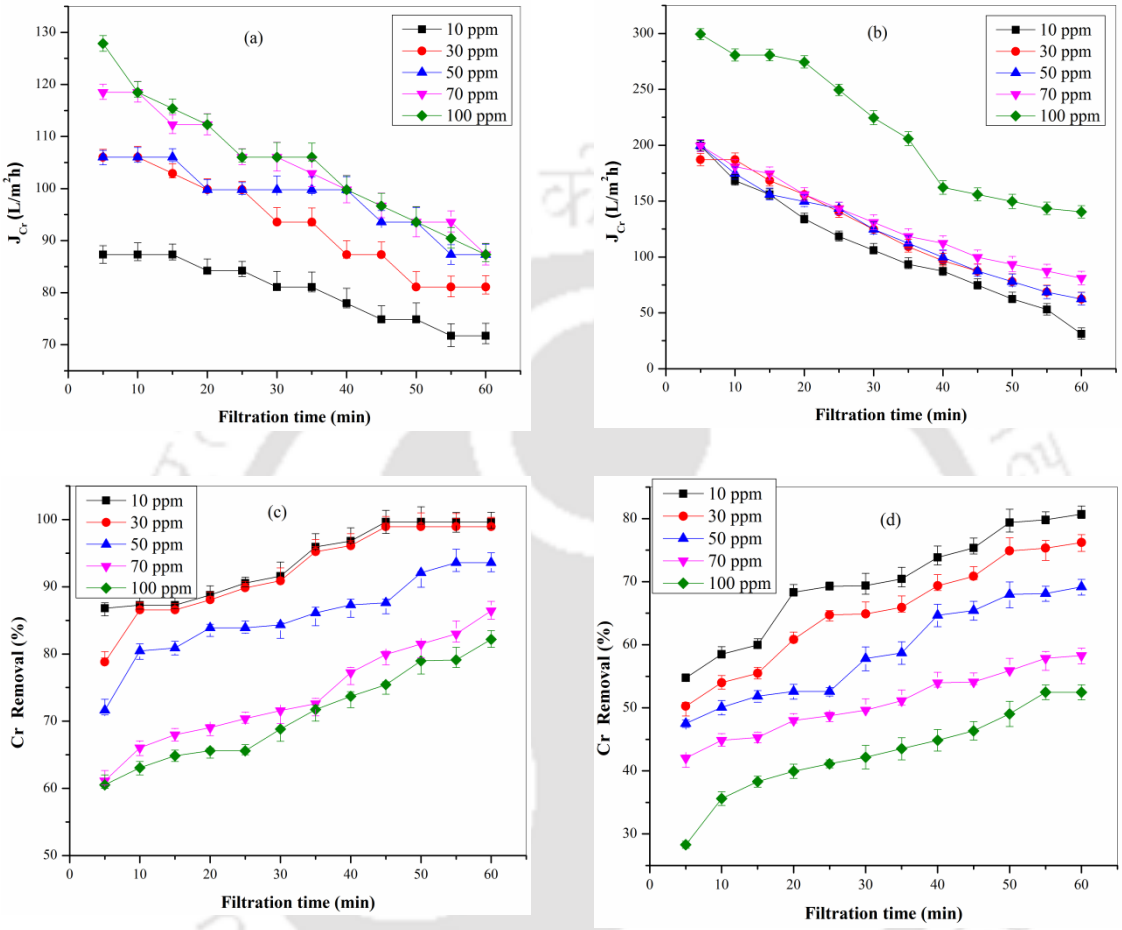

Fig. 5.8 Effect of concentration on Cr (VI) ion permeate flux results of the CA/Ti-TEPA membrane at (a) pH=3.5, (b) pH=7 and Cr (VI) ion removal % at (c) pH=3.5, (d) pH=7 (ΔP=150 kPa, @ 200 rpm)

5.1.1.7. Washing/regeneration performance study

In this study, four washing/regeneration cycles were conducted to evaluate the fouling and removal performance of CA/Ti-TEPA membrane using KCl solution and 10 ppm Cr (VI) ion solution where the results are presented in **Fig. 5.9.** As clearly shown in **Fig. 5.9 (a),** the uniform decrease in KCl and chromium fluxes were realized to be highly noticeable which are credited to

the decreasing in porosity of the membrane due to an interior adsorption of Cr (VI) ion which further could lead to pore blocking.

Therefore, the KCl flux results for 1st, 2nd, 3rd, and 4th cycles are 639.7, 546.4, 481.8, and 438.6 L m^{-2} h^{-1}, respectively, at pH of 7.0. On the other hand, the KCl flux results are 483.8, 390.4, 325.9, and 282.6 L m^{-2} h^{-1} at pH of 3.5. The Cr (VI) removal percentages for both pH values were observed to decrease with increasing the regeneration cycles. At the first cycle, the Cr (VI) removal percentage at pH 3.5 was observed to decrease slightly. The maximum Cr (VI) removal results for four washing/regeneration cycles are 99.6 %, 99.5 %, 98.6 % and, 96.6 %, respectively. As already explained previously, the pH dependence of ζ values for the TEPA modified membranes has influenced the chromium ion removal performances. As seen from the ζ study in **Table 5.1**, the TEPA modified TiO_2 NPs exhibited high positive ζ value at pH 3.5. Therefore, higher Cr (VI) removal percentage of CA/Ti-TEPA membrane at pH of 3.5 was attained due to the availability of more active sites for the adsorption of the negatively charged Cr (VI) ions. Thus, even after four washing/regeneration cycles, the Cr (VI) removal percentage remained at 96.6 %. On the other hand, the membranes exhibited negative charges at pH of 7.0 and the removal of Cr (VI) in this case is due to the electrostatic repulsion between Cr (VI) ion and the membrane surfaces charges. The removal performances were decreased for the pH 7.0 (72.4 %, 69.1%, 67.0 % and 64.9 %, respectively), where the lower removal performances of the membrane were detected at this pH. These results were accredited mainly due to the low Cr (VI) removal capacity of CA/Ti-TEPA membrane at higher pH (7.0) due to the availability of lesser sites. From the above results, it can be suggested that the CA/Ti-TEPA membrane can be a good candidate for the removal of low concentration Cr (VI).

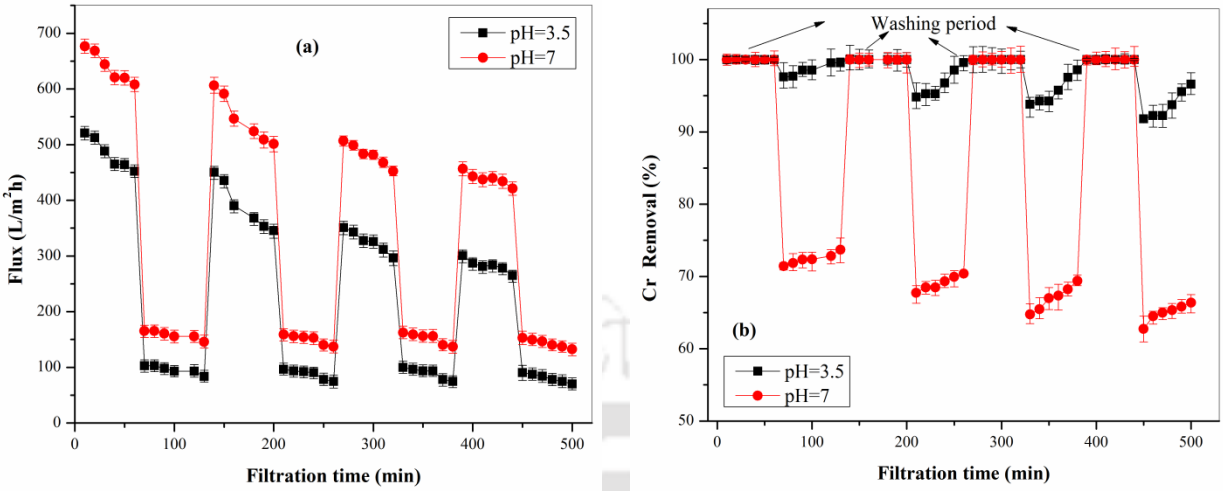

Fig.5.9. (a) Cr (VI) flux and (b) removal efficiency of CA/Ti-TEPA membrane during the filtration cycle (Cr (VI) concentration: 10 ppm, pressure: 150 kPa, washing operation: 2.5 g/L KCl @ 200 rpm).

Thus, the authors strongly believe that this work will have a substantial contribution to the current state-of-the-art on the modification and enhancement of the properties of conventional cellulose acetate membranes for specific applications than the previous studies **[48, 196]**.

5.1.2. Summary

In the present study, Cr (VI) ion removal experiments were carried out using CA/U-Ti, CA/Ti-HMTA, CA/Ti-EDA, and CA/Ti-TEPA membranes. The Cr (VI), ion removal efficiency, was influenced by the metal ion concentration, the pH of the solution, and type of amine. The optimized pH was 3.5 for the removal of Cr (VI) ions for all the membranes. CA/Ti-TEPA showed the best removal efficiency. The highest removal of Cr (VI) ions result was attained at low concentration (10 ppm) due to the availability of excess binding sites for Cr (VI) ions removal. The removal results for 10 ppm, 30 ppm, 50 ppm, 70 ppm, and, 100 ppm at pH 3.5 are 99.6 %, 98.9 %, 93.6 %, 86.4 %, and 82.2 %, respectively. The maximum removal efficiency results of Cr (VI) ions at pH of 3.5 using CA/U-Ti, CA/Ti-HMTA, CA/Ti-EDA, and CA/Ti-TEPA membranes were 47.2 %, 86.4 %, 93.6 % and 99.8 %, respectively. The maximum Cr (VI) removal results for four washing/regeneration cycles are 99.6 %, 99.5 %, 98.6 % and, 96.6 %,

respectively. The removal performances were decreased for the pH 7.0 (72.4 %, 69.1%, 67.0 % and 64.9 %, respectively), where the lower removal performances of the membrane were detected at this pH. Therefore, there are good prospects for CA/Ti-TEPA membrane for the removal of Cr (VI) ions from water and wastewater in practical applications.

5.2. Grafting copolymerization of poly methyl methacrylate (PMMA) onto cellulose acetate modified with amine group for removal of humic acids

Graft copolymerization of cellulose acetate (CA) and poly (methyl methacrylate) (PMMA) was synthesized through free radical polymerization in the presence of cerium sulfate (CS) as an initiator under the nitrogen atmosphere in an aqueous solution. During the grafting reactions, the effects of polymerization time and temperature on the grafting were investigated. Furthermore, functionalization of the synthesized product was done using amine group (tetraethylenepentamine, TEPA). The results from Nuclear Magnetic Resonance (1H NMR) spectra and Fourier-transform infrared spectroscopy (ATR-FTIR) confirmed a successful grafting of PMMA on the CA membrane surfaces. Zeta potential (ζ), field emission scanning electron microscopy (FESEM), and atomic absorption spectrophotometer (AAS) studies were done to characterize the membranes in terms of surface charge, morphology, and HA removal percentage, respectively. The maximum removal efficiencies for un-grafted CA (un-g-CA), CA-g-PMMA, and CA-g-PMMA-TEPA membranes at pH of 7.0 were 34.5 %, 83.3 %, and 99.1 %, respectively. The removal percentage results were detected to increase with increasing in the regeneration cycles. At the end of the fourth cycle, the HA removal percentages were 41.6 %, 87.4 %, and 99.9 % for un-g-CA, CA-g-PMMA and CA-g-PMMA-TEPA membranes, respectively.

5.2.1. Results and discussion

5.2.1.1. Graft polymerization

The free radical locations were produced on a cellulose acetate backbone through direct oxidation by using Ce^{4+} ion. The redox potentials of the Ce^{4+} metal ion are the key factors in defining the grafting effectiveness. Metal ions having lower oxidation potentials are chosen for enhanced grafting effectiveness. Therefore, the suggested tool for such practice has attributed to the intermediate development of a polymer chelate and metal ion complexes; where ceric ion is

well-known, to develop complexes with hydroxyl groups on a CA backbone and can be dissociated through one electron transfer to provide free radicals.

$$Ce^{4+} + R_{Pol.}OH \rightarrow Complex \rightarrow R_{Pol.}O^{\bullet} + Ce^{3+} + H^{+} \quad \textbf{(5.1)}$$

$$R_{Pol.}O^{\bullet} + M \rightarrow R_{Pol.}OM \rightarrow R_{Pol.}OMM^{\bullet} \quad \textbf{(5.2)}$$

In this study, the tentative reaction mechanism during the grafting polymerization using sulfuric acid solution with the presence of ceric sulfate complex is well-known and the reaction mechanisms are suggested as follows **[197]**:

$$Ce_4^{+} + HSO_4^{-} \Leftrightarrow CeSO_4^{2+} + H^{+} \quad \textbf{(5.3)}$$

$$CeSO_4^{2+} + HSO_4^{-} \Leftrightarrow Ce(SO_4)_2 + H^{+} \quad \textbf{(5.5)}$$

$$Ce(SO_4)_2 + HSO_4^{-} \Leftrightarrow Ce(SO_4)_3^{2-} + H^{+} \quad \textbf{(5.6)}$$

$$HSO_4^{-} \Leftrightarrow SO_4^{2-} + H^{+} \quad \textbf{(5.7)}$$

During the polymerization reaction, only one species or all of these CS species are maybe reactive and having their equilibrium constants for the formation of complexes, dissociation, and termination **[198, 199]**. The concentrations of the above species are dependent on the hydrogen and sulfate ion concentration. Therefore, the resultant covalent bond between the CA and the acetate vinyl monomer was suggested due to the formation of free radicals on the vinyl monomer and initiated hydroxyl groups of cellulose acetate. The competitive reaction for the graft of the homopolymerization can be occurred due to the active species present in the aqueous medium (i.e. −H and –OH). To investigate the optimum grafting of MMA onto cellulose acetate which was initiated by the redox reaction of cellulose acetate and Ce (IV) ion, factors like, pH of polymerization medium, CS, and MMA concentrations were kept constant. On the other hand, the duration of polymerization and temperature of grafting were varied, and the effects were investigated. Therefore, initiation of graft polymerization of MMA onto cellulose acetate powder using Ce(IV) ion in sulfuric acid medium proceeds due to oxidizing of the substrate (i.e. cellulose acetate). Consequently, the reaction complexes break down to provide CA macro radicals, H^{+} and Ce(III) ion. These radicals may mainly result from sulfur−hydrogen rather than

oxygen−hydrogen bonds of the CA because of the sulfur−hydrogen form weaker covalent bonds when compared with oxygen−hydrogen. Consequently, the free radical grafting copolymerization of MMA onto the cellulose acetate powder is expected to be attained. Development of CA macro radicals includes an electron transferring method from the acetate group to the Ce(IV) ions. Thus, $Ce(SO_4)_2$ is supposed to be the reactive species of CS where later has changed to the highly stable and colorless Ce(III) ion. Moreover, it is evidently observed that the color of Ce (IV) sulfate initiator with yellow color disappears when the grafting reaction time continues.

During the modification of cellulose acetate powder, the grafting polymerization of MMA onto CA powder was proposed using CS as an initiator. The polymerization was attained in a heterogeneous system (i.e. monomer–polymer), and the commercial CA powder was first purified to achieve a better diffusion of the monomer in the peripheral layer of CA during the grafting process. For initiation of vinyl polymerizations, CS has been commonly used as a source of radicals. The general processes assumed for the synthesizing of CA-g-PMMA_TEPA are presented in **Fig 5.10**. It is suggested that the free radical fragments may abstract hydroxyl groups of CA from the backbone to generate macro radicals, introducing graft polymerization. On the other hand, the other suggested reaction mechanism was that the radicals could react with the monomer to develop an increasing monomeric radical. Therefore, the increasing monomeric radical was able to transfer its radical character to the CA chain and the MMA graft copolymerization as well as homopolymerization was induced. The effective chemical grafting of MMA onto CA chains were investigated using ^{1}H NMR and the spectra of CA, MMA, and CA-g-PMMA is presented in **Fig. 5.11**.

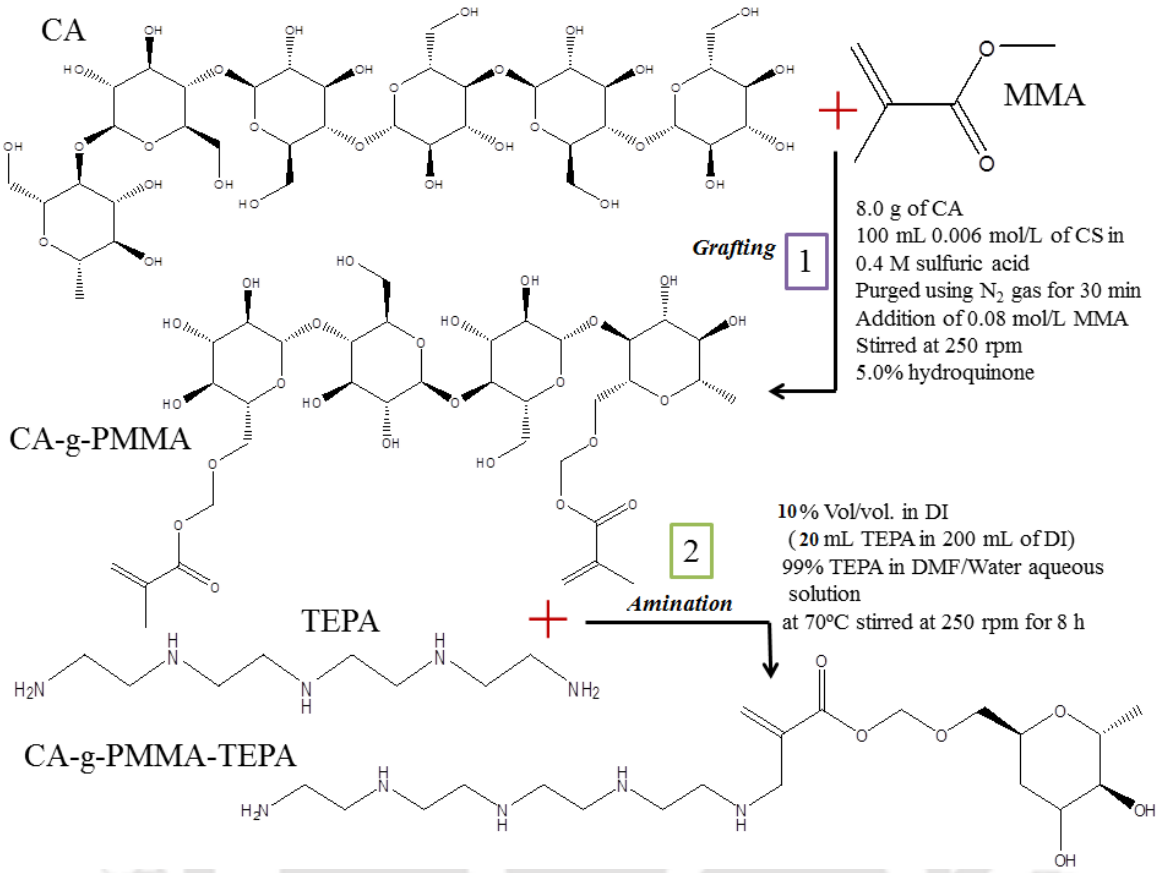

Fig. 5.10 Scheme for preparation of PMMA, CA-g-PMMA and, CA-g-PMMA_TEPA

As clearly seen from the figures, a significant shift and splitting of the CA peaks were detected after grafting of the PMMA, and a successful graft polymerization was achieved. Subsequently, un-grafted PMMA was completely detached from the CA surface by Soxhlet extraction followed by washing using methanol and deionized water. NMR results confirmed that the CS was able to initiate graft polymerization of MMA on CA properly. Obviously, the chemical integrity of the CA and PMMA was observed after graft polymerization, as the peaks corresponding to both CA and MMA were observed in the ^{1}H NMR spectrum of the CA-g-PMMA, though, the level of integrity was observed to be dependent on polymerization time and temperature.

Table 5.3 ^{1}H NMR results of prepared samples

Sample	Shift	H's	Integral
CA	1.95	9	8.90
	2.54	2	2.09
	3.52	35	35.01
MMA	3.67	10	10.00
	1.86	10	9.83
	5.60	3	3.03
	6.02	3	3.19
CA-PMMA (2/25)	1.93	10	10.06
	2.50	1	0.96
	3.85	121	120.98
CA-PMMA (2/60)	1.94	14	13.93
	2.50	1	0.98
	3.77	127	127.09
CA-PMMA (6/45)	1.95	24	24.00
	2.50	2	2.02
	3.59	118	117.98
CA-PMMA (6/70)	1.95	12	11.98
	2.50	1	1.09
	3.63	84	83.94
CA-PMMA (8/25)	1.94	10	10.02
	3.63	64	64.10
	2.50	1	0.88
CA-PMMA (8/60)	2.50	2	1.99
	1.97	23	22.91
	3.64	150	150.10

5.2.1.2. Effect of polymerization time and temperature

To examine the effects of temperature on the grafting polymerization of MMA onto cellulose acetate was conducted at 25, 45, 60, and 70 ºC, where the concentrations of MMA and CS were kept at 6 mmole/L and 8 mmole/L, respectively, and the pH of the polymerization medium was kept at 2.0. On the other hand, the reaction time was varied as 2, 6, and 8 h. The ^{1}H NMR results of CA, MMA, CA-PMMA (2/25), CA-PMMA (2/60), CA-PMMA (6/45), CA-PMMA (6/70), CA-PMMA (8/25), and CA-PMMA (8/60) are shown in **Fig. 5.11** and the results (**Table 5.3**) are ^{1}H NMR (600 MHz, DMSO) δ 3.60 – 3.45 (m, 35H), 2.54 (t, *J* = 33.2 Hz, 2H), 2.18 – 1.63 (m, 9H); ^{1}H NMR (600 MHz, DMSO) δ 6.05 – 5.97 (m, 3H), 5.60 (dd, *J* = 4.1, 3.5 Hz, 3H), 3.67 (s, 10H), 3.32 – 3.27 (m, 1H), 1.86 (d, *J* = 1.2 Hz, 10H); ^{1}H NMR (600 MHz, DMSO) δ 4.05 – 3.72 (m, 121H), 2.56 – 2.43 (m, 1H), 2.10 – 1.76 (m, 10H); ^{1}H NMR (600 MHz, DMSO) δ 4.04 – 3.55 (m, 127H), 2.58 – 2.41 (m, 1H), 2.10 – 1.78 (m, 14H); ^{1}H NMR (600 MHz, DMSO) δ 3.78 – 3.38 (m, 118H), 2.55 – 2.45 (m, 2H), 2.12 – 1.75 (m, 24H); ^{1}H NMR (600 MHz, DMSO) δ 3.89 – 3.44 (m, 84H), 2.50 (s, 1H), 2.14 – 1.73 (m, 12H); ^{1}H NMR (600 MHz, DMSO) δ 3.63 (d, *J* = 9.6 Hz, 64H), 2.50 (s, 1H), 1.94 (dd, *J* = 66.6, 49.2 Hz, 10H) and ^{1}H NMR (600 MHz, DMSO) δ 3.96 – 3.48 (m, 150H), 2.50 (s, 2H), 2.13 – 1.76 (m, 23H), respectively. From these results, the CA signals at 2.54 and 2.18-1.63 ppm were significantly improved after the grafting of the PMMA. However, the chemical shifts and the peak intensities were varied with the time and temperature. In this study, the combined effects of the time and temperature were observed, and the appearances of the peaks having higher intensities were detected for CA-PMMA 6/45, CA-PMMA 6/70, and CA-PMMA 8/60. It is obvious that the grafting is time and temperature dependent, where the combination of time and temperature at 8 h and 60 ºC (i.e. CA-PMMA, 8/60) seems to be the optimum temperature and time for the grafting of MMA onto CA by the CA−Ce (IV) sulfate redox system. Moreover, the peak for CA at around 3.60 – 3.45 ppm was split after the graft polymerization reaction of PMMA onto the CA backbone. The chemical shift and splitting of the proton at 3.6 ppm are accredited to protons of $–OCH_3$ in PMMA, which is an indication of the successful attachment of the MMA monomers on the CA backbone **[200]**. Upon raising the temperature while keeping the time constant enhances the effectiveness of the redox instigation system and in turn improves the degree of the grafting reaction. If we observe the graphs for CA-PMMA, 8/25 and CA-PMMA, 8/60, new peaks with higher intensities were detected at 60 ºC than 25 ºC. Nonetheless, the contribution of

the higher polymerization time, the higher temperature has played a great role for the enhancement of the grafting process. The polymerization temperature is one of the key factors that govern the kinetics of grafting copolymerization. The grafting efficiency improves with higher temperature until the optimum bound is achieved. The reason for this result can be due to increasing of the monomeric diffusional process in the polymeric backbone with rising temperature and then be simplifying the grafting process. During the grafting of MMA on CA, the grafting efficiency increased considerably as the temperature was raised due to a larger swelling of the CA backbone and a resultant improved degree of the monomers' diffusion within the locality of CA backbone. On the other hand, the results can be explained due to an increased thermal decomposition rate of CS and its capacity in generating free radicals on the polymer backbone with increasing temperature. Therefore, this incident can cause in increased CA polymer macro radicals concentration, and consequently improved the graft polymerization. The effect of variation of reaction time was also investigated during the grafting polymerization. A better grafting efficiency was observed when the reaction time was increased. Regardless of the effect of temperature, an increase in the reaction time increases the rate of grafting. As clearly observed from the graphs presented in **Fig 5.11**, CA-PMMA, 2/60 and CA-PMMA, 8/60, peaks with higher intensities were detected for the polymerization time of 8 h. This result is explained as the polymerization time increases the CA backbone, MMA monomer, and CS initiator interactions increase. Moreover, compared with other efforts to chemical modification of CA, the functionalization method would keep the main-chain structures of CA integral without altering much its unique physical properties. Moreover, the graft percentage *(Gp)* of CA-g-PMMA and the weight gain percentage *(W_{gp})* of CA-g-PMMA_TEPA were calculated using Eq. (1) and (2). The *Gp* results for CA-PMMA (2/25), CA-PMMA (2/60), CA-PMMA (8/25), CA-PMMA (6/45), CA-PMMA (6/70), and CA-PMMA (8/60) were found to be 19.4, 20.2, 23.1, 25.8, 28.3, and 36.3 %, respectively. It was observed that the effects of time and temperature were indicated clearly from the *Gp* results of the samples and the highest grafting percentage was attained for CA-PMMA (8/60). Accordingly, CA-PMMA (8/60) sample was selected for the amination process. Furthermore, the weight gain percentage *(W_{gp})* of CA-g-PMMA-TEPA was calculated as 33.3 %. The results indicate that the grafting and amination process were successful in this study.

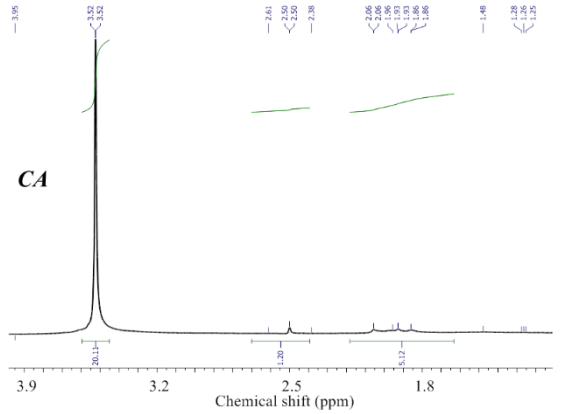

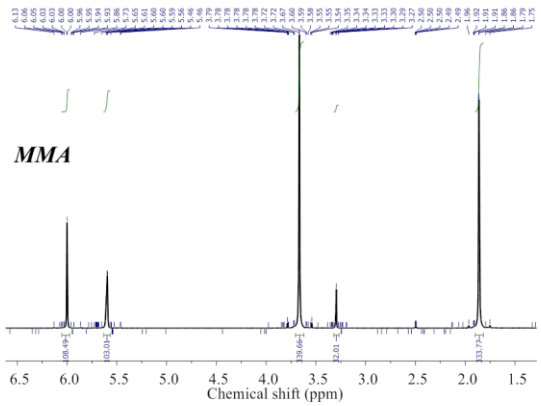

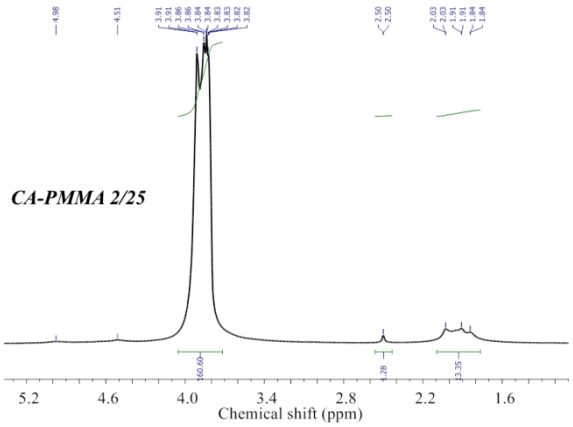

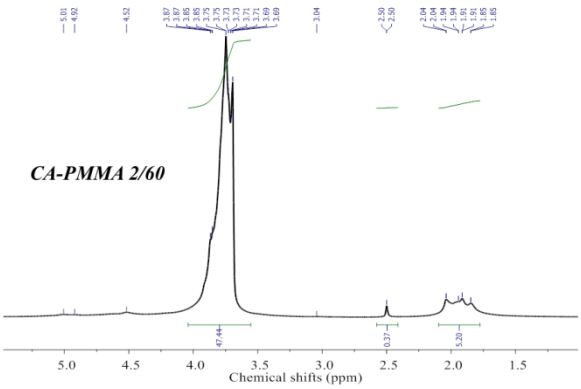

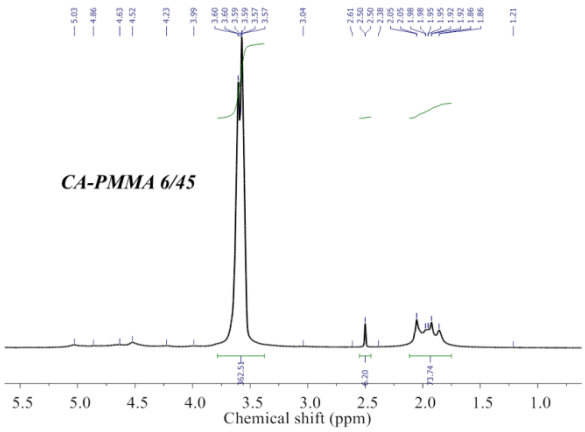

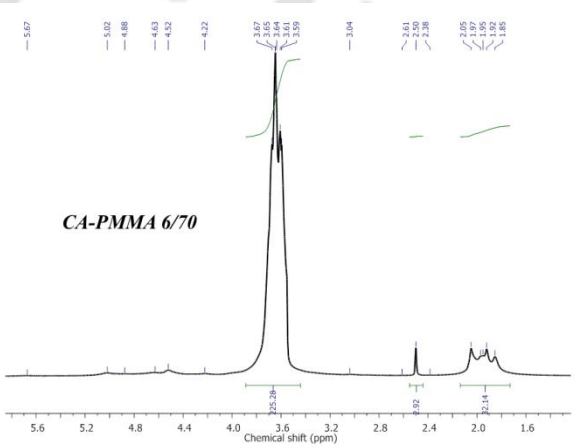

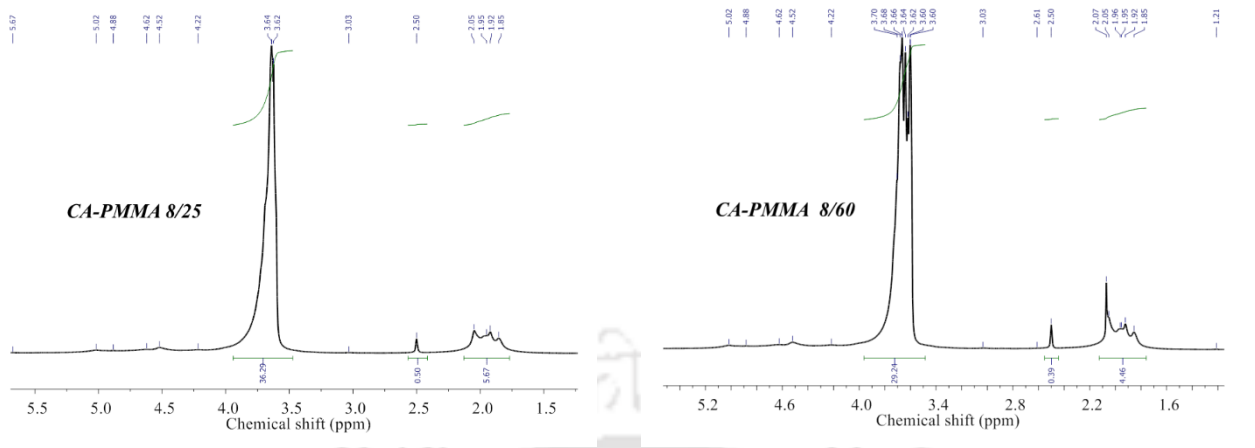

Fig. 5.11 ^{1}H NMR spectra of CA, MMA, and CA -g- PMMA dissolved in DMSO-d6 at different polymerization time and temperature

5.2.1.3. ATR-FTIR Spectroscopy and zeta potential analysis

To examine the chemical structure of the synthesized samples, the ATR-FTIR analysis was done. Therefore, the functional groups of CA, MMA, CA-g-PMMA, and CA-g-PMMA_TEPA were characterized and presented in **Fig. 5.12 (a)**. In the spectra of pure CA, the broadband detected at 3419 cm^{-1} corresponded to −OH stretching because of the strong hydrogen bond of intermolecular and intra-molecular kinds. The characteristic band of 2960 cm^{-1} attributed to the C−H stretching **[120]**. In the IR spectrum of CA-g-PMMA_TEPA, the stretching vibrations of C–H bonds are present at 2890 cm^{-1}. The peaks of N–H bonds and C–N bonds are present at 1720 and 1250 cm^{-1}, respectively. Thus, the results show that TEPA was effectively introduced onto the surface of the CA-g-PMMA. The spectrum for all the samples, except MMA, show considerable peaks attributed to O–H group at 3419 cm^{-1}, 3423 cm^{-1} and 3396 cm^{-1} for CA, CA-g-PMMA, and CA-g-PMMA_TEPA, respectively. This result is due to the interaction of CA with MMA and TEPA successfully. Comparing the FTIR spectrum of the CA-g-PMMA and CA-g-PMMA_TEPA to that of the unmodified CA, the broadening peak of hydroxyl groups in the glucose rings turn into smaller after the reaction of the CA with MMA and PMMA_TEPA. This result indicates that some of the hydroxyl groups were replaced during the synthesizing process. Furthermore, the zeta potential (ζ) values of the modified and unmodified CA at pH of 7.0 are presented in **Fig. 5.12 (b).** Zeta potential analysis is one of the

most important methods used to obtain information on the electrical charge properties **[188]**. Therefore, the ζ or electrical charge properties of the powder or film polymers impact their performances towards specific applications. As seen from the figure, the un-grafted CA powder displayed low negative ζ value (i.e. -5.1 mV). On the other hand, the ζ values of the grafted powders (G_1-G_6, **Table 2.9, Chapter 2**) at different temperature and time displayed higher negative values than the un-grafted powder. The high negative ζ values for the PMMA grafted samples is due to an increase in the extent of –COOH groups on the surface of CA **[180].** A variation in zeta potential results as a function of time and temperature was confirmed by this study. On the other hand, high positive ζ value (+44.4 mV) was detected for the CA-g-PMMA modified with TEPA. This positive ζ result was attained due to the introduction of the amine group (TEPA) through the ring opening reaction of the methyl groups of the copolymer in the polymer amination process **[201, 202]**.

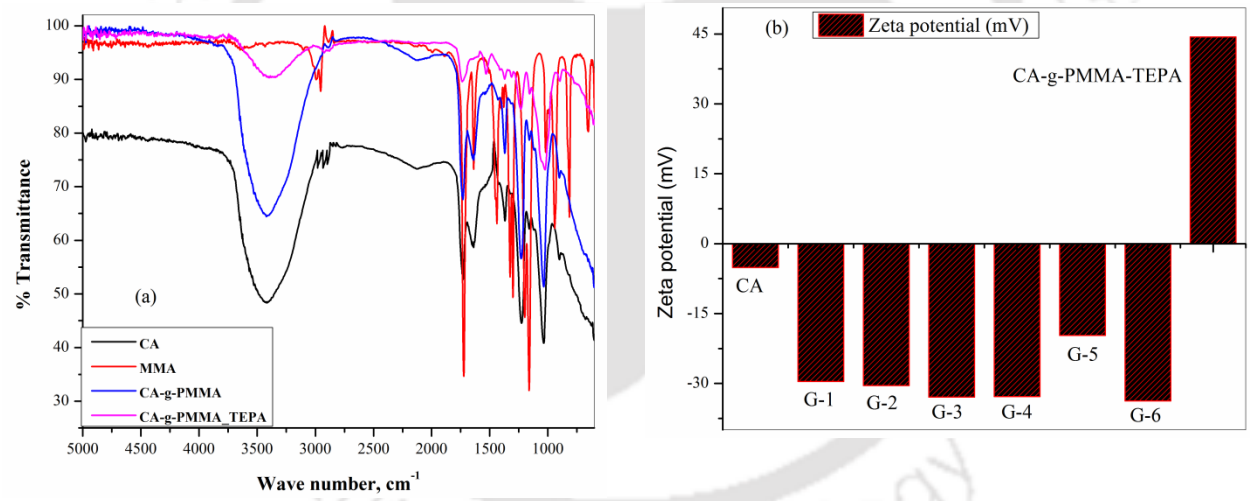

Fig. 5.12 (a) FTIR spectra and (b) zeta potential (ζ) results of the unmodified and modified CA

5.2.1.4. Membrane morphological and physicochemical studies

The surface morphologies of the prepared membranes were investigated using FESEM, and the top surfaces and cross-sectional images are presented in **Fig. 5.13**. As seen from **Fig. 5.13 (a),** the CA-g-PMMA and CA-g-PMMA-TEPA membranes displayed porous network

structures with many open pores. On the other hand, the porous network structures were not observed in the case of un-grafted CA membranes. However, after the amination process, the porous network structures on the membrane were observed to be smooth without showing major microscopic defects. The membranes were having an asymmetric structure consisting of a thin dense top-layer and porous sub layer and without the development of macro voids were observed. The formation of macro-voids occurs under rapid precipitation condition, and the precipitations are faster at high coagulation temperature **[53]**. In the present study, the coagulation bath temperature and evaporation time (i.e. before immersion) were fixed to 28±2 ºC and 30 s, respectively, during the preparation of all the membranes. As explained in detailed in the previous study, an additional important factor which can influence the development or suppression of macro-voids is the type of de-mixing happened during the phase separation process, where, the instantaneous de-mixing and the delayed de-mixing depend on the mutual affinity of the solvent and non-solvent in the ternary system **[103]**. The suppression or the formation of macro-voids was may be due to adding of the PEG and TiO_2 additives to the ternary (polymer/solvent/non-solvent) system. The presence of theses additives can increase the concentration/viscosity of the casting solution which may diminish the diffusional exchange rate of the solvent and non-solvent during the membrane formation process. Consequently, this may hinder the instantaneous liquid-liquid de-mixing process which suppresses the formation of macro-voids **[140].** As observed from **Fig. 5.13 (b)**, when the modified CA solution was cast, finger-like structure-free and porous cross-section were attained, unlike the unmodified CA, where some finger-like structures with less porous cross-section were detected. Therefore, the grafting of PMMA onto the CA surface made the membrane structure more porous. Since the top layer is highly porous to form the resistance layer which can limit many nuclei development in the sub-layer, the porous membrane with no finger-like structures can be developed under the highly less stable system **[201]**. Therefore, the porous top layer is believed to suppress the formation of finger-like structures in the sub-layer and result in porous, finger-like structure-free cross-section. Furthermore, a highly porous membrane (CA-g-PMMA-TEPA) was obtained with the addition of TEPA to the grafted polymer due to the development of quaternary aminated polymer. Unlike the CA-g-PMMA membrane, a porous structure was observed below the top layer in the cross-section in the case of CA-g-PMMA-TEPA membrane. Therefore, with the addition of TEPA to the grafted polymer, the top layer can lead the liquid–liquid phase

separation instantly, causing in the development of many pores in the top layer of the membrane. Moreover, the top layer of the membrane was porous enough to lead the large amounts of the non-solvent into the sub layer to start a number of nuclei creations. The open pore structures developed in the membranes are formed by nucleation and development of the polymer-lean phase in the metastable area between the bi-nodal and the spinodal curve **[139, 141]**. Nevertheless, the top layer structure of the ultrafiltration membrane frequently doesn't reveal an open pore structures and not a completely uniform gel-layer, which is stated as a nodular structure. The development of nodular structures can't be described by nucleation of the polymer lean part. It is also not common that nucleation of the polymer-rich part happens because this only occurs at initially low polymer concentrations, below the critical point. A possible explanation for the formation of a nodular structure on the top surface of the membranes could be due to the spinodal de-mixing because the diffusion process throughout the development of the top layer is faster for the homogenous system to develop greatly unstable and crosses the spinodal curvature **[102]**. The top surface with improved inter-connected pores structures is observed more prominently in the case of CA-g-PMMA-TEPA membrane which is achieved due to the spinodal decomposition

Studying of compaction factor (CF) of the prepared membranes is very important to distinguish the morphological structures (i.e. pore arrangements) of the membranes particularly the membrane sub-layer configuration. Therefore, membranes having high CF indicate that these are highly compacted and indicate the existence of defective pore structures in the membrane sub-layer. The compaction factor and hydraulic characteristics of all prepared membranes are presented in **Table 5.4**. It was observed that for both CA-g-PMMA and CA-g-PMMA-TEPA membranes, the CF decreases to 1.4±0.5 and 1.2±0.7, respectively, from 2.2±0.2 (i.e. un-g-CA). These results were attained may be due to the modification process, membranes appear to be free of finger-like structures. Furthermore, the CA-g-PMMA-TEPA membrane exhibited the smallest compaction factor result (i.e. 1.2±0.7) because of less microscopic defects as compared with CA-g-PMMA membrane.

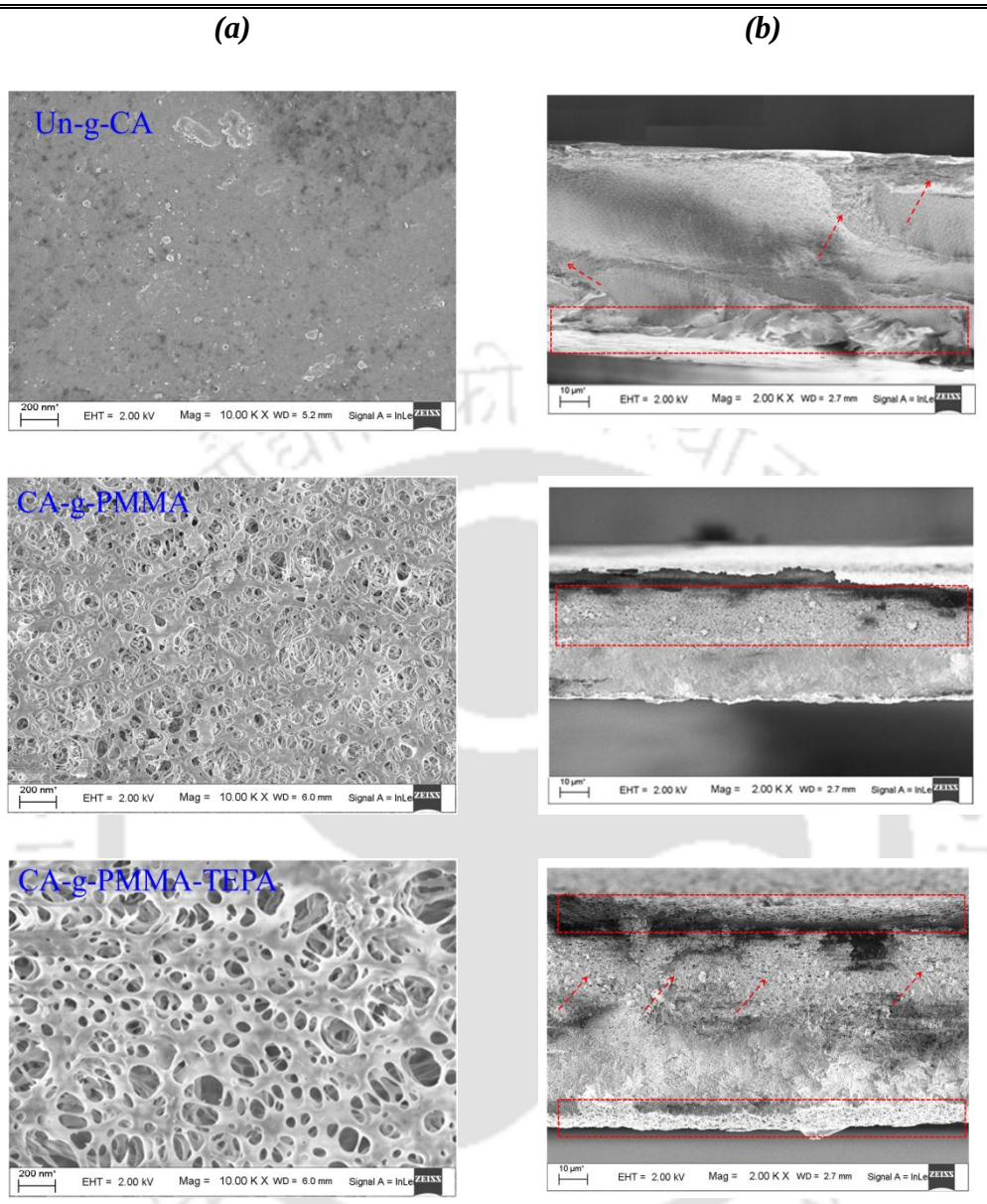

Fig. 5.13 (a) Top surface and (b) cross-sectional FESEM images of un-g-CA, CA-g-PMMA and CA-g-PMMA-TEPA membranes

The hydraulic resistance *(R_m)*, EWC, average pore radius, porosity, and thickness of all the prepared membranes are reported in **Table 5.4.** The average pore size and pore size distributions were determined using water filtration velocity method and using ImageJ software from FESEM images, and the results are presented in **Fig. 5.14** and **Table 5.4**. The measured average pore size results for un-g-CA, CA-g-PMMA, and CA-g-PMMA-TEPA membranes were 42.4 nm, 56.7 nm, and 62.8 nm, respectively.

Table 5.4 Compaction and hydraulic characteristics of the prepared membranes at 250 kPa

Membrane	*CF*	R_m ($\times 10^{-10} m^{-1}$)	J_w (L/m^2h)	*EWC* (%)	ε (%)	r_m (nm)	Thickness (μm)
Un-g-CA	2.2±0.2	0.95	292.7	81.2±4.1	74.9±3.5	42.4±4.4	82.7
CA-g-PMMA	1.4±0.5	0.80	312.2	85.4±3.2	77.2±2.3	56.7±3.2	71.8
CA-g-PMMA_TEPA	1.2±0.7	0.79	334.5	87.7±2.7	82.4±1.5	62.8±2.3	73.5

As seen from these results the hydraulic resistance of un-g-CA (i.e. $0.95\times10^{-10}m^{-1}$) was greater than CA-g-PMMA (i.e. $0.80\times10^{-10}m^{-1}$) and CA-g-PMMA-TEPA (i.e. $0.79\times10^{-10}m^{-1}$) membranes. This higher resistance of un-g-CA is because of its less porous nature than the other membranes which can resist the water flux than the other membranes. From the porosity measurement results it is shown that all the membranes have shown a satisfactory results (i.e. 74.9 %, 77.2 %, and 82.4 % for un-g-CA, CA-g-PMMA, and CA-g-PMMA-TEPA, respectively) which is accredited to the lower concentration of the membrane forming polymer (10.5 wt. %) as well as due to the addition of PEG additives and TiO_2 NPs together with the type of solvent used and type of de-mixing occurred **[103]**.

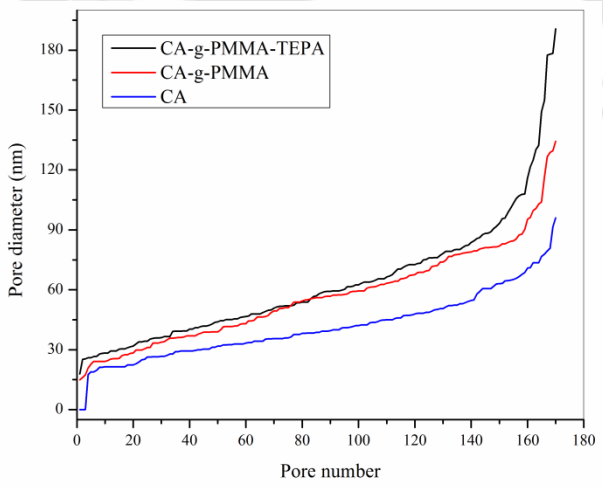

Fig. 5.14 Pore size distribution of CA, CA-g-PMMA and CA-g-PMMA-TEPA membranes

5.2.1.5. Ultrafiltration of PW and HA solutions

The pure water flux (PWF) studies were performed to investigate the effect of the grafting and amination of the prepared membranes, and the PWF results and the effect of the operating pressures are presented in **Fig. 5.15 (a)** and **(b)**, respectively.

As clearly presented in **Table 5.4**, the PWF results of un-g-CA, CA-g-PMMA and CA-g-PMMA-TEPA membranes at 250 kPa are 292.7, 312.2, and 334.5 Lm^{-2} h^{-1}, respectively. The pure water flux results of the membranes are consistent with their pore size and porosity results. Nevertheless, the PWF results of all the prepared membranes are suitable for their efficient use in filtration processes. The PWF results at different operating pressures are presented in **Fig. 5.15 (b)**. The results of PWF for all the membranes were increased almost uniformly with increasing in an operating pressure from 100 to 300 kPa. On the other hand, the permeate flux results and HA removal efficiencies of the prepared membranes were investigated using 10 ppm HA solution at pH of 7.0, and the results are presented in **Fig. 5.15 (c)** and **(d)**, respectively. The uniform decrease in HA fluxes with increasing time was suggested due to susceptible pore blocking of the membranes because of HA molecules adsorption and deposition on the membrane surface and inner channels of the pore, where the effect of concentration polarization was reduced by rigorous stirring (200 rpm) on the surface of the membrane. As seen from the figure, the un-g-CA, CA-g-PMMA, and CA-g-PMMA-TEPA membranes exhibited lower HA flux values as compared with PWF results.

Furthermore, the grafted and aminated membranes (CA-g-PMMA and CA-g-PMMA-TEPA, respectively) have revealed considerably higher removal efficiency for HA than the unmodified membrane (un-g-CA). The enhanced HA rejection efficiencies of the modified membranes were mainly due to the introduction of PMMA and TEPA through grafting and amination processes, respectively. These results confirmed that the introduction of PMMA and TEPA on the surface and within the matrix of CA indeed improved the characteristics of the membranes towards the removal of HA. Therefore, the HA rejection was suggested due to the electrostatic interaction between the membranes and HA molecules. As already explained in the previous section in **Fig. 5.12 (b)**, the results of zeta potential study showed that the surface charge value of un-g-CA (−5.1 mV) was increased to −33.7 mV (i.e. CA-g-PMMA).

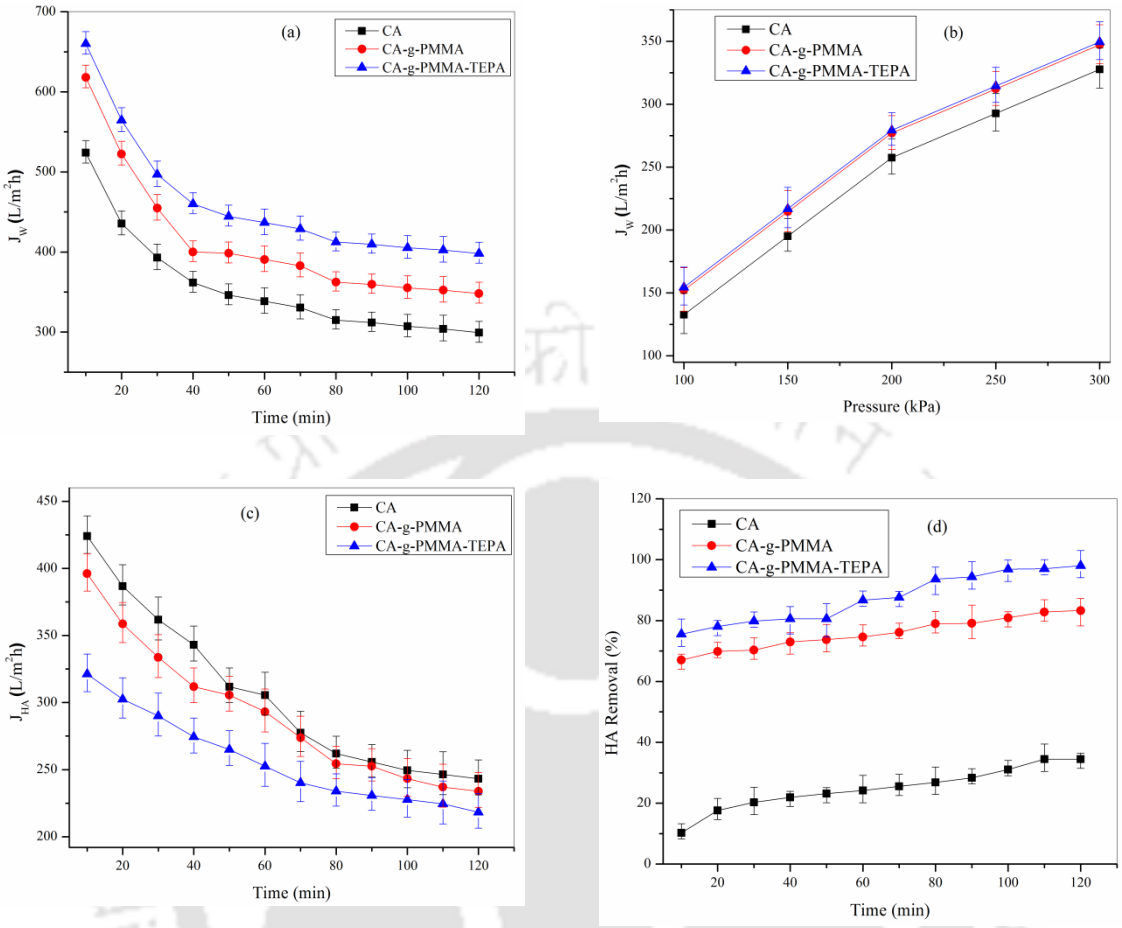

Fig. 5.15 (a, b) PWF, (c) HA flux, and (d) removal % results of un-g-CA, CA-g-PMMA and CA-g-PMMA-TEPA membranes at pH=7, HA concentration= 10 ppm, ΔP=150 kPa, @ 200 rpm)

On the other hand, after the amination process of CA-g-PMMA using TEPA, the surface charge result for CA-g-PMMA-TEPA was +44.4 mV. Whereas the measured zeta potential value of HA solution at pH of 7.0 was −60 mV **[203]**. As seen from the **Fig. 5.15 (d),** the HA molecule removal performance for un-g-CA membrane was lower as compared with modified membranes. This result is clear that more negative charges are required to remove (repulsion in this case) of the HA molecules with high negative charge. However, the negative charges of un-g-CA (−5.1 mV) were not enough to attain higher repulsion of the HA molecules with −60 mV. On the other hand, higher removal efficiencies were observed for CA-g-PMMA and CA-g-PMMA-TEPA membranes. Therefore, the HA molecules removal phenomenon for CA-g-PMMA membrane is due to electrostatic repulsion as both the high negatively surface charged membrane (−33.7 mV)

and the negatively charged of the HA aggregates would result in high electrostatic repulsion **[204]**. Furthermore, the highest removal efficiency was achieved for CA-g-PMMA-TEPA membranes due to the availability of high positive charges (+44.4 mV) for the adsorption of negatively charged HA molecules. Therefore, the maximum removal efficiencies for un-g-CA, CA-g-PMMA, and CA-g-PMMA-TEPA membranes at pH of 7.0 were 34.5 %, 83.3 %, and 99.1 %, respectively. The main assumption of this study was that the surface charges of the modified membranes were altered after the grafting and amination process of the CA polymer. Grafting method has numerous benefits, such as the capacity of modifying the polymer surfaces to have distinctive properties by choosing the various monomers. The introduction of grafting chains with a high density and an exact localization on the substrate surface can be done easily and well-regulated without changing the properties of the bulk polymer. Moreover, graft chains onto a substrate surface with covalent attachments and promising long-term chemical stability, in contrast to physically coated polymer chains, can be introduced. Initially, -OCH_3 of PMMA was covalently attached by replacing the –H atom of the –OH groups in CA (**Fig. 5.10**). Secondly, the TEPA was introduced through the ring opening reaction between the methyl groups of the PMMA and –NH_2 of the TEPA. As confirmed by the zeta potential study, the negatively and positively charges were introduced on the layer of the CA polymer alternatively. The schematic diagram for the membrane grafting, amination process and adsorption of HA molecules in UF process is presented in **Fig. 5.16**.

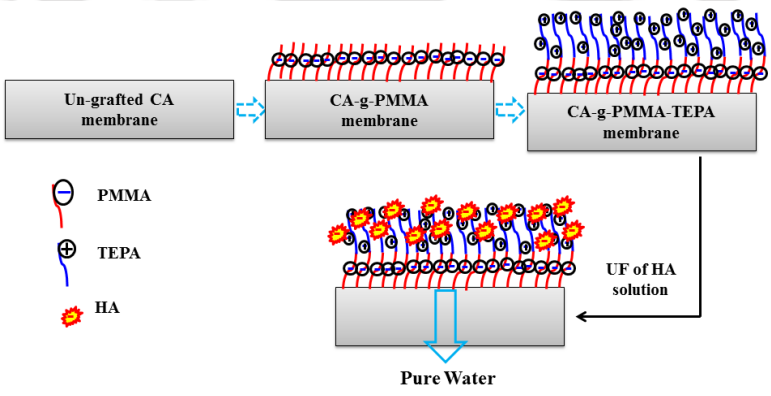

Fig. 5.16 Schematic diagram for the membrane grafting and amination process and adsorption of HA in UF process

5.2.1.6. Membrane regeneration performance study

To investigate the fouling and HA rejection performances of the un-g-CA, CA-g-PMMA, and CA-g-PMMA-TEPA membranes, four washing/regeneration cycles were conducted using 10 ppm HA solution and the results are shown in **Fig. 5.17**. After filtration of HA solutions, fouled membranes were cleaned with 0.05 M NaOH solution followed by rinsing using DI water for 30 min and the DI water fluxes of the tested membranes were measured. As clearly shown in **Fig. 5.17 (a)**, the uniform decrease in DI water and HA fluxes were understood to be highly noticeable which are attributed to the reduction in porosity (pore blocking) of the membranes due to an interior adsorption of HA molecules. Consequently, the DI water flux results for the four filtration cycles at pH of 7.0 for un-g-CA membrane are 311, 299, 288, and 274 L m^{-2} h^{-1}, respectively; for CA-g-PMMA membrane are 360, 346, 334, and 321 L m^{-2} h^{-1}, respectively; and for CA-g-PMMA-TEPA membrane are 409, 394, 381, and 366 L m^{-2} h^{-1}, respectively. On the other hand, the HA flux results for the four washing/regeneration cycles are 255, 243, 233, and 221 L m^{-2} h^{-1}, respectively, for un-g-CA membrane; 249, 236, 227, and 216 L m^{-2} h^{-1}, respectively, for CA-g-PMMA membrane; and 229, 214, 206, and 195 L m^{-2} h^{-1}, respectively, for CA-g-PMMA-TEPA membrane. The HA rejection efficiencies of all the prepared membranes at pH of 7.0 are presented **Fig. 5.17 (b)**. The removal percentage results were detected to increase with increasing of the regeneration cycles. At the end of the fourth cycle, the HA rejection percentages were 41.6 %, 87.4 %, and 99.9 % for un-g-CA, CA-g-PMMA, and CA-g-PMMA-TEPA membranes, respectively. The increasing in the removal performances of the membranes with increasing the regeneration cycles can be attributed due to the permanent deposition of the HA molecules onto the membrane surface and within the membrane pores which could be accredited to structural interaction **[60]**. In addition to the electrostatic interaction phenomena the HA rejection for the membrane with increasing the regeneration cycle was also considered as an indicator of considerable removal due to its structural interaction. Therefore, the surface and pore channel depositions of HA molecules can provide extra resistance to solute transport. From this study, it can be suggested that the CA-g-PMMA-TEPA membrane can be a good candidate for the removal of HA molecules from aqueous solutions.

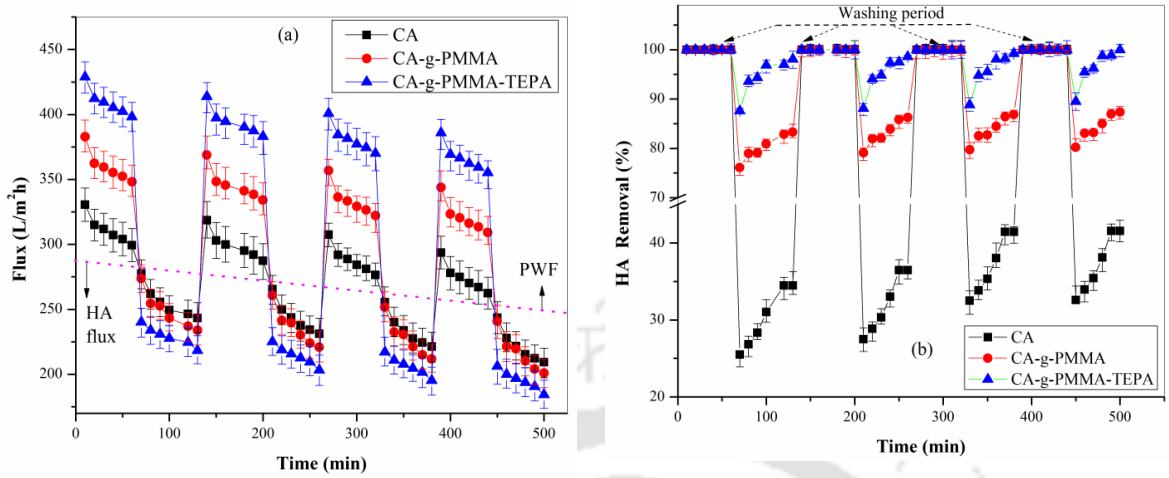

Fig. 5.17 Washing/regeneration study of un-g-CA, CA-g-PMMA, and CA-g-PMMA-TEPA membranes at pH=7, HA concentration= 10 ppm, ΔP=150 kPa, @ 200 rpm)

5.2.2. Summary

The feasibility of grafting of PMMA onto CA polymer using CS as the redox initiator was investigated in the present work. The polymerization reaction conditions, such as initiator concentration and monomer concentration were kept constant. On the other hand, the polymerization reaction time and temperature were varied and had a great impact on grafting copolymerization. Moreover, the functionalization of the synthesized product was done using TEPA amine. The study of ^{1}H NMR and FTIR spectra results indicated that the graft copolymerization and functionalization were successfully achieved. A highly porous membrane (CA-g-PMMA-TEPA) was obtained with the addition of TEPA to the grafted polymer due to the development of quaternary aminated polymer. Unlike the CA-g-PMMA membrane, a porous structure was observed below the top layer in the cross-section in the case of CA-g-PMMA-TEPA membrane. The maximum removal efficiencies for un-g-CA, CA-g-PMMA, and CA-g-PMMA-TEPA membranes at pH of 7.0 were 34.5 %, 83.3 %, and 99.1 %, respectively. The removal percentage results were detected to increase with increasing in the regeneration cycles. At the end of the fourth cycle, the HA removal percentages were 41.6 %, 87.4 %, and 99.9 % for un-g-CA, CA-g-PMMA, and CA-g-PMMA-TEPA membranes, respectively. Therefore, the grafted and aminated membrane, CA-g-PMMA-TEPA, has shown a higher HA removal efficiency and can be used for various industrial applications.

Chapter 6: Overall Conclusions and Scope of the Future Work

In this chapter, overall conclusions and scope of the future work are presented briefly.

6.1. Overall Conclusions

An attempt to prepare and modify synthetic membranes has been done using two different techniques, namely phase-inversion and electro-spinning to investigate their morphological structures and to evaluate their efficiency towards wastewater treatment applications. The objective of this research work has been addressed successfully, and vital conclusions have been drawn in terms of membrane preparation, functionalization, characterization, and applications. The entire research works has been focused on three major findings: (a) Preparation, characterization, and application of electro-spun composite membranes; (b) Preparation, characterization, and application of phase-inverted membranes; and (c) Modification, characterization, and application of cellulose acetate membranes.

Therefore, the major findings of this research work in the preparation, modification, and application of electro-spun and phase-inverted membranes are summarized as follows:

- The addition of TiO_2 NPs on cellulose acetate caused the formation of largely interconnected fiber networks. The specific surface areas of the adsorbent were increased from 38.47 to 48.47 m^2g^{-1} as the amounts of TiO_2 nanoparticles in the adsorbent matrix were increased from 1.0 to 2.5 wt. %. The highest removal efficiencies of lead and copper ions with CA/TiO_2 adsorbent were estimated to be 99.7 % and 98.9 % under the optimized conditions of TiO_2 amounts (2.5 wt. %), pH (5.2 and 5.8 for Pb (II) and Cu

(II), respectively), agitation period (5 h), adsorbent dosage (2 g/L) and temperature (35 °C). Repeated adsorption–desorption experimentations after four phases revealed that CA/TiO_2 adsorbent showed a high elimination of copper and lead ions.

- The finger-like voids and macro-voids in the M_1 membrane sub-layer were significantly reduced after the addition of PEG regardless the effect of TiO_2 in M_3 membrane. The TiO_2 are highly stable at high temperatures, and therefore the degradation temperature of the M_1 and M_4 membranes were significantly improved after addition of TiO_2. The highest PWF was attained for the M_3 membrane with the introduction of both PEG and TiO_2 simultaneously. The improvement in the average pore size, porosity, and hydrophilicity of the M_1 membranes was also revealed. CA-TiO_2 blended with PEG membrane (i.e. M_3) exhibited highest BSA flux permeates and flux recovery ratios for the three fouling/rinsing cycles. The CAT blended with PVP membrane (i.e. CAPT) exhibited best BSA flux permeates and flux recovery ratios for the three fouling/rinsing cycles.

- The highest rejection/ adsorption of Cr (VI) ions result was attained at low concentration (10 ppm) due to the availability of excess binding sites for Cr (VI) ions at a pH of 3.5 for CA/Ti-TEPA membrane. The rejection/ adsorption results for 10 ppm, 30 ppm, 50 ppm, 70 ppm, and, 100 ppm for CA/Ti-TEPA membrane at pH 3.5 are 99.6 %, 98.9 %, 93.6 %, 86.4 %, and 82.2 %, respectively. The maximum removal efficiency results of Cr (VI) ions at pH of 3.5 using CA/U-Ti, CA/Ti-EDA, CA/Ti-HMTA, and CA/Ti-TEPA membranes were 47.2 %, 86.4 %, 93.6 % and 98.9 %, respectively. The maximum Cr (VI) rejection results for CA/Ti-TEPA membrane for washing/regeneration cycles are 99.6 %, 99.5 %, 98.6 % and, 96.6 %, respectively. Therefore, there are good prospects

for CA/Ti-TEPA membrane for the removal of Cr (VI) ions from water and wastewater in practical applications.

- The study of ^{1}H NMR spectra results indicated that the graft copolymerization and functionalization of PMMA onto CA were successfully achieved. A highly porous membrane (CA-g-PMMA-TEPA) was obtained with the addition of TEPA to the grafted polymer due to the development of quaternary aminated polymer. Unlike the CA-g-PMMA membrane, a porous structure was observed below the top layer in the cross-section in the case of CA-g-PMMA-TEPA membrane. The maximum removal efficiencies for un-g-CA, CA-g-PMMA and CA-g-PMMA-TEPA membranes at pH of 7 were 34.5 %, 83.3 %, and 99.1 %, respectively. At the end of the fourth cycle, the HA removal percentages were 41.6 %, 87.4 %, and 99.9 % for un-g-CA, CA-g-PMMA and CA-g-PMMA-TEPA membranes, respectively. Therefore, the grafted and aminated membrane, CA-g-PMMA-TEPA, has shown a higher HA removal efficiency and can be used for various industrial applications.

6.2. Future recommendations

The possible scopes for further improvement on the preparation and modifications of the membranes are also identified in this research work. Furthermore, the specific objectives on the preparation, characterization, modification and application of the polymeric membranes have been discussed extensively. In addition, this section introduces possible recommendations in this area which would give valuable research inputs for further study on preparation, modification, and application of electro-spun and phase inverted membranes. Some of the important recommendations are listed as follows:

- Preparation of novel membranes by combining electro-spinning and phase inversion techniques.
- Preparation of CA-g-PMMA_amine membranes for potential removal of heavy metals.
- In addition, the functionalized membranes would be evaluated towards the removal of other metals (such as Arsenic, Cadmium, Mercury, and Cobalt).
- Finally, evaluating the resistance to fouling performances of the fabricated membranes over long periods of time, during multiple cycles (filtration/ cleaning) in a wide range of operating conditions (transmembrane pressure, hydrodynamics, temperature, pH, feed concentration) and for a variety of feed compositions.

Furthermore, the modification and functionalized of polymer and/or membranes would be considered in our future work. For example, the modification with chitosan and other quaternary amine groups to capture different heavy metals would be considered.

Appendix

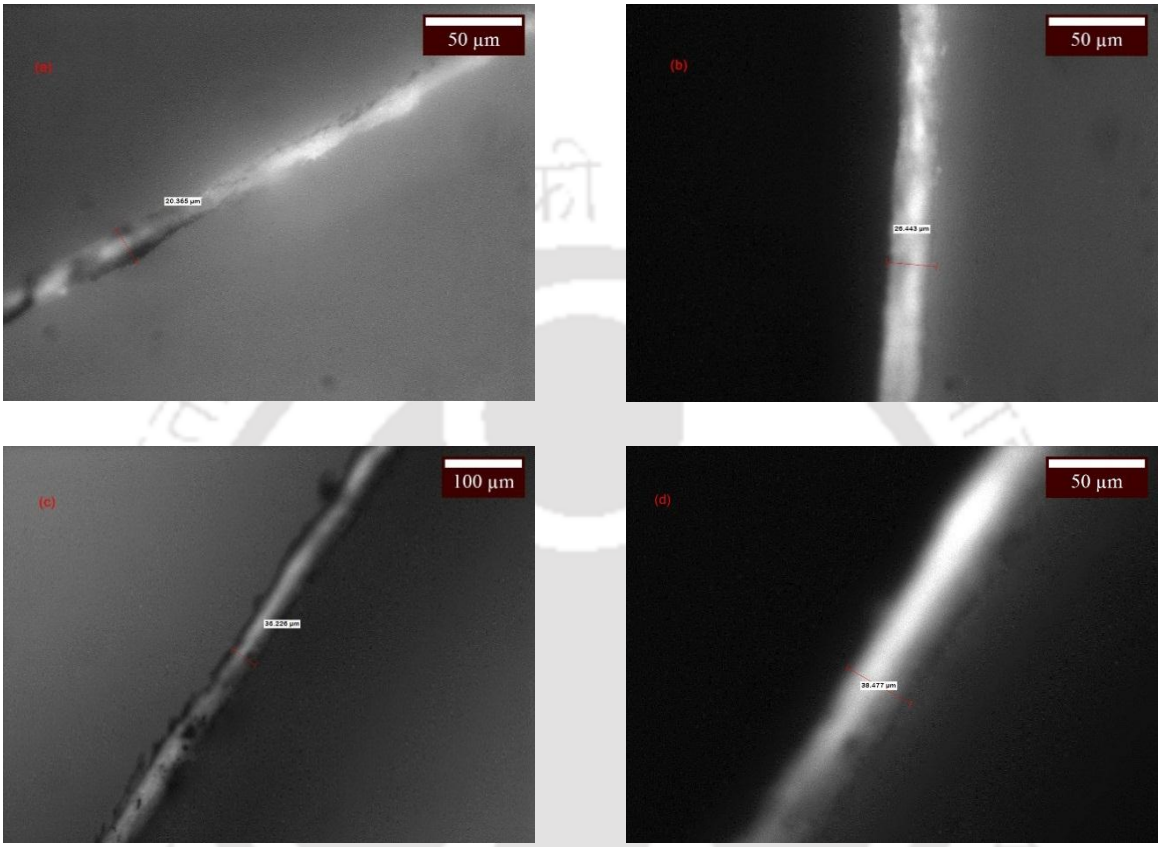

Fig. S3.1 Microscopic images of the ePVA fibers at different process times, (a) 25 min, (b) 35 min, (c) 45 min and (d) 60 min.

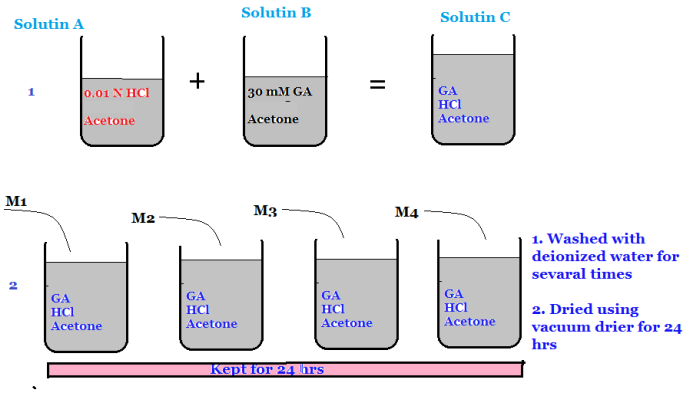

Fig. S3.2. Preparation of cross-linking solution **(1)** and immersing the membranes into the solution **(2).**

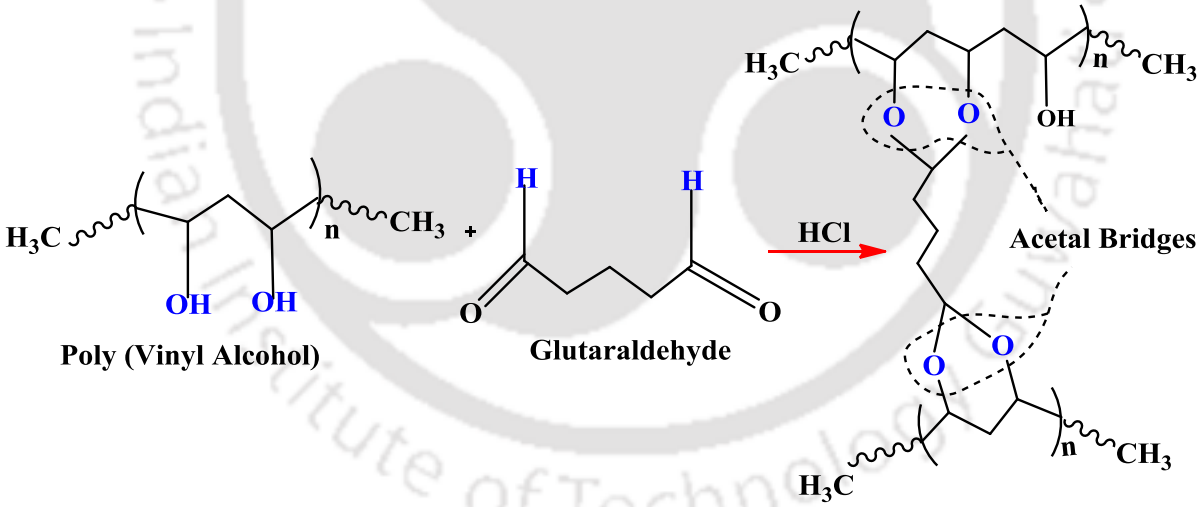

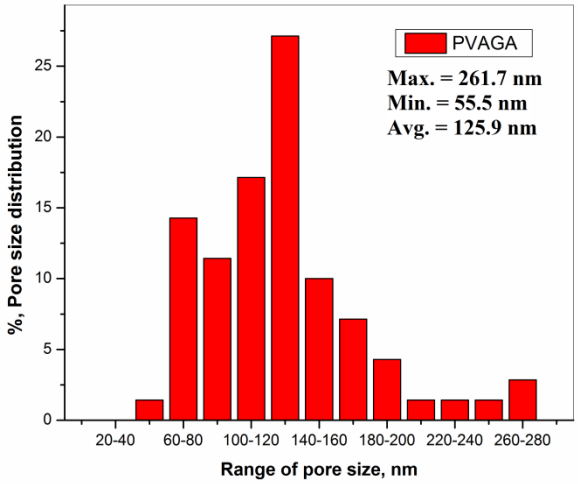

Fig.S3.4. % Surface pore size diameter distribution of ePVA/GA membranes obtained at 45 min electro-spinning duration.

Specific surface area analysis

The nitrogen adsorption and desorption isotherm for electro-spun PVA nanofiber membranes are shown in **Fig. S3.5**. Adsorption isotherms show the quantity of molecules adsorbed on the surface of a solid as a function of equilibrium pressure at a given (constant) temperature.

It is observed from **Fig. S3.5** that initially the adsorption volume quickly raises at lower relative pressure, once the monolayer development of the adsorbed molecules is achieved and multilayer development begins to occur in matching to the sharp-knee of the isotherm which indicates that the isotherm graphs are of Type IV which is characteristics of the mesoporouse structure.

The shapes of the hysteresis loop are also associated with the different pore shapes, for the case of nonporous material, those desorption isotherm curves repeat the adsorption curves. Nevertheless, for the macroporous and mesoporous, desorption isotherm curve does not repeat the adsorption curve causing in a wide loop as seen from the isotherm graphs **(Fig. S3.5 a & b)**. The pore volume decreased as the electro-spun deposition time increases from 25 to 60 min. In addition, the BET study indicated that the specific surface area of the e-PVA membranes was 21.8, 27.3, 34.2 and 53.5 m^2/g for electro-spinning durations of 25, 35, 45 and 60, respectively.

The specific surface areas were increased considerably from 21.8 to 53.5m^2/g as the electro-spinning duration was increased from 25 to 60 min. This improvement in surface area was explained due to increasing in the entanglements of the fibers and due to an increasing of the depth/flowing channel within the membrane matrix as the thickness of the membrane increased. In other words, increasing the electro-spinning duration allows the entanglement of more fibers onto the collector which in turn permits to increase the thickness as well as the depth of the membrane pores. So, the key factor to increase the specific surface in this study was explained as the increase in membrane channel due to the deposition of more entangled fibers on to the collector plate. The total pore volume of the membranes has found to be in the range from 0.06 to 0.28 cm^3/g.

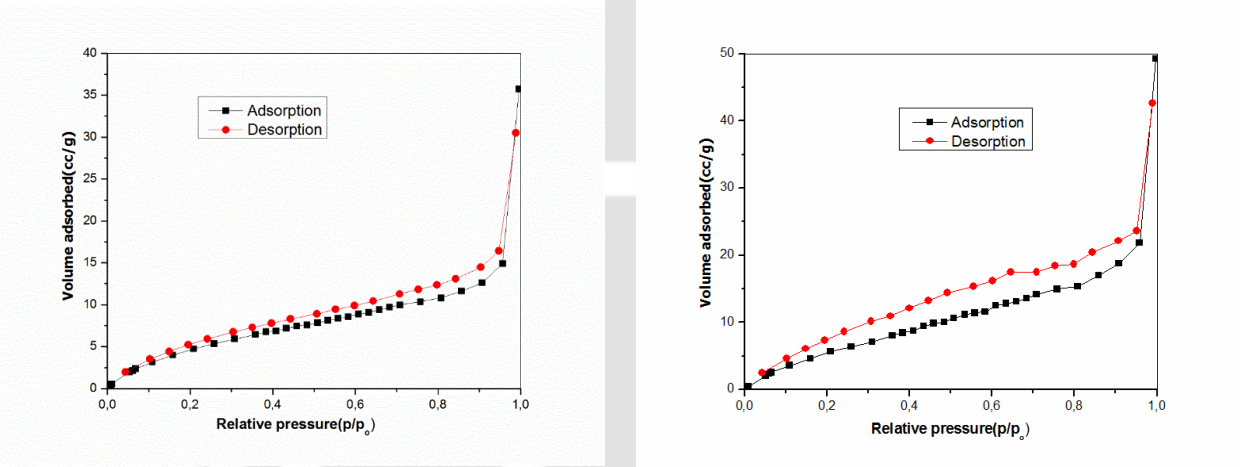

Fig. S3.5. Adsorption desorption isotherm graph of ePVA membranes at **(a)** 45 min and **(b)** 60 min process times.

X-Ray Powder Diffractometer (XRD)

XRD patterns of the ePVA nanofiber membranes deposited at various times are shown in **Fig. S3.6**. No sharp peak is detected for ePVA 25 and ePVA 35 on the XRD pattern. This indicates that these membranes are amorphous. As shown in **Fig. S3.6,** two weak peaks appeared for ePVA 45 and ePVA 60 at around 2θ= 20º, analogous with (101) plane of semi-crystalline of polyvinyl alcohol membranes **(wu et al. (2010))** and this may be due to the entanglement of more fibers as the time of deposition increases.

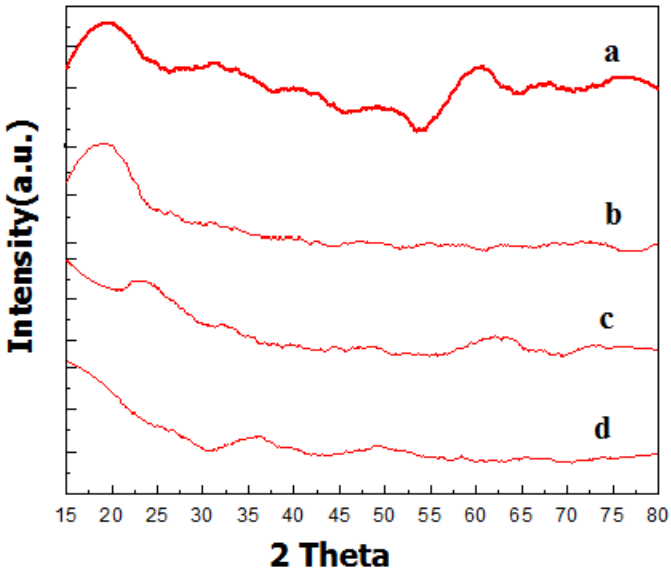

Fig. S3.6. XRD patterns of ePVA fibers using 10% w/v at different deposition times, **(a)** 60 min, **(b)** 45 min, **(c)** 35 min and **(d)** 25 min.

Cross-linking e-PVA nanofibere membranes

The second objective of this work was to evaluate the effect of cross-linking on the properties the membranes. When the electro-spun PVA membrane is immersed in water or used for water treatment applications, it can be dissolved slowly. In other words, the specific nanofibrous structures of e-PVA membranes are not stable in aqueous condition. It is already well-known that polyvinyl alcohol can be cross-linked chemically with a range of aldehydes, like, glutaraldehyde and glyoxal. **[21]** The interaction is because of the development of acetal-bridges among the −OH within PVA and the aldehyde molecules.**[32, 205]** Crosslinking of electro-spun the membrane was done at room temperature. Acetone, which is a water-miscible and a non-solvent for PVA, was mixed with hydrochloric acid (35 w %) and gultaraldehyde aqueous solutions (25 wt. %) in order to prepare the crosslinking solution. The procedure of crosslinking solution preparation is clearly presented in **Fig. S3.2**. No evidence of shrinkages was shown after the e-PVA membrane was dipped into crosslinking solutions.

The tested ePVA membranes were cross-linked using a mixture of acetone and 30 mM glutaraldehyde at 25 °C for 24 hrs. **[206] Fig. S3.3** shows the predicted chemical cross-linking reaction among the polyvinyl alcohol chains and glutaraldehyde catalysed using HCl. **[207]**

The crosslinked ePVA membranes were rinsed numerous times and soaked in water for 48 hours and then dried. As observed from the images **Fig. S3.7 (a-d)**, the surface pore size and the diameters of each fiber were measured by using image J from FESM images. The results indicated that the diameters of fibers were ranging from 69 to 200 nm with the average fiber diameter being 98 nm. The membrane fabricated at 45 min electro-spinning duration was selected for Image J evaluation. The surface pore diameter distribution of the cross-linked membrane is presented in **Fig. S3.4**.

The maximum, minimum and average surface pore sizes are 261.7 nm, 55.5 nm and 125.9 nm respectively. It was clearly observed that no substantial changes both in surface pore sizes and fiber diameters when compared with the non-cross-linked fibers, but uniform arrangement and rigidity of the fibers was observed, which may be due to the strong acetal bridge between the PVA monomers after crosslinking. Moreover, no shrinkages in the membranes were observed after the crosslinking process. These results agreed with the FTIR and TGA results which make us draw the conclusion that the cross linker (GA) has reacted properly and the formation of acetal bridge is confirmed.

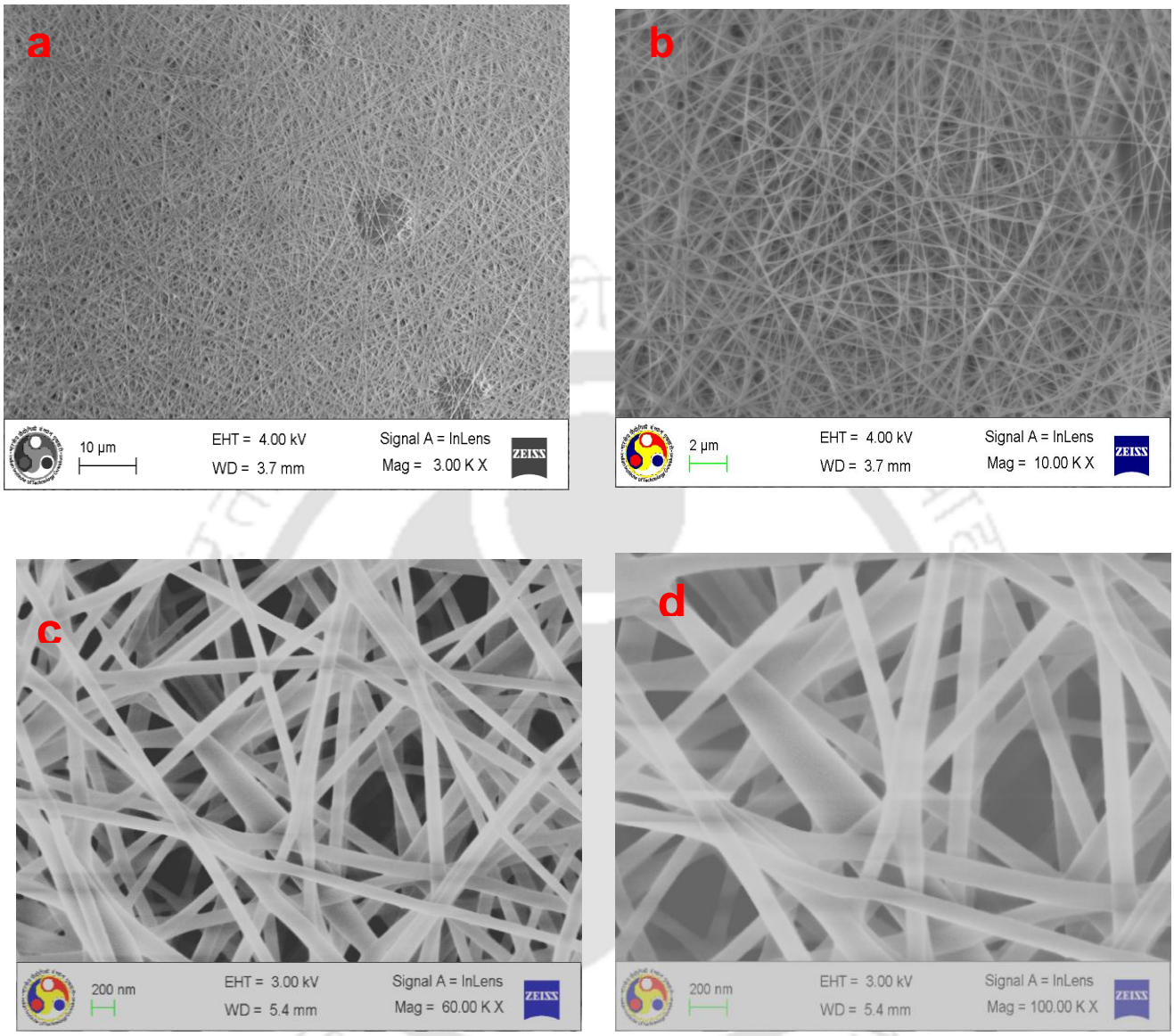

Fig. S3.7. FESEM images of crosslinked ePVA membranes with glutaraldehyde (ePVA/GA); **(a)** 3 KX magnified, **(b)** 10 KX magnified, **(c)** 50 KX magnified and **(d)** 100 KX magnified.

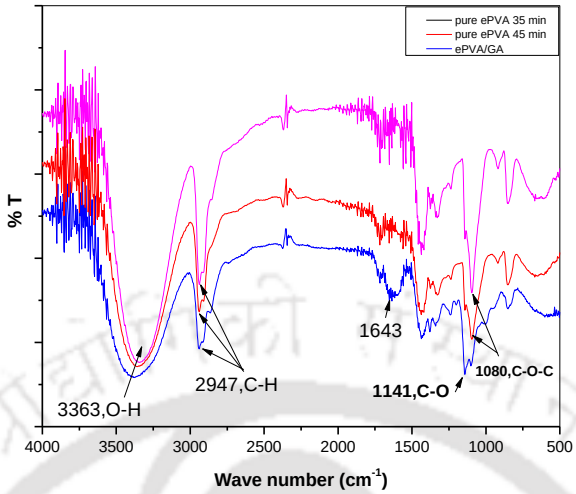

Fig. S3.8. FTIR results of Electro-spun PVA cross-linked with glutaraldehyde (ePVA/GA).

As shown in **Fig. S3.8**, the interaction between PVA and GA catalyzed by hydrochloric acid resulted in a substantial decrease in the intensity of the O–H peak, showing the development of acetal-bridges between the pendant hydroxyl groups of PVA chains. **[207] Table S3.1** shows the typical band assignment of ePVA cross-linked with GA. As shown in **Fig. S2.8, t**he broad bands observed at 3363 cm^{-1} are assigned to −OH stretching because of the presence of the strong bond (hydrogen bonding) of intra-molecular and inter-molecular type. The distinguishing bands at 1095, 1430 and 2947 cm^{-1} were attributed to the C−O stretching, C−H bending and C−H stretching of PVA, respectively. The band observed at 1714 cm^{-1} is may be due to the C=O stretching bands of remaining acetate group, residual after the synthesis of PVA during polyvinyl acetate hydrolysis process. The spectra show that there is no change in the molecular species and their interconnectivity when the process time is varied from 25 to 60 min.

Table S3.1. Characteristic bands of ePVA crosslinked with GA and their assignments

Range of wavelengths (cm^{-1})	Assignment	Wave number, (cm^{-1})	Reference
3000–2850	C–H stretch	2947	----
3500–3200	O–H stretch, H–bonded	3350	----
1670–1640	Carboxylic groups	1643	---
1150-1085	C–O–C	1080	**[32]**
1320–1000	C–O (Crystallinity)	1141	**[207, 208]**

The presence of aldehyde peaks (ν=1643 cm^{-1}) could be because of the partial reaction of glutaraldehyde with the hydroxyl groups within the polyvinyl alcohol throughout the cross-linked network development. One aldehyde group could react with −OH groups within the polymeric chain by means of developing hemi-acetal structures due to its bi-functional cross-linker property, whereas the other one does not interact could be related with some kinetics drawbacks.

Thermogravimetric Analysis (TGA)

The Thermogravimetric Analysis (TGA) and differential Thermogravimetry (DTG) curves for pure ePVA and ePVA/GA membranes are presented in **Fig.S2.9. a** and **b** respectively. The Pure PVA showed two main degradation steps at around 220^{o}C and 440 ^{o}C where the first stage was main degradation step and indicates the decomposition of side PVA chain **[109].** Whereas, the second smaller step related to the splintering of the central chain of the pure ePVA membrane. The TGA curve for the ePVA/ GA membrane also indicated two main degradation stages at around 291 ^{o}C and 480 ^{o}C, and the first stage was main degradation step. It is clearly observed that the degradation temperatures of the ePVA/GA membranes are greater than that of pure ePVA membranes, which further indicates a rise in the thermal stability of the membrane after cross-linking process.

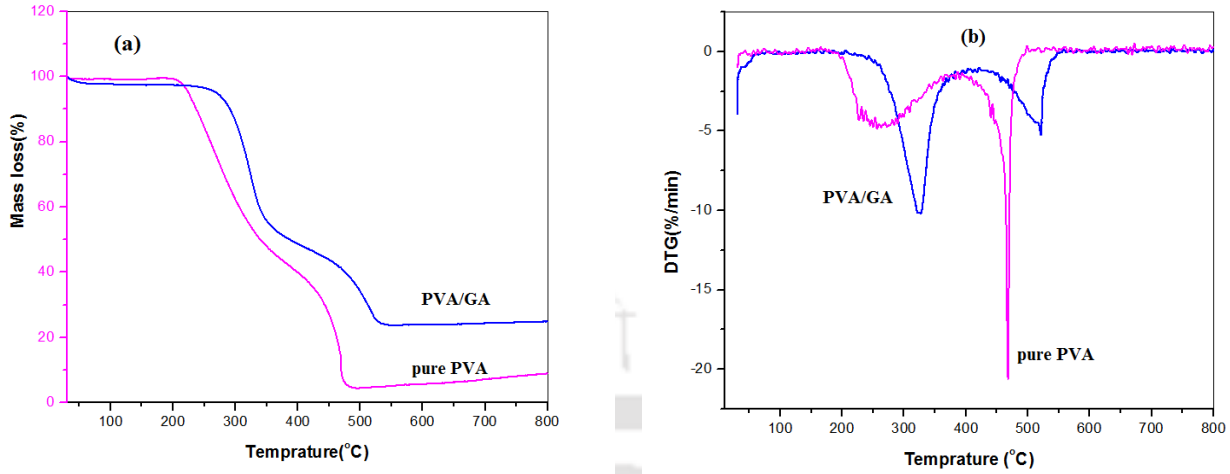

Fig.S3.9. (a) TGA and **(b)** DTG curves of pure ePVA and ePVA/GA membranes.

Table S 4.1

Results for resistances due to membrane (R_m), fouled layer (R_f) and polarization (R_P).

Membrane	**CA0**	**CA1**	**CA2**	**CA3**	**CA4**	**CA5**
$\Delta p/\mu J_{bs}$	3.81	2.82	3.53	6.07	5.28	5.47
R_f	0.24	0.048	0.37	0.53	0.049	0.82
R_m	0.55	0.46	0.40	1.75	0.94	0.81
R_p	3.02	2.31	2.79	3.80	4.29	3.83

** All the units are in ($\times 10^{-10}$ m^{-1})*

References

[1] R.F. Service, Desalination Freshens Up, *Science (2006) 1088–1090*.
[2] W.-L. Huang, E.W. Welch, E.A. Corley, Public sector voluntary initiatives: the adoption of the environmental management system by public waste water treatment facilities in the United States, *J. Environ. Plan. Manag. 57 (2013) 1531-1551*.
[3] M. Aliabadi, M. Irani, J. Ismaeili, H. Piri, M.J. Parnian, Electrospun nanofiber membrane of PEO/Chitosan for the adsorption of nickel, cadmium, lead and copper ions from aqueous solution, *Chem. Eng. J. 220 (2013) 237-243.*
[4] Y.L. Ran Wang, Brandon Li, Benjamin S. Hsiao, Benjamin Chu, Electrospun nanofibrous membranes for high flux microfiltration, *J. Membr. Sci. 392-393 (2012) 167-174.*
[5] M.C. Porter, Handbook of Industrial Membrane Technology, *Noyes Publications, California, 1990.*
[6] B.S. Lalia, V. Kochkodan, R. Hashaikeh, N. Hilal, A review on membrane fabrication: Structure, properties and performance relationship, *Desalination 326 (2013) 77-95.*
[7] K.F. Seeram Ramakrishna, Wee-Eong Teo.Teik-Cheng Lim & Zuwei Ma, An Introduction to Electrospinning and Nanofibers, *1st edi., World Scientific Publishing Co. Pte. Ltd, 2005.*
[8] A. Koski, K. Yim, S. Shivkumar, Effect of molecular weight on fibrous PVA produced by electrospinning, *Mater. Lett. 58 (2004) 493-497*.
[9] M. Mohammad Ali Zadeh, M. Keyanpour-Rad, T. Ebadzadeh, Effect of viscosity of polyvinyl alcohol solution on morphology of the electrospun mullite nanofibres, *Ceram. Int. 40 (2014) 5461-5466.*
[10] S.F. Fennessey, R.J. Farris, Fabrication of aligned and molecularly oriented electrospun polyacrylonitrile nanofibers and the mechanical behavior of their twisted yarns, *Polymer 45 (2004) 4217-4225.*
[11] R.S. Barhate, C.K. Loong, S. Ramakrishna, Preparation and characterization of nanofibrous filtering media, *J. Membr. Sci. 283 (2006) 209-218.*
[12] G. Singh, D. Rana, T. Matsuura, S. Ramakrishna, R.M. Narbaitz, S. Tabe, Removal of disinfection byproducts from water by carbonized electrospun nanofibrous membranes, *Sep. Purif. Technol. 74 (2010) 202-212.*
[13] S.R.W. D. Bhattacharyya, Sylvia Daunert, Responsive Membranes and Materials in, *A John Wiley & Sons, Ltd., Publication, New Delhi, 2013.*
[14] J.J. Dong-an Wang, and Lin-Xian Feng, Surface Analysis of Poly(ether urethane) Blending Stearyl Poly(ethyleneoxide) Coupling Polymer, *Macromolecules 33 (2000) 8472-8478.*
[15] S. Zhang, L. Yan, M. Altman, M. Lassle, H. Nugent, F. Frankel, D.A. Lauenburger, G.M. Whitesides, A. Rich, Biological surface engineering: a simple system for cell pattern formation, *Biomaterials 20 (1999) 1213-1220.*

[16] Y. Zhu, C. Gao, T. He, X. Liu, J. Shen, Layer-by-Layer Assembly To Modify Poly(l -lactic acid) Surface toward Improving Cytocompatibility to Human Endothelial Cells, *Biomacromolecules 4 (2003) 446-452.*

[17] C. Mit-uppatham, M. Nithitanakul, P. Supaphol, Ultrafine Electrospun Polyamide-6 Fibers: Effect of Solution Conditions on Morphology and Average Fiber Diameter, *Macromol. Chem. Phy., 205 (2004) 2327-2338.*

[18] J.D.K. J.M. Deitzel, J.K. Hirvonen, N.C. Beck Tan, Controlled deposition of electrospun poly(ethylene oxide) fibers, *Polymer 42 (2001) 8163-8170.*

[19] R.V.N. Krishnappa, K. Desai, C. Sung, Morphological study of electrospun polycarbonates as a function of the solvent and processing voltage.pdf, *J. Membr. Sci. 38 (2013) 2357 – 2365.*

[20] S.-S. Choi, Y.S. Lee, C.W. Joo, S.G. Lee, J.K. Park, K.-S. Han, Electrospun PVDF nanofiber web as polymer electrolyte or separator, *Electrochim. Acta 50 (2004) 339-343.*

[21] E. Yang, X. Qin, S. Wang, Electrospun crosslinked polyvinyl alcohol membrane, *Mater. Lett. 62 (2008) 3555-3557.*

[22] C. Tsioptsias, K.G. Sakellariou, I. Tsivintzelis, L. Papadopoulou, C. Panayiotou, Preparation and characterization of cellulose acetate–Fe_2O_3 composite nanofibrous materials, *Carbohyd. Polym. 81 (2010) 925-930.*

[23] R.-Y. Tsai, S.-C. Hung, J.-Y. Lai, D.-M. Wang, H.-J. Hsieh, Electrospun chitosan–gelatin–polyvinyl alcohol hybrid nanofibrous mats: Production and characterization, *J. Tai. Inst. Chem. Eng. 45 (2014) 1975-1981.*

[24] N. Kimura, T. Sakumoto, Y. Mori, K. Wei, B.-S. Kim, K.-H. Song, I.-S. Kim, Fabrication and characterization of reinforced electrospun poly(vinylidene fluoride-co-hexafluoropropylene) nanofiber membranes, *Comp. Sci. Technol. 92 (2014) 120-125.*

[25] Y. Sueyoshi, C. Fukushima, M. Yoshikawa, Molecularly imprinted nanofiber membranes from cellulose acetate aimed for chiral separation, *J. Membr. Sci. 357 (2010) 90-97.*

[26] C. Feng, K.C. Khulbe, T. Matsuura, S. Tabe, A.F. Ismail, Preparation and characterization of electro-spun nanofiber membranes and their possible applications in water treatment, *Sep. Purif. Technol. 102 (2013) 118-135.*

[27] X. Qu, P.J.J. Alvarez, Q. Li, Applications of nanotechnology in water and wastewater treatment, *Wat. Res. 47 (2013) 3931-3946.*

[28] R. Gopal, S. Kaur, Z. Ma, C. Chan, S. Ramakrishna, T. Matsuura, Electrospun nanofibrous filtration membrane, *J. Membr. Sci. 281 (2006) 581-586.*

[29] X. Wang, D. Fang, K. Yoon, B.S. Hsiao, B. Chu, High performance ultrafiltration composite membranes based on poly(vinyl alcohol) hydrogel coating on crosslinked nanofibrous poly(vinyl alcohol) scaffold, *J. Membr. Sci. 278 (2006) 261-268.*

[30] K. Yoon, K. Kim, X. Wang, D. Fang, B.S. Hsiao, B. Chu, High flux ultrafiltration membranes based on electrospun nanofibrous PAN scaffolds and chitosan coating, *Polymer 47 (2006) 2434-2441.*

[31] S.J. Kim, Y.S. Nam, D.M. Rhee, H.-S. Park, W.H. Park, Preparation and characterization of antimicrobial polycarbonate nanofibrous membrane, *Eur. Polym. J. 43 (2007) 3146-3152.*

[32] C.-H. Zhang, F.-l. Yang, W.-J. Wang, B. Chen, Preparation and characterization of hydrophilic modification of polypropylene non-woven fabric by dip-coating PVA (polyvinyl alcohol), *Sep. Purif. Technol. 61 (2008) 276-286.*

[33] D. Aussawasathien, C. Teerawattananon, A. Vongachariya, Separation of micron to sub-micron particles from water: Electrospun nylon-6 nanofibrous membranes as pre-filters, *J. Membr. Sci. 315 (2008) 11-19.*

[34] K. Yoon, B.S. Hsiao, B. Chu, High flux ultrafiltration nanofibrous membranes based on polyacrylonitrile electrospun scaffolds and crosslinked polyvinyl alcohol coating, *J. Membr. Sci. 338 (2009) 145-152.*

[35] G.-R. Xu, J.-N. Wang, C.-J. Li, Preparation of hierarchically nanofibrous membrane and its high adaptability in hexavalent chromium removal from water, *Chem. Eng. J. 198-199 (2012) 310-317.*

[36] A. Mahapatra, B.G. Mishra, G. Hota, Electrospun Fe2O3–Al2O3 nanocomposite fibers as efficient adsorbent for removal of heavy metal ions from aqueous solution, *J. Hazard. Mater. 258-259 (2013) 116-123.*

[37] M. Li, X. Xue, D. Wang, Y. Lu, Z. Wu, H. Zou, High performance filtration nanofibrous membranes based on hydrophilic poly(vinyl alcohol-co-ethylene) copolymer, *Desalination 329 (2013) 50-56.*

[38] H. You, X. Li, Y. Yang, B. Wang, Z. Li, X. Wang, M. Zhu, B.S. Hsiao, High flux low pressure thin film nanocomposite ultrafiltration membranes based on nanofibrous substrates, *Sep. Purif. Technol. 108 (2013) 143-151.*

[39] Y. Liu, R. Wang, H. Ma, B.S. Hsiao, B. Chu, High-flux microfiltration filters based on electrospun polyvinylalcohol nanofibrous membranes, *Polymer 54 (2013) 548-556.*

[40] M. Mulder, Basic Principles of Membrane Technology, *Second ed., Kluwer Academic Publishers, London, 1996.*

[41] T.-H. Young, L.-W. Chen, Pore formation mechanism of membranes from phase inversion process, *Desalination 103 (1995) 233-247.*

[42] T. Mohammadi, E. Saljoughi, Effect of production conditions on morphology and permeability of asymmetric cellulose acetate membranes, Desalination 243 (2009) 1-7.

[43] H. Strathmann, K. Kock, The Formation Mechanism of Phase Inversion Membranes, *Desalination 21 (1977) 241-255.*

[44] B. Chakrabarty, A.K. Ghoshal, M.K. Purkait, Preparation, characterization and performance studies of polysulfone membranes using PVP as an additive, *J. Membr. Sci. 315 (2008) 36-47.*

[45] Z. Zhu, J. Xiao, W. He, T. Wang, Z. Wei, Y. Dong, A phase-inversion casting process for preparation of tubular porous alumina ceramic membranes, *J. Eur. Ceram. Soc. 35 (2015) 3187-3194.*

[46] M. Algarra, M.I. Vázquez, B. Alonso, C.M. Casado, J. Casado, J. Benavente, Characterization of an engineered cellulose based membrane by thiol dendrimer for heavy metals removal, *Chemi. Eng. J. 253 (2014) 472-477.*

[47] R. Konwarh, N. Karak, M. Misra, Electrospun cellulose acetate nanofibers: The present status and gamut of biotechnological applications, *Biotechnol. Adv. 31 (2013) 421-437.*

[48] R. Abedini, S. M. Mousavi, R. Aminzadeh, A novel cellulose acetate (CA) membrane using TiO_2 nanoparticles: Preparation, characterization and permeation study, *Desalination 277 (2011) 40-45.*

[49] K.A. Gebru, C. Das, Cellulose acetate−modified−Titanium dioxide (TiO_2) nanoparticles electro-spun composite membranes: Fabrication and characterization", *J. Inst. Eng. Article in press, (2017)*

[50] E. Saljoughi, T. Mohammadi, Cellulose acetate (CA)/polyvinylpyrrolidone (PVP) blend asymmetric membranes: Preparation, morphology and performance, *Desalination 249 (2009) 850-854.*

[51] B. Chakrabarty, A.K. Ghoshal, M.K. Purkait, Effect of molecular weight of PEG on membrane morphology and transport properties, *J. Membr. Sci. 309 (2008) 209-221.*

[52] J.-H. Kim, K.-H. Lee, Effect of PEG additive on membrane formation by phase inversion, *J. Membr. Sci. 138 (1998) 153-163.*

[53] E. Saljoughi, M. Amirilargani, T. Mohammadi, Effect of PEG additive and coagulation bath temperature on the morphology, permeability and thermal/chemical stability of asymmetric CA membranes, *Desalination 262 (2010) 72-78.*

[54] S. Wongchitphimon, R. Wang, R. Jiraratananon, L. Shi, C.H. Loh, Effect of polyethylene glycol (PEG) as an additive on the fabrication of polyvinylidene fluoride-co-hexafluropropylene (PVDF-HFP) asymmetric microporous hollow fiber membranes, *J. Membr. Sci. 369 (2011) 329-338.*

[55] M. Yang, S. Xie, Q. Li, Y. Wang, X. Chang, L. Shan, L. Sun, X. Huang, C. Gao, Effects of polyvinylpyrrolidone both as a binder and pore-former on the release of sparingly water-soluble topiramate from ethylcellulose coated pellets, *Int. J. Pharm. 465 (2014) 187-196.*

[56] S.H. Yoo, J.H. Kim, J.Y. Jho, J. Won, Y.S. Kang, Influence of the addition of PVP on the morphology of asymmetric polyimide phase inversion membranes: effect of PVP molecular weight, *J. Membr. Sci. 236 (2004) 203-207.*

[57] S. Zhao, Z. Wang, X. Wei, X. Tian, J. Wang, S. Yang, S. Wang, Comparison study of the effect of PVP and PANI nanofibers additives on membrane formation mechanism, structure and performance, *J. Membr. Sci. 385-386 (2011) 110-122.*

[58] F. Shi, Y. Ma, J. Ma, P. Wang, W. Sun, Preparation and characterization of PVDF/TiO_2 hybrid membranes with different dosage of nano-TiO_2, *J. Membr. Sci. 389 (2012) 522-531.*

[59] S.H. Kim, S.-Y. Kwak, B.-H. Sohn, T.H. Park, Design of TiO_2 nanoparticle self-assembled aromatic polyamide thin-film-composite (TFC) membrane as an approach to solve biofouling problem, *J. Membr. Sci. 211 (2003) 157-165.*

[60] X. Cao, J. Ma, X. Shi, Z. Ren, Effect of TiO_2 nanoparticle size on the performance of PVDF membrane, *App. Surf. Sci. 253 (2006) 2003-2010.*

[61] N. Maximous, G. Nakhla, W. Wan, K. Wong, Preparation, characterization and performance of Al_2O_3/PES membrane for wastewater filtration, *J. Membr. Sci. 341 (2009) 67-75.*

[62] L. Yan, Y. Li, C. Xiang, S. Xianda, Effect of nano-sized Al2O3-particle addition on PVDF ultrafiltration membrane performance, *J. Membr. Sci. 276 (2006) 162-167.*

[63] A. Bottino, G. Capannelli, A. Comite, Preparation and characterization of novel porous PVDF-ZrO_2 composite membranes, *Desalination 146 (2002) 35-40.*

[64] N. Saffaj, S.A. Younssi, A. Albizane, A. Messouadi, M. Bouhria, M. Persin, M. Cretin, A. Larbot, Preparation and characterization of ultrafiltration membranes for toxic removal from wastewater, *Desalination 168 (2004) 259-263.*

[65] Z. Ma, M. Kotaki, T. Yong, W. He, S. Ramakrishna, Surface engineering of electrospun polyethylene terephthalate (PET) nanofibers towards development of a new material for blood vessel engineering, *Biomaterials 26 (2005) 2527-2536.*

[66] K. Saeed, S. Haider, T.-J. Oh, S.-Y. Park, Preparation of amidoxime-modified polyacrylonitrile (PAN-oxime) nanofibers and their applications to metal ions adsorption, *J. Membr. Sci. 322 (2008) 400-405.*

[67] H. Zhang, H. Nie, D. Yu, C. Wu, Y. Zhang, C.J.B. White, L. Zhu, Surface modification of electrospun polyacrylonitrile nanofiber towards developing an affinity membrane for bromelain adsorption, *Desalination 256 (2010) 141-147.*

[68] Q. Shi, Y. Su, X. Ning, W. Chen, J. Peng, Z. Jiang, Graft polymerization of methacrylic acid onto polyethersulfone for potential pH-responsive membrane materials, *J. Membr. Sci. 347 (2010) 62-68.*

[69] M. Teng, F. Li, B. Zhang, A.A. Taha, Electrospun cyclodextrin-functionalized mesoporous polyvinyl alcohol/SiO_2 nanofiber membranes as a highly efficient adsorbent for indigo carmine dye, *Coll. Surf. A: Phy.chem. Eng. Asp. 385 (2011) 229-234.*

[70] A.A. Taha, Y.-n. Wu, H. Wang, F. Li, Preparation and application of functionalized cellulose acetate/silica composite nanofibrous membrane via electrospinning for Cr(VI) ion removal from aqueous solution, *J. Environ. Manag. 112 (2012) 10-16.*

[71] S. Abbasizadeh, A.R. Keshtkar, M.A. Mousavian, Preparation of a novel electrospun polyvinyl alcohol/titanium oxide nanofiber adsorbent modified with mercapto groups for uranium(VI) and thorium(IV) removal from aqueous solution, *Chem.Eng. J. 220 (2013) 161-171.*

[72] X. Yu, S. Tong, M. Ge, L. Wu, J. Zuo, C. Cao, W. Song, Synthesis and characterization of multi-amino-functionalized cellulose for arsenic adsorption, *Carbohyd. Polym. 92 (2013) 380-387.*

[73] G. Arthanareeswaran, P. Thanikaivelan, K. Srinivasn, D. Mohan, M. Rajendran, Synthesis, characterization and thermal studies on cellulose acetate membranes with additive, *Eur. Polym. J. 40 (2004) 2153-2159.*

[74] D. Shen, Y. Huang, The synthesis of CDA-g-PMMA copolymers through atom transfer radical polymerization, *Polymer 45 (2004) 7091-7097.*

[75] A. Bhattacharya, Grafting: a versatile means to modify polymersTechniques, factors and applications, *Prog. Polym. Sci. 29 (2004) 767-814.*

[76] M. Khayet, M.N.A. Seman, N. Hilal, Response surface modeling and optimization of composite nanofiltration modified membranes, *J. Membr. Sci. 349 (2010) 113-122.*

[77] M.-m. Kim, N.H. Lin, G.T. Lewis, Y. Cohen, Surface nano-structuring of reverse osmosis membranes via atmospheric pressure plasma-induced graft polymerization for reduction of mineral scaling propensity, *J. Membr. Sci. 354 (2010) 142-149.*

[78] A. Linggawati, A.W. Mohammad, Z. Ghazali, Effect of electron beam irradiation on morphology and sieving characteristics of nylon-66 membranes, *Eur.Polym. J. 45 (2009) 2797-2804.*

[79] A. Linggawati, A.W. Mohammad, C.P. Leo, Effects of APTEOS content and electron beam irradiation on physical and separation properties of hybrid nylon-66 membranes, *Mater. Chem. Phy. 133 (2012) 110-117.*

[80] P. Mukherjee, K. Jones, J. Abitoye, Surface modification of nanofiltration membranes by ion implantation, *J. Membr. Sci. 254 (2005) 303-310.*

[81] P. Wanichapichart, W. Bootluck, P. Thopan, L.D. Yu, Influence of nitrogen ion implantation on filtration of fluoride and cadmium using polysulfone/chitosan blend membranes, *Nuc.Inst. Meth. Phy. Res. 326 (2014) 195-199.*

[82] M. Sacak, F. Oflaz, Benzoyl-Peroxide-Initiated Graft Copolymerization of Poly (ethylene terephthalate) Fibers with Acrylic Acid, *J. App. Polym. Sci. 50 (1993) 1909-1916.*

[83] M. Sacak, E. Pulat, Benzoyl-Peroxide-Initiated Graft Copolymerization of Poly(ethyleneTerephthalate) Fibers with Acrylamide, *J. App. Polym. Sci. 38 (1989) 539-546.*

[84] M. Pulat, D. Babayigit, Graft Copolymerization of PU Membranes with Acrylic Acid and Crotonic Acid Using Benzoyl Peroxide Initiator, *J. App. Polym. Sci. 80 (2001) 2690-2695.*

[85] M. Sacak, F. Sertkaya, M. Talu, Grafting of Poly (ethylene Terephthalate) Fibers with Methacrylic Acid Using Benzoyl Peroxide, *J. App. Polym. Sci. 44 (1992) 1737-1742.*

[86] M. Pulat, C. Isakoca, Chemically induced graft copolymerization of vinyl monomers onto cotton fibers, *J. App. Polym. Sci. 100 (2006) 2343-2347.*

[87] O. Sanli, H.I. Ünal, Graft Copolymerization of 2-Hydroxy Ethyl Methacrylate on Dimethyl Sulfoxide Pretreated Poly(Ethylene Terephthalate) Films Using Benzoyl Peroxide, *J. Macrom. Sci. Part A 39 (2002) 447-465.*

[88] A.Y. Kulkarni, P.C. Mehta, Ceric Ion Induced Redox Polymerization of Acrylonitrile in Presence of Cellulose, *Ahmed. Tex. Ind. Res. Ass. (1965) 2633.*

[89] A.Y. Kulkarni, P.C. Metha, Ceric Ion-Induced Redox Polymerization of Acrylonitrile on Cellulose, *J. App. Polym. Sci. 12 (1968) 1321-1342.*

[90] A. Hebeish, P.C. Mehta, Cerium-Initiated Grafting of Acrylonitrile onto Cellulosic Materials, *J. App. Polym. Sci. 12 (1968) 1625-1647.*

[91] J.M. Joshi, V.K. Sinha, Ceric ammonium nitrate induced grafting of polyacrylamide onto carboxymethyl chitosan, *Carbohyd. Polym, 67 (2007) 427-435.*

[92] S. Tungprapa, T. Puangparn, M. Weerasombut, I. Jangchud, P. Fakum, S. Semongkhol, C. Meechaisue, P. Supaphol, Electrospun cellulose acetate fibers: effect of solvent system on morphology and fiber diameter, *Cellulose 14 (2007) 563-575.*

[93] D. Baş, İ.H. Boyacı, Modeling and optimization I: Usability of response surface methodology, *J.Food Eng. 78 (2007) 836-845.*

[94] O.S. Yördem, M. Papila, Y.Z. Menceloğlu, Effects of electrospinning parameters on polyacrylonitrile nanofiber diameter: An investigation by response surface methodology, *Mater. Des. 29 (2008) 34-44.*

[95] M.A. Bezerra, R.E. Santelli, E.P. Oliveira, L.S. Villar, L.A. Escaleira, Response surface methodology (RSM) as a tool for optimization in analytical chemistry, *Talanta 76 (2008) 965-977.*

[96] S.L.C. Ferreira, R.E. Bruns, E.G.P. da Silva, W.N.L. dos Santos, C.M. Quintella, J.M. David, J.B. de Andrade, M.C. Breitkreitz, I.C.S.F. Jardim, B.B. Neto, Statistical designs and response surface techniques for the optimization of chromatographic systems, *J. Chromatog.: A 1158 (2007) 2-14.*

[97] H.M. Khanlou, B.C. Ang, S. Talebian, M.M. Barzani, M. Silakhori, H. Fauzi, Multi-response analysis in the processing of poly (methyl methacrylate) nano-fibres membrane by electrospinning based on response surface methodology: Fibre diameter and bead formation, *Measurement 65 (2015) 193-206.*

[98] M. Ahmadipourroudposht, E. Fallahiarezoudar, N.M. Yusof, A. Idris, Application of response surface methodology in optimization of electrospinning process to fabricate (ferrofluid/polyvinyl alcohol) magnetic nanofibers, *Mater. Sci. Eng.: C 50 (2015) 234-241.*

[99] H. Liu, Y.-L. Hsieh, Ultrafine fibrous cellulose membranes from electrospinning of cellulose acetate, *J. Polym. Sci. Part B: Polym. Phy. 40 (2002) 2119-2129.*

[100] C.S. Ong, W.J. Lau, P.S. Goh, B.C. Ng, A.F. Ismail, Preparation and characterization of PVDF–PVP–TiO_2 composite hollow fiber membranes for oily wastewater treatment using submerged membrane system, *Desal. Wat. Treat. (2013) 1-11.*

[101] X. Yu, S. Tong, M. Ge, L. Wu, J. Zuo, C. Cao, W. Song, Synthesis and characterization of multi-amino-functionalized cellulose for arsenic adsorption, *Carbohyd. Polym. 92 (2013) 380-387.*

[102] K.A. Gebru, C. Das, Effects of solubility parameter differences among PEG, PVP and CA on the preparation of ultrafiltration membranes: Impacts of solvents and additives on morphology, permeability and fouling performances, *Ch. J. Chem. Eng. 10.1016/j.cjche.2016.11.017 (2017).*

[103] K.A. Gebru, C. Das, Preparation and characterization of CA−PEG−TiO_2 membranes Effect of PEG and TiO_2 on morphology, flux and fouling performance, *J. membr. Sci. Res. (2016)*

[104] J. Garcia-Ivars, M.-I. Alcaina-Miranda, M.-I. Iborra-Clar, J.-A. Mendoza-Roca, L. Pastor-Alcañiz, Enhancement in hydrophilicity of different polymer phase-inversion ultrafiltration membranes by introducing PEG/Al_2O_3 nanoparticles, *Sep. Purif. Technol. 128 (2014) 45-57.*

[105] E. Yuliwati, A.F. Ismail, T. Matsuura, M.A. Kassim, M.S. Abdullah, Effect of modified PVDF hollow fiber submerged ultrafiltration membrane for refinery wastewater treatment, *Desalination 283 (2011) 214-220.*

[106] Y.-F. Zhao, L.-P. Zhu, Z. Yi, B.-K. Zhu, Y.-Y. Xu, Improving the hydrophilicity and fouling-resistance of polysulfone ultrafiltration membranes via surface zwitterionicalization mediated by polysulfone-based triblock copolymer additive, *J. Membr. Sci. 440 (2013) 40-47.*

[107] Y.-q. Wang, T. Wang, Y.-l. Su, F.-b. Peng, H. Wu, Z.-y. Jiang, Remarkable Reduction of Irreversible Fouling and Improvement of the Permeation Properties of Poly(ether sulfone) Ultrafiltration Membranes by Blending with Pluronic F127, *Langmuir 21 (2005) 11856-11862.*

[108] G. Wu, S. Gan, L. Cui, Y. Xu, Preparation and characterization of PES/TiO2 composite membranes, *App. Surf. Sci. 254 (2008) 7080-7086.*

[109] C. Santos, C.J. Silva, Z. Büttel, R. Guimarães, S.B. Pereira, P. Tamagnini, A. Zille, Preparation and characterization of polysaccharides/PVA blend nanofibrous membranes by electrospinning method, *Carbohyd. Polym. 99 (2014) 584-592.*

[110] S. Bose, C. Das, Role of Binder and Preparation Pressure in Tubular Ceramic Membrane Processing: Design and Optimization Study Using Response Surface Methodology (RSM), *Ind. Eng. Chem. Res. 53 (2014) 12319-12329.*

[111] Z. Ma, M. Kotaki, S. Ramakrishna, Electrospun cellulose nanofiber as affinity membrane, *J. Membr. Sci. 265 (2005) 115-123.*

[112] R. Nigmatullin, R. Lovitt, C. Wright, M. Linder, T. Nakari-Setälä, M. Gama, Atomic force microscopy study of cellulose surface interaction controlled by cellulose binding domains, *Colloid. Surf. B: Biointerf. 35 (2004) 125-135.*

[113] D.L. Liao, G.S. Wu, B.Q. Liao, Zeta potential of shape-controlled TiO_2 nanoparticles with surfactants, *Coll. Surf. A: Phy.chem. Eng. Asp. 348 (2009) 270-275.*

[114] Hem Raj Pant, Madhab Prasad Bajgai, Ki Taek Nam, Yun A. Seo, Dipendra Raj Pandeya, Seong Tshool Hong, H.Y. Kim, Electrospun nylon-6 spider-net like nanofiber mat containing TiO_2 nanoparticles, *J. Hazard. Mater. 185 (2011) 124–130.*

[115] T.-H. Bae, I.-C. Kim, T.-M. Tak, Preparation and characterization of fouling-resistant TiO2 self-assembled nanocomposite membranes, *J. Membr. Sci. 275 (2006) 1-5.*

[116] S.H. Kim, S.-Y. Kwak, B.-H. Sohn, T.H. Park, Design of TiO_2 nanoparticle self-assembled aromatic polyamide thin-film-composite (TFC) membrane as an approach to solve biofouling problem, *J. Membr. Sci. 211 (2003) 157–165.*

[117] S.-D. Wang, Q. Ma, H. Liu, K. Wang, L.-Z. Ling, K.-Q. Zhang, Robust electrospinning cellulose acetate@TiO_2 ultrafine fibers for dyeing water treatment by photocatalytic reactions, *RSC Adv. 5 (2015) 40521-40530.*

[118] Y. Yang, H. Zhang, P. Wang, Q. Zheng, J. Li, The influence of nano-sized TiO_2 fillers on the morphologies and properties of PSF UF membrane, *J. Membr. Sci. 288 (2007) 231-238.*

[119] H. Song, J. Shao, Y. He, B. Liu, X. Zhong, Natural organic matter removal and flux decline with PEG–TiO_2-doped PVDF membranes by integration of ultrafiltration with photocatalysis, *J. Membr. Sci. 405-406 (2012) 48-56.*

[120] X. Jin, J. Xu, X. Wang, Z. Xie, Z. Liu, B. Liang, D. Chen, G. Shen, Flexible TiO_2/cellulose acetate hybrid film as a recyclable photocatalyst, *RSC Adv., 4 (2014) 12640.*

[121] S. Bagheri, K. Shameli, S.B. Abd Hamid, Synthesis and Characterization of Anatase Titanium Dioxide Nanoparticles Using Egg White Solution via Sol-Gel Method, *J. Chem., (2013) 1-5.*

[122] A. Dabrowski, Adsorption from theory to practice, *Adv. Coll. Interf. Sci. 93 (2001) 135-224.*

[123] H.-T. Kim, C.-H. Lee, Y.-G. Shul, J.-K. Moon, E.-H. Lee, Evaluation of PAN–TiO_2 Composite Adsorbent for Removal of Pb(II) Ion in Aqueous Solution, *Sep. Sci. Technol. 38 (2003) 695-713.*

[124] D. Kovacevic, A. Pohlmeier, H.-D.N. G. Ozbas, M.J.N. Kallay, The adsorption of lead species on goethite, *Coll. Surf. A: Phy.chem. Eng. Asp. 166 (2000) 225-233.*

[125] A. Garcia Sanchez, E. Alvarez Ayuso, O. Jimenez De Blas, Sorption of heavy metals from industrial waste water by low-cost mineral silicates, *Clay Miner. 34 (1999) 469-477.*

[126] N.A. Abdelwahab, N.S. Ammar, H.S. Ibrahim, Graft copolymerization of cellulose acetate for removal and recovery of lead ions from wastewater, *Int. J. Bio. Macromol. 79 (2015) 913-922.*

[127] Y. Tian, M. Wu, R. Liu, Y. Li, D. Wang, J. Tan, R. Wu, Y. Huang, Electrospun membrane of cellulose acetate for heavy metal ion adsorption in water treatment, *Carbohyd. Polym. 83 (2011) 743-748.*

[128] F. Ji, C. Li, B. Tang, J. Xu, G. Lu, P. Liu, Preparation of cellulose acetate/zeolite composite fiber and its adsorption behavior for heavy metal ions in aqueous solution, *Chem. Eng. J. 209 (2012) 325-333.*

[129] D. Zhou, L. Zhang, J. Zhou, S. Guo, Cellulose/chitin beads for adsorption of heavy metals in aqueous solution, *Wat. Res. 38 (2004) 2643-2650.*

[130] Metcalf & Eddy, George Tchobanoglous, Franklin L. Burton, H.D. Stensel, Wastewater Engineering - Treatment and Reuse, *1st ed, McGraw Hill Education inc., Newyork, 2004.*

[131] A. Günay, E. Arslankaya, İ. Tosun, Lead removal from aqueous solution by natural and pretreated clinoptilolite: Adsorption equilibrium and kinetics, *J. Hazard. Mater. 146 (2007) 362-371.*

[132] T.Z. BULUT Yasemin, Removal of heavy metals from aqueous solution by sawdust adsorption, *J. Environ. Sci. 19 (2007) 160–166.*

[133] S. Shahmohammadi-Kalalagh, H. Babazadeh, A.H. Nazemi, M. Manshouri, Isotherm and Kinetic Studies on Adsorption of Pb, Zn and Cu by Kaolinite, *Caspian J. Env. Sci. 9 (2011) 243-255.*

[134] I.H. Lee, Y.-C. Kuan, J.-M. Chern, Equilibrium and kinetics of heavy metal ion exchange, *J. Ch. Inst.Chem. Eng. 38 (2007) 71-84.*

[135] Ming-Shen Chiou, H.-Y. Li, Equilibrium and kinetic modeling of adsorption of reactive dye on cross-linked chitosan beads, *J. Hazard. Mater. 93 (2002) 233–248.*

[136] Naparat Jiwalak, Saowanee Rattanaphani, John B. Bremner, V. Rattanaphani, Equilibrium and Kinetic Modeling of the Adsorption of Indigo Carmine onto Silk, *Fib. Polym. 11 (2010) 572-579.*

[137] F.G. Paulsen, S.S. Shojaie, W.B. Krantz, Effect of evaporation step on macrovoid formation in wet-cast polymeric membranes, *J. Membr. Sci. 91 (1994) 265-282.*

[138] P.S.T. Machado, A.C. Habert, C.P. Borges, Membrane formation mechanism based on precipitation kinetics and membrane morphology: flatat and hollow fiber polysulfone membranes, *J. Membr. Sci. 155 (1999) 171-183.*

[139] R.M. Boom, I.M. Wlenk, T.v.d. Boomgaard, C.A. Smolders, Microstructures in phase inversion membranes. Part 2. The role of a polymeric additive, *J. Membr. Sci. 73 (1992) 277-292.*

[140] J.-J. Qin, Y. Li, L.-S. Lee, H. Lee, Cellulose acetate hollow fiber ultrafiltration membranes made from CA/PVP 360 K/NMP/water, *J. Membr. Sci. 218 (2003) 173-183.*

[141] C.A. Smolders, A.J. Reuvers, R.M. Boom, I.M. Wienk, Microstructures in phase-inversion membranes. Part 1. Formation of macrovoids, *J. Membr. Sci. 73 (1992) 259-275.*

[142] B. Reuvers, Membrane formation: Diffusion induced demixing processes in ternary polymeric systems, *University of Twente, Amersfoort, 1956.*

[143] J. Marchese, M. Ponce, N.A. Ochoa, P. Prádanos, L. Palacio, A. Hernández, Fouling behaviour of polyethersulfone UF membranes made with different PVP, *J. Membr. Sci. 211 (2003) 1-11.*

[144] D.B. Mosqueda-Jimenez, R.M. Narbaitz, T. Matsuura, G. Chowdhury, G. Pleizier, J.P. Santerre, Influence of processing conditions on the properties of ultrafiltration membranes, *J. Membr. Sci. 231 (2004) 209-224.*

[145] A.G. Fane, C.J.D. Fell, A.G. Waters, The relationship between membrane surface pore characteristics and flux for ultrafiltration membranes, *J. Membr. Sci. 9 (1981) 245-262.*

[146] C.J.D. Fell, K.J. Kim, V. Chen, D.E. Wiley, A.G. Fane, Factors Determining Flux and Rejection of Ultrafiltration Membranes, *Chem. Eng. Process 27 (1990) 165-173.*

[147] A. Idris, L.K. Yet, The effect of different molecular weight PEG additives on cellulose acetate asymmetric dialysis membrane performance, *J. Membr. Sci. 280 (2006) 920-927.*

[148] W.-L. Chou, D.-G. Yu, M.-C. Yang, C.-H. Jou, Effect of molecular weight and concentration of PEG additives on morphology and permeation performance of cellulose acetate hollow fibers, *Sep. Purif.Technol. 57 (2007) 209-219.*

[149] H. Matsuyama, A. Yamamoto, H. Yano, T. Makia, M. Teramoto, K. Mishima, K. Matsuyama, Effect of organic solvents on membrane formation by phase separation with supercritical CO_2, *J. Membr. Sci. 204 (2002) 81-87.*

[150] R. Guana, H. Dai, C. Li, J. Liu, J. Xu, Effect of casting solvent on the morphology and performance of sulfonated polyethersulfone membranes, *J. Membr. Sci. 277 (2006) 148-156.*

[151] D. Lu, H. Zou, R. Guan, H. Dai, L. Lu, Sulfonation of Polyethersulfone by Chlorosulfonic Acid, *Polym. Bull. 54 (2005) 21-28.*

[152] B. Kruczek, Development and characterization of dense membranes for gas separation made from high molecular weight sulfonated poly (phenylene oxide): Effect of casting conditions on the morphology and performance of the membranes, *Ottawa University, Ottawa, 1998.*

[153] C.M. Hansen, The three dimensional solubility parameter and solvent diffusion coefficient: Their importance In surface coating formulation, *Danish Technical Press, Copenhagen, 1967.*

[154] G.C. Vebber, P. Pranke, C.N. Pereira, Calculating Hansen Solubility Parameters of Polymers with Genetic Algorithms, *J. Appl. Polym. Sci. (2013) 1-12.*

[155] R. Nair, N. Nyamweya, S. Gonen, L.J. Martınez-Miranda, S.W. Hoag, Influence of various drugs on the glass transition temperature of poly(vinylpyrrolidone): a thermodynamic and spectroscopic investigation, *Int. J. Pharm. 225 (2001) 83-96.*

[156] C. Özdemir, A. Güner, Solubility profiles of poly(ethylene glycol)/solvent systems, I: Qualitative comparison of solubility parameter approaches, *Eur. Polym. J. 43 (2007) 3068-3093.*

[157] R.W. Kopitzke, C.A. Linkous, H.R. Anderson, G.L. Nelson, Conductivity and water uptake of aromatic-based proton exchange membrane electrolytes, *J. Electrochem. Soc. 147 (2000) 1677-1681.*

[158] H. Shi, Y. He, Y. Pan, H. Di, G. Zeng, L. Zhang, C. Zhang, A modified mussel-inspired method to fabricate TiO2 decorated superhydrophilic PVDF membrane for oil/water separation, *J. Membr. Sci. 506 (2016) 60-70.*

[159] B.K. Dutta, Principles of mass transfer and separation process, *PHI Learning Private Limited, New Delhi, 2009.*

[160] J.-H. Jiang, L.-P. Zhu, X.-L. Li, Y.-Y. Xu, B.-K. Zhu, Surface modification of PE porous membranes based on the strong adhesion of polydopamine and covalent immobilization of heparin, *J. Membr. Sci. 364 (2010) 194-202.*

[161] S. Robinson, P.A. Williams, Inhibition of Protein Adsorption onto Silica by Polyvinylpyrrolidone, *Langmuir 18 (2002) 8743-8748.*

[162] J. Wu, Z. Wang, W. Lin, S. Chen, Investigation of the interaction between poly(ethylene glycol) and protein molecules using low field nuclear magnetic resonance, *Acta Biomater. 9 (2013) 6414-6420.*

[163] Z. Yang, J.A. Galloway, H. Yu, Protein Interactions with Poly(ethylene glycol) Self-Assembled Monolayers on Glass Substrates: Diffusion and Adsorption, *Langmuir 15 (1999) 8405-8411.*

[164] J. Garcia-Ivars, M.-I. Alcaina-Miranda, M.-I. Iborra-Clar, J.-A. Mendoza-Roca, L. Pastor-Alcañiz, Enhancement in hydrophilicity of different polymer phase-inversion ultrafiltration membranes by introducing PEG/Al_2O_3 nanoparticles, *Sep. Purif. Technol. 128 (2014) 45-57.*

[165] N. Maximous, G. Nakhla, W. Wan, K. Wong, Performance of a novel ZrO_2/PES membrane for wastewater filtration, *J. Membr. Sci. 352 (2010) 222-230.*

[166] Q. Shi, Y. Su, W. Zhao, C. Li, Y. Hu, Z. Jiang, S. Zhu, Zwitterionic polyethersulfone ultrafiltration membrane with superior antifouling property, *J. Membr. Sci. 319 (2008) 271-278.*

[167] Y.P. Tang, J.X. Chan, T.S. Chung, M. Weber, C. Staudt, C. Maletzko, Simultaneously covalent and ionic bridging towards antifouling of GO-imbedded nanocomposite hollow fiber membranes, *J. Mater. Chem. A 3(2015) 10573–10584.*

[168] Y. Feng, G. Han, L. Zhang, S.-B. Chen, T.-S. Chung, M. Weber, C. Staudt, C. Maletzko, Rheology and phase inversion behavior of polyphenylenesulfone (PPSU) and sulfonated PPSU for membrane formation, *Polymer 99 (2016) 72-82.*

[169] Y. Liu, G.H. Koops, H. Strathmann, Characterization of morphology controlled polyethersulfone hollow fiber membranes by the addition of polyethylene glycol to the dope and bore liquid solution, *J. Membr. Sci. 223 (2003) 187-199.*

[170] E. Yuliwati, A.F. Ismail, Effect of additives concentration on the surface properties and performance of PVDF ultrafiltration membranes for refinery produced wastewater treatment, *Desalination 273 (2011) 226-234.*

[171] J. Garcia-Ivars, M.-I. Iborra-Clar, M.-I. Alcaina-Miranda, B. Van der Bruggen, Comparison between hydrophilic and hydrophobic metal nanoparticles on the phase separation phenomena during formation of asymmetric polyethersulphone membranes, *J. Membr. Sci. 493 (2015) 709-722.*

[172] L.F. Greenlee, N.S. Rentz, Influence of nanoparticle processing and additives on PES casting solution viscosity and cast membrane characteristics, *Polymer 103 (2016) 498-508.*

[173] A. Sotto, A. Boromand, R. Zhang, P. Luis, J.M. Arsuaga, J. Kim, B. Van der Bruggen, Effect of nanoparticle aggregation at low concentrations of TiO_2 on the hydrophilicity, morphology, and fouling resistance of PES–TiO_2 membranes, *J. Coll. Interf. Sci. 363 (2011) 540-550.*

[174] K.H. Chan, E.T. Wong, M. Irfan, A. Idris, N.M. Yusof, Enhanced Cu(II) rejection and fouling reduction through fabrication of PEG-PES nanocomposite ultrafiltration membrane with PEG-coated cobalt doped iron oxide nanoparticle, *J. Tai. Ins. Chem.Eng. 47 (2015) 50-58.*

[175] M. Zafar, M. Ali, S.M. Khan, T. Jamil, M.T.Z. Butt, Effect of additives on the properties and performance of cellulose acetate derivative membranes in the separation of isopropanol/water mixtures, *Desalination 285 (2012) 359-365.*
[176] M.d.C.C. Lucena, A.E. V. de Alencar, S.E. Mazzeto, S.d.A. Soares, The effect of additives on the thermal degradation of cellulose acetate, *Polym. Degrad. Stab. 80 (2003) 149-155.*
[177] M. Ali, M. Zafar, T. Jamil, M.T.Z. Butt, Influence of glycol additives on the structure and performance of cellulose acetate/zinc oxide blend membranes, *Desalination 270 (2011) 98-104.*
[178] T.-H. Bae, T.-M. Tak, Effect of TiO_2 nanoparticles on fouling mitigation of ultrafiltration membranes for activated sludge filtration, *J. Membr. Sci. 249 (2005) 1-8.*
[179] J. Garcia-Ivars, M.-I. Iborra-Clar, M.-I. Alcaina-Miranda, J.-A. Mendoza-Roca, L. Pastor-Alcañiz, Development of fouling-resistant polyethersulfone ultrafiltration membranes via surface UV photografting with polyethylene glycol/aluminum oxide nanoparticles, *Sep. Purif. Technol. 135 (2014) 88-99.*
[180] M. Kumar, Z. Gholamvand, A. Morrissey, K. Nolan, M. Ulbricht, J. Lawler, Preparation and characterization of low fouling novel hybrid ultrafiltration membranes based on the blends of GO−TiO_2 nanocomposite and polysulfone for humic acid removal, *J. Membr. Sci. 506 (2016) 38-49.*
[181] H. Mo, K.G. Tay, H.Y. Ng, Fouling of reverse osmosis membrane by protein (BSA): Effects of pH, calcium, magnesium, ionic strength and temperature, *J. Membr. Sci. 315 (2008) 28-35.*
[182] J.-J. Qin, Y. Li, L.-S. Lee, H. Lee, Cellulose acetate hollow fiber ultrafiltration membranes made from CA/PVP 360 K/NMP/water, *J. Membr. Sci. 218 (2003) 173-183.*
[183] P.K. Chatterjee, Thermogravimetric Analysis of Cellulose, *J. Polym. Sci. Part B: Polym.Phy. 6 (1968) 3217-3233.*
[184] L.-Y. Yu, H.-M. Shen, Z.-L. Xu, PVDF-TiO_2 composite hollow fiber ultrafiltration membranes prepared by TiO_2 sol-gel method and blending method, *J. Appl. Polym. Sci. 113 (2009) 1763-1772.*
[185] Z. Yuan, X. Dan-Li, Porous PVDF/TPU blends asymmetric hollow fiber membranes prepared with the use of hydrophilic additive PVP (K30), *Desalination 223 (2008) 438-447.*
[186] C.-W. Li, Y.-S. Chen, Fouling of UF membrane by humic substance: Effects of molecular weight and powder-activated carbon (PAC) pre-treatment, *Desalination 170 (2004) 59-57.*
[187] J.-J. Shieh, T.S. Chung, Effect of liquid-liquid demixing on the membrane morphology, gas permeation, thermal and mechanical properties of cellulose acetate hollow fibers, *J. Membr. Sci. 140 (1998) 67-79.*
[188] K. Kato, E. Uchida, E.-T. Kang, Y. Uyama, Y. Ikada, Polymer surface with graft chains, *Prog. Polym. Sci. 28 (2003) 209–259.*

[189] Z. Dong, H. Wei, J. Mao, D. Wang, M. Yang, S. Bo, X. Ji, Synthesis and responsive behavior of poly(N,N-dimethylaminoethyl methacrylate) brushes grafted on silica nanoparticles and their quaternized derivatives, *Polymer 53 (2012) 2074-2084.*

[190] Z. Yao, S. Du, Y. Zhang, B. Zhu, L. Zhu, A.E. John, Positively charged membrane for removing low concentration Cr(VI) in ultrafiltration process, *J. Wat.Proc. Eng. 8 (2015) 99-107.*

[191] K.A. Gebru, C. Das, Removal of Pb (II) and Cu (II) ions from wastewater using composite electrospun cellulose acetate/titanium oxide (TiO2) adsorbent, *J. Wat. Proc. Eng. 16 (2017) 1-13.*

[192] H. Zarrabi, M.E. Yekavalangi, V. Vatanpour, A. Shockravi, M. Safarpour, Improvement in desalination performance of thin film nanocomposite nanofiltration membrane using amine-functionalized multiwalled carbon nanotube, *Desalination 394 (2016) 83-90.*

[193] V. Vatanpour, M. Esmaeili, M.H.D.A. Farahani, Fouling reduction and retention increment of polyethersulfone nanofiltration membranes embedded by amine-functionalized multi-walled carbon nanotubes, *J. Membr. Sci. 466 (2014) 70-81.*

[194] G. Bayramoglu, M. Yakuparica, Adsorption of Cr(VI) onto PEI immobilized acrylate-based magnetic beads: Isotherms, kinetics and thermodynamics study, *Chem. Eng. J. 139 (2008) 20-28.*

[195] M.K. Aroua, F.M. Zuki, N.M. Sulaiman, Removal of chromium ions from aqueous solutions by polymer-enhanced ultrafiltration, *J. Hazard. Mater. 147 (2007) 752-758.*

[196] M. Muthukrishnan, B.K. Guha, Effect of pH on rejection of hexavalent chromium by nanofiltration, *Desalination 219 (2008) 171-178.*

[197] M.K. Zahran, Grafting of Methacrylic Acid and Other Vinyl Monomers Onto Cotton Fabric Using Ce (IV) Ion–Cellulose Thiocarbonate Redox System, J. Polym. Res., 13 (2005) 65-71.

[198] H.L. Hintz, D.C. Johnson, The Mechanism of Oxidation of Cyclic Alcohols by Cerium(1V), *J. Chem. Soc. 29 (1962) 556-564.*

[199] K. Kaliyamuthy, P. Elayaperumal, T. Balakrishnan, M. Santappa, Kinetics of polymerization of vinyl monomers initiated by manganese (III) acetate (II), *Polym. J. 14 (1982) 107-113.*

[200] J.-F. Zhong, X.-S. Chai, S.-Y. Fu, Homogeneous grafting poly (methyl methacrylate) on cellulose by atom transfer radical polymerization, Carbohydr. *Polym. 87 (2012) 1869-1873.*

[201] B. Tang, T. Xu, M. Gong, W. Yang, A novel positively charged asymmetry membranes from poly(2,6-dimethyl-1,4-phenylene oxide) by benzyl bromination and in situ amination: membrane preparation and characterization, *J. Membr. Sci. 248 (2005) 119-125.*

[202] X. Tongwen, A novel positively charged composite membranes for nanofiltration prepared from poly(2,6-dimethyl-1,4-phenylene oxide) by in situ amines crosslinking, *J. Membr. Sci. 215 (2003) 25-32.*

[203] M.R. Esfahani, J.L. Tyler, H.A. Stretz, M.J.M. Wells, Effects of a dual nanofiller, nano-TiO_2 and MWCNT, for polysulfone-based nanocomposite membranes for water purification, *Desalination 372 (2015) 47-56.*

[204] K.L. Jones, C.R. O'Melia, Protein and humic acid adsorption onto hydrophilic membrane surfaces: effects of pH and ionic strength, *J. Membr. Sci. 165 (2000) 31-46.*

[205] R.W. Yang Liu, Hongyang Ma, Benjamin S. Hsiao, Benjamin Chu, High-flux microfiltration filters based on electrospun polyvinylalcohol nanofibrous membranes, *Polymer 54 (2013) 548-556.*

[206] Xuefen wang, xuming chen, kyunghwan yoon, dufei fang, benjamin s. hsiao, b. chu, High Flux Filtration Medium Based on Nanofibrous Substrate with Hydrophilic Nanocomposite Coating.pdf, *Environ. Sci. Technol. 39 (2005) 7684- 7691*.

[207] H.S. Mansur, C.M. Sadahira, A.N. Souza, A.A.P. Mansur, FTIR spectroscopy characterization of poly (vinyl alcohol) hydrogel with different hydrolysis degree and chemically crosslinked with glutaraldehyde, *Mater. Sci. Eng.: C 28 (2008) 539-548.*

[208] A.K. Deepak A. Musale, Effects of surface crosslinking on sieving characteristics of chitosan:poly(acrylonitrile) composite nanofiltration membranes, *Sep. Purif. Technol. 21 (2000) 27-38.*